UNIVERSIDAD NACIONAL AUTÓNOMA DE MÉXICO
PROGRAMA DE POSGRADO EN ASTROFÍSICA

Instituto de Radioastronomía y Astrofísica

ASTROMETRÍA ULTRAPRECISA CON INTERFEROMETRÍA DE MUY LARGA BASE EN EL CENTIMÉTRICO Y MILIMÉTRICO

TESIS
QUE PARA OPTAR POR EL GRADO DE:
DOCTOR EN CIENCIAS (ASTROFÍSICA)

PRESENTA:
GISELA NOEMÍ ORTIZ LEÓN

TUTOR
DR. LAURENT RAYMOND LOINARD,
INSTITUTO DE RADIOASTRONOMÍA Y ASTROFÍSICA

MORELIA, MICHOACÁN, ENERO DE 2017

Astrometría ultraprecisa con interferometría de muy larga base en el centimétrico y milimétrico

por

Gisela Noemí Ortiz León

Resumen

En el trabajo presentado en esta tesis estudiamos dos escenarios diferentes utilizando la técnica de Interferometría de Muy Larga Línea de Base (VLBI), que consiste en combinar radiotelescopios separados miles de kilómetros para alcanzar las resoluciones espaciales más altas en astronomía. Primero, realizamos mediciones astrométricas muy precisas hacia regiones de formación estelar; segundo, estudiamos la emisión milimétrica proveniente del Centro Galáctico, con observaciones a escalas de ~ 1 UA.

La determinación de parámetros estelares fundamentales, e.g. distancias, tamaños y masas, es de gran importancia en el campo de la formación estelar. Los modelos teóricos que explican las etapas más tempranas de los procesos de formación estelar se pueden probar al comparar propiedades de los sistemas con observaciones, pero esto requiere que dichas propiedades, que son una función de la distancia, sean medidas con precisión. El primer objetivo de esta tesis fue obtener mediciones precisas de distancias y movimientos propios hacia varias estrellas jóvenes en las regiones de Ofiuco y Serpens/Aquila, mediante observaciones VLBI en múltiples épocas realizadas con el Arreglo de Líneas de Base muy Largas (VLBA). Con las distancias medidas a diferentes estrellas distribuidas en las regiones, investigamos su estructura a lo largo de la línea de visión, mientras que los modelos orbitales de sistemas binarios nos permitieron obtener masas estelares. También investigamos la relación entre las propiedades de estrellas jóvenes, e.g. etapa evolutiva y multiplicidad, y el nivel de emisión de radio detectable con VLBI que éstas producen.

La segunda parte de la tesis se enfocó en el estudio de la fuente Sgr A*, cuya emisión está asociada al agujero negro supermasivo más cercano, en el centro Galáctico. Las resoluciones angulares que solamente se pueden obtener con VLBI a longitudes de onda milimétricas son necesarias para detectar las escalas más pequeñas e investigar fenómenos relacionados con acreción alrededor de agujeros negros y formación de jets. Iniciamos operaciones en el Gran Telescopio Milimétrico para realizar observaciones junto con el VLBA a 3.5 mm. A esta longitud de onda, el efecto de la atmósfera sobre las visibilidades interferométricas es significativo, por lo que desarrollamos y utilizamos métodos para estudiar la emisión milimétrica de Sgr A* sin reconstrucción de imágenes. Determinamos la forma y orientación intrínseca de la fuente en épocas individuales, e interpretamos la detección de subestructura en la emisión como posiblemente introducida por el medio interestelar en la dirección del centro Galáctico.

Astrometría ultraprecisa con interferometría de muy larga base en el centimétrico y milimétrico

by

Gisela Noemí Ortiz León

Abstract

The work presented in this thesis uses the Very Long Baseline Interferometry (VLBI) technique, which combines radio telescopes separated by thousand of kilometers to achieve the highest spatial resolutions in all of astronomy, in two different scenarios. On one hand, we carried out high-precision astrometric measurements towards star-forming regions and, on the other hand, we studied the millimeter emission from the Galactic Center with observations at ~ 1 AU scales.

The determination of basic stellar parameters such as distances, sizes, and masses, is essential in the star-formation field. Theoretical models that explain the earliest phases of the star-formation processes can be tested by comparing predicted observational signatures with actual observations, but this requires the observables, which are a function of the distance, to be accurately measured. The first goal of this work was to obtain precise measurements of distances and proper motions of several young stars in the Ophiuchus and the Serpens/Aquila regions by performing multi-epoch VLBI observations with the Very Long Baseline Array (VLBA). By using the distance measurements, we were able to further investigate the structure of the clouds, while the orbital modeling of binary systems allowed us to obtain stellar masses. We also examined the relation between the properties of young stars, such as evolutionary stage and multiplicity, and their level of radio emission detectable on VLBI baselines.

The second part of the thesis focuses on the source Sgr A*, which is associated with the nearest supermassive black hole, at the Galactic Center. High angular resolutions, only attainable with VLBI at millimeter wavelengths, are needed in order to detect the smallest scales and investigate phenomena related to black hole accretion and jet launching. We initiated operations for mm-VLBI observations at the Large Millimeter Telescope and performed a 3.5-mm VLBI experiment in concert with the VLBA. Because at this short wavelength the effect of the atmosphere on interferometric visibilities becomes severe, we developed and used non-imaging methods to study the millimeter emission from Sgr A*. We determined the intrinsic shape and orientation of the source at individual epochs, and interpreted the detection of substructure in the source image as possibly introduced by the interstellar medium in the direction of the Galactic Center.

A mis padres Petra y Ricardo
por su apoyo incondicional,
y a mis hermanos Xóchitl y Elihu
por acompañarme en esta travesía.

Agradecimientos

Me gustaría agradecer a Laurent R. Loinard, no solamente por proponerme el trabajo desarrollado en esta tesis, sino por invitarme a participar en varios de sus proyectos durante mi prolongada estadía en el CRyA (ahora IRyA). Laurent me ha mostrado que se puede hacer ciencia de calidad atacando problemas básicos pero fundamentales y me ha transmitido una gran fascinación hacia la astrometría y la VLBI. Fueron las diversas conversaciones sobre el trabajo aquí presentado las que me han guiado a aterrizar los conceptos fundamentales de la radiointerferometría. También, agradezco el cálido recibimiento que él y su familia me han brindado, en particular durante mi estancia en Bonn.

De igual manera, agradezco a Luis F. Rodríguez por las innumerables veces que ha atendido mis inquietudes y por introducirme en el campo de la radioastronomía. Sin lugar a dudas, las aportaciones a esta tesis por parte del resto de los miembros del grupo del censo de distancias del cinturón de Gould también han sido de gran relevancia. El departamento administrativo del IRyA me ha auxiliado en incontables ocasiones para planificar la asistencia a congresos y realizar trámites académicos.

Shep Doeleman y su grupo de trabajo siempre me recibieron con mucho entusiasmo en Haystack y Cambridge. A ellos les agradezco por su confianza depositada en mi para dirigir la publicación asociada a las observaciones VLBI en el GTM. No podría no mencionar a los observadores y personal de planta del GTM, quienes contribuyeron en gran medida al éxito de las observaciones VLBI en el sitio.

La culminación de este proyecto no hubiera sido posible sin el constante afecto y apoyo que he recibido de mis amigos más cercanos. Extendiendo un especial agradecimiento a Ezequiel M., con quien he compartido muchas experiencias agradables fuera de la academia durante mi estancia en Morelia. Mariana R. y Carolina R., mis compañeras de oficina y casa, gracias por soportarme durante todos estos años. Alba L., gracias por tu cálida amistad. Mayor es mi gratitud a Talía L., quien siempre me ha brindado su consejo y apoyo en varios momentos críticos.

Finalmente agradezco a CONACyT por la asignación de la beca doctoral No. 339802 y a la fundación von Humboldt por el apoyo financiero para mi visita al MPIfR.

Publicaciones

La presente tesis es una compilación de las publicaciones I–IV, las cuales se derivaron directamente del trabajo realizado por el autor.

I Ortiz-León, G. N., Loinard, L., Mioduszewski, A. J., Dzib, S. A., Rodríguez, L. F., Pech, G., Rivera, J. L., Torres, R. M., Boden, A. F., Hartmann, L., Evans, II, N. J., Briceño, C., Tobin, J., Kounkel, M. A., and González-Lópezlira, R. A.
The Gould's Belt Very Large Array Survey. II. The Serpens Region
The Astrophysical Journal (**2015**), 805, 9

II Ortiz-León, G. N., Loinard, L., Dzib, S. A., Mioduszewski, A. J., Rodríguez, L. F., Torres, R. M., González-Lópezlira, R. A., Pech, G., Rivera, J. L., Kounkel, M. A., Hartmann, L., Boden, A. F., , Evans, II, N. J., Briceño, C., Tobin, J., and Galli, P. A. B.
The Gould's Belt Distances Survey (GOBELINS) I. Trigonometric parallax distances and depth of the Ophiuchus complex
The Astrophysical Journal (**2016**), en prensa.

III Ortiz-León, G. N., Loinard, L., Kounkel, M. A., Dzib, S. A., Mioduszewski, A. J., Rodríguez, L. F., Torres, R. M., Pech, G., Rivera, J. L., Hartmann, L., Boden, A. F., , Evans, II, N. J., Briceño, C., Tobin, J., Galli, P. A. B., and Gudehus, D.
The Gould's Belt Distances Survey (GOBELINS) III. The distance to the Serpens/Aquila Molecular Complex
The Astrophysical Journal (**2016**), en prensa.

IV Ortiz-León, G. N., Johnson, M. D., Doeleman, S. S., Blackburn, L., Fish, V. L., Loinard, L., Reid, M. J., Castillo, E., Chael, A. A., Hernández-Gómez, A., Hughes, D. H., León-Tavares, J., Lu, R.-S., Montaña, A., Narayanan, G., Rosenfeld, K., Sánchez, D., Schloerb, F. P., Shen, Z.-q., Shiokawa, H., SooHoo, J., and Vertatschitsch, L.
The Intrinsic Shape of Sagittarius A at 3.5 mm Wavelength*
The Astrophysical Journal (**2016**), 824, 40

Publicaciones no incluidas en esta tesis, donde el autor realizó una contribución significativa:

- Dzib, S. A., Ortiz-León, G. N., Loinard, L., Mioduszewski, A. J., Rodríguez, L. F., Torres, R. M., and Deller, A.
  VLBA determination of the distance to nearby star-forming regions VII. Monoceros R2
  The Astrophysical Journal (**2016**), 826, 201.

- Kounkel, M. A., Hartmann, L., Loinard, L., Ortiz-León, G. N., Mioduszewski, A. J., Rodríguez, L. F., Dzib, S. A., Torres, R. M., Pech, G., Galli, P. A. B., Rivera, J. L., Boden, A. F., , Evans, II, N. J., Briceño, C., and Tobin, J.
  The Gould's Belt Distances Survey (GOBELINS) II. Distances and structure towards the Orion molecular clouds
  The Astrophysical Journal (**2016**), en prensa.

Artículos publicados antes de la presente disertación como primer autor:

- Ortiz-León, G. N., Rodríguez, L. F., and Tapia, M.
  Extended Non-Thermal Emission Possibly Associated with Cyg OB2 #5
  Revista Mexicana de Astronomía y Astrofísica (**2012**), 48, 85

- Ortiz-León, G. N., Loinard, L., Rodríguez, L. F., Mioduszewski, A. J., and Dzib, S. A.
  The Non-thermal, Time-variable Radio Emission from Cyg OB2 #5: A Wind-collision Region
  The Astrophysical Journal (**2011**), 737, 30

Índice general

Capítulo 1

Introducción

Una tarea fundamental de la astronomía es ubicar objetos estelares con respecto al Sol u otros objetos. Para ello, además de una medición precisa de la posición en el plano del cielo, es necesario obtener la posición del objeto estelar a lo largo de la línea de visión. Para objetos en la vecindad solar ($d \lesssim 1$ kpc), el monitoreo periódico de la fuente en una escala temporal comparable a la vida humana permite derivar su movimiento propio, mientras que observaciones de alta precisión en el curso de 1–2 años son necesarias para obtener la distancia a través de la *paralaje trigonométrica* (Sección 1.1.1). Si además se conoce la velocidad radial del objeto, entonces se tiene la información completa de su posición y velocidad en el espacio tridimensional. La obtención de tales mediciones es el principal objetivo de la *astrometría*.

La resolución angular de un telescopio con apertura circular de diámetro D está dada por el límite de difracción de Rayleigh: dos estrellas no se pueden resolver si la segunda estrella está posicionada dentro del primer mínimo, $\theta_{\rm min}$, del disco de Airy de la otra estrella, donde

$$\theta_{\rm min} = 1.22\lambda/D, \tag{1-1}$$

y λ es la longitud de onda observada. Entonces, la resolución angular mejora con un

incremento del tamaño de la apertura u observando a longitudes de onda corta. Sin embargo, a menos que en tiempo real se ejecuten ajustes complejos al sistema óptico, la turbulencia atmosférica impide que la resolución angular de telescopios ópticos en tierra mejore con el aumento del tamaño de la apertura. En este caso la precisión astrométrica se ve limitada a una escala de ~ 1 segundo de arco (van Altena, 2013).

En la banda de radio correspondiente a ondas centimétricas, el efecto de la turbulencia atmosférica se reduce considerablemente y la resolución angular está totalmente determinada por el límite de difracción. Precisiones astrométricas de microsegundos de arco (μas) son ahora posibles gracias al gran desarrollo que la interferometría de radio ha experimentado en las últimas cuatro décadas. Esta técnica consiste en combinar las señales registradas en arreglos extendidos de antenas para obtener imágenes del cielo con muy alta resolución angular y precisión astrométrica (Thompson *et al.*, 2007). Dicha resolución está dada por la ecuación 1-1, donde ahora la separación máxima entre las antenas B sustituye al diámetro D. Los arreglos de línea de base muy larga (llamados arreglos VLBI por el ingés *Very Long Baseline Interferometry*) utilizan separaciones continentales, de varios miles de kilómetros, por lo que observando a longitudes de onda centimétrica alcanzan resoluciones angulares por abajo del milisegundo de arco. Además de permitir estudiar a detalle la estructura de fuentes de radio, los arreglos VLBI permiten medir la posición relativa de fuentes de radio brillantes con una precisión típica de unas cuantas decenas de μas (Reid y Honma, 2014). Movimientos propios y paralajes trigonométricas pueden por lo tanto medirse con un error fraccional $< 10\,\%$ para objetos situados a $d < 5$ kpc.

La primera parte de esta tesis pretende aplicar la técnica VLBI para obtener mediciones astrométricas precisas hacia estrellas en regiones de formación estelar cercanas. Particularmente, nuestro estudio se concentra en regiones que pertenecen a la estructura Galáctica conocida como el cinturón de Gould (Sección 1.1.2). En este primer capítulo, describimos la motivación detrás de nuestro trabajo, a la vez que introducimos algunos conceptos claves que se utilizarán ampliamente durante el desarrollo del mismo.

1.1. Motivación

1.1.1. Astrometría de objetos estelares jóvenes

Los modelos teóricos que explican las etapas más tempranas de la formación estelar requieren observables precisas para acotar el espacio de parámetros libres. Las observables, por ejemplo el tamaño físico de la fuente, la luminosidad y la masa estelar, por mencionar algunas, son en general una función de la distancia. Debido a que las estrellas en formación se encuentran embebidas en nubes densas de gas molecular y polvo, la luz estelar radiada a longitudes de onda corta es absorbida casi en su totalidad. Por esta razón, la distancia a objetos estelares jóvenes, y por consecuencia, la distancia a la región que habitan no está bien determinada. Entonces, los errores asociados a la distancia (que típicamente son 20–30 %), constituyen la principal fuente de error en la determinación de parámetros físicos estelares. Sin embargo, las nubes moleculares son transparentes a la radiación en radiofrecuencias, y los objetos estelares jóvenes comúnmente son fuentes de radio. Resulta entonces casi obvio que una alternativa a los telescopios ópticos es la de utilizar la técnica VLBI para obtener mediciones de la distancia a regiones de formación estelar.

El método más directo para medir distancias fuera de nuestro sistema solar es la paralaje trigonométrica. El ángulo subtendido por el semieje mayor de la elipse trazada por una estrella cercana debido a la traslación de la Tierra alrededor del Sol es el ángulo de paralaje, y está relacionado con la distancia d a la fuente mediante,

$$\frac{r}{d} = \tan\varpi \approx \varpi, \tag{1-2}$$

donde r es la distancia Tierra-Sol r y $\varpi \ll 1$ se mide en radianes. Usando la definición de que un *parsec* (pc) es la distancia de una fuente hipotética para la cual la paralaje es exactamente $\varpi = 1''$ y con la conversión de segundos de arco a radianes se obtiene

$$d = \left(\frac{\varpi}{1''}\right)^{-1} \text{pc}. \tag{1-3}$$

Tomando el desarrollo de Taylor hasta primer orden de la expresión anterior, se sigue que una buena aproximación del error en la distancia está dado por $\Delta d = \sigma_\varpi / \varpi^2$, donde σ_ϖ es la incertidumbre en la medición de la paralaje. Entonces, dentro de esta aproximación, el error fraccional en d es igual al error fraccional en ϖ. Por ejemplo, dada una precisión astrométrica de 100 μas, un valor que es alcanzable con observaciones VLBI, el error fraccional en la distancia resulta ser 5 % para objetos a 500 pc.

Ajustes astrométricos

El movimiento de una estrella respecto al Sol presenta al menos tres componentes: (1) el movimiento del Sol respecto al sistema local de reposo (la velocidad peculiar del Sol), (2) el movimiento inducido por la paralaje anual y (3) un movimiento de la estrella respecto al sistema local de reposo que le corresponde (su velocidad peculiar). Existe también una contribución que resulta de la rotación diferencial Galáctica debido a que radios Galactocéntricos diferentes tienen una velocidad circular distinta. Sin embargo, esta contribución se puede despreciar ya que las regiones que estudiamos están lo suficientemente cercanas al Sol para no estar afectadas por la rotación diferencial. Loinard *et al.* (2007) señalan que la ascensión recta (α) y declinación (δ) de un fuente aislada se pueden expresar como una función del tiempo de acuerdo a

$$\begin{aligned} \alpha(t) &= \alpha_0 + (\mu_\alpha \cos\delta)t + \varpi f_\alpha(t), \\ \delta(t) &= \delta_0 + \mu_\delta t + \varpi f_\delta(t), \end{aligned} \tag{1-4}$$

donde (α_0, δ_0) es la posición de la fuente en una época de referencia dada, (μ_α, μ_δ) el movimiento propio, que incluye las componentes (1) y (3) del movimiento aparente, y f_α y f_δ las proyecciones de la elipse paraláctica sobre α y δ, respectivamente.

Dicho la anterior, nuestro primer objetivo consistirá en medir (α, δ) en un número significativo de épocas. Usando este conjunto de datos, el valor de ϖ y del resto de los

parámetros astrométricos se derivarán mediante un ajuste de χ^2, siguiendo la formulación dada en Loinard *et al.* (2007). Si bien este enfoque ha sido aplicado con éxito en estrellas aisladas (por ejemplo, Torres *et al.*, 2007, 2009), un tratamiento más complejo debe aplicarse en el caso de que los objetos formen parte de sistemas binarios o de mayor multiplicidad. El movimiento propio de una estrella en un sistema múltiple estará acelerado y curvado debido a la influencia gravitacional de los otros miembros del sistema. Para tomar en cuenta la multiplicidad, podemos añadir términos de aceleración a_α y a_δ, a la ecuación 1-4 (la cual considera que el movimiento propio es uniforme y lineal), de tal forma que,

$$\begin{aligned} \alpha(t) &= \alpha_0 + (\mu_{\alpha 0}\cos\delta)t + \varpi f_\alpha(t) + \frac{1}{2}(a_\alpha\cos\delta)t^2, \\ \delta(t) &= \delta_0 + \mu_{\delta 0}t + \varpi f_\delta(t) + \frac{1}{2}a_\delta t^2, \end{aligned} \tag{1-5}$$

donde $\mu_{\alpha 0}$ y $\mu_{\delta 0}$ son los movimientos propios en la época de referencia. Ésta es una buena aproximación siempre y cuando la aceleración permanezca constante en el intervalo de tiempo cubierto por las observaciones VLBI, pero, evidentemente, la aceleración cambiará notablemente si el objeto completa una órbita o una fracción considerable de ésta durante dicho intervalo de tiempo.

Ajuste astrométrico de estrellas binarias

Los sistemas jóvenes de múltiples estrellas son el resultado de la fragmentación de núcleos densos en colapso gravitacional. Las resoluciones angulares que típicamente se obtienen en observaciones VLBI permitirán resolver componentes en sistemas múltiples que posean separaciones angulares del orden de 0.010 segundos de arco. El periodo orbital de dichos sistemas es comparable a la escala de tiempo que comúnmente se emplea en monitoreos con VLBI (cf. Capítulo 3), y por tanto los efectos del movimiento orbital no se pueden ignorar en los ajustes astrométricos. Si las posiciones de cada componente en un sistema binario se colectan en un número suficiente de épocas, entonces es posible

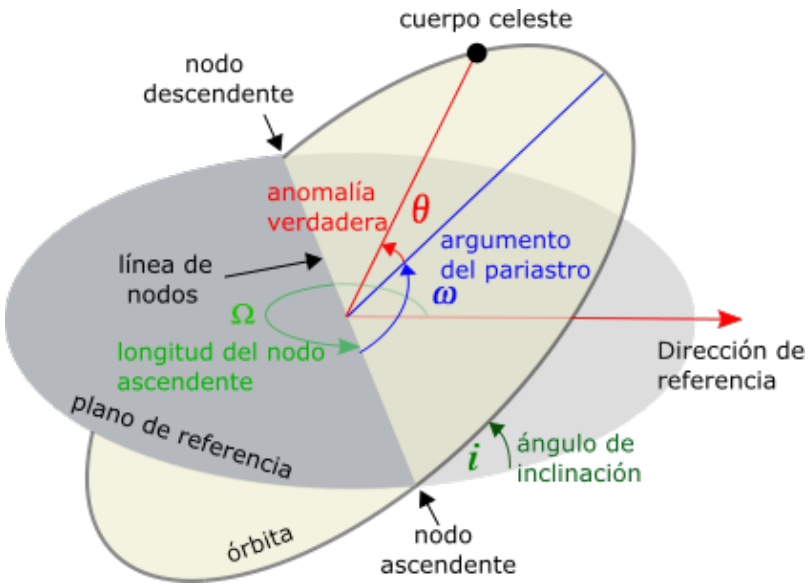

Figura 1-1 Elementos de una órbita Kepleriana.

modelar la órbita del sistema.

Una órbita Kepleriana está completamente definida si se conocen los siguientes siete parámetros (e.g., Roy, 2005): semi-eje mayor a, periodo orbital P, excentricidad e, ángulo desde la línea de nodos al periastro u argumento del periastro[1] ω, época del paso por el periastro T_P, ángulo de inclinación i y ángulo de posición del nodo ascendente (Ω, Figura 1-1). Debido a que la técnica VLBI nos permite medir la posición absoluta de componentes individuales en un sistema binario, entonces es posible analizar las características de la órbita de cada componente. Consideremos por ahora a la componente primaria del sistema, cuya órbita alrededor del centro de masa tiene semieje mayor a_1. La contribución de la órbita al movimiento de esta componente en una época dada t se determina a partir

[1]La palabra *argumento* viene del Latín y su uso aquí significa "dejar en claro" la posición del periastro.

de los parámetros orbitales como a continuación se muestra. Dada la anomalía[2] media M,

$$M = \frac{2\pi}{P}(t - T_P), \tag{1-6}$$

la anomalía excéntrica E se obtiene al resolver numéricamente la ecuación de Kepler:

$$M = E - e\sin E. \tag{1-7}$$

Entonces la anomalía verdadera θ y la distancia r de la componente respecto al centro de masa se derivan usando,

$$\tan\left(\frac{\theta}{2}\right) = \left(\frac{1+e}{1-e}\right)^{1/2} \tan\left(\frac{E}{2}\right) \text{ y} \tag{1-8}$$

$$r = \frac{(1-e^2)}{1+e\cos\theta}. \tag{1-9}$$

Conociendo θ y r, la órbita proyectada en el plano del cielo de la componente primaria alrededor del centro de masa del sistema se obtiene mediante

$$\begin{aligned} \alpha(t)\cos\delta &= a_1 r(\cos(\theta+\omega)\sin\Omega - \sin(\theta+\omega)\cos\Omega\cos i), \\ \delta(t) &= a_1 r(\sin(\theta+\omega)\sin\Omega\cos i + \cos(\theta+\omega)\cos\Omega). \end{aligned} \tag{1-10}$$

Para la componente secundaria basta con sustituir a_1 por a_2 (el cual se obtiene a partir de la relación $q = a_1/a_2 = m_2/m_1$) y θ por $\theta + 180^o$. El movimiento en el plano del cielo de cada componente en un sistema binario está entonces descrito por la suma de los términos de las expresiones 1-4 y 1-10. Como veremos en el Capítulo 3, Kounkel *et al.* (2016) han desarrollado un código que permite obtener los parámetros orbitales junto con los 5 parámetros astrométricos por un método de minimización de χ^2. Para esto, el código explora una malla de valores iniciales en P, T_P y ω, y ajusta el resto de los parámetros

[2]Kepler utilizó la palabra *anomalía* para referirse a la desviación del movimiento real de un planeta respecto al caso hipotético de un movimiento circular perfecto con el Sol en el centro. Ésta desviación la midió en términos de tres ángulos u *anomalías*.

directamente. El ángulo de inclinación de la órbita queda definido sin ambigüedades por la dirección del movimiento de las componentes en el plano del cielo, es decir, si éste ocurre en el mismo sentido o sentido contrario al giro de las manecillas del reloj (Figura 1-1). Finalmente, dado que la distancia al sistema queda determinada en el ajuste, las masas de cada componente del sistema se derivan de manera inmediata combinando la tercera Ley de Kepler con el cociente de masas.

1.1.2. Estructura tridimensional de nubes moleculares

Las estrellas se forman a partir del colapso gravitacional de grandes aglomeraciones de gas molecular y polvo, llamadas nubes moleculares. El estado dinámico y la estructura de las nubes gobiernan los procesos de formación estelar, ya que determinan tanto la tasa de formación estelar como los sitios de formación de nuevas estrellas. Nuestro conocimiento actual sobre la estructura de nubes moleculares se ha obtenido a partir de observaciones de líneas moleculares y censos de emisión de continuo de polvo realizados principalmente con las misiones espaciales *Spitzer* y *Herschel*. Estas misiones se han enfocado, pero no limitado, a cinco regiones, que por su cercanía, representan laboratorios ideales para el estudio de fenómenos relacionados con la formación estelar: Tauro, Ofiuco, Orión, Serpens y Perseo. El interés hacia estas regiones también se debe a que éstas se distribuyen en una banda estrecha a la cual se le conoce en la literatura como el cinturón de Gould (Figura 1-2), que posiblemente corresponde a la proyección de una estructura plana o disco inclinado con respecto al plano Galáctico (Poppel, 1997). Por su parte, además de tratarse de la región más cercana al Sol con actividad de formación estelar, el Cinturón de Gould contiene un mayor número, con respecto al disco Galáctico local, de asociaciones de estrellas masivas tipo OB, cúmulos estelares, complejos de nubes moleculares y supernovas (e.g. Bobylev 2016), razón por la cual su estructura y evolución es estudiada actualmente por varios autores.

Los diversos censos observacionales dirigidos hacia el cinturón de Gould han per-

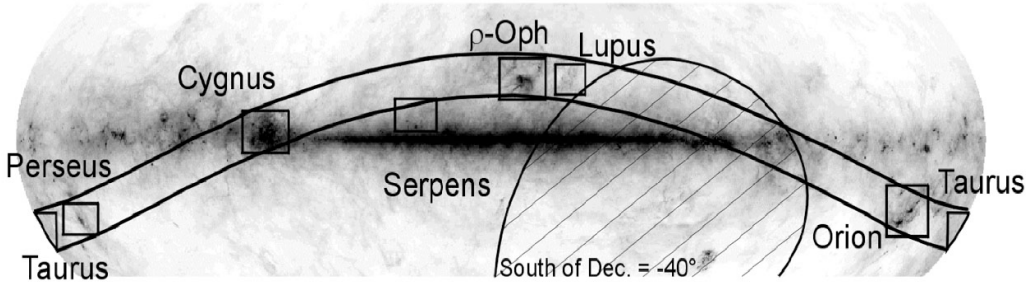

Figura 1-2 El cinturón de Gould visto en proyección sobre la Vía Láctea.

mitido la caracterización global de nubes moleculares. Sin embargo, aún se desconoce tanto la estructura como la cinemática interna de las mismas. La determinación de estas características es esencial porque, como mencionamos anteriormente, establecen las condiciones iniciales a partir de las cuales se forman nuevas estrellas mediante un proceso de colapso gravitacional.

Usando mediciones precisas de la distancia a cuatro estrellas jóvenes en la región de Tauro (con incertidumbres menores al 1 %), Torres *et al.* (2009) determinaron la distancia a diferentes subestructuras dentro de la nube, y encontraron que éstas se distribuyen abarcando una profundidad de 30 pc dentro de la nube. Sus resultados demostraron que la estructura tridimensional y cinemática interna de nubes moleculares cercanas puede determinarse con mediciones astrométricas precisas de una muestra mayor de estrellas en cada una de las nubes. Nuestro objetivo en la primera parte de esta tesis es expandir el trabajo iniciado por Torres *et al.* (2007), Loinard *et al.* (2007), Loinard *et al.* (2008), Hirota *et al.* (2008, 2011), Torres *et al.* (2009) y Dzib *et al.* (2010) hacia las cinco regiones listadas anteriormente como parte del proyecto *"El censo de distancias del cinturón de Gould"* (Loinard, 2013), al cual nos referiremos como GOBELINS[3] en el resto de la tesis.

Hasta antes de GOBELINS solo se conocían del orden de 15 estrellas, distribuidas en varias regiones de formación estelar cercanas, cuya emisión de radiocontinuo es detectable

[3]GOBELINS es el acrónimo inglés para el nombre del proyecto *the GOuld's BELt dIstaNces Survey* y hace referencia a los tapices elaborados en una fábrica que lleva el mismo nombre en París, Francia.

con arreglos VLBI. Es necesario entonces buscar nuevas fuentes de radio que estén asociadas con objetos estelares jóvenes y que presenten características idóneas para estudios astrométricos con VLBI. Las regiones de formación estelar contienen típicamente varios cientos de estrellas jóvenes distribuidas en áreas de varios parsecs de diámetro. En la primera fase de GOBELINS se utilizó el Arreglo muy Grande (VLA por el inglés Very Large Array) para realizar mapeos extendidos en cada una de las regiones de interés e identificar la muestra de fuentes que serán observadas con VLBI. En la presente tesis, analizaremos y discutiremos las observaciones VLA hacia las regiones de Serpens y la Grieta del Aquila, mientras que las observaciones correspondientes a las otras regiones se reportan en Dzib *et al.* (2013), Kounkel *et al.* (2014), Dzib *et al.* (2015) y Pech *et al.* (2016).

Distancias y velocidades de nubes moleculares derivadas de GOBELINS servirán eventualmente para determinar la expansión y/o rotación del Cinturón de Gould e investigar su origen. Varios trabajos en la literatura han explorado modelos que expliquen la formación y la cinemática de esta estructura, pero a la fecha no han sido concluyentes. Perrot y Grenier (2003), por ejemplo, sugirieron que la estructura podría haberse formado a partir de una onda de choque expansiva en el medio interestelar, la cual pudo haber resultado de la explosión múltiple de supernovas. Comeron y Torra (1994, 1992), por otro lado, propusieron que el impacto oblicuo contra el disco de la Galaxia de una nube de hidrógeno molecular moviéndose a alta velocidad puede dar lugar al origen del Cinturón de Gould.

1.2. VLBI milimétrica

El desarrollo de la VLBI a longitudes de onda corta ha sido más paulatino comparado con la VLBI centimétrica, principalmente porque la primera exige instrumentación, diseño de antenas y técnicas de análisis de datos más complejos. A una longitud de onda menor a 1 cm, la profundidad óptica de la tropósfera se hace significativa, por lo que la emisión atmosférica introduce ruido adicional al sistema receptor de las antenas. Por otro lado, los cambios en la densidad columnar del vapor de agua en la atmósfera se

traducen en variaciones del camino óptico de la radiación y a su vez en variaciones de la fase interferométrica. El *tiempo de coherencia* atmosférico, que corresponde a la escala temporal sobre la cual las visibilidades interferométricas se pueden integrar sin pérdidas de amplitud, es del orden de unas cuantas decenas de segundos. Esto reduce considerablemente el cociente de señal a ruido de las visibilidades, las cuales deben promediarse sobre estos cortos intervalos de tiempo. Además, a altas frecuencias la demanda en la precisión de la superficie reflectora de la antena y del apuntado de la misma es mayor. Por estas razones, las observaciones astrométricas con VLBI a longitudes de onda corta están limitadas hasta $\lambda = 1.3$ cm (e.g., Hachisuka *et al.*, 2015), pero otros estudios que requieren muy alta resolución angular, prescindiendo de la precisión astrométrica, pueden observar hasta $\lambda = 0.13$ cm.

Comúnmente, la VLBI milimétrica es empleada para estudiar fuentes aisladas, contrario al caso centimétrico, donde es común llevar a cabo monitoreos extensivos en grandes regiones del cielo. En este contexto, la fuente de radio situada en el centro de nuestra Galaxia, Sagittarius A* (Sgr A*) ha sido en los últimos años un foco de mucho interés por la comunidad de astronómos dedicados a la VLBI milimétrica. Sgr A* está asociada a un agujero negro supermasivo de $\sim 4 \times 10^6$ $M_\odot$ (Ghez *et al.*, 2008), cuya emisión milimétrica está confinada a una región de tamaño ~ 37 μas (Doeleman *et al.*, 2008). Si bien es ampliamente aceptada la presencia de acreción de materia hacia Sgr A*, los procesos que dan lugar a la emisión milimétrica no están completamente determinados. Motivados por la demanda de observables necesarias para acotar el espacio de parámetros libres en los diversos modelos astrofísicos de Sgr A*, en la segunda parte de la tesis utilizamos la técnica VLBI, a una longitud de onda de 3.5 mm, para caracterizar la estructura de la fuente a escalas muy cercanas al horizonte de eventos. Este trabajo involucró la primera participación del Gran Telescopio Milimétrico (GTM), situado en Puebla, México, en un proyecto VLBI.

1.3. Estructura de la tesis

El Capítulo 2 está dedicado a describir observaciones de radio obtenidas con el VLA hacia la región de formación estelar Serpens. Como se mencionó anteriormente, estas observaciones nos permitirán realizar la identificación de estrellas jóvenes con características idóneas para la astrometría VLBI de la región. En el Capítulo 3 describimos primeramente el proyecto GOBELINS. Posteriormente detallamos la estrategia adoptada para realizar las observaciones astrométricas con el Arreglo Interferométrico de muy Larga Base (VLBA) hacia cinco regiones de formación estelar en el cinturón de Gould. Enseguida describimos nuestro método de calibración y análisis de datos obtenidos específicamente hacia la región de Ofiuco y discutimos las propiedades de las fuentes detectadas en esta región. Los Capítulos 3 y 4 describen la obtención de la astrometría de objetos estelares jóvenes en Ofiuco y Serpens, respectivamente.

La segunda parte de esta tesis presenta el trabajo en el cuál extendemos el uso de la técnica VLBI a longitudes de onda milimétricas. El Capítulo 5 resume la integración y puesta en marcha del sistema VLBI en el GTM, y enseguida describe las primeras observaciones VLBI desde México hacia el agujero negro supermasivo en el centro de la Vía Láctea, Sgr A*. Finalmente las conclusiones se presentan el Capítulo 6.

Parte I

Astrometría de estrellas jóvenes con VLBI

Capítulo 2

Observaciones sensitivas de radio hacia la región de Serpens

La nube molecular de Serpens es una región con formación estelar de baja masa. Contiene cientos de objetos estelares jóvenes embebidos en un área de aproximadamente 1 grado^2, con centro en $\alpha_{J2000} = 18^h29^m00^s$, $\delta_{J2000} = +00^o30'00''$ (Strom *et al.*, 1974). La gran mayoría de estos objetos han sido identificados, junto con su estado evolutivo, principalmente a partir de su distribución espectral de energía, detección de emisión en rayos-X y posición en el diagrama color-color en el mediano infrarrojo. Una revisión completa de la población estelar de la región se puede consultar en el trabajo de Eiroa *et al.* (2008). Serpens se encuentra proyectada en el plano del cielo muy cerca de *La Grieta del Aquila*, una gran estructura de nubes obscuras distinguible en mapas de extinción en el óptico (Figura 2-1).

Embebidos dentro de la región del Aquila, y a $\sim 3^o$ al sur de Serpens, se encuentran los cúmulos estelares Serpens Sur ($\alpha_{J2000} = 18^h30^m00^s$, $\delta_{J2000} = -02^o02'00''$; Gutermuth *et al.*, 2008) y W40 ($\alpha_{J2000} = 18^h31^m29^s$, $\delta_{J2000} = -02^o05'24''$; Sharpless, 1959), que también albergan a un gran número de estrellas en formación. Estos cúmulos han sido observados extensivamente en el infrarrojo, submilimétrico y rayos-X, pero al igual que Serpens, sólo pocos estudios se han dedicado a caracterizar su emisión en el centimétrico. Los dos

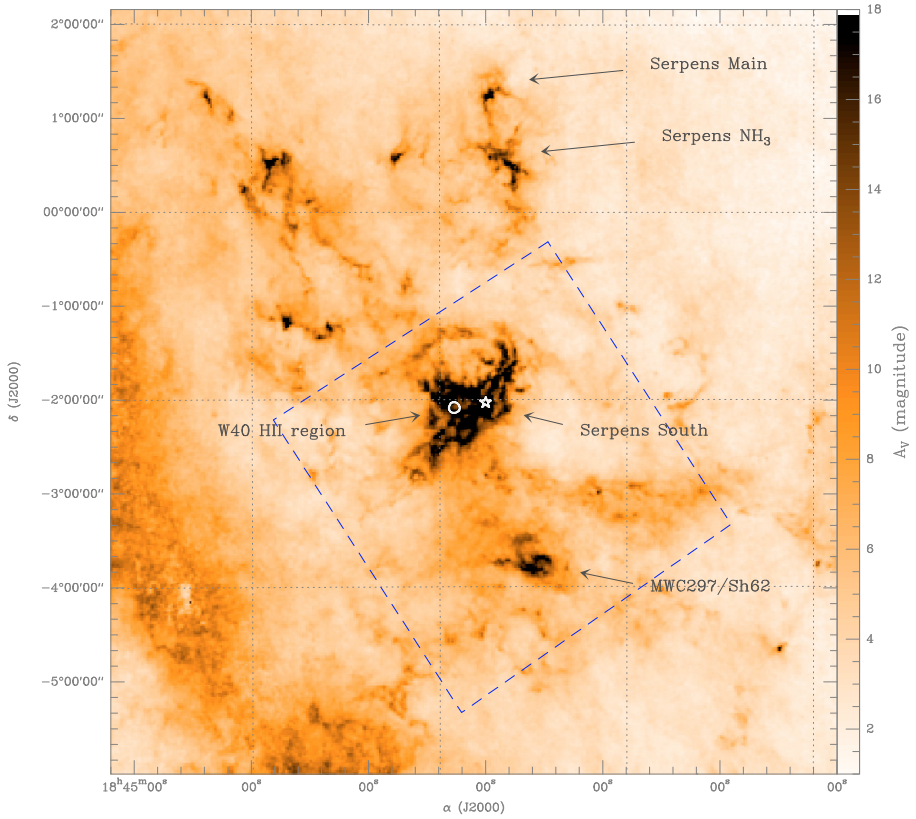

Figura 2-1 Mapa de extinción visual hacia la región de Serpens y La grieta del Aquila. Serpens se ubica en la parte Norte del mapa, mientras que La Grieta del Aquila es la estructura alargada que se extiende del noreste al suroeste, justo por arriba del plano Galáctico que también se distingue claramente en la parte inferior izquierda de la imagen. Figura tomada de Bontemps *et al.* (2010).

trabajos más importantes en el radio realizados previo a nuestras observaciones en 2011 son los de Eiroa *et al.* (2005) en Serpens y Rodríguez *et al.* (2010) en W40. Serpens Sur, por otra parte, ha recibido un particular interés en los últimos años, ya que se encuentra en una fase muy temprana de formación y representa uno de los sitios con mayor actividad de formación estelar dentro de 1 kpc (Kern *et al.*, 2016).

Mucho se ha discutido en la literatura sobre la distancia a Serpens, W40 y Serpens

Sur. A la fecha, no existe un consenso sobre si las tres regiones son parte de una misma estructura o si se encuentran a diferentes profundidades sobre la línea de visión. En el Capítulo 4 haremos una revisión de las estimaciones de distancia existentes a cada una de éstas. Sin embargo, es importante señalar aquí que usualmente se usa para Serpens y Serpens Sur el valor de 260 pc determinado por Straižys *et al.* (1996). Por otro lado, para W40 comúnmemente se utiliza una distancia de $\sim 500 \pm 50$ pc, la cual fue derivada por Kuhn *et al.* (2010) y Shuping *et al.* (2012) por métodos indirectos. Kuhn *et al.* (2010) escalaron la función de luminosidad en rayos-X derivada de observaciones de Chandra hacia Orión para ajustar la distribución observada en W40, mientras que Shuping *et al.* (2012) ajustaron modelos de atmósferas estelares a la distribución espectral de energía en el infrarrojo determinada para cuatro estrellas del cúmulo en secuencia principal. Como parte de los trabajos que antecedieron al proyecto GOBELINS, Dzib *et al.* (2010) obtuvieron la primera medición directa de la distancia a Serpens por medio de la determinación de la paralaje trigonométrica al objeto protoestelar EC 95, encontrando 415 ± 25 pc. Este último resultado ha desatado algo de controversia ya que representa un incremento de 60 % en la distancia, con respecto al valor más aceptado, lo cual se traduce en cambios por factores significativos en los parámetros estelares. Por ejemplo, los objetos en Serpens serían en realidad ~ 160 % más luminosos de lo que se estimaba con base a una distancia de 260 pc. Es necesario, entonces, obtener nuevas mediciones precisas de la distancia a objetos en las regiones de Serpens y la Grieta del Aquila para confirmar el resultado de Dzib *et al.* (2010). En caso de corroborarse, una distancia mayor tendría implicaciones importantes sobre el estado de formación estelar en las regiones. A continuación extendemos la discusión sobre la importancia de observaciones de radio en el contexto de formación estelar, y posteriormente presentamos las observaciones realizadas con el VLA hacia Serpens, W40 y Serpens Sur. En particular, estas observaciones nos permitirán identificar fuentes que puedan servir para la obtención de paralajes trigonométricas en las tres regiones.

2.1. Emisión de radio asociada a estrellas jóvenes de baja masa

La emisión de radiocontinuo asociada a estrellas jóvenes de baja masa se observa tanto en objetos protoestelares muy jóvenes (Clase 0 y I), los cuales se encuentran embebidos en envolventes y discos de gas que alimentan a la estrella en formación, hasta en objetos más evolucionados (Clase II y III), con poca o casi nula acreción. Para deshacerse del exceso de momento angular del disco de acreción, los objetos de clase 0 y I eyectan flujos bipolares y jets colimados con velocidades típicas de varios cientos hasta miles de kilómetros por segundo. El choque entre el material veloz del jet y el medio interestelar circundante ioniza la base del jet y da lugar a la emisión térmica o libre-libre (Rodríguez, 1997; Anglada *et al.*, 2015). El espectro libre-libre está caracterizado por una ley de potencias de la forma $S_\nu \propto \nu^\alpha$, donde el índice espectral α varía de -0.1 para el caso ópticamente delgado, a $+2$ para emisión ópticamente gruesa (Güdel, 2002). Para un flujo colimado, Reynolds (1986) encontró que el índice espectral depende tanto de la geometría del jet como del perfil de densidad del medio ambiente. A partir de cálculos analíticos, sugirió que el índice espectral de un radiojet oscila entre +0.25 y +1.1. El valor canónico de +0.6 corresponde al caso de un jet completamente ionizado con temperatura, velocidad y ángulo de apertura constante.

Las estrellas jóvenes con masas $\lesssim 2$ M$_\odot$ experimentan en general actividad magnética porque sus interiores son completamente convectivos, y pueden generar campos magnéticos superficiales intensos de hasta $\sim$1 kG a través del mecanismo dínamo. En la corona estelar, eventos de reconexión magnética, similares a los que ocurren en el Sol pero amplificados por varios órdenes de magnitud, aceleran partículas cargadas a velocidades medianamente relativistas. Estas partículas que giran alrededor de las líneas de campo radian emisión de radio no térmica, cuyo índice espectral es 5/2 para el caso ópticamente delgado o $1.22 - 0.9\delta$, en el caso ópticamente grueso, donde $2 \lesssim \delta \lesssim 7$ es el índice de la ley de potencias de la distribución de electrones (Dulk, 1985; Güdel, 2002). Frecuentemente este tipo de emisión es variable en escalas de tiempo de horas a meses y muestra polarización

circular. Hayashi *et al.* (1996) propusieron, por otro lado, que la interacción del disco de acreción con la magnetósfera en objetos protoestelares puede dar lugar a eventos de reconexión por la torcedura de estructuras magnéticas cerradas que conectan la estrella central con el disco en rotación. Este proceso también originaría emisión de radio no térmica.

En resumen, en estrellas de baja masa ocurren tanto procesos térmicos como no térmicos que dan lugar a radiación en longitudes de onda de radio. En efecto, gran parte de nuestro conocimiento actual sobre procesos energéticos en estrellas jóvenes es gracias a observaciones en el radio (ver por ejemplo Feigelson y Montmerle, 1999). Sin embargo, veremos a continuación que solamente objetos con emisión de radio no térmica son apropiados para hacer astrometría VLBI.

Fuentes apropiadas para VLBI

El ancho a potencia media del haz sintetizado, o resolución angular, de un arreglo VLBI equivale al de una antena hipotética cuyo diámetro es igual al de la máxima línea de base, que usualmente es de varios miles de kilómetros. En el siguiente análisis vemos que una alta resolución angular impone una restricción importante en la temperatura de brillo que un objeto puede tener para detectarse con VLBI.

La temperatura de brillo de un objeto corresponde a la temperatura de un cuerpo negro que produciría un brillo superficial igual al medido hacia dicho objeto (Wilson *et al.*, 2009). Para una fuente con un flujo medido S_ν y un tamaño angular θ, la temperatura de brillo es

$$T_b = 1.36\left(\frac{\lambda}{\mathrm{cm}}\right)^2\left(\frac{\theta}{\mathrm{arcsec}}\right)^{-2}\left(\frac{S_\nu}{\mathrm{mJy}}\right)\ \mathrm{K}. \tag{2-1}$$

Por otro lado, el ancho a potencia media del haz sintetizado del interferómetro está dado por,

$$\theta = 2.063\left(\frac{\lambda}{\mathrm{cm}}\right)\left(\frac{B_{\mathrm{max}}}{\mathrm{km}}\right)^{-1}\ \mathrm{arcsec}. \tag{2-2}$$

Sustituyendo la ecuación 2-2 en la expresión 2-1, y normalizando B_{max} a la línea de base

máxima del VLBA resulta,

$$T_b = 10^6 \left(\frac{S}{40\mu\text{Jy}} \right) \left(\frac{B_{\text{max}}}{8612 \text{ km}} \right)^2 \text{ K.} \tag{2-3}$$

Se sigue entonces que un objeto necesita tener una temperatura de brillo arriba de 10^6 K para ser detectado con el VLBA. Recordemos, además, que la emisión térmica posee típicamente $T_b \lesssim 10^4$ K y solamente la emisión no térmica posee una temperatura de brillo que excede valores de 10^6 K. Por consiguiente, nos interesan aquellos objetos estelares jóvenes que posiblemente posean emisión de radio no térmica. Si para un objeto en particular no existen observaciones VLBI disponibles, podemos usar otros diagnósticos observacionales y distinguir entre emisión térmica y no térmica tal y como explicamos a continuación.

2.2. Caracterización de la emisión de radio de objetos estelares en Serpens

Las estrellas jóvenes abundan en regiones de formación estelar, por tanto es de esperarse que también abunden fuentes de radio en tales regiones. Entonces, los mapeos extensos de regiones de formación estelar con observaciones sensitivas de radio nos permitirían i) identificar emisión de radiocontinuo asociada a estrellas jóvenes, ii) distinguir entre emisión térmica y no térmica y iii) localizar nuevas estrellas nacientes. La primera etapa del proyecto GOBELINS consistió en utilizar el VLA para caracterizar la población de fuentes de radio en cinco de las regiones más importantes del cinturón de Gould: Ofiuco (Dzib *et al.*, 2013), Orión (Kounkel *et al.*, 2014), Serpens (Ortiz-León *et al.*, 2015), Tauro (Dzib *et al.*, 2015) y Perseo (Pech *et al.*, 2016). Como ya se mencionó anteriormente, el presente capítulo se centra solamente en la región de Serpens.

Las observaciones presentadas en este capítulo se realizaron con el VLA (Figura 2-2). Dicho instrumento experimentó recientemente una etapa de expansión al incrementar el ancho de banda de sus receptores. Esto se ha traducido en una mejora, hasta por un factor

de 10, en la sensitividad del instrumento, permitiendo que sea posible detectar fuentes de radio intrínsicamente débiles con un menor uso de tiempo de telescopio. Las observaciones correspondientes a la primera parte del proyecto GOBELINS se efectuaron durante la etapa de modernización del VLA, y por tanto constituyen observaciones de gran sensitividad hacia regiones de formación estelar cercanas.

Las observaciones fueron obtenidas a 4.5 y 7.5 GHz sobre un área de $\sim 30' \times 27'$ en Serpens, $\sim 20' \times 25'$ en W40 y $\sim 9' \times 30'$ en Serpens Sur. Tres épocas separadas por aproximadamente un mes fueron dedicadas a Serpens y Serpens Sur y dos épocas a W40, requiriendo en cada una de ellas un tiempo de integración de ~ 0.7 horas por región. Construimos mapas con los datos de cada época alcanzando niveles de ruido en el intervalo de $19-73$ μJy beam^{-1}, dependiendo de la región y ventana de frecuencia. Con el objetivo de identificar fuentes de radio intrínsecamente débiles, combinamos para cada región los datos de diferentes épocas y obtuvimos mapas con niveles de ruido entre $13-27$ μJy beam^{-1}.

De un total de 146 fuentes de radio detectadas, 29 de ellas están asociadas a estrellas jóvenes, 2 son objetos de secuencia principal y 5 más podrían estar asociados con

Figura 2-2 El Arreglo Muy Extendido.

fenómenos relacionados a objetos protoestelares (e.g. frentes de choque en jets). El resto de las fuentes están muy probablemente asociadas a fuentes de fondo, aunque pudiera haber dentro de éstas una pequeña fracción de objetos estelares jóvenes (que no han sido identificadas por otros medios). Los diagnósticos que utilizamos para decidir si la emisión de radio de un objeto estelar joven es de naturaleza térmica o no térmica fueron el índice espectral de la fuente, la variación temporal de su flujo y la detección de radiación polarizada circularmente. Recordemos que la emisión térmica por procesos libre-libre en estrellas de baja masa proviene de regiones ionizadas (que poseen una escala física del orden de 100 UA) en la base de flujos colimados eyectados por la protoestrella. En general este tipo de emisión muestra moderada o casi nula variabilidad, mientras que la emisión no térmica puede variar por factores significativos en la escala temporal cubierta por nuestras observaciones. La emisión no térmica frecuentemente posee un espectro que decae con la frecuencia, pues su índice espectral es típicamente menor a -0.1. Nótese, sin embargo, que de acuerdo a lo discutido en párrafos anteriores, un valor positivo en el índice espectral puede ser atribuido tanto a procesos térmicos como a no térmicos. En base a esto, designamos como posibles fuentes de emisión no térmica a aquellas fuentes de radio que posean cualquiera de las siguientes propiedades i) factores altos de variabilidad (aquí adoptamos que la diferencia entre los valores de flujo máximo y mínimo normalizada al máximo valor fuera mayor al 50 %), ii) un índice espectral negativo, ó iii) detección de polarización circular. En total, 19 objetos estelares jóvenes poseen características que indican que su emisión de radio es muy probablemente de naturaleza no térmica. De estas 19 estrellas jóvenes, 9 tienen un flujo de radio máximo mayor a 200 μJy y pueden ser detectadas con el VLBA en tiempos de integración de unas cuantas horas. Adicionalmente, otras 9 fuentes, que no han sido clasificadas en la literatura, poseen factores de variabilidad entre 50 % y hasta 96 %, por lo que las consideramos como candidatas a estrellas jóvenes. Estas fuentes también podrían detectarse con el VLBA en su fase de máximo flujo. Entonces, en total hay 18 potenciales candidatos cuya astrometría se puede determinar utilizando la técnica

VLBI.

Una fracción significativa de las estrellas jóvenes con emisión de radio tienen asignada una clase evolutiva en base a su distribución espectral de energía, colores infrarrojos o emisión de rayos-X. Dzib *et al.* (2013) y Dzib *et al.* (2015) encontraron en sus observaciones con el VLA hacia las regiones de Ofiuco y Tauro, que la variación del flujo de radio es en promedio mayor para objetos más evolucionados. Es decir, los objetos de clase 0 y I son, en promedio, menos variables en radio que los objetos de Clase II y III, un resultado similar a lo encontrado por Liu *et al.* (2014) a partir de observaciones VLA hacia el cúmulo R Coronae Australis. Dzib *et al.* también hallaron que el índice espectral es más negativo para objetos más evolucionados. En el caso de los objetos estelares jóvenes en Serpens, pareciera que su variación de flujo sigue la tendencia determinada para las otras dos regiones, aunque la correlación en este caso no es estadísticamente significativa. Una interpretación a lo encontrado por Dzib *et al.* es que los objetos más evolucionados tienden a mostrar más niveles de actividad magnética. Los objetos más jóvenes también poseen coronas con actividad magnética y emiten radiación no térmica, sin embargo, esta radiación debe ser absorbida por el material ionizado que oculta al objeto central. Existirán casos, sin embargo, de objetos de Clase I y II, donde la orientación del jet con respecto a la línea de visión será favorable para que la emisión producida en la magnetósfera estelar no quede oculta por el medio ionizado del jet.

A continuación incluimos el artículo donde reportamos los resultados discutidos en este capítulo y el cual fue publicado en la revista *The Astrophysical Journal* (ApJ) en el 2015.

The Astrophysical Journal, 805:9 (19pp), 2015 May 20 doi:10.1088/0004-637X/805/1/9

THE GOULD'S BELT VERY LARGE ARRAY SURVEY. II. THE SERPENS REGION

Gisela N. Ortiz-León[1], Laurent Loinard[1,2], Amy J. Mioduszewski[3], Sergio A. Dzib[2], Luis F. Rodríguez[1,4], Gerardo Pech[1], Juana L. Rivera[1], Rosa M. Torres[5], Andrew F. Boden[6], Lee Hartmann[7], Neal J. Evans II[8], Cesar Briceño[9], John Tobin[10,11], Marina A. Kounkel[7], and Rosa A. González-Lópezlira[1]
[1] Centro de Radioastronomía y Astrofísica, Universidad Nacional Autónoma de Mexico, Morelia 58089, Mexico; g.ortiz@crya.unam.mx
[2] Max Planck Institut für Radioastronomie, Auf dem Hügel 69, D-53121 Bonn, Germany
[3] National Radio Astronomy Observatory, Domenici Science Operations Center, 1003 Lopezville Road, Socorro, NM 87801, USA
[4] King Abdulaziz University, P.O. Box 80203, Jeddah 21589, Saudi Arabia
[5] Instituto de Astronomía y Meteorología, Universidad de Guadalajara, Av. Vallarta 2602, Col. Arcos Vallarta, 44130, Guadalajara, Jalisco, México
[6] Division of Physics, Math and Astronomy, California Institute of Technology, 1200 East California Boulevard, Pasadena, CA 91125, USA
[7] Department of Astronomy, University of Michigan, 500 Church Street, Ann Arbor, MI 48105, USA
[8] Department of Astronomy, The University of Texas at Austin, 2515 Speedway, Stop C1400, Austin, TX 78712-1205, USA
[9] Cerro Tololo Interamerican Observatory, Casilla 603, La Serena, Chile
[10] National Radio Astronomy Observatory, Charlottesville, VA 22903, USA
Received 2014 January 27; accepted 2015 March 12; published 2015 May 13

ABSTRACT

We present deep (∼17 μJy) radio continuum observations of the Serpens molecular cloud, the Serpens south cluster, and the W40 region obtained using the Very Large Array in its A configuration. We detect a total of 146 sources, 29 of which are young stellar objects (YSOs), 2 of which are BV stars, and 5 more of which are associated with phenomena related to YSOs. Based on their radio variability and spectral index, we propose that about 16 of the remaining 110 unclassified sources are also YSOs. For approximately 65% of the known YSOs detected here as radio sources, the emission is most likely non-thermal and related to stellar coronal activity. As also recently observed in Ophiuchus, our sample of YSOs with X-ray counterparts lies below the fiducial Güdel & Benz relation. Finally, we analyze the proper motions of nine sources in the W40 region. This allows us to better constrain the membership of the radio sources in the region.

Key words: astrometry – magnetic fields – radiation mechanisms: non-thermal – radio continuum: stars – techniques: interferometric

1. INTRODUCTION

Radio continuum observations toward star-forming regions are relevant because they provide insights into thermal and non-thermal emission in young stellar objects (YSOs), stellar coronal activity of YSOs, and magnetic fields. Different processes are invoked to explain the origin of the radio emission in these different kinds of objects. Embedded Class I protostars have most often been detected as thermal bremsstrahlung sources, and this emission is predominantly due to collimated thermal winds or jets. In the case of more massive stars, the radio emission can also originate from optically thick or thin compact H II regions (Hughes 1988; Estalella et al. 1991; Gómez et al. 2000), or from ionized winds (Felli et al. 1998). Non-thermal (gyrosynchrotron) emission has also been detected in a number of sources. This mechanism produces radiation characterized by high brightness temperature, high variability, and often a negative spectral index and some level of circular polarization (e.g., Hughes 1991; Hughes et al. 1995; Garay et al. 1996). This non-thermal radio emission is generally present in more evolved YSOs (Class III sources), but it has also been detected in a number of Class II and even in a few Class I sources (e.g., Forbrich et al. 2007; Dzib et al. 2010; Deller et al. 2013). We note that very little has been done on the characterization of the Serpens, Serpens South, and W40 regions at radio wavelengths.

The Aquila rift/Serpens complex is one of the clouds selected for observations as part of *The Gould's Belt Distance Survey*, which is a large project designed to determine accurate distances to stars in the most often studied star-forming sites (Loinard 2013). In this paper we report on new sensitive and high angular resolution radio observations of the Serpens, Serpens South, and W40 regions. This paper is the second (after that by Dzib et al. 2013, which dealt with the Ophiuchus region) in a series that will focus on the analysis of the radio emission from YSOs in the star-forming regions of the Gould's Belt using the Karl G. Jansky Very Large Array (JVLA). The observations cover large fields of view of the three regions: 900, 290, and 280 square arcminutes in Serpens, Serpens South, and W40, respectively, i.e., considerably larger than previous observations carried out at radio wavelengths toward these regions.

The Serpens molecular cloud has been studied via multi-wavelength observations ever since it was recognized as an active star-forming region by Strom et al. (1974). The cloud belongs to a larger complex of local optically dark molecular clouds called the Aquila rift, which, in turn, is part of the Gould's Belt (e.g., Dame et al. 1987; Perrot & Grenier 2003). The Serpens cloud shows large-scale irregular dark structures in optical images, and several nebulae can be distinguished. One of the most prominent is the Serpens nebula, which is illuminated by the pre-main-sequence (PMS) star SVS 2 (Strom et al. 1974, 1976; Worden & Grasdalen 1974; King et al. 1983; Warren-Smith et al. 1987; Gomez de Castro et al. 1988). The region, about 6′ across centered on the Serpens nebula, is known as the Serpens cloud core and was described in early observations by Loren et al. (1979) as a nearly circular, high-density formaldehyde (H_2CO) core. A more elongated structure extends in a north west/south east direction as seen,

[11] Hubble Fellow

for instance, on maps of far-IR and NH_3 emission (e.g., Torrelles et al. 1989). The Serpens core is populated by more than ~300 objects found in many different evolutionary stages and coexisting within the central ~0.5–0.7 pc of the core (Eiroa et al. 2008 and references therein).

Near- and mid-infrared (IR) observations have identified a large number of Class II PMS stars, flat-spectrum sources, and Class I protostars embedded in the cloud core (Eiroa & Casali 1992; Sogawa et al. 1997; Giovannetti et al. 1998; Kaas 1999; Kaas et al. 2004). Class 0 protostars and protostellar condensations have also been found by means of submillimeter, millimeter, and far-IR observations (Casali et al. 1993; Hurt & Barsony 1996; Testi & Sargent 1998). In addition, some of these YSOs have X-ray counterparts (Preibisch 1998, 2003, 2004; Giardino et al. 2007). *Spitzer*/IRAC and MIPS observations extend to a larger region of ~6–9 pc (Harvey et al. 2006, 2007a, 2007b; Oliveira et al. 2010). Briefly, these most recent works identified at least two main centers of star formation, which were named Clusters A and B. Cluster A is the already described region referred to as the Serpens core, while Cluster B, ~35′ to the south of Cluster A and also referred to as Serpens G3-G6, was not observed by us. At radio wavelengths, the Serpens core has been observed by Eiroa et al. (2005) with the Very Large Array (VLA). A total of 22 radio continuum sources were detected, 16 of which were proposed to be associated with Class 0, Class I, flat spectrum, and Class II YSOs of the core. AMI Consortium et al. (2012) carried out deep radio continuum observations at 1.8 cm with the Arcminute Microkelvin Imager Large Array (providing an angular resolution of ~30 arcsec) of the 19 protostellar cores reported in the *Spitzer* catalog of Dunham et al. (2008). They detected eight radio sources, six possibly associated with deeply embedded YSOs.

At an angular distance of ~3° to the south of the center of the Serpens core lies the star-forming region known as W40. Assuming a distance of 415 pc (see discussion below), this corresponds to a spatial distance of ~22 pc. Three main components are recognized in this region. First is the cold molecular cloud G28.8+3.5 (Goss & Shaver 1970) with an extent of ~1 deg, centered around the smaller (~20′) dense molecular core, TGU 279–P7 (Dobashi et al. 2005). Second, there is a blister H II region (W40) of diameter ~6′ centered on J2000 coordinates $18^h30^m29^s$, −2°05′.4 and adjacent to the molecular cloud (Westerhout 1958). Finally, the W40 region hosts an embedded OB star cluster that is the primary excitation source for the W40 H II region (Smith et al. 1985). There is evidence for ongoing star formation from dense molecular material in this region, as suggested by the detection of an *IRAS* source, a cold ammonia core, and a number of millimeter-wave sources associated with the cluster (Molinari et al. 1996; Maury et al. 2011).

The stellar population of W40 has also been investigated through observations at different wavelengths. Crutcher & Chu (1982) and Smith et al. (1985) found seven IR bright sources with optical counterparts behind 9–10 mag of visual extinction within the central 3′ of W40. According to the spectral energy distributions (SEDs) from the IR through the millimeter obtained by Smith et al. (1985) and Vallee & MacLeod (1994), most of these bright sources are surrounded by significant amounts of circumstellar material. A cluster of near-IR sources is detected in the 2MASS images within the central 5′ (Smith et al. 1985). Recently, Rodríguez et al. (2010) observed the W40 region at 3.6 cm with the VLA. They found a cluster of 20 compact sources in the central portion of the W40 IR cluster, many of which correspond to the known IR sources. The W40 cluster has also been observed with the *Chandra X-ray Observatory*. These observations reveal approximately 200 sources associated with the cluster, the majority of which are thought to be low-mass YSOs (Kuhn et al. 2010). More recently, Shuping et al. (2012) determined the spectral classification and SEDs of the brightest members of the central stellar cluster in the W40 region. They identified four main-sequence OB stars, two Herbig AeBe stars, and two low-mass YSOs (Class II).

Very close to W40 in projection on the plane of the sky lies an embedded cluster of IR sources referred to as Serpens South. This cluster was recently discovered by Gutermuth et al. (2008) from *Spitzer* observations of the Aquila rift region. They identified 54 sources classified as either Class I or flat SED and 37 Class II YSOs within a 14′ × 10′ region.

Both clusters, Serpens South and W40, have been observed at 70–500 μm with the *Herschel Space Telescope* as part of the Gould Belt program (André et al. 2010; Bontemps et al. 2010; Könyves et al. 2010). The region observed toward the Aquila rift is ~3.°3 × 3.°3 in size, with seven YSOs safely classified as Class 0 objects, only in the reduced area of Serpens South (Bontemps et al. 2010). Additionally, around 45 (for $T_{\rm bol}^{70-500} < 27$ K) and 60 ($L_{\rm submm}^{\lambda>350}/L_{\rm bol}^{70-500} > 0.03$) objects in the entire field of Aquila (W40, Serpens South, and the H II region Sh2-62) were proposed to be Class 0 YSOs. Maury et al. (2011) carried out a 1.2 mm dust continuum mapping of the Aquila complex with the MAMBO bolometer array on the IRAM 30 m telescope. Twenty-five continuum sources were identified in the Serpens South protocluster and their evolutionary stages were estimated, resulting in nine starless sources, nine Class 0, and seven Class 0/I protostars. In the W40 region, 35 sources were detected from these observations, separated into 14 starless, 8 Class 0, 4 Class 0/I, and 9 Class I YSOs.

Additionally, a larger number of YSOs have been identified in the Aquila/Serpens region by the c2d ("from Molecular cores to Planet-forming Disks") and GB ("*Spitzer* Gould Belt Survey") surveys (Dunham et al. 2013; L. E. Allen et al. 2015, in preparation). A total of 1524 YSOs with determined IR spectral indexes and belonging to these regions are reported in their catalogs.

Early estimates of the distance to the Serpens molecular cloud seemed to converge toward a value of 260 pc (see the discussion in Eiroa et al. 2008). On the basis of radial velocity measurements from molecular line observations, Gutermuth et al. (2008) suggest that the Serpens South cluster is comoving with the Serpens Main embedded cluster 3° to the north, and, therefore, that it should be part of Serpens. They also assign a distance of 260 pc to the cluster, which corresponds to the distance to the front edge of the Aquila rift (Straižys et al. 1996). Based on spectral types determined for a few main-sequence stars in the W40 region, Shuping et al. (2012) estimated a distance to the W40 cluster of between 455 and 535 pc. Therefore, the W40 region and the Serpens South cluster (thought to be at 260 pc) are usually regarded as separate objects. On the other hand, Bontemps et al. (2010) argue that the W40 region, the Aquila rift, and Serpens Main are parts of the same star-forming region, located at a common distance of 260 pc. However, more recently, based on a comparison of the X-ray luminosity function of the Serpens

Table 1
JVLA Observations

Region	Epoch[a]	Time[b] (UTC)	Phase Center J2000	Synthesized Beam ($\theta_{maj} \times \theta_{min}$; P.A.)		rms Noise[c] (μJy beam^{-1})	
				4.5 GHz	7.5 GHz	4.5 GHz	7.5 GHz
Serpens cloud (mosaic)	1	Jun 17 07:59	$18^h30^m00^s.0$ + 01d12′37″.0	0.42×0.36; −58.8	0.23×0.22; +100.7	19.3	21.5
	2	Jul 19 04:25	⋯	0.49×0.38; +63.7	0.31×0.23; +66.9	19.9	23.9
	3	Sep 12 03:47	⋯	0.39×0.37; +58.6	0.25×0.23; +50.4	25.0	29.6
	C	⋯	⋯	0.40×0.39; +96.1	0.25×0.23; +62.2	12.7	14.4
W40 (mosaic)	1	Jun 17 09:30	$18^h31^m20^s.0$ − 02d05′00″.0	0.45×0.39; +90.4	0.26×0.23; +54.2	22.8	28.0
	2	Jul 16 06:35	⋯	0.40×0.39; +12.0	0.25×0.24; +33.9	21.3	23.1
	C	⋯	⋯	0.41×0.40; +75.8	0.25×0.23; +40.5	16.0	18.3
Serpens South (field 1)	1	Jun 17 07:59	$18^h30^m19^s.9$ − 02d13′42″.0	0.46×0.33; +124.0	0.29×0.21; −56.6	38.2	29.9
	2	Jul 19 04:25	⋯	0.53×0.39; +86.3	0.34×0.24; +86.8	41.5	32.4
	3	Sep 12 03:47	⋯	0.37 × 0.34; −13.3	0.23 × 0.22; −40.0	47.8	33.8
	C	⋯	⋯	0.44×0.37; -67.1	0.27×0.23; −70.3	24.0	18.5
Serpens South (field 2)	1	Jun 17 07:59	$18^h30^m07^s.8$ − 02d02′49″.1	0.45×0.33; −56.1	0.29×0.21; +123.4	39.1	31.0
	2	Jul 19 04:25	⋯	0.53×0.39; +89.9	0.33×0.24; +85.3	41.9	34.3
	3	Sep 12 03:47	⋯	0.37×0.34; −13.0	0.23×0.22; −36.9	48.1	36.5
	C	⋯	⋯	0.44×0.37; +114.2	0.27×0.23; −70.7	24.6	19.4
Serpens South (field 3)	1	Jun.17 07:59	$18^h29^m49^s.2$ − 01d49′45″.0	0.45×0.33; −57.5	0.23×0.22; −50.7	38.4	28.7
	2	Jul 19 04:25	⋯	0.52×0.39; +83.0	0.33×0.24; +83.1	37.8	31.8
	3	Sep 12 03:47	⋯	0.35×0.35; −36.5	0.23×0.22; −52.0	47.1	33.6
	C	⋯	⋯	0.43×0.37; −72.0	0.25×0.23; +94.2	23.3	18.1
Serpens South (field 4)	1	Jun 17 07:59	$18^h29^m45^s.1$ − 01d56′17″.4	0.45 × 0.33; +123.5	0.23 × 0.22; −45.9	39.6	29.3
	2	Jul 19 04:25	⋯	0.51×0.39; +80.4	0.33×0.24; +82.0	41.0	31.5
	3	Sep 12 03:47	⋯	0.37×0.34; +2.1	0.23×0.22; −25.0	74.1	73.0
	C	⋯	⋯	0.45×0.38; −72.2	0.26×0.23; +93.9	27.1	20.9

[a] C indicates parameters measured in the images after combining the epochs.
[b] Start time of the observing sessions. All epochs were observed in 2011.
[c] Measured at the center of the Stokes *I* image.

cluster with the previously published Orion Nebula cluster, Winston et al. (2010) obtained a new distance for the Serpens core of 360^{+22}_{-13} pc, while Dzib et al. (2010) claimed a distance of 415 ± 5 pc to the same, based on a VLBA parallax of the embedded young AeBe star EC95. Given that the estimation of Dzib et al. (2010) is the most recent and accurate, in this paper we adopt a distance of 415 pc for the three regions in the Aquila complex, including Serpens, Serpens South, and W40.

The rest of this paper is organized as follows. In Section 2 we present details of the JVLA observations; in Section 3 we describe the results, which are analyzed and discussed in Sections 4 and 5. Section 6 is a summary of our results.

2. OBSERVATIONS AND DATA REDUCTION

The Serpens molecular cloud, the W40 region, and the Serpens South cluster were observed with the JVLA in its A configuration. Two frequency sub-bands, each 1 GHz wide and centered at 4.5 and 7.5 GHz, respectively, were recorded simultaneously. The Serpens molecular cloud and the Serpens South cluster were observed in the same observing sessions on three different epochs (2011 June 17, July 19, and September 12 UT), using 25 and 4 pointings, respectively. The W40 region, on the other hand, was only observed on two epochs (2011 June 17 and July 16), using 13 pointings. This dual-frequency strategy was chosen to enable the characterization of the spectral index of the detected sources, while the multi-epoch observations were aimed at determining the radio flux variability and helping in the identification of the emission mechanisms (thermal versus non-thermal). The details of the observations are listed in Table 1. The 25 pointings were used to map an area of 900 (530) square arcminutes at 4.5 (7.5) GHz of the Serpens molecular cloud (see Figure 1). The covered area of the W40 region using the 13 pointings was 415 (280) square arcminutes at 4.5 (7.5) GHz. The four pointings used for the Serpens South cluster covered an area of 290 (110) square arcminutes at 4.5 (7.5) GHz (see Figure 1). The number of individual pointings observed toward the Serpens molecular cloud and the W40 region and the spacing between them were chosen to optimize the compromise between uniform sensitivity and inclusion of the largest possible number of known young stars.

3C 286 and J1804+010 were used as the standard flux and phase calibrator, respectively. The observations of the Serpens molecular cloud and the Serpens South cluster were carried out in 2 hr scheduling blocks, while the observations of the W40 region in 1 hr scheduling blocks. Each epoch consists of a 9-minute observation of the flux calibrator, followed by a series of two to four different target pointings (for 3 minutes each) bracketed by phase calibrator observations of 1 minute. Thus, 3 minutes were spent on each target field in each epoch. The data were edited and calibrated in a standard fashion using the Common Astronomy Software Applications package (CASA) version 3.4. Once calibrated, the data at each frequency were imaged (Stokes parameter *I*) using the CASA task `clean`. The 25 target pointings toward the Serpens molecular cloud were used to construct a mosaic of 22,400 × 20,412 pixels with a pixel size of 0.″09 at 4.5 GHz. This was done by setting the *imagermode* parameter to "mosaic" in the `clean` task. For the W40 region, the 13 target pointings were used to obtain a mosaic of 15,552 × 18,522 pixels with a pixel size of 0.″09 at

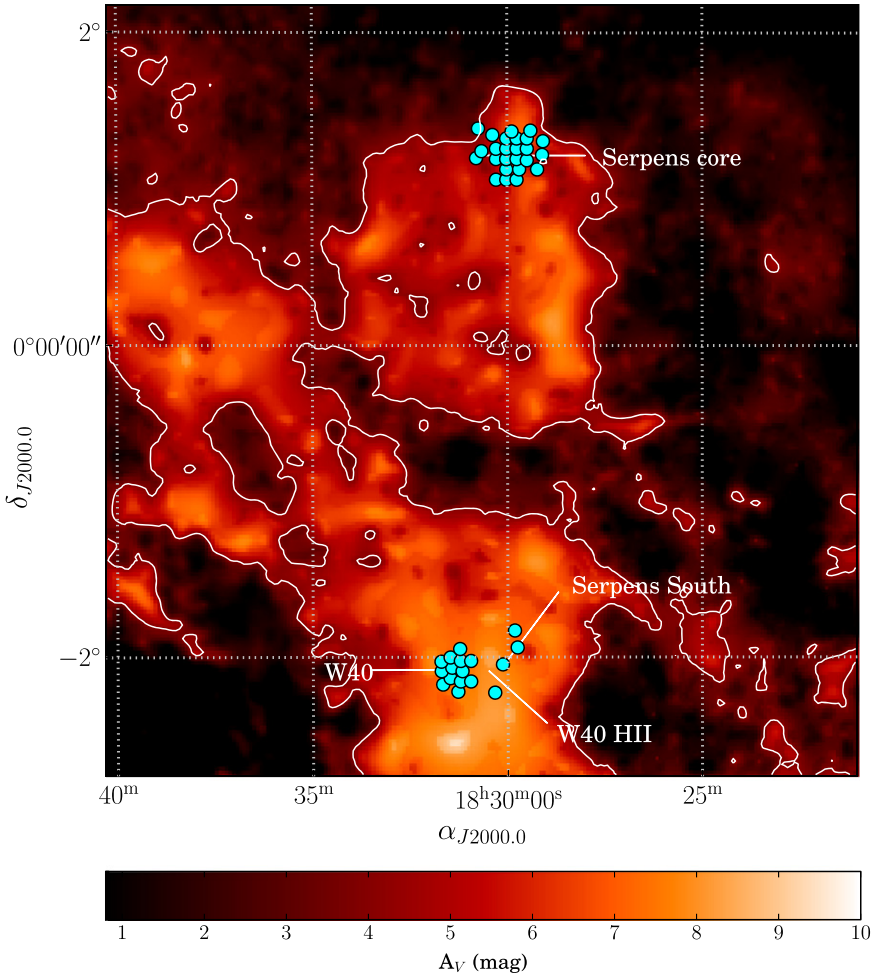

Figure 1. Extinction map of the Serpens star-forming region obtained as part of the COMPLETE project, based on the STScI Digitized Sky Survey data (Cambrésy 1999). The small cyan circles represent the size at 7.5 GHz of the fields observed in each region.

4.5 GHz. The phase centers of the mosaics are indicated in Table 1. The four Serpens South cluster fields were imaged separately, using an image size of 6750 pixels in each dimension and a pixel size of 0.″09 at 4.5 GHz. The pixel size for the images at 7.5 GHz was 0.″055, and the number of pixels was adjusted to cover the same area as the images at 4.5 GHz. In order to take into account the non-coplanarity of the baselines far from the phase center, we set the *gridmode* parameter to "widefield" with *wprojplanes* = 128 and *facets* = 1. We also correct the images for the primary beam attenuation. The rms noise levels reached at each frequency and epoch are given in Table 1.

To produce images with improved sensitivity, the three or two epochs (in Serpens and W40, respectively) were combined and jointly imaged. The rms noise levels achieved after combining the epochs, as well as the synthesized beam (angular resolution) of the final maps, are also given in Table 1.

Gyrosynchrotron emission often (but not always) exhibits some level of circular polarization (Dulk 1985). To test for circular polarized radio emission, we produced images of the Stokes parameter *V*. The brightness distribution of the Stokes parameter V is obtained by applying the Fourier transform to the Stokes visibility function V_V, which is given by $V_V = 1/2(V_{RR} - V_{LL})$, where V_{RR} is the correlation of the right circularly polarized responses and V_{LL} is the correlation of those left circularly polarized.

We imaged the Stokes parameter *V* for all 42 fields (25 of the Serpens molecular cloud, 4 of the Serpens South cluster, and 13 of the W40 region), separately at each frequency, and combined the three or two epochs. We did not apply any polarization correction in addition to the standard 6 cm continuum calibration. Also, in order to avoid beam squint (Dzib et al. 2013), only the inner quarter (in area) of the primary beam was tested, producing images of 4′ × 4′ in size.

3. RESULTS

3.1. Source Identification

The identification of the radio sources was done through a visual inspection using the deep radio images. For the Serpens molecular cloud and the W40 region this means that we used the mosaics obtained after combining the epochs. For the Serpens South cluster we used the combined individual fields.

Once the sources were identified in those images, their fluxes and their positions at 4.5 and 7.5 GHz were obtained by performing two-dimensional Gaussian fittings, using the CASA task `imfit`. The results of these fittings are listed in Table 2. Sources are named GBS-VLA J*hhmmss.ss—ddmmss.s*, where GBS-VLA stands for Gould's Belt VLA Survey and *hhmmss.ss —ddmmss.s* are the coordinates of the source. We considered for the quoted flux densities in the table three sources of error: an error resulting from the statistical noise in the images, a

Table 2
Radio Sources Detected in Serpens

GBS-VLA Name/Position	New Detection?[a]	Flux Density (4.5 GHz) (mJy)	Variability (4.5 GHz) (%)	Flux Density (7.5 GHz) (mJy)	Variability (7.5 GHz) (%)	Spectral Index
Detected Sources in the Serpens Molecular Cloud:						
J182850.71+011102.7	Y	0.28 ± 0.05	38 ± 19	…	…	…
J182851.30+010908.6	N	8.77 ± 1.72	14 ± 24	…	…	…
J182851.48+010947.3	Y	0.16 ± 0.03	50 ± 17	…	…	…
J182854.44+011859.7	Y	0.18 ± 0.02	6 ± 22	0.12 ± 0.03	25 ± 31	−0.9 ± 0.3
J182854.46+011823.7	Y	3.13 ± 0.32	44 ± 9	5.72 ± 1.18	17 ± 24	1.2 ± 0.1
J182854.87+011753.0	Y	0.08 ± 0.02	>44 ± 19	0.10 ± 0.03	–A–	0.4 ± 0.5
J182901.40+010434.7	N	0.45 ± 0.08	26 ± 19	…	…	…
J182903.06+012331.0	Y	0.36 ± 0.07	25 ± 21	…	…	…
J182903.13+010346.0	Y	0.06 ± 0.02	–A–	…	…	…
J182905.07+012309.0	N	0.12 ± 0.02	38 ± 20	…	…	…
J182906.84+011742.7	N	6.46 ± 0.39	8 ± 8	6.10 ± 0.53	14 ± 11	−0.1 ± 0.1
J182907.07+011801.9	Y	2.82 ± 0.18	Extended	1.67 ± 0.16	Extended	−1.1 ± 0.2
J182907.62+012125.1	N	0.10 ± 0.02	29 ± 22	<0.04	…	<−1.9 ± 0.3
J182910.17+012559.5	N	1.41 ± 0.25	71 ± 8	…	…	…
J182911.94+012119.4	Y	0.35 ± 0.05	28 ± 16	0.41 ± 0.11	18 ± 31	0.3 ± 0.2
J182912.01+011415.1	Y	0.08 ± 0.01	>14 ± 21	0.07 ± 0.02	>45 ± 25	−0.2 ± 0.5
J182913.17+010906.4	N	0.51 ± 0.04	19 ± 12	0.60 ± 0.08	8 ± 18	0.3 ± 0.2
J182913.36+011544.3	Y	0.20 ± 0.03	19 ± 20	0.07 ± 0.02	>40 ± 25	−2.1 ± 0.5
J182913.79+010738.6	N	0.06 ± 0.01	36 ± 25	0.10 ± 0.02	>26 ± 20	0.9 ± 0.5
J182916.11+010437.5	N	0.21 ± 0.03	41 ± 16	0.25 ± 0.06	52 ± 19	0.4 ± 0.2
J182918.23+011757.7	N	0.38 ± 0.05	32 ± 15	0.26 ± 0.07	41 ± 24	−0.8 ± 0.2
J182926.71+012342.1	N	0.18 ± 0.02	30 ± 13	0.11 ± 0.02	34 ± 25	−1.0 ± 0.4
J182928.02+011156.5	N	0.19 ± 0.02	18 ± 18	0.09 ± 0.02	–A–	−1.5 ± 0.5
J182928.28+011205.7	N	0.21 ± 0.04	52 ± 19	<0.05	…	<−3.1 ± 0.4
J182929.78+012158.1	N	0.07 ± 0.01	–A–	0.06 ± 0.02	–A–	−0.2 ± 0.6
J182930.71+010048.3	N	32.10 ± 5.60	Extended	…	…	…
J182932.21+012104.6	Y	0.10 ± 0.01	52 ± 15	0.06 ± 0.02	>20 ± 27	−0.8 ± 0.5
J182933.07+011716.3	N	0.27 ± 0.03	73 ± 5	0.32 ± 0.05	74 ± 9	0.3 ± 0.2
J182934.12+010810.9	Y	2.06 ± 0.17	16 ± 11	2.14 ± 0.33	20 ± 18	0.1 ± 0.1
J182934.32+011513.9	N	0.73 ± 0.13	Extended	0.12 ± 0.02	>48 ± 12	−3.7 ± 0.5
J182935.02+011503.2	N	0.35 ± 0.05	21 ± 15	0.21 ± 0.03	34 ± 18	−1.0 ± 0.3
J182935.11+011503.6	N	0.50 ± 0.07	Extended	<0.05	…	<−4.8 ± 0.3
J182936.50+012317.0	N	0.29 ± 0.04	35 ± 14	0.21 ± 0.05	39 ± 24	−0.7 ± 0.2
J182937.76+010314.6	N	0.60 ± 0.06	13 ± 16	0.33 ± 0.06	32 ± 19	−1.2 ± 0.2
J182938.87+011850.4	Y	0.15 ± 0.02	30 ± 16	0.13 ± 0.02	35 ± 23	−0.4 ± 0.3
J182939.09+011233.6	Y	0.13 ± 0.02	9 ± 24	0.05 ± 0.02	>19 ± 33	−1.9 ± 0.6
J182940.03+011051.2	Y	0.09 ± 0.01	>32 ± 15	0.09 ± 0.02	45 ± 23	0.0 ± 0.4
J182944.07+011921.1	N	4.49 ± 0.24	21 ± 6	4.64 ± 0.27	5 ± 8	0.1 ± 0.1
J182948.83+010647.4	N	0.50 ± 0.05	29 ± 13	0.76 ± 0.13	6 ± 23	0.8 ± 0.2
J182948.92+011523.8*	Y	0.06 ± 0.01	>62 ± 10	<0.04	…	<−0.5 ± 0.5
J182949.42+011526.2	Y	0.72 ± 0.09	Extended	0.28 ± 0.05	Extended	−1.9 ± 0.4
J182949.50+011955.8	Y	2.44 ± 0.16	18 ± 8	1.63 ± 0.16	7 ± 13	−0.8 ± 0.1
J182949.54+011523.8	Y	0.16 ± 0.02	76 ± 7	<0.04	…	<−2.5 ± 0.3
J182949.60+011522.9	Y	0.18 ± 0.02	71 ± 8	0.14 ± 0.03	64 ± 14	−0.5 ± 0.4
J182949.79+011520.4	N	0.88 ± 0.07	43 ± 9	0.99 ± 0.10	23 ± 13	0.2 ± 0.2
J182950.34+011515.3	Y	0.33 ± 0.04	11 ± 20	0.20 ± 0.04	>61 ± 18	−1.0 ± 0.4
J182951.04+011533.8	N	0.61 ± 0.05	41 ± 9	0.58 ± 0.07	46 ± 11	−0.1 ± 0.2
J182951.17+011640.4	N	0.09 ± 0.02	>51 ± 16	0.07 ± 0.02	>30 ± 22	−0.3 ± 0.5
J182951.17+010529.7	Y	0.09 ± 0.01	–A–	<0.04	…	<−1.7 ± 0.3
J182951.22+012132.0	N	3.80 ± 0.22	20 ± 7	2.09 ± 0.17	6 ± 11	−1.2 ± 0.2
J182951.26+012130.3	Y	2.46 ± 0.16	26 ± 8	1.56 ± 0.13	9 ± 12	−0.9 ± 0.2
J182952.22+011547.4	N	0.12 ± 0.02	16 ± 23	<0.05	…	<−1.7 ± 0.3
J182953.99+011229.5	N	0.08 ± 0.01	46 ± 19	<0.04	…	<−1.4 ± 0.3
J182954.30+012011.2	Y	0.14 ± 0.02	>75 ± 5	<0.04	…	<−2.3 ± 0.3
J182954.31+010309.6	N	0.59 ± 0.05	17 ± 14	0.60 ± 0.09	11 ± 20	0.0 ± 0.2
J182954.36+010350.4	Y	0.07 ± 0.01	>22 ± 18	<0.04	…	<−0.8 ± 0.4
J182954.86+011129.3	Y	0.10 ± 0.01	61 ± 21	0.07 ± 0.02	>22 ± 26	−0.7 ± 0.5
J182955.76+010440.3	Y	0.14 ± 0.02	14 ± 21	0.12 ± 0.02	28 ± 26	−0.4 ± 0.3
J182956.96+011247.6	N	<0.04	…	0.08 ± 0.02	>57 ± 14	>1.1 ± 0.4
J182957.60+011300.2	N	0.05 ± 0.01	47 ± 20	<0.05	…	<−0.1 ± 0.5
J182957.85+011251.1	N	0.05 ± 0.01	>43 ± 19	<0.08	…	<0.8 ± 0.5

Table 2
(Continued)

GBS-VLA Name/Position	New Detection?[a]	Flux Density (4.5 GHz) (mJy)	Variability (4.5 GHz) (%)	Flux Density (7.5 GHz) (mJy)	Variability (7.5 GHz) (%)	Spectral Index
J182957.89+011246.0	N	3.20 ± 0.24	65 ± 4	3.32 ± 0.41	62 ± 8	0.1 ± 0.2
J182959.55+011158.1	N	0.07 ± 0.01	>48 ± 12	<0.05	⋯	<−0.9 ± 0.4
J182959.94+011311.3	N	0.12 ± 0.02	42 ± 20	0.10 ± 0.02	18 ± 30	−0.3 ± 0.4
J183000.65+011340.0	N	0.16 ± 0.02	>82 ± 3	0.10 ± 0.02	>75 ± 8	−0.9 ± 0.4
J183001.24+010205.4	N	0.27 ± 0.04	Extended	<0.06	⋯	<−3.1 ± 0.3
J183002.42+012405.6	N	0.25 ± 0.05	Extended	<0.04	⋯	<−3.7 ± 0.4
J183002.67+012258.1	Y	0.15 ± 0.02	25 ± 18	0.16 ± 0.04	14 ± 31	0.1 ± 0.3
J183004.14+011239.7	Y	0.11 ± 0.01	28 ± 19	0.07 ± 0.02	>18 ± 29	−0.8 ± 0.5
J183004.62+012234.1	N	0.97 ± 0.11	49 ± 10	1.06 ± 0.25	19 ± 27	0.2 ± 0.2
J183004.65+011353.7	Y	0.07 ± 0.01	>43 ± 25	<0.04	⋯	<−1.2 ± 0.4
J183004.98+012226.9	Y	0.30 ± 0.05	Extended	<0.04	⋯	<−3.9 ± 0.3
J183007.29+010324.8	Y	0.12 ± 0.02	43 ± 24	0.10 ± 0.02	34 ± 25	−0.3 ± 0.4
J183008.31+011519.1	N	0.13 ± 0.02	42 ± 15	0.07 ± 0.02	>6 ± 34	−1.2 ± 0.5
J183008.69+010631.3	N	3.18 ± 0.29	11 ± 12	1.99 ± 0.35	5 ± 24	−0.9 ± 0.1
J183008.77+010257.7	Y	0.08 ± 0.01	–A–	0.06 ± 0.02	>30 ± 27	−0.5 ± 0.6
J183010.31+012345.2	N	0.77 ± 0.12	48 ± 12	⋯	⋯	⋯
J183010.60+010320.7	N	0.19 ± 0.02	22 ± 18	0.17 ± 0.03	36 ± 22	−0.3 ± 0.3
J183012.58+011226.8	N	0.07 ± 0.01	>51 ± 14	<0.04	⋯	<−1.2 ± 0.4
J183014.25+010924.1	Y	<0.03	⋯	0.10 ± 0.03	>22 ± 29	>2.1 ± 0.6
J183014.71+011629.6	Y	0.13 ± 0.02	40 ± 15	0.10 ± 0.02	27 ± 26	−0.6 ± 0.4
J183015.53+012203.9	Y	0.20 ± 0.02	32 ± 13	0.18 ± 0.03	43 ± 20	−0.2 ± 0.3
J183016.56+011304.3	Y	0.07 ± 0.01	>36 ± 15	0.11 ± 0.02	19 ± 36	0.8 ± 0.5
J183016.74+010856.2	Y	0.27 ± 0.03	22 ± 16	0.21 ± 0.05	22 ± 28	−0.5 ± 0.2
J183018.05+011819.2	Y	<0.03	⋯	0.09 ± 0.03	>43 ± 27	>2.0 ± 0.4
J183022.13+011738.1*	Y	0.06 ± 0.01	–A–	0.05 ± 0.02	>32 ± 52	−0.2 ± 0.7
J183024.87+011323.5	N	0.07 ± 0.01	>20 ± 23	0.08 ± 0.02	>43 ± 20	0.5 ± 0.6
J183025.10+012304.3	N	0.08 ± 0.01	37 ± 26	0.10 ± 0.02	>59 ± 20	0.6 ± 0.5
J183031.05+011257.3	N	0.08 ± 0.02	43 ± 21	<0.05	⋯	<−1.0 ± 0.4
J183052.19+011915.5	N	0.10 ± 0.02	21 ± 30	⋯	⋯	⋯
J183059.74+012511.7	N	0.96 ± 0.15	31 ± 16	⋯	⋯	⋯
J183059.83+012516.5	Y	0.16 ± 0.03	34 ± 20	⋯	⋯	⋯
J183059.86+012519.0	Y	0.20 ± 0.04	18 ± 24	⋯	⋯	⋯
J183104.32+011309.0	Y	0.25 ± 0.05	42 ± 17	⋯	⋯	⋯
Detected Sources in the W40 Region:						
J183044.11-020145.6	N	1.57 ± 0.20	9 ± 16	1.27 ± 0.32	15 ± 31	−0.4 ± 0.2
J183023.27-020731.4	Y	0.25 ± 0.06	31 ± 24	0.12 ± 0.06	36 ± 48	−1.5 ± 0.4
J183101.07-021136.8	Y	0.19 ± 0.03	6 ± 20	0.14 ± 0.03	10 ± 34	−0.6 ± 0.4
J183102.25-015658.3	Y	3.25 ± 0.37	4 ± 15	1.32 ± 0.31	0 ± 33	−1.8 ± 0.2
J183102.41-015706.2	Y	2.73 ± 0.33	Extended	0.96 ± 0.22	2 ± 32	−2.1 ± 0.2
J183102.94-015917.0	Y	0.21 ± 0.03	25 ± 16	0.26 ± 0.06	50 ± 18	0.4 ± 0.3
J183105.01-020247.6	N	0.09 ± 0.02	>56 ± 10	0.09 ± 0.02	>41 ± 22	−0.0 ± 0.6
J183109.41-015442.1	Y	0.22 ± 0.03	3 ± 24	0.16 ± 0.04	Extended	−0.7 ± 0.4
J183113.05-021012.1	Y	4.70 ± 0.40	Extended	1.87 ± 0.22	Extended	−1.9 ± 0.3
J183113.23-021011.1	Y	20.78 ± 1.22	Extended	11.50 ± 0.95	Extended	−1.2 ± 0.2
J183114.31-020852.1	Y	0.13 ± 0.02	45 ± 14	0.09 ± 0.02	12 ± 36	−0.7 ± 0.5
J183114.82-020350.1	N	0.36 ± 0.04	44 ± 9	0.42 ± 0.07	50 ± 13	0.3 ± 0.3
J183115.28-020415.2	N	0.80 ± 0.07	5 ± 12	0.44 ± 0.07	1 ± 22	−1.2 ± 0.2
J183118.68-015455.9	Y	0.68 ± 0.07	11 ± 14	0.50 ± 0.10	2 ± 27	−0.6 ± 0.2
J183119.86-020006.1	Y	0.19 ± 0.03	19 ± 16	0.23 ± 0.05	15 ± 25	0.3 ± 0.3
J183120.65-020943.6	N	0.09 ± 0.02	>44 ± 12	0.13 ± 0.03	9 ± 33	0.7 ± 0.5
J183122.32-020619.6	N	0.67 ± 0.07	91 ± 2	1.13 ± 0.22	96 ± 5	1.1 ± 0.2
J183122.81-020930.7	N	0.09 ± 0.02	7 ± 35	0.11 ± 0.03	>25 ± 23	0.4 ± 0.5
J183123.62-020535.8	N	3.52 ± 0.27	15 ± 9	3.32 ± 0.45	16 ± 16	−0.1 ± 0.1
J183124.56-020231.9	N	0.07 ± 0.02	>21 ± 28	<0.06	⋯	<−0.3 ± 0.5
J183125.77-015506.7	Y	2.90 ± 0.38	27 ± 13	3.05 ± 0.83	5 ± 37	0.1 ± 0.2
J183126.02-020517.0	N	1.00 ± 0.07	52 ± 5	0.75 ± 0.09	61 ± 9	−0.6 ± 0.2
J183126.27-020630.7	Y	0.25 ± 0.06	>39 ± 10	<0.11	⋯	<−1.7 ± 0.5
J183126.85-021042.4	Y	0.22 ± 0.03	9 ± 19	0.14 ± 0.03	40 ± 25	−1.0 ± 0.4
J183127.30-020504.5	N	0.51 ± 0.05	20 ± 11	0.45 ± 0.07	36 ± 14	−0.2 ± 0.3
J183127.45-020512.0	N	2.71 ± 0.19	96 ± 1	3.17 ± 0.34	97 ± 5	0.3 ± 0.2
J183127.64-020513.5	N	0.88 ± 0.08	Extended	0.65 ± 0.11	Extended	−0.6 ± 0.3
J183127.65-020509.7	N	0.74 ± 0.05	19 ± 9	0.77 ± 0.08	13 ± 14	0.1 ± 0.2

Table 2
(Continued)

GBS-VLA Name/Position	New Detection?[a]	Flux Density (4.5 GHz) (mJy)	Variability (4.5 GHz) (%)	Flux Density (7.5 GHz) (mJy)	Variability (7.5 GHz) (%)	Spectral Index
J183127.67-020519.7	N	3.45 ± 0.24	6 ± 9	3.49 ± 0.40	6 ± 15	0.0 ± 0.2
J183127.78-020449.5	N	0.12 ± 0.02	23 ± 22	0.11 ± 0.02	5 ± 42	−0.2 ± 0.5
J183127.78-020823.0	Y	0.33 ± 0.03	6 ± 14	0.23 ± 0.02	14 ± 15	−0.7 ± 0.3
J183127.80-020521.9	N	1.47 ± 0.12	17 ± 9	1.24 ± 0.15	3 ± 17	−0.3 ± 0.2
J183128.01-020517.9	N	0.61 ± 0.06	27 ± 10	0.50 ± 0.07	18 ± 16	−0.4 ± 0.2
J183128.65-020529.8	N	6.76 ± 0.55	Extended	4.79 ± 0.71	Extended	−0.7 ± 0.2
J183128.67-020522.2	N	0.31 ± 0.04	17 ± 14	0.25 ± 0.04	3 ± 22	−0.4 ± 0.3
J183129.41-020541.1	N	0.18 ± 0.03	2 ± 31	0.12 ± 0.03	−A−	−0.8 ± 0.5
J183130.54-020530.7	N	0.26 ± 0.05	18 ± 27	<0.07	⋯	<−2.8 ± 0.4
J183148.61-020700.7	N	0.08 ± 0.02	>41 ± 16	<0.05	⋯	<−0.7 ± 0.4
J183153.39-020959.9	N	0.13 ± 0.02	36 ± 20	0.08 ± 0.03	>6 ± 44	−0.9 ± 0.5
J183201.69-020243.2	Y	0.71 ± 0.13	4 ± 25	⋯	⋯	⋯
J183201.76-021012.1	Y	0.15 ± 0.03	21 ± 27	⋯	⋯	⋯
Detected Sources in the Serpens South cluster:						
J182933.58-014530.4	Y	0.24 ± 0.06	>32 ± 24	⋯	⋯	⋯
J182940.34-015127.9	N	<0.08	⋯	0.11 ± 0.03	-A-	>0.6 ± 0.3
J182952.73-015159.9	Y	0.23 ± 0.03	25 ± 25	0.21 ± 0.04	40 ± 26	−0.2 ± 0.3
J183003.72-014944.3	Y	0.12 ± 0.03	>45 ± 19	⋯	⋯	⋯
J183004.81-020227.8	N	<0.06	⋯	0.08 ± 0.02	-A-	>0.7 ± 0.5
J183009.68-020032.7	Y	0.57 ± 0.06	43 ± 10	0.64 ± 0.12	19 ± 23	0.2 ± 0.2
J183018.69-020249.8	Y	0.20 ± 0.04	>18 ± 19	<0.09	⋯	<−1.5 ± 0.3
J183025.24-021051.9	N	0.10 ± 0.03	-A-	<0.10	⋯	<−0.0 ± 0.4
J183031.68-020954.3	Y	0.25 ± 0.05	>47 ± 13	⋯	⋯	⋯
J183037.08-021503.3	Y	1.06 ± 0.18	7 ± 23	⋯	⋯	⋯
J183038.25-021100.4	Y	0.26 ± 0.07	>8 ± 23	⋯	⋯	⋯

Note. Flux densities are measured in the combined epoch images. The quoted flux errors comprise the statistical error provided by IMFIT, the 5% absolute flux uncertainty, and the uncertainty induced by the pointing error of the VLA primary beam. The asterisk indicates a source without reported counterparts detected with an integrated flux $<5\sigma$, but with a peak flux $\geqslant 5\sigma$. The *A* annotation indicates a source not detected at three times the noise level on individual epochs, but detected on the image of the concatenated epochs.

[a] Y = source without reported counterparts at any frequency. N = source with known counterpart.

systematic uncertainty of 5% from possible errors in the absolute flux calibration, and the uncertainty induced by the pointing error of the VLA primary beam, which was included following Dzib et al. (2014). Adding the three errors in quadrature, we obtained the total flux uncertainties listed in columns 3 and 5 of Table 2. When a source is detected only at one frequency, an upper limit on the flux density of that source at the other band is given. The upper limit corresponds to three times the rms noise of the area around the source position. We adopted the same criteria as Dzib et al. (2013) to consider a detection as firm. For new sources, i.e., those without reported counterparts in the literature, we considered 5σ detections, where σ is the rms noise of the area around the source. For known sources with counterparts in the literature, on the other hand, we included 4σ detections. According to these criteria, we detected 94 sources in the Serpens molecular cloud, 41 in the W40 region, and 8 in the Serpens South cluster, for a total of 143 detections. Out of the 143 sources, 69 are new detections (see Section 3.2).

In order to compare the flux density between epochs and then to estimate the flux variability on a timescale of months, we searched in the images obtained from the individual epochs the sources detected in the combined ones. The flux densities and positions of the sources in these individual images are not shown for the sake of brevity.

We investigated the number of false positives that could appear given the considerably large size of our mosaics. Assuming a Gaussian noise distribution, we estimated that the number of possible false sources with a 5σ flux level is 7 at both 4.5 and 7.5 GHz in the Serpens mosaic. In the W40 mosaic, the number of possible false sources is 4 and 9 at 4.5 and 7.5 GHz, respectively. For a 6σ flux level, we found that the number of false sources is below 0.03 for both mosaics and at both frequencies. In Serpens, five sources were detected at 4.5 GHz with flux levels between 5σ and 6σ and without counterparts at any other wavelengths (including counterparts at 7.5 GHz). At 7.5 GHz, only one source without counterparts (including counterparts at 4.5 GHz) was detected with a 5σ–6σ flux level. Therefore, these six sources could be false detections. In W40, all the sources without counterparts (including counterparts at 4.5 or 7.5 GHz) were detected above 6σ, and therefore all sources reported in that region are real detections. We noted that in both mosaics, we consider a radio source to have a counterpart at either 4.5 or 7.5 GHz only if it is detected at above 6σ.

3.2. Source Counterparts

GBS-VLA source positions were compared with source positions from X-ray, optical, near-IR, mid-IR, and radio catalogs. GBS-VLA sources were considered to have a counterpart at another wavelength when the positional coincidences were better than the combined uncertainties of the two data sets. These were about $1''$ for the IR catalogs. For the X-ray and radio catalogs it depends on the instrument and its

Table 3
Radio Sources with Known Counterparts

GBS-VLA Name	Other Names	X-ray[a]	IR[b] *SST*	IR[b] 2M	IR[b] *WISE*	Radio[c]	Object Type
Counterparts of the Serpens Molecular Cloud Sources:							
J182851.30+010908.6	…	…	…	…	…	NVSS 182851 +010908	…
J182901.40+010434.7	…	…	…	…	…	NVSS 182901 +010436	…
J182905.07+012309.0	…	…	Y	…	…	…	…
J182906.84+011742.7	…	…	Y	…	…	…	…
J182907.62+012125.1	…	…	Y	…	…	…	…
J182910.17+012559.5	…	…	Y	…	…	…	…
J182913.17+010906.4	…	…	Y	…	…	…	…
J182913.79+010738.6	…	…	Y	…	…	…	…
J182916.11+010437.5	…	…	Y	…	…	…	…
J182918.23+011757.7	…	…	Y	…	…	…	…
J182926.71+012342.1	…	…	Y	…	…	…	…
J182928.02+011156.5	…	…	Y	…	…	…	…
J182928.28+011205.7	…	…	…	…	…	NVSS 182928 +011203	…
J182929.78+012158.1	…	GFM 6	…	…	…	…	YSO
J182930.71+010048.3	PMN J1829+0101	…	…	…	…	NVSS 182930 +010048	…
J182933.07+011716.3	SVS76 Ser 14	GFM 11	Y	Y	Y	…	YSO
J182934.32+011513.9	…	…	Y	…	…	DCE08–210 5	…
J182935.02+011503.2	DCE08–210 5	…	Y	…	…	NVSS 182934 +011504	…
J182935.11+011503.6	…	…	…	…	…	DCE08–210 5	…
J182936.50+012317.0	…	…	Y	…	…	…	…
J182937.76+010314.6	…	…	…	…	…	NVSS 182937 +010316	…
J182944.07+011921.1	DCE08–210 6	…	…	…	…	NVSS 182944 +011920	…
J182948.83+010647.4	…	…	Y	…	…	…	…
J182949.79+011520.4	SERPENS SMM 1 a	…	…	…	…	DCE08–210 1	…
J182951.04+011533.8	…	…	…	…	…	ETC 8	…
J182951.17+011640.4	V371 Ser	GFM 30	Y	…	Y	ETC 9	YSO
J182951.22+012132.0	…	…	…	…	…	NVSS 182951 +012131	…
J182952.22+011547.4	Serpens SMM 10 IR	…	Y	…	Y	ETC 10	YSO
J182953.99+011229.5	…	…	Y	…	…	…	…
J182954.31+010309.6	…	…	Y	…	…	…	…
J182956.96+011247.6	EC92 84	GFM 44	Y	Y	…	ETC 14	YSO
J182957.60+011300.2	EES2009 Ser-emb 22	GFM 46	Y	Y	…	ETC 15	YSO
J182957.85+011251.1	EES2009 Ser-emb 23	GFM 53	Y	Y	…	ETC 17	YSO
J182957.89+011246.0	EC92 95	GFM 54	Y	Y	…	DCE08–215 8	YSO
J182959.55+011158.1	EES2009 Ser-emb 24	GFM 60	Y	Y	…	…	YSO
J182959.94+011311.3	EES2009 Ser-emb 19	…	Y	…	Y	…	YSO
J183000.65+011340.0	CK 6	GFM 65	Y	Y	Y	ETC 20	YSO
J183001.24+010205.4	…	…	…	…	…	NVSS 183001 +010204	…
J183002.42+012405.6	…	…	Y	…	Y	…	…
J183004.62+012234.1	P2003 J183004.7+012232	GFM 70	…	…	…	…	…
J183008.31+011519.1	…	…	Y	…	…	…	…
J183008.69+010631.3	…	…	…	…	…	NVSS 183008 +010634	…
J183010.31+012345.2	…	…	Y	…	…	…	…
J183010.60+010320.7	…	…	Y	…	…	…	…
J183012.58+011226.8	…	GFM 81	Y	…	…	…	…
J183024.87+011323.5	HD 170634	…	Y	Y	Y	…	B7V
J183025.10+012304.3	…	…	Y	…	…	…	…
J183031.05+011257.3	…	…	Y	…	…	…	…
J183052.19+011915.5	…	…	Y	…	…	…	…
J183059.74+012511.7	…	…	…	…	…	NVSS 183059 +012512	…

Table 3
(Continued)

GBS-VLA Name	Other Names	X-ray[a]	IR[b] *SST*	IR[b] 2M	IR[b] *WISE*	Radio[c]	Object Type
Counterparts of the W40 Region Sources:							
J183044.11–020145.6	…	…	…	Y	…	…	…
J183105.01–020247.6	CXOW40 J183105.02–020247.5	KGF 18	…	Y	…	…	YSO
J183114.82-020350.1	W 40 IRS 5	KGF 36	…	Y	…	RRR W40-VLA 1	B1V
J183115.28-020415.2	CXOW40 J183115.30-020415.2	KGF 38	…	…	…	RRR W40-VLA 2	…
J183120.65-020943.6	CXOW40 J183120.65-020944.1	KGF 71	…	Y	…	…	YSO
J183122.32-020619.6	CXOW40 J183122.32-020619.5	KGF 82	…	Y	…	RRR W40-VLA 3	YSO
J183122.81-020930.7	CXOW40 J183122.82-020930.5	KGF 88	…	Y	…	…	YSO
J183123.62-020535.8	CXOW40 J183123.62-020535.7	KGF 97	…	Y	…	RRR W40-VLA 5	YSO
J183124.56-020231.9	CXOW40 J183124.57-020231.9	KGF 102	…	Y	…	…	YSO
J183126.02-020517.0	W 40 IRS 1 c	KGF 122	…	Y	Y	RRR W40-VLA 8	YSO
J183127.30-020504.5	…	…	…	Y	…	RRR W40-VLA 9	YSO?
J183127.45-020512.0	CXOW40 J183127.46-020511.9	KGF 133	…	Y	…	RRR W40-VLA 10	YSO?
J183127.64-020513.5	CXOW40 J183127.64-020513.5	KGF 136	…	Y	…	RRR W40-VLA 12	gyrosynchrotron source?
J183127.65-020509.7	W 40 IRS 1 d	KGF 138	…	Y	…	RRR W40-VLA 13	YSO
J183127.67-020519.7	…	…	…	Y	…	RRR W40-VLA 14	gyrosynchrotron source?
J183127.78-020449.5	CXOW40 J183127.78-020449.5	KGF 139	…	Y	…	…	YSO
J183127.80-020521.9	W 40 IRS 1 a N	…	…	Y	…	RRR W40-VLA 15	YSO
J183128.01-020517.9	CXOW40 J183128.01-020517.1	KGF 144	…	Y	…	RRR W40-VLA 16	YSO
J183128.65-020529.8	W 40 IRS 1 b	KGF 145	…	Y	…	RRR W40-VLA 18	YSO
J183128.67-020522.2	…	…	…	…	…	RRR W40-VLA 19	shock front?
J183129.41-020541.1	CXOW40 J183129.45-020541.2	KGF 153	…	Y	…	…	YSO
J183130.54-020530.7	CXOW40 J183130.56-020530.6	KGF 162	…	Y	…	…	YSO
J183148.61-020700.7	CXOW40 J183148.64-020755.5	KGF 220	…	Y	Y	…	YSO
J183153.39-020959.9	…	…	…	Y	Y	…	…
Counterparts of the Serpens South Sources:							
J182940.34-015127.9	…	…	Y	…	…	…	YSO
J183004.81-020227.8	…	…	Y	…	…	…	YSO
J183025.24-021051.9	…	…	Y	…	…	…	YSO

[a] GFM—Giardino et al. (2007), KGF—Kuhn et al. (2010).
[b] *SST*—Evans et al. (2009), c2d-GB clouds catalog (Dunham et al. 2013), 2M—Cutri et al. (2003), and *WISE*—Wright et al. (2010).
[c] ETC—Eiroa et al. (2005); NVSS—Condon et al. (1998), DCE08—AMI Consortium et al. (2012), RRR—Rodríguez et al. (2010).

configuration. The search was done in SIMBAD and included all the major catalogs (listed explicitly in the footnote of Table 3). We have also accessed the lists with all YSOs in the c2d-GB clouds compiled by Dunham et al. (2013) and L. E. Allen et al. (2015, in preparation). In total, 354 c2d-GB sources lie inside the regions observed by us. In order to find their radio counterparts, we imaged regions of 64 pixels in each dimension, centered in the c2d-GB positions, and combining accordingly with each region, the three or two epochs. For this search we only used the field whose phase center was closest to the source. Three additional radio sources were found in Serpens South in this pursuit, increasing the number of the radio detections to 146.

Out of 146 GBS-VLA sources, only 36 had previously been detected at radio wavelengths (column 7 of Table 3), while the other 110 are new radio detections from this survey. On the other hand, we found a total of 63 counterparts at X-ray, near-IR, and mid-IR wavelengths, some of which have known radio counterparts. In total, the number of sources that were previously known (at any frequency) is 77, while 69 of the sources in our sample are reported here for the first time.

The classification of the sources shown in column 8 of Table 3 was taken from the literature and is based on the IR and X-ray properties of the sources. A total of 29 of the 77 sources with counterparts are firmly classified as YSOs, while HD 170634 (GBS-VLA J183024.87+011323.5) and W 40 IRS 5 (GBS-VLA J183114.82–020350.1) are typed as B7V and B1V stars, respectively. Two additional sources (GBS-VLA J183127.30–020504.5 and J183127.45–020512.0) are considered YSO candidates (Rodríguez et al. 2010). Three other sources have been associated with phenomena related to YSOs. Rodríguez et al. (2010) suggest that GBS-VLA J183128.67–020522.2 could correspond to a shock front from a thermal jet (possibly powered by GBS-VLA J183128.65–020529.8) interacting with the ambient interstellar medium. The sources GBS-VLA J183127.64–020513.5 and J183127.67–020519.7 have been considered as ultracompact H II (UCH II) region candidates, centered around young massive stars. However, Shuping et al. (2012) argue that this classification is unlikely, as the size of the unresolved radio sources at a distance of 500 pc would be less than 100 AU, much smaller than a typical UCH II region (Kurtz 2005). Instead, they propose that the 3.6 cm continuum flux could be due to free–free emission from shocked gas within 100 AU of the YSO caused by a jet or outflow. We note that, out of the 15 radio sources reported by Rodríguez et al. (2010) with IR counterparts, 7 were found by them not to be time variable (sources GBS-VLA J183114.82–020350.1, J183122.32–020619.6, J183127.64–020513.5, J183127.67–020519.7, J183127.80–020521.9, J183128.01–020517.9, and J183128.65–020529.8). In our new observations, only GBS-VLA J183114.82–020350.1 and J183122.32–020619.6 are found to have high flux variability. However, when comparing our 7.5 GHz observations made in 2011 to those made at 8.3 GHz in 2003 and 2004 by Rodríguez et al. (2010), remarkably, all sources show significant variations, typically by factors of ∼2 (see the Appendix). We then conclude that the interpretation of the sources GBS-VLA J183127.64–020513.5 and J183127.67–020519.7 as steady UCH II regions (Rodríguez et al. 2010) is not correct, and that they are possibly gyrosynchrotron sources of slow time variability. If this is the case, they should be detectable as VLBI sources. The remaining 41 GBS-VLA sources with known counterparts at other wavelengths are, to our knowledge, not classified in the literature. In summary, we report a total of 110 unclassified sources, i.e., the 69 new detections plus the 41 sources that have previously been detected at other wavelengths but without a classification given in the literature.

3.3. Spectral Index, Variability, and Circular Polarization

An estimation of the radio spectral index α (the flux density $S_\nu \propto \nu^\alpha$) was obtained for most of the sources using $\alpha = \log(S_\nu\ (4.5)/S_\nu\ (7.5))/\log(4.5\ \mathrm{GHz}/7.5\ \mathrm{GHz})$, where $S_\nu(4.5)$ and $S_\nu\ (7.5)$ are the flux densities at 4.5 and 7.5 GHz, respectively, and ν is the frequency of the incoming radiation. The spectral index is given in column 7 of Table 2.

The repeated observations allowed us to estimate the flux variation between the observed epochs at each frequency. Specifically, we determined the highest and lowest fluxes ($S_{\nu,\max}$ and $S_{\nu,\min}$, respectively) of the three or two epochs. The level of variability was then estimated as the ratio of the difference between these values to the highest measured flux, i.e., $\text{variability} = (S_{\nu,\max} - S_{\nu,\min})/S_{\nu,\max}$. The resulting values, expressed in percentages, are given in columns 4 and 6 of Table 2. The quoted uncertainties in the table for the variability and spectral index were obtained, using standard error propagation theory, from the errors of the flux density (see Section 3.1). We considered as statistically significant only those variations that are above 3σ, where σ is the variability error of the source. In other words, we consider a source as variable if the normalized difference between its highest and lowest flux density is greater than zero within an error of 3σ.

Table 4
Sources Detected in Circular Polarization

GBS-VLA Name	Degree of Circular Polarization	
	4.5 GHz (%)	7.5 GHz (%)
J183113.23-021011.1	1 (L)	1 (R)
J183123.62-020535.8	5 (R)	8 (R)

Note. The letters indicate left (L) or right (R) circular polarization.

Circular polarized radio emission was detected only from two sources in W40 (see Table 4). The identification of these sources was done also through a visual inspection in the Stokes V images and searching around the position of the radio sources detected in Stokes I emission. We required the signal-to-noise ratio in the Stokes V images to be greater than 5. Since the degree of circular polarization ($|V|/I$) of both sources is lower than 10%, we cannot safely associate the radio emission to gyrosynchrotron. As a consequence of the smaller size of the Stokes V images ($4' \times 4'$), only 76 sources out of 143 were tested. The rest of them lie outside of the Stokes V maps, but they could have circular polarization.

Given the existing deep X-ray, IR, millimeter, and submillimeter surveys carried out toward these regions, it is unlikely that a large fraction of the 110 unclassified sources are unidentified YSOs; however, we cannot rule out this possibility. In order to characterize the nature of the unclassified sources, we analyze their radio properties. We find that 15 radio sources in the Serpens molecular cloud and one source in the W40 region (Table 5) are compact and have high levels of variability ($\gtrsim$50% at a 3σ level) or a positive spectral index ($\geqslant +0.2$ within 1σ). Extragalactic sources do not usually show high variability on such a short timescale (e.g., Hovatta et al. 2007, 2008; Lovell et al. 2008) or have a positive spectral index, while the radio emission seen in many Class III and some youngest objects is highly variable (e.g., Feigelson & Montmerle 1985; Feigelson et al. 1998).

We propose then that these 16 unclassified sources are YSO candidates. The remaining 94 unclassified sources are then considered by us as extragalactic sources. Notice that sources with spectral indices larger that −0.1 could also be due to free–free radiation (Rodriguez et al. 1993). To firmly establish the nature of a radio continuum source, we need observations of its morphology, spectral index, polarization, and time variability (Rodríguez et al. 2012).

4. DISCUSSION

4.1. The Lack of Radio Emission from Serpens South

Approximately 120 YSOs from the c2d-GB catalog lie inside the region mapped by us in the Serpens South cluster. The detection of their radio counterparts is, surprisingly, very

Table 5
Young Stellar Object Candidates Based Just on Their Radio Properties

GBS-VLA Name	Variability (4.5 GHz) (%)	Variability (7.5 GHz) (%)	Spectral Index
YSO Candidates in the Serpens Molecular Cloud			
J182854.46+011823.7	44 ± 9	17 ± 24	1.2 ± 0.1
J182910.17+012559.5	71 ± 8	…	…
J182913.79+010738.6	36 ± 25	>26 ± 20	0.9 ± 0.5
J182916.11+010437.5	41 ± 16	52 ± 19	0.4 ± 0.2
J182932.21+012104.6	52 ± 15	>20 ± 27	-0.8 ± 0.5
J182948.83+010647.4	29 ± 13	6 ± 23	0.8 ± 0.2
J182948.92+011523.8	>62 ± 10	…	<-0.5 ± 0.5
J182949.54+011523.8	76 ± 7	…	<-2.5 ± 0.3
J182949.60+011522.9	71 ± 8	64 ± 14	-0.5 ± 0.4
J182950.34+011515.3	11 ± 20	>61 ± 18	-1.0 ± 0.4
J182954.30+012011.2	>75 ± 5	…	<-2.3 ± 0.3
J183012.58+011226.8	>51 ± 14	…	<-1.2 ± 0.4
J183014.25+010924.1	…	>22 ± 29	>2.1 ± 0.6
J183016.56+011304.3	>36 ± 15	19 ± 36	0.8 ± 0.5
J183018.05+011819.2	…	>43 ± 27	>2.0 ± 0.4
YSO Candidates in the W40 Region			
J183127.45-020512.0	96 ± 1	97 ± 5	0.3 ± 0.2

low. C2d-GB sources have only three radio counterparts in Serpens South (see Tables 2 and 3). These counterparts were detected with fluxes of $\lesssim$0.10 mJy (or radio luminosities of $\lesssim 21 \times 10^{15}$ erg s^{-1} Hz^{-1}, assuming a distance of 415 pc). Millimeter dust continuum data in combination with IR *Spitzer* observations have suggested that the Serpens South cluster is very young (a few times 10^5 yr; Fernández-López et al. 2014). It is then expected that the radio emission from most of the YSOs in the cluster is dominated by thermal emission from strong winds. Using Equation (24) of Panagia & Felli (1975) and following Rodriguez et al. (1989), we estimated that for a spherical wind with a terminal velocity $v = 200$ km s^{-1}, an electron temperature $T_e = 10^4$ K, and a mass-loss rate of $10^{-7}\,M_\odot$ yr^{-1}, the radio flux density at a distance of 415 pc is ~0.34 mJy at 4.5 GHz. If the cluster is more distant, i.e., at 700 pc, the radio flux decreases to ~0.12 mJy at 4.5 GHz, which is just equal to the sensitivity limit of our observations toward that region ($5\sigma = 0.12$ mJy). It is then possible that we are not detecting the radio flux from the YSO population in Serpens South because the cluster is more distant than thought.

4.2. Background Sources

We see from the previous section that a considerable fraction of the radio sources detected are likely extragalactic objects (67 in the Serpens cloud, 19 in W40, and 8 in Serpens South, giving a total of 94 sources). In order to estimate the number of expected background radio sources, we follow Anglada et al. (1998), who took into account the Gaussian primary-beam response of the VLA antennas. Considering that at 4.5 GHz the half-power width of the primary beam of the VLA is ~10′, we find that the number of expected radio sources in each field with a flux greater than $S_{4.5}$ at 4.5 GHz is given by

$$N_{4.5} = 1.21 \left(\frac{S_{4.5}}{\mathrm{mJy}} \right)^{-0.75}. \quad (1)$$

The 25 pointings used to map the Serpens molecular cloud correspond to a total area of $25 \cdot \pi \cdot (10'/2)^2 = 1963.5$ square arcminutes at 4.5 GHz. However, because of the overlapping between them, the effective covered area was 900 square arcminutes at 4.5 GHz, which is equivalent to 11 fields.

Therefore, using Equation (1), we find that 105 background sources with a flux $\geqslant$64 μJy (5σ) at 4.5 GHz are predicted to lie within the mapped area of the Serpens molecular cloud. The same exercise gives 40 and 23 background sources expected in the W40 region and the Serpens South cluster, respectively. Hence, we have detected fewer extragalactic objects than expected by the count of Anglada et al. (1998) in the three regions, and we are statistically justified to assume that all of them are background and not associated with the region. Of course, this is subject to statistical variations.

4.3. Radio Properties of the YSO Population

We analyze the radio properties of the YSOs detected in our observations. A subset of the detected YSOs with radio emission have an SED classification reported in the literature (see Table 6 and references listed in its column 7). Out of the 29 YSOs, 8 are Class I or Flat, 5 Class II, and 12 Class III objects. In Figure 2 we plot the spectral index of these 25 objects as a function of evolutionary status. The mean values of each category are indicated by the large blue circles. We see that, given the large uncertainties involved, it is not possible to distinguish between different evolutionary classes based on the spectral index from flux densities at 4.5 and 7.5 GHz. We note, however, that there are two Class I stars with a very negative spectral index. This will be discussed later in Section 5. Notice also that most of the Class I YSOs we have detected have flux densities below 75 μJy (6σ). For those sources, systematic errors are important, and the spectral index and variability errors are large. For example, GBS-VLA J182957.60 + 011300.2 could have a positive index (+0.4) if we consider 1σ dispersion.

Table 6
Young Stellar Objects Detected in the Radio Observations

GBS-VLA Name	Spectral Type	SED Classification[a]	High[b] Variability	α[b]	X-ray	Reference[c]
		YSOs in the Serpens Molecular Cloud				
J182929.78+012158.1	⋯	Class II	⋯	N	Y	1
J182933.07+011716.3	G2.5	Class III	Y	P	Y	1, 5
J182951.17+011640.4	⋯	Class I	Y	N	Y	1, 7
J182952.22+011547.4	⋯	Class I	N	N	N	2, 7
J182956.96+011247.6	M3.0	Class II	Y	P	Y	1, 5
J182957.60+011300.2	⋯	Class I	N	F	Y	2, 7
J182957.85+011251.1	⋯	Class I	N	P	Y	2, 7
J182957.89+011246.0	K1.0	P-HAeBe	Y	F	Y	6
J182959.55+011158.1	⋯	Class I	N	N	Y	2, 7
J182959.94+011311.3	⋯	Class I	N	N	N	2, 7
J183000.65+011340.0	M0.5	Class III	Y	N	Y	1, 5
		YSOs in the W40 Region				
J183105.01–020247.6	⋯	Class III	Y	F	Y	3
J183120.65–020943.6	⋯	Class III	N	P	Y	3
J183122.32–020619.6	⋯	Class III	Y	P	Y	3
J183122.81–020930.7	⋯	Class III	N	P	Y	3
J183123.62–020535.8	⋯	Class III	N	F	Y	3
J183124.56–020231.9	⋯	Class III	N	N	Y	3
J183126.02–020517.0	⋯	Class II	Y	N	Y	4
J183127.65–020509.7	⋯	HAeBe?[d]	N	F	Y	3
J183127.78–020449.5	⋯	Class III	N	F	Y	3
J183127.80–020521.9	⋯	HAeBe	N	N	N	4
J183128.01–020517.9	⋯	…	N	N	Y	3
J183128.65–020529.8	⋯	Class II	Extended	N	Y	4
J183129.41–020541.1	⋯	Class III	N	N	Y	3
J183130.54–020530.7	⋯	Class III	N	N	Y	3
J183148.61–020700.7	⋯	Class III	N	N	Y	3
		YSOs in Serpens South				
J182940.34–015127.9	⋯	Flat	⋯	P	N	7
J183004.81–020227.8	⋯	Class I	⋯	P	N	7
J183025.24–021051.9	⋯	Class II	⋯	F	N	7

[a] This classification was taken from the literature; references are given in column 7.
[b] High variability = Y when the flux variability is $\gtrsim$50% at a 3σ level in at least one frequency; N when the variability is <50% at both frequencies. α refers to the spectral index and is given as P (for positive) when it is higher than 0.2; F (for flat) when it is between −0.2 and +0.2; and N (for negative) when it is lower than −0.2. X-ray = Y when there is an X-ray flux reported in literature, N when it is not.
[c] (1) Giardino et al. (2007), (2) Enoch et al. (2009), (3) Kuhn et al. (2010), (4) Shuping et al. (2012), (5) Winston et al. (2010), (6) Preibisch (1999), (7) = c2d-GB cloud catalog (Dunham et al. 2013).
[d] This source has a mass of $\sim$4 $M_{\odot}$ and no K_s-band excess. We therefore consider it as an HAeBe candidate.

Out of the 25 detected Class I–III objects, 20 have a variability determination at either 4.5 or 7.5 GHz. Figure 3 shows the level of variability as a function of the evolutionary status for these 20 objects. We see that the older class (Class III) is populated by objects with very high variable emission. In the same plot, we show the weighted average of variability for each evolutionary class. While Class I and Class II sources have weighted average variability lower than 50%, the weighted average variability of Class III is ∼80%. In order to test if variability increases with age, as is suggested by the plot, we carried out a Kolmogorov–Smirnov test on the three YSO classes. The null hypothesis to test is that the variability distributions of different classes are drawn from the same distribution. Figure 4 shows the cumulative probability distributions. The D statistic gives the absolute maximum distance between the cumulative distributions of two samples. The D statistic is $D_{\rm I-II} = 1.16$ for class I and II distributions, $D_{\rm I-III} = 0.89$ for class I and III distributions, and $D_{\rm II-III} = 0.65$ for class II and III distributions. The p-value gives the probability of obtaining the observed distributions when the null hypothesis is true. We obtained a p-value of $p_{\rm I-II} = 0.13$ for class I and II distributions, $p_{\rm I-III} = 0.4$ for class I and III distributions, and $p_{\rm II-III} = 0.79$ for class II and III distributions. Assuming that sample pairs with $p < 0.10$ are taken from different distribution functions with high significance, we cannot reject the null hypothesis. This result may be affected by the small number of YSOs in the samples and the large uncertainties of the variability. However, we are interested in testing this tendency in a forthcoming paper, using the whole sample of YSOs detected toward the Ophiuchus, Orion, Perseus, and Taurus-Auriga regions.

We weighted average the variability of the YSO candidates identified in our observations (Table 5). This average is shown

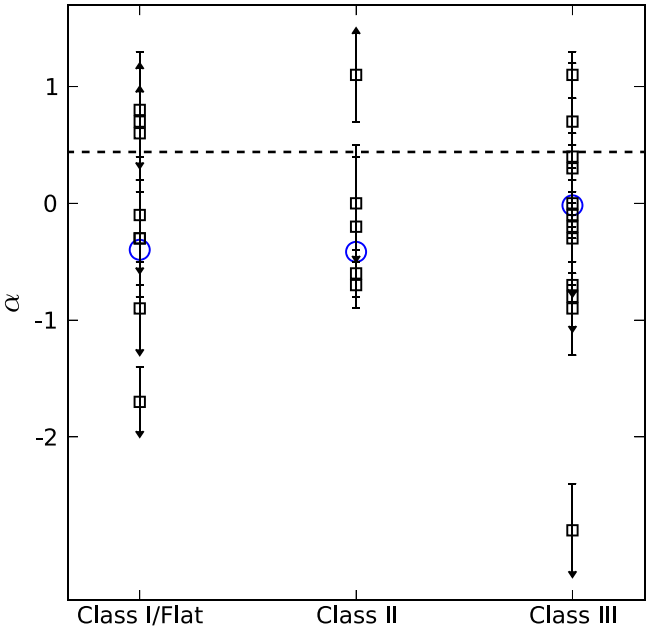

Figure 2. Spectral index as a function of evolutionary status of the 25 detected Class I–III YSOs. Values for the individual sources are shown with squares, and weighted mean values with circles. The arrows indicate upper and lower limits. The horizontal dashed line marks the weighted average spectral index of the YSO candidates listed in Table 5.

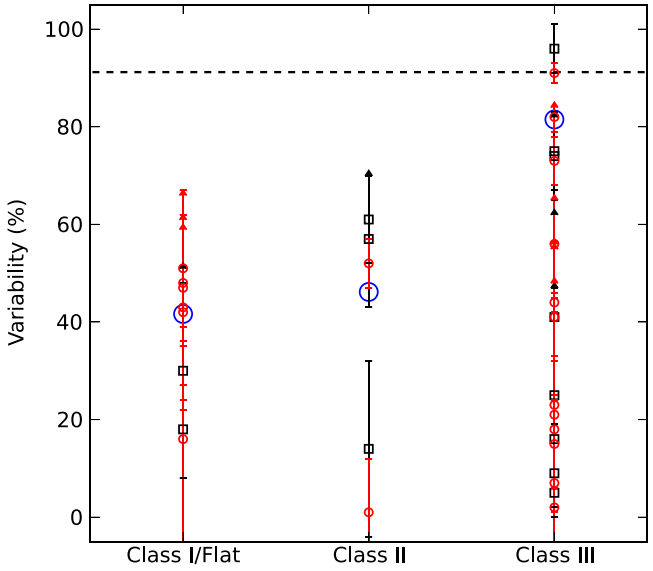

Figure 3. Variability as a function of the evolutionary status of 20 Class I–III YSOs. Values for the individual sources are shown with red circles (variability at 4.5 GHz) and black squares (variability at 7.5 GHz). Some sources have a variability determination at both frequencies. The blue circles are the weighted average for each class. The arrows indicate lower limits. The horizontal line marks the weighted average variability at both frequencies of the YSO candidates listed in Table 5.

as a horizontal line in Figure 3. Interestingly, we find that the weighted average variability (∼90%) of the YSO candidates is closest to the averaged variability of the Class III known YSOs. This suggests that it might be the largest population of Class III sources out of our YSO candidates.

4.4. The X-Ray—Radio Relation

For active stellar coronae, Güdel & Benz (1993) found a correlation between X-ray and radio luminosities, L_X and L_R, respectively, which holds for X-ray luminosities over six orders of magnitude. The interpretation of this empirical relation is that the mechanism responsible for accelerating the non-thermal electrons that emit in the radio continuum also heats the coronal plasma, and this gives rise to the thermal X-ray flux. Class Me dwarfs, Ke dwarfs, and BY Dra stars, which typically have low luminosities, satisfy

$$\frac{L_X}{L_R} \approx 10^{15.5\pm1} \text{ [Hz]}. \quad (2)$$

More luminous classes (WTTS, RS CVn's binaries, Algols, and FK Com stars) are systematically less X-ray bright compared to their radio luminosity and fulfill

$$L_X/L_R \lesssim 10^{15.5} \text{ [Hz]}. \quad (3)$$

We study the L_X-L_R relation for the YSOs with X-ray counterparts in our sample. A total of 29 radio sources have X-ray counterparts, 23 of which are YSOs. However, we consider only YSOs with high radio variability or with a negative or flat spectral index (a subset of 18 Class I–III sources), thereby excluding sources that could be not coronal. Also, we have corrected all X-ray luminosities to the distance of 415 pc adopted in this work (see the discussion in Section 1). The corrected luminosity L_0 was obtained using $L_0 = (d_0/d)^2 L$,

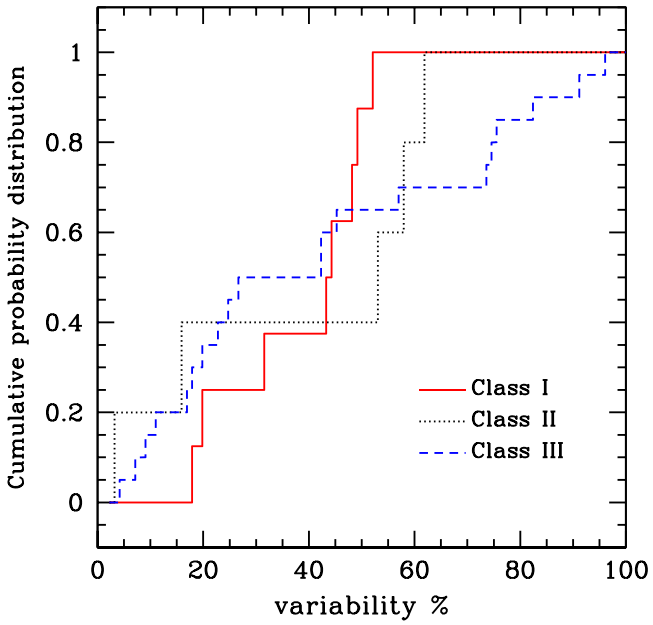

Figure 4. K–S test: cumulative probability distributions of variability in the three classes of YSOs. Red solid line: Class I; black dotted line: Class II; blue dashed line: Class III.

where L is the luminosity of the source assuming a distance d, and d_0 is the new adopted distance.

Following Güdel & Benz (1993), we place our subset of YSOs in the L_X-L_R diagram (Figure 5) and compare with the relations already determined for stars of different classes with magnetic activity. Also plotted in Figure 5 are the YSOs detected in the Ophiuchus complex by Dzib et al. (2013). We find that the YSOs we have detected in Serpens and W40, as

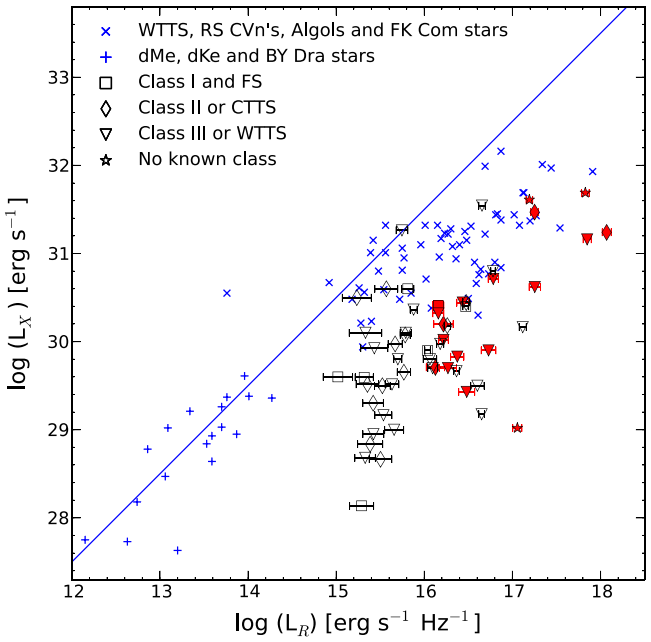

Figure 5. $L_X - L_R$ relation for stars following Güdel & Benz (1993). Symbols indicate different classes of stars as explained at the top left of the diagram. Radio and X-ray luminosities of active stellar coronae represented by blue vertical and diagonal crosses were taken from Güdel et al. (1993) and Drake et al. (1989). The solid line with slope 1 is the fit obtained by Güdel & Benz (1993) for the dM(e), dK(e), and BY Dra stars (blue vertical crosses), which occupy the lower left portion of the diagram. Open symbols correspond to YSOs detected in the Ophiuchus complex (Dzib et al. 2013). The YSOs detected by us in the Serpens and W40 regions with X-ray counterparts and with possible coronal radio emission are shown as red filled symbols. The radio luminosity used for GBS-VLA sources is the average of the luminosities at 4.5 and 7.5 GHz.

well as the sample of YSOs in Ophiuchus, do not follow the Güdel–Benz relation for dwarf stars (Equation (2)). Conversely, they fulfill $L_X/L_R \lesssim 10^{15.5}$ [Hz]. Güdel & Benz (1993) proposed that the deviation from the relation with slope equal to 1 is likely a result of the sources having larger magnetospheres, which causes longer trapping times for the radio-emitting high-energy particles.

Lower X-ray fluxes than the relation given by Equation (2) could also be explained if the photons are absorbed by gas in front of the clouds. Kuhn et al. (2010) determined the visual absorption A_V toward their W40 sources from a J versus J–H diagram. Our radio sources with counterparts in the catalog of Kuhn et al. (2010) have visual absorptions ranging from 6 to 22 mag. Using the standard conversion $N_{\rm H} = (1.8 \pm 0.3) \times 10^{21}\,{\rm cm}^{-2} \times A_V$ (Predehl & Schmitt 1995), we find that the values of $A_V = 6$–22 imply absorbing column densities of $N\,({\rm H}) \sim (1-4) \times 10^{22}\,{\rm cm}^{-2}$. In the Serpens core, Giardino et al. (2007) report column densities of $N\,({\rm H}) \sim (0.5-7.4) \times 10^{22}\,{\rm cm}^{-2}$ for our YSOs with radio emission. Another possibility for the deviation from relation (2) is a bias toward the brightest sources at the X-ray band in the Güdel–Benz relation. According to this interpretation, the full area below the relation could be populated with fainter coronal sources. In fact, the YSOs in Serpens and Ophiuchus lie below the stars analyzed in the original study of Güdel & Benz (1993).

4.5. Proper Motions of YSOs in the W40 Region

Rodríguez et al. (2010) observed the W40 region at 3.6 cm with the VLA in its A and B array configurations. We use the observations obtained with the A configuration (2004 September 18) to estimate the angular displacement of the sources between then and our own observations 7 yr later, in 2011. The phase calibrator J1804+010 was used in all observing runs. In total, only nine compact sources are detected at both epochs (see Table 7). Notice that the displacement of the sources generated by their trigonometric parallax ($p('') = 1/D$ [pc]) is 2.4 mas for a distance of $D = 415$ pc, which is comparable to or even lower, by one order of magnitude, than the position errors of these sources (2–15 mas). Therefore, we do not consider the contribution from the parallax to the angular displacement of the sources. The proper motions in R.A., $\mu_\alpha \cos(\delta)$, and decl., μ_δ, are given in Table 7 and plotted in Figure 6. We also see that, with the exception of GBS-VLA J183122.32–020619.6 (RRR W40-VLA 3), all the sources are moving in the same direction with a mean absolute value $\mu_{\rm total} = 12.7\,{\rm mas\,yr}^{-1}$. The average proper motions in R.A. and decl. of these eight sources are $\mu_\alpha \cos(\delta) = -8.0\,{\rm mas\,yr}^{-1}$ and $\mu_\delta = -9.7\,{\rm mas\,yr}^{-1}$. The sources GBS-VLA J183122.32–020619.6, J183123.62–020535.8, J183126.02–020517.0, and J183128.65–020529.8 (RRR W40-VLA 3, 5, 8, and 18) are associated with YSOs and, in fact, they all have non-zero proper motions. Rodríguez et al. (2010) suggested that GBS-VLA J183127.30–020504.5 (RRR W40-VLA 9) is a YSO candidate, while we propose that GBS-VLA J183127.67–020519.7 (RRR W40-VLA 14) is a gyrosynchrotron source. The movements of these sources are similar to most of the stars reported in Table 7, confirming that both objects are Galactic. It has been posited by Rodríguez et al. (2010) that GBS-VLA J183128.67–020522.2 (RRR W40-VLA 19) is a shock front from a thermal jet (possibly powered by GBS-VLA J183128.65–020529.8). We note that this source has not been detected at IR, optical, or X-ray wavelengths, which suggests that it is not a YSO. Its proper motion is the largest of the group, and this could be due to an intrinsic motion. The expected proper motions for objects in the direction toward W40 at a distance of 415 pc are $\mu_\alpha \cos(\delta) = 0.76\,{\rm mas\,yr}^{-1}$ and $\mu_\delta = -5.61\,{\rm mas\,yr}^{-1}$. These values are smaller than our estimations, and probably this could be due to a systematic error (like an offset in the position of the phase calibrator in the archive data). However, we have investigated this possibility and do not find any offset. It is also possible that the cluster has a peculiar velocity.

5. COMMENTS ON INDIVIDUAL SOURCES

The source W40 IRS 1 d (GBS-VLA J183127.65–020509.7) was classified as a single source by Smith et al. (1985), but it has been recently resolved in the near-IR into a small cluster of at least seven distinct sources by Shuping et al. (2012). The position of the X-ray source associated with it, however, comes from a high-resolution (0.″5) X-ray image of the *Chandra* telescope. The source is classified as an intermediate-mass YSO ($\sim 4\,M_\odot$; Kuhn et al. 2010) and coincident, within the error, with the position of the radio source. Thus, we will consider that W40 IRS 1d is associated with this young star. Also, this source does not show K_s-band excess (Kuhn et al. 2010), a fact that, along

Table 7
Proper Motions of Some Radio Sources in W40

GBS-VLA Name	RRR W40-VLA Number[a]	$\mu_\alpha \cos(\delta)$ (mas yr^{-1})	μ_δ (mas yr^{-1})	$\mu_{\rm total}$ (mas yr^{-1})
J183122.32-020619.6	3	5.13 ± 1.99	-12.1 ± 2.15	13.14
J183123.62-020535.8	5	-2.43 ± 0.4	-6.83 ± 0.42	7.25
J183126.02-020517.0	8	-7.58 ± 2.41	-12.27 ± 2.59	14.43
J183127.30-020504.5	9	-7.54 ± 3.96	-10.32 ± 4.22	12.78
J183127.67-020519.7	14	-9.17 ± 0.64	-7.77 ± 0.67	12.02
J183127.80-020521.9	15	-6.94 ± 1.0	-9.95 ± 1.06	12.13
J183128.01-020517.9	16	-6.79 ± 2.28	-7.56 ± 2.43	10.16
J183128.65-020529.8	18	-8.29 ± 2.04	-12.24 ± 2.14	14.78
J183128.67-020522.2	19	-14.97 ± 3.8	-10.38 ± 4.14	18.22

[a] The labels in this column refer to the VLA source number in the catalog of Rodríguez et al. (2010).

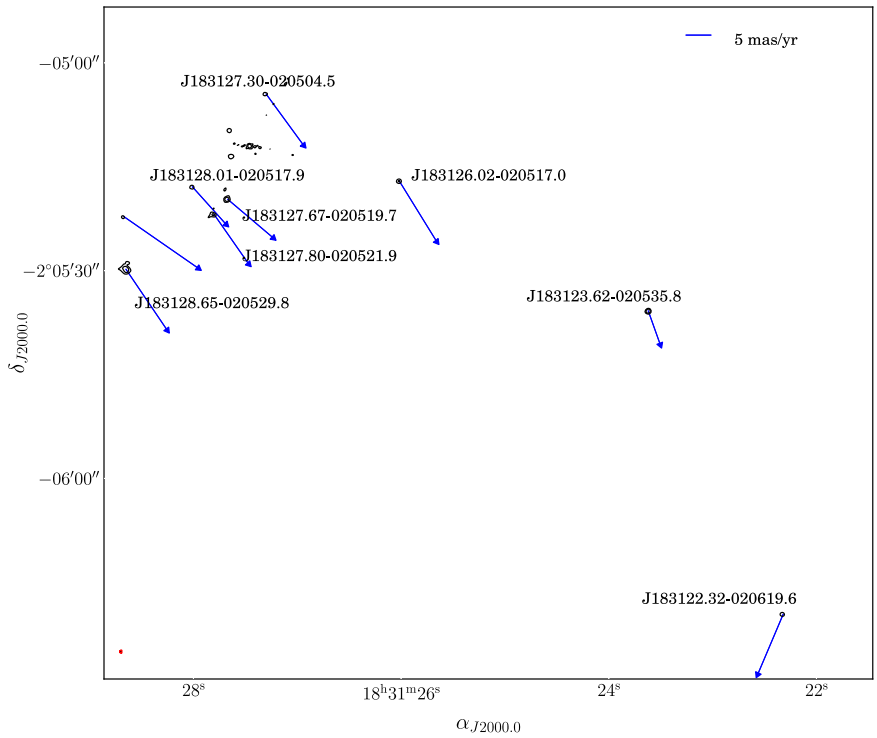

Figure 6. 6 cm radio continuum images of the W40 region. The arrows indicate the direction and length of the total proper motion of radio sources in the cluster, detected by us and by Rodríguez et al. (2010). The $\theta_{\rm maj} \times \theta_{\rm min} = 0\farcs41 \times 0\farcs40$, P.A. $= +75\fdg8$ synthesized beam is shown in the bottom left of the map. Contours are 5 and 25 times 32 μJy beam^{-1}, the rms noise of the image.

with its determined mass, suggests that the source may be an HAeBe star. The source W40 IRS 5 (GBS-VLA J183114.82–020350.1) was first classified as a foreground star due to its lack of significant IR absorption (Kuhn et al. 2010). However, more recently, Shuping et al. (2012) classified this source as a B1V star. They also obtained an extinction toward it similar to that of other stars in the cluster. Moreover, the distance determined to this source (~469 pc) is coincident with that determined to three additional OB stars in the region. This strongly suggests that W40 IRS 5 is part of the cluster and not a foreground star, as proposed by Kuhn et al. (2010).

The sources NVSS 182934+011504 and NVSS182951 + 012131, from the catalog of Condon et al. (1998), are resolved into double sources in our observations (Figures 7 and 8), while NVSS 183059+012512 is resolved into a triple source (Figure 9). Given the angular separation between the GBS-VLA sources and the peak of their NVSS counterparts, as well as the uncertainties in their positions, we associated NVSS 182934+011504, NVSS 182951 +012131, and NVSS 183059+012512 with GBS-VLA J182935.02+011503.2, GBS-VLA J182951.22+012132.0, and GBS-VLA J183059.74+012511.7, respectively (Table 3). Three GBS-VLA sources lie inside the source DCE08-210 5 (size ~1′; Figure 7), detected by AMI Consortium et al. (2012), and it is likely that this source includes multiple contributions, so it is difficult to attribute the 16 GHz emission conclusively to a specific GBS-VLA source. On the other hand, although DCE08-210 1 is resolved into six sources (Figure 10), GBS-VLA J182949.79+011520.4 is the strongest source closer to the peak of the 16 GHz emission; therefore, we associate DCE08-210 5 with GBS-VLA J182949.79+011520.4.

Table A1
W40 Sources of the Catalog of Rodríguez et al. (2010) Detected in Our Observations

GBS-VLA Name	RRR W40-VLA Number[a]	RRR Flux Density (8.3 GHz) (mJy)	GBS Flux Density (7.5 GHz) (mJy)	Spectral Index	RRR Extrapolated Flux Density (7.5 GHz) (mJy)
J183114.82–020350.1	1	0.92 ± 0.18	0.42 ± 0.07	+0.3 ± 0.2	0.89 ± 0.18
J183115.28–020415.2	2	0.90 ± 0.18	0.44 ± 0.07	−1.2 ± 0.2	1.02 ± 0.20
J183122.32–020619.6	3	0.47 ± 0.09	1.13 ± 0.22	+1.1 ± 0.2	0.42 ± 0.08
J183123.62–020535.8	5	3.97 ± 0.79	3.32 ± 0.45	−0.1 ± 0.1	4.01 ± 0.80
J183126.02–020517.0	8	3.27 ± 0.65	0.75 ± 0.09	−0.6 ± 0.2	3.48 ± 0.70
J183127.30–020504.5	9	0.99 ± 0.20	0.45 ± 0.07	−0.2 ± 0.3	1.01 ± 0.20
J183127.45–020512.0	10	0.82 ± 0.16	3.17 ± 0.34	+0.3 ± 0.2	0.80 ± 0.16
J183127.64–020513.5	12	1.64 ± 0.33	0.65 ± 0.11	−0.6 ± 0.3	1.74 ± 0.35
J183127.65–020509.7	13	0.86 ± 0.17	0.77 ± 0.08	+0.1 ± 0.2	0.85 ± 0.17
J183127.67–020519.7	14	5.78 ± 1.16	3.49 ± 0.40	+0.0 ± 0.1	5.78 ± 1.16
J183127.80–020521.9	15	1.71 ± 0.34	1.24 ± 0.15	−0.3 ± 0.2	1.76 ± 0.35
J183128.01–020517.9	16	0.94 ± 0. 19	0.50 ± 0.07	−0.4 ± 0.2	0.98 ± 0.20
J183128.65–020529.8	18	11.1 ± 2.22	4.79 ± 0.71	−0.7 ± 0.2	11.9 ± 2.38
J183128.67–020522.2	19	0.20 ± 0.04	0.25 ± 0.04	−0.4 ± 0.3	0.21 ± 0.04

[a] The numbers in this column refer to the VLA source number in the catalog of Rodríguez et al. (2010).

5.1. Non-thermal Radio Emission from YSOs

In Table 6 we list the radio properties of the 29 YSOs detected. As we already mentioned, non-thermal gyrosynchrotron radio emission is characterized by high radio variability and often a negative spectral index and some level of circular polarization. Out of the 12 Class III objects detected, 8 show high levels of variability or have a negative spectral index. We thus consider these eight objects as possible sources of non-thermal emission. Four Class II objects and, interestingly, four Class I sources could also be non-thermal. Additionally, the Herbig AeBe star GBS-VLA J183127.80–020521.9, the proto-Herbig AeBe star (P-HAeBe) GBS-VLA J182957.89+011246.0, and the source GBS-VLA J183128.01–020517.9 are likely non-thermal radio sources. This gives us a high fraction (65%) of the YSOs detected in our observations being non-thermal radio sources. An independent clue of the nature of the emission of these objects will be provided by their detection (or lack thereof) in forthcoming VLBA observations.

The Class I objects with possible non-thermal emission are GBS-VLA J182951.17+011640.4, J182952.22+011547.4, J182959.55+011158.1, and J182959.94+011311.3. Previously, some Class I objects in different star-forming regions have been reported as non-thermal emitters (Feigelson et al. 1998; Forbrich et al. 2007; Deller et al. 2013). One explanation for the detection of non-thermal radio emission from these objects (which should be absorbed by the ionized wind of the star) is a geometrical effect. According to this scenario, if the star is seen nearly pole-on or nearly edge-on, then the non-thermal radio emission originating in the corona might be less absorbed by the surrounding material and can reach the observer. Another possibility is tidal clearing of circumstellar material in a tight binary system (Dzib et al. 2010).

5.2. EC 95

EC 95 = GBS-VLA J182957.89+011246.0 is a tight binary (angular separation of ∼15 mas) consisting of a proto-Herbig AeBe star and a possibly low-mass T Tauri companion. Both components were detected with the VLBA and are therefore non-thermal radio sources (Dzib et al. 2010). The origin of this non-thermal emission has been proposed to be intrinsic magnetic activity in the stars. The magnetic activity in the low-mass T Tauri companion is related to magnetic reconnection in the stellar surface. Electrons are then accelerated to mildly relativistic velocities and generate gyrosynchrotron radiation. On the other hand, intermediate-mass stars are not expected to be magnetically active. Some processes have been suggested to explain the origin of the non-thermal radio emission in the proto-Herbig AeBe star (see Dzib et al. 2010), but still need to be tested.

We derive a spectral index for the system of 0.1 ± 0.2, which is consistent within 1σ with an early estimation by Smith et al. (1999), who found −0.26 ± 0.26. We determined a high variability at 4.5 and 7.5 GHz (65% and 62%, respectively). We note that in the VLBA observations obtained by Dzib et al. (2010) both components were found to be very variable, at levels of ∼94%, and so the variability we derive should be associated with the intrinsic variability of the stars. In conclusion, the radio properties we obtain for this system are consistent with the non-thermal nature of the sources.

6. SUMMARY

We have carried out new radio observations of three regions in the Aquila complex of local dark molecular clouds, namely, the Serpens molecular cloud, the Serpens South cluster, and the W40 region. We covered a large field of view (∼0.45 deg^2), and, combined with high angular resolution (∼0.″3) and sensitivity (∼17 μJy), our study surpasses previous observations of these regions. We have detected a total of 146 sources. Twenty-nine of them are associated with YSOs and 110 are new radio detections. The multi-epoch and dual-frequency strategy allows us to speculate on the nature of the radio emission of the sources. In particular, we find that 16 of the unclassified sources have a positive spectral index or exhibit high variability. They might, hence, correspond to a small population of as-yet-unidentified YSOs. What is more interesting is that approximately 65% of the identified YSOs are non-thermal sources, of which 50% are bright enough and therefore excellent targets for future astrometric observations with VLBI instruments.

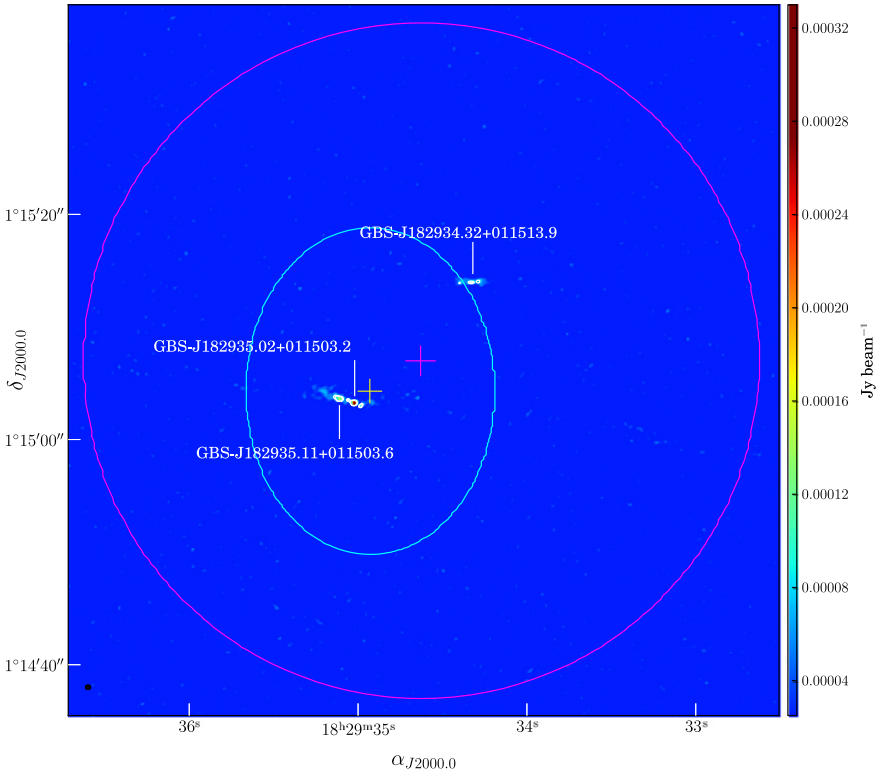

Figure 7. 6 cm radio continuum image of three GBS-VLA sources in the Serpens molecular cloud. The $\theta_{\rm maj} \times \theta_{\rm min} = 0\farcs40 \times 0\farcs39$, P.A. $= +96\fdg1$ synthesized beam is shown in the bottom left of the map. Contours are 5 and 6 times 15 μJy beam^{-1}, the rms noise of the image. The cyan ellipse indicates the size of the source NVSS 182934+011504 ($29\farcs0 \times 22\farcs1$), from the catalog of Condon et al. (1998). The yellow cross marks, with error bars, the position of the NVSS source. The magenta circle indicates the size ($\sim 1'$) of the source DCE08-210 5, detected in the observations of AMI Consortium et al. (2012) at 1.8 cm. The magenta cross marks, with error bars, the position of the 1.8 cm source.

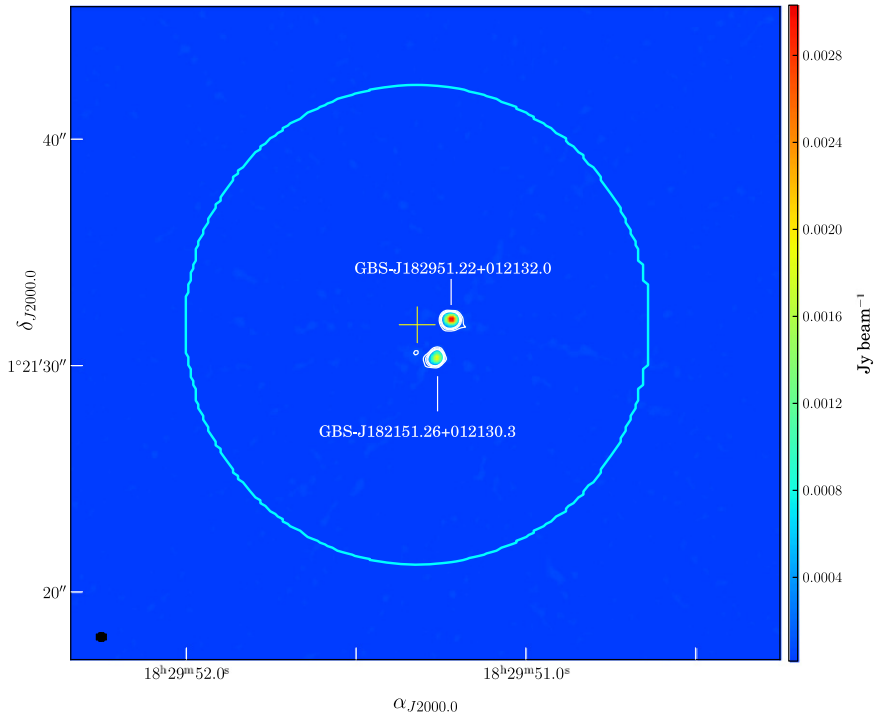

Figure 8. 6 cm radio continuum image of two GBS-VLA sources in the Serpens molecular cloud. The $\theta_{\rm maj} \times \theta_{\rm min} = 0\farcs40 \times 0\farcs39$, P.A. $= +96\fdg1$ synthesized beam is shown in the bottom left of the map. Contours are 5, 10, 15, and 20 times 19 μJy beam^{-1}, the rms noise of the image. The cyan ellipse indicates the size of the source NVSS 182951+012131 ($21\farcs2 \times 20\farcs5$), from the catalog of Condon et al. (1998). The yellow cross marks, with error bars, the position of the NVSS source.

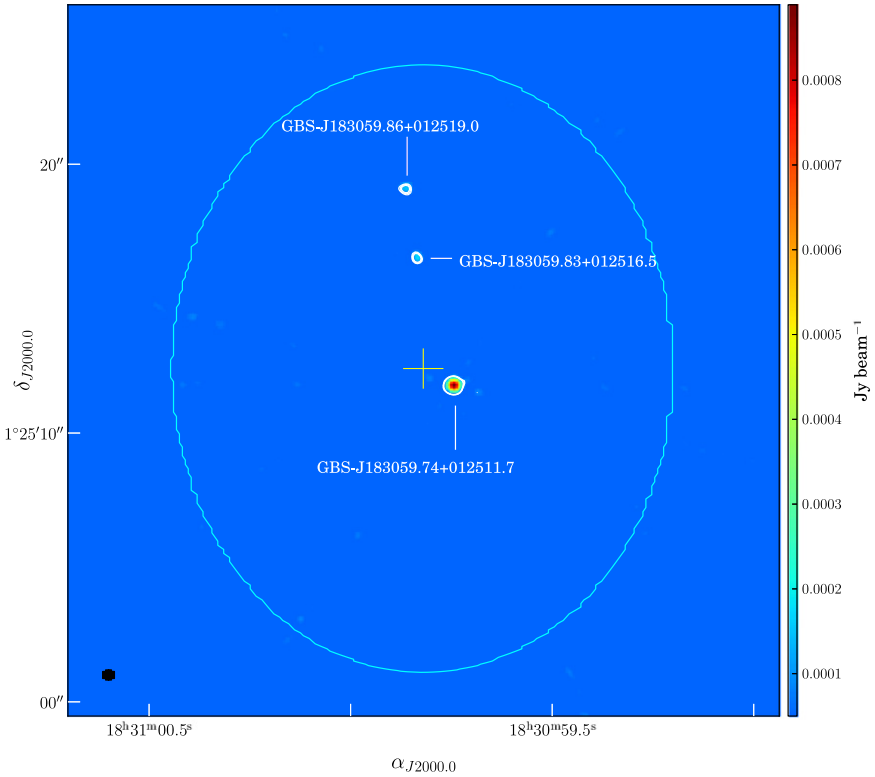

Figure 9. 6 cm radio continuum image of three GBS-VLA sources in the Serpens molecular cloud. The $\theta_{maj} \times \theta_{min} = 0.''40 \times 0.''39$, P.A. $= +96.^\circ1$ synthesized beam is shown in the bottom left of the map. Contours are 5, 6, and 7 times 17 μJy beam^{-1}, the rms noise of the image. The cyan ellipse indicates the size of the source NVSS 183059+012512 ($22.''6 \times 18.''6$), from the catalog of Condon et al. (1998). The yellow cross marks, with error bars, the position of the NVSS source.

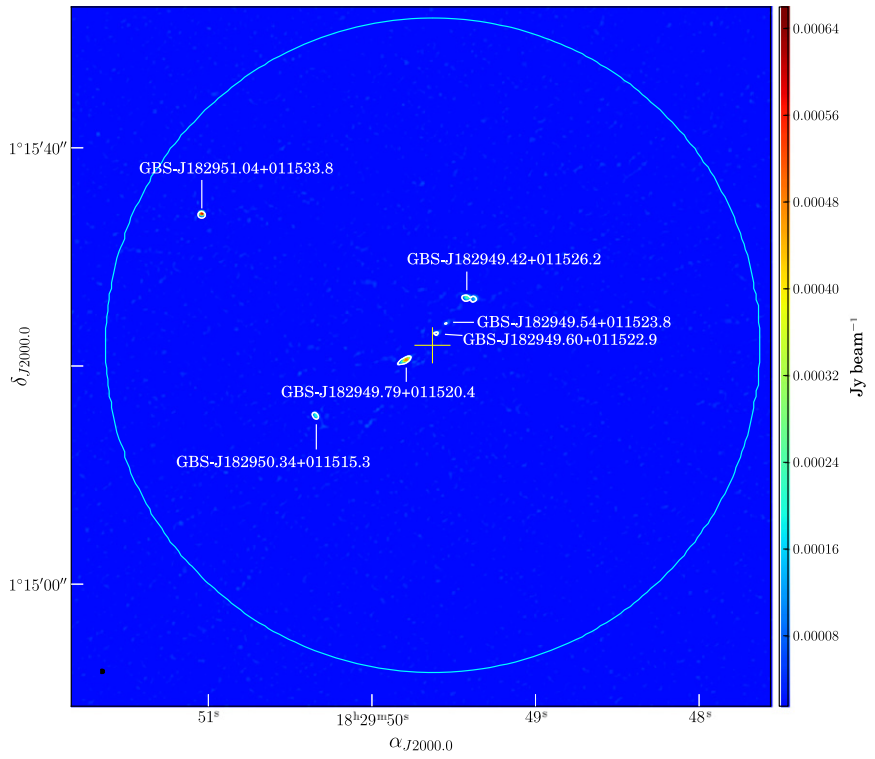

Figure 10. 6 cm radio continuum image of six GBS-VLA sources in the Serpens molecular cloud. The $\theta_{maj} \times \theta_{min} = 0.''40 \times 0.''39$, P.A. $= +96.^\circ1$ synthesized beam is shown in the bottom left of the map. Contours are 5 and 6 times 16 μJy beam^{-1}, the rms noise of the image. The cyan circle indicates the size ($\sim 1'$) of the source DCE08-210 1, detected in the observations of AMI Consortium et al. (2012) at 1.8 cm. The yellow cross marks, with error bars, the position of the 1.8 cm source.

This work is supported by CONACyT, Mexico, and PAPIIT, UNAM. We thank M. Dunham and L. Allen for providing us with a list of known young stellar objects in the c2d-GB clouds prior to publication, and A. J. Maury for providing data of the Serpens South cluster. The National Radio Astronomy Observatory is operated by Associated Universities, Inc., under cooperative agreement with the National Science Foundation.

APPENDIX

For the 14 sources of the catalog by Rodríguez et al. (2010) that are detected in our observations we carried out an independent analysis of variability. In order to compare the flux densities of our observations at 7.5 GHZ with the fluxes of Rodríguez et al. (2010) at 8.3 GHz, we extrapolated using the corresponding spectral indices (see Table A1). Unfortunately, in the paper of Rodríguez et al. (2010) no errors are given for the flux densities of the sources (because the flux densities reported are the average of the two epochs observed). Assuming a typical error of 20%, we find that the flux densities of 3 of the 14 sources detected in both studies are consistent within $\pm 1\sigma$. The remaining 11 sources show different flux densities for the two studies. Nine of the sources show a stronger flux density in the Rodríguez et al. (2010) paper, while the remaining two show a stronger flux density in this paper. This diversity seems to rule out that the sources are steady and that there is a systematic calibration error in one of the two studies (because then we would expect all sources to appear as brighter in one of the two studies). Finally, it should be stressed that in the Rodríguez et al. (2010) paper, which reported observations in two different epochs separated by 0.88 yr (2003 November 3 and 2004 September 18), 3 of these 11 sources were already reported as time variable. Since the present paper offers a larger time baseline (about a decade), we expect the sources to exhibit even more variability between the two studies.

REFERENCES

AMI Consortium, Scaife, A. M. M., Hatchell, J., et al. 2012, MNRAS, 420, 1019
André, P., Men'shchikov, A., Bontemps, S., et al. 2010, A&A, 518, L102
Anglada, G., Villuendas, E., Estalella, R., et al. 1998, AJ, 116, 2953
Bontemps, S., André, P., Könyves, V., et al. 2010, A&A, 518, L85
Cambrésy, L. 1999, A&A, 345, 965
Casali, M. M., Eiroa, C., & Duncan, W. D. 1993, A&A, 275, 195
Condon, J. J., Cotton, W. D., Greisen, E. W., et al. 1998, AJ, 115, 1693
Crutcher, R. M., & Chu, Y. H. 1982, Regions of Recent Star Formation, 93, 53
Cutri, R. M., Skrutskie, M. F., van Dyk, S., et al. 2003, VizieR Online Data Catalog, 2246, 0
Dame, T. M., Ungerechts, H., Cohen, R. S., et al. 1987, ApJ, 322, 706
Deller, A. T., Forbrich, J., & Loinard, L. 2013, A&A, 552, A51
Dobashi, K., Uehara, H., Kandori, R., et al. 2005, PASJ, 57, 1
Drake, S. A., Simon, T., & Linsky, J. L. 1989, ApJS, 71, 905
Dulk, G. A. 1985, ARA&A, 23, 169
Dunham, M. M., Arce, H. G., Allen, L. E., et al. 2013, AJ, 145, 94
Dunham, M. M., Crapsi, A., Evans, N. J., II, et al. 2008, ApJS, 179, 249
Dzib, S., Loinard, L., Mioduszewski, A. J., et al. 2010, ApJ, 718, 610
Dzib, S. A., Loinard, L., Mioduszewski, A. J., et al. 2013, ApJ, 775, 63
Dzib, S. A., Loinard, L., Rodríguez, L. F., & Galli, P. 2014, ApJ, 788, 162
Eiroa, C., & Casali, M. M. 1992, A&A, 262, 468
Eiroa, C., Djupvik, A. A., & Casali, M. M. 2008, in Handbook of Star Forming Regions, Vol. 2, The Southern Sky ASP Monograph Publications, Vol. 5, ed. B. Reipurth (San Francisco, CA: ASP), 693
Eiroa, C., Torrelles, J. M., Curiel, S., & Djupvik, A. A. 2005, AJ, 130, 643
Enoch, M. L., Evans, N. J., II, Sargent, A. I., & Glenn, J. 2009, ApJ, 692, 973
Estalella, R., Anglada, G., Rodriguez, L. F., & Garay, G. 1991, ApJ, 371, 626
Evans, N. J., II, Dunham, M. M., Jørgensen, J. K., et al. 2009, ApJS, 181, 321
Feigelson, E. D., Carkner, L., & Wilking, B. A. 1998, ApJL, 494, L215
Feigelson, E. D., & Montmerle, T. 1985, ApJL, 289, L19
Felli, M., Taylor, G. B., Neckel, T., & Staude, H. J. 1998, A&A, 329, 243
Fernández-López, M., Arce, H. G., Looney, L., et al. 2014, ApJL, 790, LL19
Forbrich, J., Massi, M., Ros, E., Brunthaler, A., & Menten, K. M. 2007, A&A, 469, 985
Garay, G., Ramirez, S., Rodriguez, L. F., Curiel, S., & Torrelles, J. M. 1996, ApJ, 459, 193
Giardino, G., Favata, F., Micela, G., Sciortino, S., & Winston, E. 2007, A&A, 463, 275
Giovannetti, P., Caux, E., Nadeau, D., & Monin, J.-L. 1998, A&A, 330, 990
Gómez, Y., Rodríguez, L. F., & Garay, G. 2000, ApJ, 531, 861
Gomez de Castro, A. I., Eiroa, C., & Lenzen, R. 1988, A&A, 201, 299
Goss, W. M., & Shaver, P. A. 1970, AuJPA, 14, 1
Güdel, M., & Benz, A. O. 1993, ApJL, 405, L63
Güdel, M., Schmitt, J. H. M. M., Bookbinder, J. A., & Fleming, T. A. 1993, ApJ, 415, 236
Gutermuth, R. A., Bourke, T. L., Allen, L. E., et al. 2008, ApJL, 673, L151
Harvey, P., Merín, B., Huard, T. L., et al. 2007a, ApJ, 663, 1149
Harvey, P. M., Chapman, N., Lai, S.-P., et al. 2006, ApJ, 644, 307
Harvey, P. M., Rebull, L. M., Brooke, T., et al. 2007b, ApJ, 663, 1139
Hovatta, T., Nieppola, E., Tornikoski, M., et al. 2008, A&A, 485, 51
Hovatta, T., Tornikoski, M., Lainela, M., et al. 2007, A&A, 469, 899
Hughes, V. A. 1988, ApJ, 333, 788
Hughes, V. A. 1991, ApJ, 383, 280
Hughes, V. A., Cohen, R. J., & Garrington, S. 1995, MNRAS, 272, 469
Hurt, R. L., & Barsony, M. 1996, ApJL, 460, L45
Kaas, A. A. 1999, AJ, 118, 558
Kaas, A. A., Olofsson, G., Bontemps, S., et al. 2004, A&A, 421, 623
King, D. J., Scarrott, S. M., & Taylor, K. N. R. 1983, MNRAS, 202, 1087
Könyves, V., André, P., Men'shchikov, A., et al. 2010, A&A, 518, L106
Kuhn, M. A., Getman, K. V., Feigelson, E. D., et al. 2010, ApJ, 725, 2485
Kurtz, S. 2005, Massive Star Birth: A Crossroads of Astrophysics, 227, 111
Loinard, L. 2013, in IAU Symp. 289, Advancing the Physics of Cosmic Distances, ed. R. de Gris & G. Bono (Cambridge: Cambridge Univ. Press), 36
Loren, R. B., Evans, N. J., II, & Knapp, G. R. 1979, ApJ, 234, 932
Lovell, J. E. J., Rickett, B. J., Macquart, J.-P., et al. 2008, ApJ, 689, 108
Maury, A. J., André, P., Men'shchikov, A., Könyves, V., & Bontemps, S. 2011, A&A, 535, A77
Molinari, S., Brand, J., Cesaroni, R., & Palla, F. 1996, A&A, 308, 573
Oliveira, I., Pontoppidan, K. M., Merín, B., et al. 2010, ApJ, 714, 778
Panagia, N., & Felli, M. 1975, A&A, 39, 1
Perrot, C. A., & Grenier, I. A. 2003, A&A, 404, 519
Preibisch, T. 1998, A&A, 338, L25
Preibisch, T. 1999, A&A, 345, 583
Preibisch, T. 2003, A&A, 410, 951
Preibisch, T. 2004, A&A, 428, 569
Predehl, P., & Schmitt, J. H. M. M. 1995, A&A, 293, 889
Rodriguez, L. F., González, R. F., Montes, G., et al. 2012, ApJ, 755, 152
Rodriguez, L. F., Marti, J., Canto, J., Moran, J. M., & Curiel, S. 1993, RMxAA, 25, 23
Rodriguez, L. F., Myers, P. C., Cruz-Gonzalez, I., & Terebey, S. 1989, ApJ, 347, 461
Rodríguez, L. F., Rodney, S. A., & Reipurth, B. 2010, AJ, 140, 968
Shuping, R. Y., Vacca, W. D., Kassis, M., & Yu, K. C. 2012, AJ, 144, 116
Smith, J., Bentley, A., Castelaz, M., et al. 1985, ApJ, 291, 571
Smith, K., Güdel, M., & Benz, A. O. 1999, A&A, 349, 475
Sogawa, H., Tamura, M., Gatley, I., & Merrill, K. M. 1997, AJ, 113, 1057
Straižys, V., Černis, K., & Bartašiūte, S. 1996, BaltA, 5, 125
Strom, S. E., Grasdalen, G. L., & Strom, K. M. 1974, ApJ, 191, 111
Strom, S. E., Vrba, F. J., & Strom, K. M. 1976, AJ, 81, 638
Testi, L., & Sargent, A. I. 1998, ApJL, 508, L91
Torrelles, J. M., Verdes-Montenegro, L., Ho, P. T. P., Rodriguez, L. F., & Canto, J. 1989, ApJ, 346, 756
Vallee, J. P., & MacLeod, J. M. 1994, AJ, 108, 998
Warren-Smith, R. F., Draper, P. W., & Scarrott, S. M. 1987, MNRAS, 227, 749
Westerhout, G. 1958, BAN, 14, 215
Winston, E., Megeath, S. T., Wolk, S. J., et al. 2010, AJ, 140, 266
Worden, S. P., & Grasdalen, G. L. 1974, A&A, 34, 37
Wright, E. L., Eisenhardt, P. R. M., Mainzer, A. K., et al. 2010, AJ, 140, 1868

Capítulo 3

Distancias trigonométricas y estructura de la región de Ofiuco

Ofiuco es una de las regiones de mayor importancia en estudios relacionados con formación estelar. Observaciones realizadas en casi todas las bandas del espectro electromagnético han revelado aproximadamente 300 estrellas jóvenes en un área de $0.94^{o} \times 1.2^{o}$ con centro en RA=$16^{h}27^{m}38.5^{s}$, DEC=$-24^{o}29'34''$ (Wilking *et al.*, 2008). Ofiuco representa entonces uno de los ambientes más densos entre las regiones de formación estelar de baja masa cercanas. El censo realizado con el telescopio espacial Spitzer *"From Molecular Cores to Planet Forming Disks"* identificó 292 objetos estelares jóvenes en un área mayor, ~ 6.25 grados^2, a partir de la presencia de exceso infrarrojo en la distribución espectral de energía entre 4.5 a 24 μm (Dunham *et al.*, 2015), muchos de los cuales corresponden a objetos previamente identificados en censos anteriores.

La Figura 3-1 muestra la estructura a gran escala del complejo de Ofiuco. Se distinguen un núcleo central que corresponde a la nube Lynds 1688 (donde $A_V = 50-100$ magnitudes) y varios *filamentos* oscuros de gas molecular que se extienden hacia el este, a los que colectivamente se les conoce como "*streamers*". Extendiéndose hacia el este de Lynds 1688 se ubica Lynds 1689, que posteriormente se encuentra con Lynds 1712 y Lynds 1729,

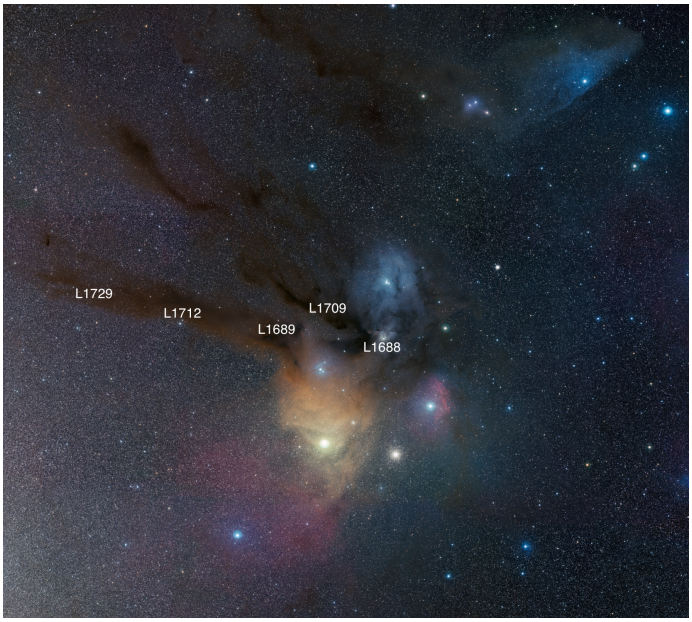

Figura 3-1 Imagen en el óptico de la nube de Ofiuco tomada por Robert Gendler, Jim Misti y Steve Mazlin.

mientras que hacia el noreste se sitúa Lynds 1709. Se ha determinado que, comparado con Lynds 1688, tanto la densidad del gas como la actividad de formación estelar en los streamers son menos prominentes (Nutter *et al.*, 2006).

En este capítulo, presentamos observaciones astrométricas hacia Lynds 1688 y Lynds 1689. Primero, introducimos la estrategia de observación y calibración de datos que adoptaremos para el estudio de las 5 regiones en el Cinturón de Gould. Enseguida, discutimos las propiedades de las fuentes de radio detectadas con el VLBA y finalmente presentamos los resultados astrométricos obtenidos para 16 fuentes en Ofiuco.

3.1. Observaciones y calibración de datos

La fase actual del proyecto GOBELINS consiste en realizar observaciones con el VLBA para medir los parámetros astrométricos, es decir la paralaje trigonométrica y los movimientos

propios, a estrellas individuales en 5 regiones del cinturón de Gould. Una vez completado el proyecto, estas observaciones nos permitirán obtener, primeramente, las distancias más precisas hacia estrellas jóvenes embebidas en las 5 regiones. Segundo, podremos ubicar también de manera muy precisa a las regiones dentro del Cinturón de Gould y la Galaxia, así como la estructura tridimensional interna de estas nubes. Finalmente, utilizaremos las velocidades transversales, determinadas hacia cada objeto a partir de la distancia y movimiento propios, junto con velocidades radiales para derivar los vectores de velocidad tridimensional. Esto nos permitirá estudiar la cinemática interna de las regiones, así como los movimientos relativos entre las nubes del cinturón de Gould y, eventualmente, entender el origen de dicha estructura.

En total, ~ 2000 horas de tiempo de telescopio se aprobaron para las observaciones del proyecto GOBELINS y a la fecha hemos completado el $\sim 85\%$ del tiempo asignado. En el presente capítulo, presentamos los resultados de las observaciones colectadas entre Marzo de 2012 y Abril de 2016 hacia la región de Ofiuco, que corresponden a un total de 86 épocas. Inicialmente las observaciones se realizaron a una frecuencia de 8 GHz. Posteriormente cambiamos a 5 GHz por razones de aumento en sensitividad después de la renovación de los receptores del VLBA a esta frecuencia. Para trabajar con este conjunto de observaciones de gran magnitud, utilizamos el código de calibración de datos semi-automatizado que fue escrito por Dzib (2013) específicamente para el proyecto. El código ejecuta sucesivamente un conjunto de *tareas* que aplican correcciones de amplitud y fase a las visibilidades interferométricas (Apéndice A) dentro de la paquetería *AIPS*. Después, los mapas de la distribución de brillo se construyen a partir de las visibilidades calibradas usando la tarea IMAGR, y por último, las posiciones y flujos de las fuentes se extraen de las imágenes mediante un ajuste Gaussiano bidimensional a la distribución de brillo, usando la tarea JMFIT.

3.2. Fuentes detectadas y propiedades de la emisión no-térmica

Un total de 26 estrellas jóvenes, y otros 31 objetos sin clasificación en la literatura, se detectaron en Ofiuco. Todos estos objetos poseen $T_B \gtrsim 10^6$ K, lo cual es consistente con emisión de origen no térmico, y representan aproximadamente la mitad de las 50 estrellas jóvenes que observamos en Ofiuco. Por tanto, confirmamos la sugerencia de Dzib *et al.* (2013) de que aproximadamente el 50 % de las estrellas con emisión de radio en Ofiuco son no térmicas. En observaciones reportadas con anterioridad en la literatura, solamente 6 de estos objetos habían sido detectados. Entonces, nuestras observaciones han cuadruplicado el número de estrellas jóvenes conocidas en Ofiuco que poseen emisión de radio detectable con VLBI.

Con la finalidad de separar las contribuciones de la emisión térmica y no térmica a la emisión de radio total en los objetos estelares jóvenes detectados con el VLBA, tomamos los flujos medidos por Dzib *et al.* (2013) en las imagenes del VLA ($S_{\rm VLA}$) y los comparamos con los flujos medidos aquí en las imágenes del VLBA ($S_{\rm VLBA}$). La comparación se muestra en la Figura 3-2, donde cada cruz azul corresponde a una estrella joven, y su tamaño indica el intervalo de flujo medido en las diferentes épocas observadas con ambos telescopios. Es claro que, con excepción de dos fuentes, todas tienen en promedio flujos VLBA comparables a sus flujos VLA y siguen la línea correspondiente a $S_{\rm VLA} = S_{\rm VLBA}$.

Esta tendencia observada sugiere que las fuentes detectadas con el VLBA tienen emisión de radio cuyo origen es únicamente no térmico. Si existiera una contribución térmica por emisión libre-libre, ésta se detectaría con el VLA pero no con el VLBA, y veríamos puntos que sistemáticamente caerían por arriba de la línea de igualdad en la Figura 3-2.

Los objetos estelares jóvenes no detectados con el VLBA se muestran en la Tabla 3-1, donde los flujos de radio medidos en las imágenes VLA por Dzib *et al.* (2013) se listan en la columna (3), mientras que los límites superiores de 3σ a 4 y 5 GHz se dan en las columnas (4) y (5), respectivamente. En la gráfica de la Figura 3-2, estos objetos corresponden a los símbolos rojos. De estos 24 objetos, dos de ellos (LFAMP 8 y VLA1623 A)

Table 3-1. Objetos estelares jóvenes en Ofiuco no detectados con el VLBA

Fuente (1)	Nombre (2)	Flujo máx.[1] (VLA) a 5 GHz (mJy) (3)	Variabilidad[1] (%) (4)	Lím. sup. de flujo a 5 GHz (mJy) (5)	Núm. de obs. (6)	Clase evolutiva (7)
J162550.51-243914.7	ROXA1	0.595	78.2 ± 15.9	<0.084	3	Class III
J162607.63-242741.7	ROXRA13	0.469	> 79.5 ± 3.0	<0.072	7	Class III
J162610.32-242054.9	GSS26	0.171	> 56.1 ± 16.8	<0.072	5	Class II
J162621.72-242250.7	LFAM1	0.295	28.8 ± 33.6	<0.075	6	Class I
J162623.57-242439.6	LFAM3	0.197	33.5 ± 48.6	<0.072	11	FS
J162626.31-242430.2	VLA1623B	0.374	63.1 ± 33.0	<0.072	12	Class 0 (?)
J162626.39-242430.9	VLA1623A	0.12	–	<0.072	12	Class 0
J162658.38-242130.5	YLW1C	0.54	> 79.4 ± 2.4	<0.072	5	Class II
J162705.96-242618.9	YLW10A	0.69	> 76.8 ± 4.5	<0.09	6	Class II
J162709.41-243719.0	YLW7	0.311	30.9 ± 36.3	<0.066	5	Class I
J162715.69-243845.7	WL20S	0.254	24.4 ± 39.6	<0.063	9	–
J162721.97-242940.0	GY256	0.183	45.9 ± 53.7	<0.069	8	Class II
J162722.96-242236.6	MPK3809	0.307	66.8 ± 31.8	<0.072	4	–
J162727.36-243116.8	DROXO63	0.29	58.6 ± 38.1	<0.081	8	Class II
J162728.00-243933.7	YLW16A	0.377	22.3 ± 30.3	<0.063	8	Class I
J162731.05-243403.4	DROXO72	0.293	> 69.3 ± 6.6	<0.072	4	Class III
J162732.68-243324.5	LFAMP7	0.257	44.7 ± 39.0	<0.072	4	Class II
J162739.42-243915.8	LFAMP8	0.119	44.5 ± 67.8	<0.066	6	Class II
J162741.49-243537.6	DROXO89	0.251	> 61.8 ± 7.8	<0.075	3	Class III
J162751.80-243145.9	YLW52	2.064	–	<0.069	3	Class I
J162751.89-244630.1	DROXO98	2.064	> 95.6±0.3	<0.069	8	Class III
J162759.95-244819.5	ROXN77	3.984	> 97.0 ± 0.3	<0.069	3	WTTS
J163115.75-243402.8	ROXS42C	0.607	> 79.2 ± 2.1	<0.072	5	WTTS
J163421.10-235625.1	WSB80	0.460	> 76.1 ± 3.6	<0.081	2	WTTS

[1]El flujo medido por el VLA y su variabilidad se tomaron de Dzib *et al.* (2013). Las incertidumbres asociadas a la variabilidad corresponden a una desviación de 3σ.

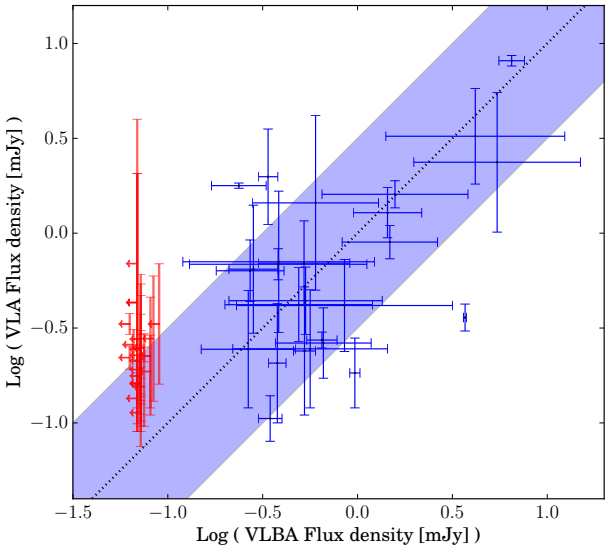

Figura 3-2 Flujo detectado a 4.5 GHz con el VLA como función del flujo detectado a 5 GHz con el VLBA. Los símbolos azules y rojos corresponden a objetos estelares jóvenes detectados y no detectados, respectivamente, en nuestras observaciones VLBA. El flujo VLBA de los objetos no detectados corresponde al límite superior igual a 3σ, donde σ es el ruido en los mapas de las fuentes.

son intrínsicamente fuentes de radio débiles, con flujos VLA menores a 150 μJy que el VLBA no puede detectar en los tiempos de integración típicos de nuestras observaciones ($\sim 1-1.6$ horas). Podemos pensar en varias razones por las cuales las otras 22 estrellas jóvenes no se detectan con el VLBA. Primero, varios de estos objetos muestran variaciones significativas en su flujo VLA, por lo que posiblemente se encontraban en una fase de mínima actividad cuando se observaron con el VLBA. Segundo, es posible que la emisión de radio detectada con el VLA en estos objetos sea térmica y esté asociada a regiones extendidas con temperaturas de brillo $\simeq 10^4$ K que el VLBA no puede detectar. Muy probablemente esto es lo que ocurre en aquellos objetos que no muestran variaciones de

flujo estadísticamente significativas y podemos sugerir que al menos 8 objetos en la Tabla 3-1 son fuentes de radio térmicas.

Aproximadamente el 30% de las estrellas jóvenes detectadas en Ofiuco son sistemas binarios o de mayor multiplicidad cuyas componentes están separadas por 0.6–44 UA. Esta fracción parece reflejar la fracción de binarias determinada en censos de multiplicidad hacia esta región, de acuerdo a los cuales la fracción es $\sim 35\%$ para separaciones entre 1.3 y 46.1 UA (Cheetham *et al.*, 2015). En contraste, la fracción observada de binarias es $\sim 50-60\%$ en estrellas de campo tipo Sol (Raghavan *et al.*, 2010), y $\sim 65-80\%$ en asociaciones jóvenes tipo Tauro-Auriga y Scorpius Superior (Kraus *et al.*, 2011). Es interesante notar, además, que solamente una de las 8 binarias en Ofiuco muestra separaciones mayores a 10 UA. Se sugiere, por tanto, que los sistemas múltiples angostos son más probables a ser fuentes de radio no térmicas en comparación con estrellas aisladas u objetos en sistemas múltiples más extendidos, aunque el mecanismo exacto por el cual esto ocurre todavía debe ser investigado. Sin embargo, no descartamos la posibilidad de que exista un efecto de selección, por ejemplo, por el hecho de que binarias con separaciones mayores podrían no detectarse debido al limitado campo de visión del VLBA (~ 10 segundos de arco a ν =5 GHz).

3.3. Astrometría

Los parámetros astrométricos se determinaron para aquellas estrellas jóvenes detectadas en al menos 3 épocas en equinoccios alternos; éstos constituyen un subconjunto de 16 estrellas. Ocho de estos objetos son sistemas de dos o más componentes y para 6 de ellos hemos modelado, además de la paralaje trigonométrica y movimiento propio, su movimiento orbital, obteniendo las masas de sus componentes así como los parámetros orbitales. También analizamos el cambio en posición de aquellos objetos detectados con el VLBA que no poseen una clasificación en la literatura. De estos 31 objetos, 27 se han detectado en más de una época, y para ellos investigamos si se tratan de objetos Galácticos

(que no son miembros de la región de Ofiuco) o fuentes de fondo extragalácticas.

Los objetos estelares jóvenes detectados con el VLBA se encuentran distribuidos principalmente en Lynds 1688, el núcleo de Ofiuco y Lynds 1689, una estructura alargada que se extiende hacia el este del núcleo. Las distancias individuales en Lynds 1688 son muy consistentes entre ellas y el promedio de éstas es $d = 137.3 \pm 1.2$ pc. Por otro lado, el promedio de distancias para las fuentes en Lynds 1689 es $d = 147.3 \pm 3.4$ pc. Entonces, nuestros resultados sugieren que el complejo de nubes en Ofiuco tiene una profundidad a lo largo de la línea de visión de ~ 10 pc. Esta última conclusión está basada en un número reducido de fuentes en Lynds 1689, y para confirmar nuestro resultado, más observaciones hacia la región se están colectando actualmente con el VLBA.

Movimientos propios

Como mencionamos en la sección 1.1.1, el movimiento propio de una estrella tiene dos contribuciones. La primera se debe al movimiento peculiar del Sol y la segunda al movimiento del objeto con respecto a su ambiente local, es decir, su sistema local de reposo (Figura 3-3). La contribución (en coordenadas galácticas) del movimiento peculiar del Sol se determina sabiendo la posición del objeto y su paralaje (en segundos de arco), mediante (e.g. Abad y Vieira 2005)

$$\mu_{l,\odot}\cos b = \frac{\varpi}{4.74}(u_\odot \sin l - v_\odot \cos l) \quad (3\text{-}1)$$

$$\mu_{b,\odot} = \frac{\varpi}{4.74}(u_\odot \cos l \sin b + v_\odot \sin l \cos b - w_\odot \cos b) \quad (3\text{-}2)$$

$$(u_\odot, v_\odot, w_\odot) = (11.1 \pm 0.7, 12.2 \pm 0.47, 7.25 \pm 0.37) \text{ km s}^{-1} \quad (3\text{-}3)$$

donde $(u_\odot, v_\odot, w_\odot)$ son las componentes rectangulares del movimiento solar en la dirección del centro galáctico, la dirección de la rotación galáctica y hacia el polo norte, respectivamente (Schönrich *et al.*, 2010), y las unidades del movimiento propio son segundos de arco yr^{-1}. Esta correción se aplicó a los movimientos propios derivados de los ajustes

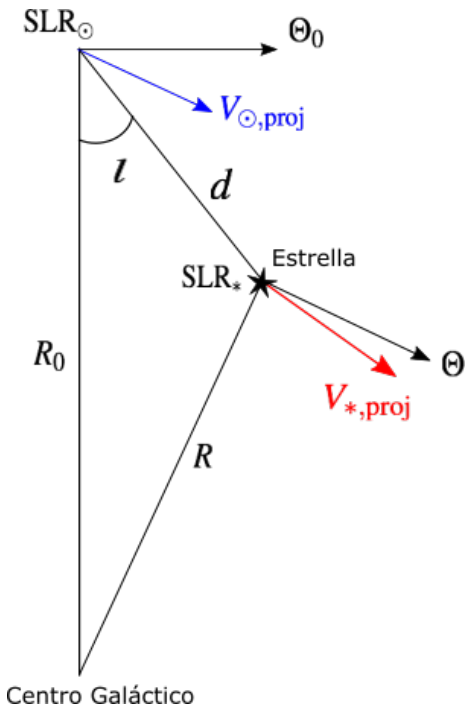

Figura 3-3 Componentes del movimiento de una estrella con respecto al Sol. $V_{\odot,\,\mathrm{proj}}$ representa el movimiento peculiar del Sol respecto al sistema local de reposo ($\mathrm{SLR}_\odot$), proyectado en el plano Galáctico, mientras que $V_{*,\,\mathrm{proj}}$ es la proyección de la velocidad peculiar de la estrella respecto a su sistema local de reposo SLR_*. En la vecindad solar, i.e. para $d \sim 100$ pc, se tiene que $\Theta \simeq \Theta_0$, por lo que la contribución por rotación diferencial se puede despreciar.

astrométricos antes de determinar las velocidades transversales de las fuentes en Ofiuco. Encontramos que la gran mayoría de los objetos se mueven hacia el sureste de la nube y que la dispersión de velocidades para los objetos en Lynds 1688 son 2.8 ± 1.8 y 3.0 ± 2.0 km s^{-1} en ascención recta y declinación, respectivamente.

El artículo con los resultados que acabamos de presentar se ha enviado al ApJ para ser considerado para su publicación y se incluye enseguida.

Draft version December 11, 2016
Preprint typeset using LaTeX style AASTeX6 v. 1.0

THE GOULD'S BELT DISTANCES SURVEY (GOBELINS) I. TRIGONOMETRIC PARALLAX DISTANCES AND DEPTH OF THE OPHIUCHUS COMPLEX

Gisela N. Ortiz-León[1], Laurent Loinard[1,2], Marina A. Kounkel[3], Sergio A. Dzib[2], Amy J. Mioduszewski[4], Luis F. Rodríguez[1,5], Rosa M. Torres[6], Rosa A. González-Lópezlira[1,13,14], Gerardo Pech[1,7], Juana L. Rivera[1], Lee Hartmann[3], Andrew F. Boden[8], Neal J. Evans II[9], Cesar Briceño[10], John J. Tobin[11], Phillip A. B. Galli[12,15], and Donald Gudehus[16]

[1]Instituto de Radioastronomía y Astrofísica, Universidad Nacional Autónoma de Mexico, Morelia 58089, Mexico

[2]Max Planck Institut für Radioastronomie, Auf dem Hügel 69, D-53121 Bonn, Germany

[3]Department of Astronomy, University of Michigan, 500 Church Street, Ann Arbor, MI 48105, USA

[4]National Radio Astronomy Observatory, Domenici Science Operations Center, 1003 Lopezville Road, Socorro, NM 87801, USA

[5]King Abdulaziz University, P.O. Box 80203, Jeddah 21589, Saudi Arabia

[6]Centro Universitario de Tonalá, Universidad de Guadalajara, Avenida Nuevo Periférico No. 555, Ejido San José Tatepozco, C.P. 48525, Tonalá, Jalisco, México.

[7] The Academia Sinica Institute of Astronomy and Astrophysics, AS/NTU. No.1, Sec. 4, Roosevelt Rd, Taipei 10617, Taiwan, R.O.C.

[8]Division of Physics, Math and Astronomy, California Institute of Technology, 1200 East California Boulevard, Pasadena, CA 91125, USA

[9]Department of Astronomy, The University of Texas at Austin, 2515 Speedway, Stop C1400, Austin, TX 78712-1205, USA

[10]Cerro Tololo Interamerican Observatory, Casilla 603, La Serena, Chile

[11]Leiden Observatory, PO Box 9513, NL-2300 RA, Leiden, The Netherlands

[12]Instituto de Astronomia, Geofísica e Ciências Atmosféricas, Universidade de São Paulo, Rua do Matão 1226, Cidade Universitária, São Paulo, Brazil

[13]Helmhotz-Institute für Strahlen-und Kernphysik (HISKP), Universität Bonn, Nussallee 14-16, D-53115 Bonn, Germany

[14]Argelander-Institut für Astronomie, Auf dem Hügel 71, D-53121, Bonn, Germany

[15]Univ. Grenoble Alpes, IPAG, 38000, Grenoble, France

[16]Department of Physics & Astronomy, Georgia State University, Atlanta, GA 30303, USA

ABSTRACT

We present the first results of the *Gould's Belt Distances Survey (GOBELINS)*, a project aimed at measuring the proper motion and trigonometric parallax of a large sample of young stars in nearby regions using multi-epoch Very Long Baseline Array (VLBA) radio observations. Enough VLBA detections have now been obtained for 16 stellar systems in Ophiuchus to derive their parallax and proper motion. This leads to distance determinations for individual stars with an accuracy of 0.3 to a few percent. In addition, the orbits of 6 multiple systems were modelled by combining absolute positions with VLBA (and in some cases, near infrared) angular separations. Twelve stellar systems are located in the dark cloud Lynds 1688; the individual distances for this sample are highly consistent with one another, and yield a mean parallax for Lynds 1688 of $\varpi = 7.28 \pm 0.06$ mas, corresponding to a distance $d = 137.3 \pm 1.2$ pc. This represents an accuracy better than 1%. Three systems for which astrometric elements could be measured are located in the eastern streamer (Lynds 1689) and yield an estimate of $\varpi = 6.79 \pm 0.16$ mas, corresponding to a distance $d = 147.3 \pm 3.4$ pc. This suggests that the eastern streamer is located about 10 pc farther than the core, but this conclusion needs to be confirmed by observations (currently being collected) of additional sources in the eastern streamer. From the measured proper motions, we estimate the one-dimensional velocity dispersion in Lynds 1688 to be 2.8±1.8 and 3.0±2.0 km s^{-1}, in R.A. and DEC., respectively; these are larger than, but still consistent within 1σ, with those found in other studies.

Keywords: astrometry - radiation mechanisms: non-thermal - radio continuum: stars - techniques: interferometric

g.ortiz@crya.unam.mx

1. INTRODUCTION

1.1. *The Gould's Belt*

The Gould's Belt (see Poppel 1997 for a comprehensive review) is a local Galactic structure containing much of the dense interstellar matter and many of the young stars within a few hundred parsecs of the Sun. It was originally identified by John Herschel (circa 1847) and Benjamin Gould (in the 1870s), who noticed that most of the brightest stars were neither randomly distributed on the sky, nor associated with the Galactic plane, but instead concentrated along a great circle tilted by about 18° from the Galactic equator. Modern studies (e.g., Perrot & Grenier 2003) have shown that the Gould's Belt is a broad elliptical ring of young stars and interstellar matter with semimajor and semiminor axes of 375 pc and 235 pc, respectively. The center of the structure is located at about 105 pc from the Sun, in the direction of the Galactic anti-center. There is ample evidence that the Gould's Belt is expanding and has a dynamical age of order 30 Myr – Perrot & Grenier (2003) find 26.4 ± 0.4 Myr. The oldest stars associated with the Gould's Belt are also about 30 Myr old (e.g., Stothers & Frogel 1974), but T Tauri stars (age 10^6–10^7 yr), as well as protostars ($\lesssim 10^5$ yr) and pre-stellar cores, are also present, showing that star-formation is still on-going.

The Gould's Belt contains several million Solar masses of interstellar material and includes all the nearby sites of active star-formation (Orion, Ophiuchus, Perseus, etc.). These have been the benchmarks against which theories of star-formation have been tested. Indeed, numerous "Gould's Belt surveys" targeting these regions have been carried out over the years –for instance, the James Clerk Maxwell Telescope Legacy Survey of Nearby Star-forming Regions in the Gould Belt (Ward-Thompson et al. 2007), the Spitzer Gould Belt (Dunham et al. 2015) and c2d (Evans et al. 2009) Legacy Surveys, and the Herschel Gould's Belt Survey (André et al. 2010). To take full advantage of this wealth of high quality information, it is fundamental to have accurate distance measurements to each of the regions in the Gould's Belt. In addition, these regions are a few hundred parsecs away and typically a few tens of parsecs across –and therefore presumably also a few tens of parsecs deep. As a consequence, using a single mean distance (however accurately measured) for all young stellar objects (YSOs) in a given region will result in typical distance errors in excess of 10% for the individual YSOs. A case in point is that of the Taurus star-forming region, which is located at a mean distance of about 145 pc, but is about 30 pc deep (Loinard et al. 2007; Torres et al. 2007, 2009, 2012). Using the mean distance to Taurus to calculate luminosities for YSOs located on the near side of the complex (at 130 pc) results in an error of 25%. Thus, it is not sufficient to have an accurate mean distance for each region. Rather, it is highly desirable to have accurate distances to a substantial sample of individual objects within each region. Such detailed information makes it possible, in addition, to reconstruct the internal 3-dimensional (3D) structure of the clouds.

Recently, Bouy & Alves (2015) used stars from the Hipparcos catalogue to determine the 3D distribution of the spatial density of OB stars within 500 pc from the Sun. They found no evidence for a ring-like structure and claimed that the Gould's Belt is the result of a 2D projection effect. They also propose that the apparent rotation and expansion of the belt is due to relative motions associated with galactic dynamics, but this needs to be investigated with accurate measurements of the dynamical state of the Belt.

1.2. *VLBI distance determinations*

Understanding the processes of star formation requires accurate observational constraints. The observational signatures predicted by star formation models have to be compared to actual observations, but a direct comparison can only be performed when the stellar properties, such as source size, luminosity and mass, are well determined. Frequently the distances to star-forming regions are poorly constrained because they are obscured by molecular gas and dust. In such cases, inaccurate distances are often the main source of error on intrinsic parameter determinations.

Numerous indirect methods can be used to estimate the distance to young stars (e.g., de Grijs 2011), but they typically result in systematic uncertainties in excess of 20%. Only trigonometric parallaxes can provide unbiased distance measurements, but they are notoriously challenging to obtain. For instance, the trigonometric parallax of a star at 200 pc is 5 milli-arcseconds (mas), so an astrometric accuracy of 50 micro-arcseconds (μas) on the parallax would be required to measure that distance to 1% accuracy. This is more than one order of magnitude better than the astrometry delivered by the Hipparcos satellite (Perryman et al. 1997). Indeed, Hipparcos did not significantly improve our knowledge of the distance to star-forming regions in the Gould's Belt (e.g., Bertout et al. 1999). Also, the Hipparcos result on the distance to the Pleiades cluster, which is commonly used for testing theoretical stellar models, disagrees with all distance determinations obtained through other methods (Melis et al. 2014; David et al. 2016). The upcoming *Gaia* astrometric mission (de Bruijne 2012) will likely reach an accuracy of a few tens of μas, sufficient for percent accuracy determinations of distances in the Gould's Belt. However, since it operates at optical wavelengths, *Gaia* will be limited to stars that have low extinction. This will be an issue in star-forming regions like Orion,

Ophiuchus, or Serpens, where values of A_V larger than 10 are common (Ridge et al. 2006; Cambrésy 1999).

For accurate astrometry, an alternative to optical-wavelength space missions is provided by Very Long Baseline Interferometry (VLBI; e.g., Thompson et al. 2007; Reid & Honma 2014). VLBI observations at centimeter wavelengths typically reach an angular resolution of order 1 mas. When VLBI observations are phase-referenced to a bright nearby source, the angular offset between the target and the reference source can be measured to an accuracy of $\sim$ 20 to 300 μas, depending on the signal-to-noise ratio of the detection, the declination of the source, and the distance between the target and the reference source (Pradel et al. 2006). The reference sources are usually distant quasars that are very nearly fixed on the celestial sphere. Thus, the measured offset between the reference source and the target can be transformed into accurate coordinates for the target. When several such observations collected over one year or more are combined, the parallax and proper motion of the target can be measured with high accuracy. Also, the astrometry quality of both VLBI and *Gaia* observations will be tested by considering objects that both instruments can detect.

Two technical points are worth mentioning here. The first is that a systematic error on the target coordinates will obviously occur if the reference quasar position is not well known. The positional errors of reference calibrators used in VLBI observations are typically between 0.5 and 10 mas, so this is the level of accuracy that can be expected on absolute coordinates derived from VLBI data. However, this additive error will equally affect all observations of a given target (as long as the same calibrator was used), and hence have no measurable effect on the parallax and proper motion measurements obtained from multi-epoch observations. The second, potentially more serious issue, is that, because of emerging jet components, the photocenter of the quasars may shift with time when accuracies of a few μas on positions and a few μas yr^{-1} on proper motions are reached (e.g., Reid & Brunthaler 2004). Because our typical positional errors are $100-300$ μas, this problem will not be relevant for the data presented here, and can be mitigated by including several reference sources in the observations and monitoring their relative positions as a function of time (e.g., Reid & Honma 2014).

VLBI astrometry can only be applied to a specific class of targets if they are detectable in VLBI observations (e.g., Thompson et al. 2007; Reid & Honma 2014). This requires that the potential targets not only be radio sources, but also have an average brightness temperature in excess of $\sim 10^6$ K within the synthesized beam (i.e. be non-thermal sources), as VLBI arrays do not have sufficient sensitivity to detect weaker emission.[1] A summary of the mechanisms that produce non-thermal radio emission in YSOs is given in Appendix A. VLBI observations of non-thermal continuum emission from young stars have been used to measure very accurate trigonometric parallaxes to individual YSOs and star-forming regions (Loinard et al. 2005, 2007, 2008; Torres et al. 2007, 2009, 2012; Dzib et al. 2010, 2011; Menten et al. 2007; Dzib et al. 2016). These observations focused on YSOs that were previously known to be non-thermal radio emitters. Building upon these successes, we have initiated a large project (the **GOuld's BELt dIstaNces Survey, hereafter GOBELINS**[2]) aimed at measuring the trigonometric parallax and proper motions of a large sample of magnetically active young stars in the Gould's Belt (specifically in Taurus, Ophiuchus, Orion, Perseus, and Serpens) using VLBI observations.

1.3. *GOBELINS*

GOBELINS was approved by the Telescope Allocation Committee of the *National Radio Astronomy Observatory* in the Spring of 2010. It followed a two-stage strategy. During the first phase, large maps of each of the regions of interest were obtained, using conventional interferometry observations, with the Karl G. Jansky Very Large Array (VLA; we called this first phase of the project the **Gould's Belt Very Large Array Survey**). These maps (published by Dzib et al. 2013, 2015; Kounkel et al. 2014; Ortiz-León et al. 2015, and Pech et al. 2016) enabled us to identify radio-bright young stellar objects in each region and attempt a first separation between thermal and non-thermal sources. For instance, in Ophiuchus, Dzib et al. (2013) identified 56 radio sources associated with young stellar objects and proposed that for $\gtrsim$ 50% of them, the emission is of non-thermal origin. The second stage consists in multi-epoch VLBI observations of the selected targets with the Very Long Baseline Array (VLBA; Napier et al. 1994), to measure the astrometric elements (trigonometric parallax and proper motion) of each target. In this paper, we report on the first VLBI observations of the sources in the Ophiuchus region.

The results from GOBELINS will be used first and foremost to pinpoint the location of the regions of star-formation within the Gould's Belt, as well as their internal three-dimensional structure. In addition, since the proper motion of each target will be measured simultaneously with its trigonometric parallax, the transverse

[1] VLBI arrays are equivalent to telescopes thousands of kilometers in diameter in terms of angular resolution, but emphatically **not** in terms of collecting area.

[2] A french word that refers to the tapestries from the Gobelin factory in Paris, France.

component of the velocity vector will be obtained. In many cases, the radial velocity will be available from the literature or could be measured with dedicated optical or near-infrared (NIR) spectroscopy. Thus, GOBELINS will also provide the complete velocity vector for many targets. This will enable us to examine both the internal dynamics of each region and the large-scale relative motions of the different clouds in the Gould's Belt (see Rivera et al. 2015, for a preliminary example). In particular, these measurements will help to characterize the overall dynamics of the Gould's Belt and will be relevant to the understanding of its very origin.

GOBELINS will also provide radio images of a large sample of young stellar objects at milli-arcsecond resolution. This is unparalleled at any other wavelength, and will enable us to characterize the population of young, very tight, binary and multiple systems (see Torres et al. 2012 and Dzib et al. 2010 for examples of young multiple systems characterized by VLBI observations), as well as the magnetic structures around young stars (R.M. Torres et al., in preparation). Finally, these results will enable us to study the physical processes underlying the radio emission. For instance, the Gould's Belt Very Large Array Survey data (Dzib et al. 2013, 2015; Kounkel et al. 2014; Ortiz-León et al. 2015; Pech et al. 2016) have shown that the radio emission from YSO's is reasonably correlated with their X-ray luminosity, following the so-called Güdel-Benz relation (Guedel & Benz 1993; Benz & Guedel 1994). The VLBI observations will enable us to unambiguously separate the thermal and non-thermal components and re-examine this relation in more detail. It will also allow us to examine the prevalence of non-thermal radio emission in young stars as a function of their age and mass, providing clues on the magnetic evolution of young stellar objects.

1.4. *The Ophiuchus region*

As mentioned earlier, in the present paper we will focus on the GOBELINS observations of the Ophiuchus region. Ophiuchus is one of the best-studied regions of star-formation (see Wilking et al. 2008 for a recent review). It consists of a centrally condensed core associated with the dark cloud Lynds 1688 (where A_V = 50 to 100 magnitudes; Wilking et al. 2008) and several filamentary clouds (collectively known as the "streamers") extending toward the east (Lynds 1689 is a particularly prominent dark cloud associated with the eastern streamer) and the north-east (see Figure 1 in this paper and Figure 1 in Dzib et al. 2013).

The distance to Ophiuchus has been discussed in some detail by Wilking et al. (2008), Lombardi et al. (2008), Loinard et al. (2008), and Mamajek (2008). The canonical value of 160 pc (Bertiau 1958; Whittet 1974; Chini 1981) remained in use until very recently. Evidence for a somewhat shorter distance (120–145 pc) started to emerge from optical photometric and astrometric studies of the nearby Upper Scorpius subgroup (de Geus et al. 1989; de Zeeuw et al. 1999). The implications for Ophiuchus itself, however, were limited by the unclear relation between Upper Scorpius and Ophiuchus (see Wilking et al. 2008 for a discussion of this topic). More recently, Mamajek (2008) used the trigonometric parallaxes of the stars illuminating seven reflection nebulae within 5° of the Ophiuchus core to derive an estimate of 135 ± 8 pc. Both Knude & Hog (1998), and Lombardi et al. (2008) combined Hipparcos parallaxes and extinction measurements to conclude that Ophiuchus is at a distance of about 120 pc. Lombardi et al. (2008), in particular, report a mean distance of 120 ± 6 pc for the entire region, with some evidence that the streamers might be ∼ 10 pc closer than the core. This would be consistent with the distance of 96 ± 9 pc derived by Le Bouquin et al. (2014); (see also Schaefer et al. 2008) for the pre-main sequence binary Haro 1-14c, located in the north-eastern streamer.

It is important to note that none of the measurements mentioned so far involve direct trigonometric parallaxes to Ophiuchus cluster members. This is, of course, because the stars in that cluster are too deeply embedded to be detectable with Hipparcos or ground-based optical telescopes. Indeed, to date, there are only two published trigonometric parallaxes for Ophiuchus and both were obtained through VLBI observations. The first measurement was reported by Imai et al. (2007) and targeted water masers associated with the Class 0 protostar IRAS 16293–2422, located in the northern part of Lynds 1689. They derive a distance of 178^{+18}_{-34} pc, significantly larger than the 120–140 pc estimates that seem to emerge from the recent studies, described above, of the Ophiuchus core. It is not clear if this discrepancy stems from issues with one or more of the distance measurements, or if it is indicative that the eastern streamer is significantly more distant than the core. The second parallax measurement was reported by Loinard et al. (2008), and focused on two young stars (DoAr 21 and S1) located toward the Ophiuchus core. They obtain 120 ± 5 pc for the mean distance to these two stars, and adopt this value as the best estimate of the distance to the Ophiuchus core.

In summary, there is a growing consensus that the Ophiuchus core is at 120–140 pc, but reducing the actual uncertainty on the distance has proven difficult. In addition, there are some conflicting results regarding the orientation of the streamers relative to the core. This unsatisfactory state of affairs largely results from the scarcity of direct parallax measurements to Ophiuchus members.

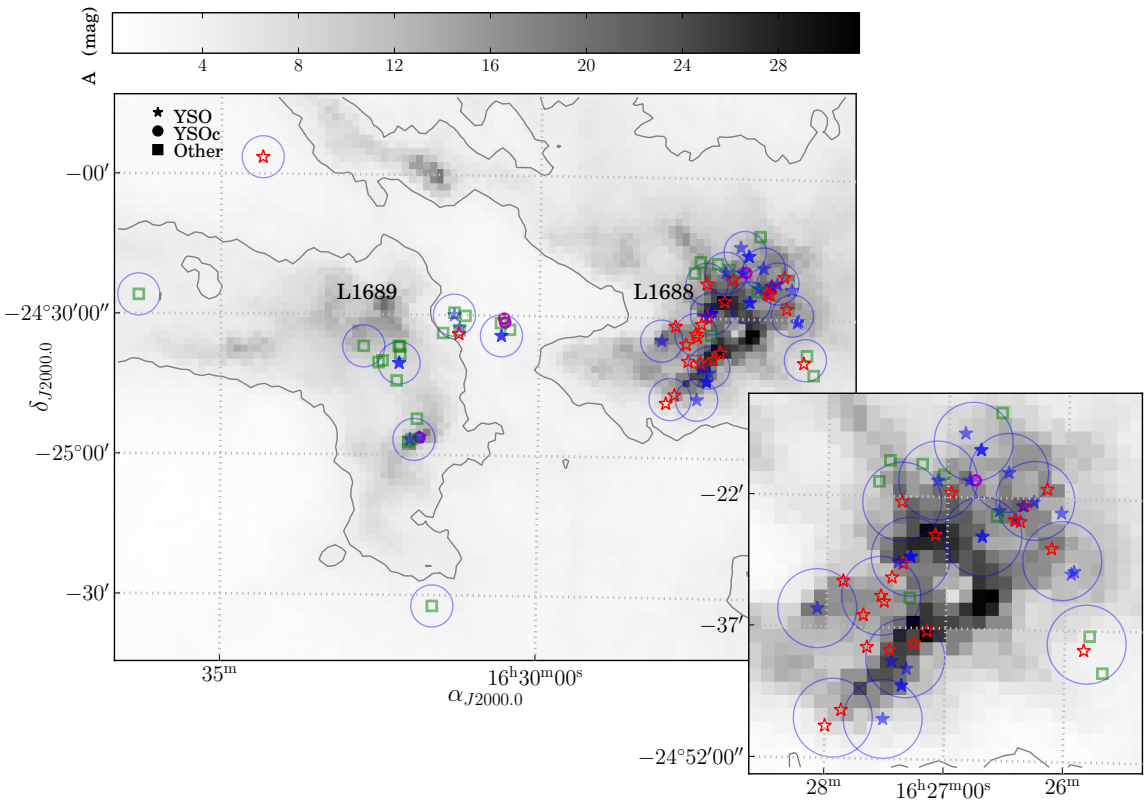

Figure 1. Spatial distribution of sources discussed in this work. Detected YSOs are shown as blue solid stars, YSO candidates as small magenta open circles, and other sources as green open squares. The YSOs not detected in our observations are shown as red open stars. The large blue circles indicate the position and size of representative VLBA fields used to observe our targets. The grey scale represents the extinction map obtained as part of the COMPLETE project (Ridge et al. 2006), based on 2MASS data (Skrutskie et al. 2006). The grey contour indicates an A_V of 4. The inset shows an enlargement of the Lynds 1688 area.

In this paper we present new VLBA observations taken over a period of 4 years as part of GOBELINS, and report on the detection of 26 young stellar systems in the Ophiuchus region (corresponding to 34 individual young stars, as some of the systems are multiple). The target sample and observing strategy are described in Section 2, the detections are described in Section 3, and the properties of the detected radio emission are analyzed in Appendix A.2. Section 4 focuses on a subset of this sample and presents the astrometry of 16 stellar systems. We first analyze single objects in Section 4.1, and then stars in multiple systems in Section 4.2 (other detected sources that are not known young stars are analyzed in Appendix B). Finally, we provide a new improved distance to the core of Ophiuchus, and a description of the cloud depth in Section 5.

2. OBSERVATIONS, CORRELATION AND DATA REDUCTION

The observations were obtained with the National Radio Astronomy Observatory's VLBA at $\nu = 5$ and 8 GHz. We report on a total of 86 projects (code BL175), observed between 2012 March and 2016 April, and scheduled either dynamically or on a fixed date basis. Observations were usually obtained within 3 weeks of the equinoxes (March 21 and September 22) in each year; this corresponds to the maximum elongation of the parallax ellipse. The data were recorded in dual polarization mode with 256 MHz of bandwidth in each polarization, covered by 8 separate 32-MHz intermediate frequency (IF) channels. Projects observed during the first ∼1.5 years of our program were taken at 8 GHz (Table 1). We switched to 5 GHz after the upgrade of the C-band receivers of the VLBA, which resulted in an increase of the bandwidth and sensitivity at that frequency.

A brief parenthesis about pointing positions and fields of view is in order here, as these concepts can be somewhat ambiguous for VLBI instruments. Observing with VLBI arrays involves two steps: (i) the actual observations when the antennas are all pointed toward a given direction (α_0, δ_0) and the data are recorded, and (ii) the correlation step (often carried out days or even weeks after the observations) when the data from the individual antennas are combined to form visibilities (see Thompson et al. 2007 for details). The field of view relevant for

the observation step corresponds to the primary beam ($\Omega_{\rm PB}$) of the individual telescopes. For the 25-meter dishes conforming the VLBA, the primary beam has a diameter of order $10'$ and $6'$, at 5 and 8 GHz, respectively. During correlation, however, the useful field of view is limited by coherence losses, due to beamwidth and time smearing, to a small *patch* typically only a few arcseconds in diameter. The center coordinates of a patch are specified during the correlation step, and can be chosen anywhere within the primary beam. In particular, they do not need to coincide with the position (α_0, δ_0) where the telescopes were pointing, as long as they are within $\Omega_{\rm PB}$ of that position. By running multiple correlations on the same data, one can reconstruct an arbitrary number of patches, each at different locations within the primary beam. These different locations are usually called *phase centers*. The VLBA correlation is now performed by a DifX digital correlator (Deller et al. 2011), that can simultaneously reconstruct multiple patches in a single pass through the data. A given VLBA observation is then defined by specifying (i) a pointing center (α_0, δ_0) where all antennas will point during the observations, and (ii) multiple phase centers at coordinates ($\alpha_{0,i}$, $\delta_{0,i}$) where correlations will be performed. In this mode, the correlator produces independent files containing the different phase centers. The first file contains the first (primary) phase center listed for each pointing center. Often, but not always, the primary phase center in a given observation corresponds to the pointing center itself.

Accounting for the foregoing discussion of positions and fields of view, our observations were set up as follows. From the *Gould's Belt Very Large Array Survey* observations of Ophiuchus reported by Dzib et al. (2013, see Section 1.3), a sample of YSOs with potentially non-thermal radio emission (our primary target list) was compiled. Here, we call YSOs those sources that have been associated with young stars in infrared and X-ray surveys, and young stellar object candidates (YSOc) those sources not classified as young stars by these surveys, but that show evidence of coronal magnetic activity in the radio (for instance flux variability). All of the YSOs in our sample have been accommodated in 44 different pointing positions of the VLBA (Table 1); representative fields are distributed across the region as shown in Figure 1. In some instances, a few primary targets could be observed simultaneously (as different phase centers) in the same observation. Within each of the 44 observed primary beams, we then included additional phase centers at the position of **all** the sources reported by Dzib et al. (2013) within the primary beam, independently of whether those sources were classified as YSOs, candidate YSOs, or extragalactic; and independently of whether the radio emission was anticipated to be thermal or non-thermal. In total, 118 sources toward the Ophiuchus region have been observed during our program, of which 50 are known YSOs.

The observations were organized in observing sessions, each with a different code, during which one or two pointing positions were observed (Table 1). The observing sessions consisted of cycles alternating between the target(s) and the main phase calibrator J1627−2427: {target — J1627−2427} for single-target sessions, and {target 1 — J1627−2427 — target 2 — J1627−2427} for those sessions where two targets were observed simultaneously. The target to calibrator angular separations were in the range from 0.1 degrees for sources in Lynds 1688 to 1.2 degrees for targets in the streamers. The on-source time was ∼110 s for each target and ∼50 s for the calibrator in every cycle. The total on-source time during each observing session was ∼ 1.6 hours in projects that observed at 8 GHz, and ∼1 hour at 5 GHz. Scans on the secondary calibrators, J1625−2417, J1625−2527, and J1633−2557, were also taken every ∼50 minutes during the observations. Unfortunately, one of the secondary calibrators, J1625−2417, was too weak to be detected in any of our observations at both 5 and 8 GHz. Finally, geodetic blocks were also included in each project, usually observed before and after the regular session.

The data reduction was done using AIPS (Greisen 2003) and following standard procedures for phase referencing VLBA observations. Initial calibration was performed as follows. Scans having elevations below 10 degrees were flagged. The delays introduced by the ionospheric content were removed, and corrections to the Earth Orientation Parameters used by the correlator were then applied. Corrections for the rotation of the RCP and LCP feeds, as well as for voltage offsets in the samplers, were also applied. Amplitude calibration was done with the $T_{\rm sys}$ method, using the provided gain curves and system temperatures to derive the System Equivalent Flux Density (SEFD) of each antenna. Instrumental single-band delays were then determined and removed using fringes detected on a single scan on the calibrator J1625−2527 or J1627−2427. Global fringe fitting was run on the main phase calibrator in order to find residual phase rates. This was done in two steps. First we used the task FRING without giving a specific source model, applied the solutions derived, split and imaged the phase calibrator data. Then we ran FRING again on the data set with all the calibration applied except global fringe fitting, and using as a source model the self-calibrated image of the phase calibrator. Finally, the phase calibrator was phase-referenced to itself, and the secondary calibrators, as well as the program sources, were phase-referenced to the phase calibrator. The rms errors in source positions achieved with this

initial calibration were as good as 0.01-0.02 mas for the strongest sources (a few mJy in flux density), and of the order of 0.1-0.3 mas for sub-mJy sources. However, these errors misrepresent the true errors because they do not incorporate systematic errors, which are dominated by unmodelled tropospheric zenith delays, ionospheric content delays, and atmospheric fluctuations above the VLBA antennas (Pradel et al. 2006).

Two calibration strategies can be adopted in order to deal with these systematic errors. One method consists in removing the tropospheric and clock errors using the all-sky calibrator blocks (Reid & Brunthaler 2004). These blocks consisted of observations of many calibrators over a wide range of elevations taken with 512 MHz total bandwidth covered by 16 IFs. The multi-band delay, i.e., the phase slope with frequency, was derived for each scan and antenna, and used to model the clock and zenith-path delay errors using the AIPS task DELZN. The corrections were then exported and applied to the phase referencing data set before global fringe-fitting. The second method uses the scans on the secondary calibrators to determine the phase gradient across the sky. The data of the secondary calibrators are split and self-calibrated after initial and DELZN corrections are applied. The position offsets of the secondary calibrators from their respective phase centers are determined and removed, and residual phases are determined for all calibrators with the task CALIB. Finally, the AIPS task ATMCA is used to determine the phase gradients across the sky and then to correct the phase of all sources. We found that the corrections incorporated with DELZN decreased the rms error positions by a factor of up to $\sim$ 2 when applied to sources at more than 1 degree from the main calibrator. On the other hand, the non-detection of the secondary calibrator J1625−2417 prevented us from applying the corrections from ATMCA in most projects. We attempted to derive these corrections using the only detected calibrators J1627−2427 and J1625−2527, but this was limited to targets that are in line (within an angle of 45°) with the two calibrators, and no significant improvement in the rms position error or image quality was achieved. Consequently, for the epochs taken during the Fall of 2015 and Spring of 2016, we replaced the secondary calibrator J1625−2417 with J1633−2557. This calibrator is well detected at both 5 and 8 GHz, and enabled us to apply the ATMCA corrections in the most recent projects. After application of ATMCA, the rms error of the position decreased, in some cases, to a quarter of its original value.

For observations where several phase centers are observed within a given primary beam, the calibration strategy described above was applied to the primary phase center data. The other phase center data were calibrated by simply copying the final calibration (CL) tables, after appropriate editing with the AIPS task TABED to account for different source ID numbering.

Finally, we imaged the calibrated visibilities using a pixel size in the range of $50 - 100$ μas and pure natural weighting (ROBUST = +5 in AIPS). We constructed maps as large as $\sim 1.2''$ to search for our sources. Typical angular resolutions are 4 mas × 2 mas ($\sim$ 0.4 AU at the distance of Ophiuchus) and 3 mas × 0.9 mas ($\sim$ 0.3 AU) at 5 and 8 GHz, respectively. The best noise level was achieved in the images at 5 GHz, and was of order of 25 μJy beam^{-1}. The fluxes of sources observed in data with multiple field centers were corrected for primary beam attenuation. In doing this, we assumed that the primary beam response of the VLBA 25 meter antennas is similar to that for the VLA 25 meter antennas. The new AIPS task CLVLB, which incorporates antenna beam parameters for the VLBA, could be used for this purpose but its performance is still under testing.

3. VLBA DETECTIONS

In Table 2 we list the YSOs detected in the Ophiuchus region. Columns (1) and (2) give the VLA position of the sources, and their names, respectively. We report sources with flux densities above a 6σ detection threshold, if they are detected in only one epoch. On the other hand, for sources with more than one detection, a threshold (in individual epochs) of 5σ was used. We give the minimum and maximum total flux densities measured at both frequencies in columns (3) to (6), but we note that some sources were not observed at 8 GHz. In epochs where sources were observed but not detected, we give an upper flux density limit of 3σ. Six objects are resolved into multiple components; for those, we report the flux densities for each component separately. Brightness temperature (see Appendix A.2 for details) is given in column (7). The evolutionary status of the detected YSOs is indicated in column (8), and the number of detections and observed epochs in column (9). Notice that the number of observations carried out toward each source differs considerably between sources. This is partly because our program was running in dynamic scheduling during the first 1.5 years, and partly because observations on all the 50 targeted YSOs were not fully completed in each equinox even during the fixed-date observations. The spatial distribution of our VLBA-detected sources is shown in Figure 1. The majority of the YSOs belong to the core, with only 5 YSOs distributed across the eastern streamer cloud Lynds 1689. The other detected sources are more evenly distributed across the core and Lynds 1689.

4. ASTROMETRY

For all the objects detected with the VLBA, we have measured the source positions at each epoch by fitting

two-dimensional Gaussians to the images, using the task JMFIT in AIPS. The resulting values are listed in Table 3. Having identified single, double, and multiple sources in our images, we used different approaches for the determination of the source astrometric parameters. We will first describe the approach followed for sources that appear to be single stars, or sources that show evidence of multiplicity but for which we do not have enough data to perform a more complex analysis.

4.1. *Single stars*

Source positions were modeled to derive the trigonometric parallax (ϖ), proper motion (μ_α, μ_δ), and mean position (α_0, δ_0). The fits were performed by minimizing the associated χ^2 (e.g., Loinard et al. 2007) and solving for the five astrometric elements simultaneously. For the errors in the positions at each epoch, we used the statistical errors provided by JMFIT, which roughly represent the expected theoretical precision of VLBA astrometry. However, systematic errors may significantly contribute to the astrometric accuracy (Pradel et al. 2006) and affect the derived astrometric parameters.

We estimate the systematic errors in two different ways. First, we use the empirical relation found by Pradel et al. (2006), according to which the VLBA astrometric accuracy scales linearly with the angular separation between the source and the phase calibrator. In the core, sources are separated from the phase calibrator, J1627−2427, by up to 0.4 degrees. Given this angular separation, and a typical declination of $\sim -25^o$, the expected VLBA rms astrometric errors $\sqrt{(\Delta\alpha\cos\delta)^2 + (\Delta\delta)^2}$ are $\sim$ 210 μas. For this calculation, we have assumed that the rms errors for source coordinates, VLBA station coordinates, Earth Orientation parameters (EOPs), and wet tropospheric zenith path delays all contribute together (Tables 3 and 4 and Equation 2 in Pradel et al. 2006).

The systematic errors were also estimated by quadratically adding an error to the statistical errors given by JMFIT until a reduced χ^2 of 1 was achieved in the astrometric fits. These systematic errors are in general several times larger than those predicted by the empirical relation. We note, however, that in their simulations, Pradel et al. (2006) assumed a full track on the source, while in our observations the source is tracked during less than 4 hours, resulting in a poorer $(u - v)$ coverage. We used the latter approach (based on a measured reduced χ^2) to deal with systematic errors. As stated above, these errors were added quadratically to the statistical errors of each individual epoch and used in the last iteration of the fits.

In the following sub-sections, we will comment separately on a few of the critical sources describing the additional data that were taken from the VLBA archive, when available, and detailing the quality of the fits. In Table 4, we provide the resulting astrometric parameters and distances for the complete sample. The corresponding measured source positions and best fits are shown in Figure 2.

4.1.1. *DROXO 71*

The model that assumes a uniform and linear proper motion produces a good fit to the data. However, we discarded the last detection because it degrades the quality of the fit. We ignore the source of error that may be introduced in this particular epoch, but we found that the "expected" position from the fit to the first 7 epochs is on a sidelobe.

4.1.2. *DoAr 21*

DoAr 21 has been observed and detected at 7 epochs. Additionally to these observations, the source was observed with the VLBA prior to 2012 in projects BL128 (9 epochs from 2005 September to 2006 December) and BT093 (8 epochs from 2007 July to 2007 September). Seven epochs from project BL128 were analyzed and published in Loinard et al. (2008). Because the observing and calibration strategy adopted for GOBELINS is not exactly the same as in Loinard et al. (2008), we perform a consistency check as follows. We downloaded, calibrated and revised these prior observations, by applying the same calibration procedures as to the data from our own project. We note, however, that a large fraction of the observations taken between 2006 December and 2007 September experienced very poor weather conditions (Table 5). Such conditions affected the image quality and the rms error position was relatively high, in comparison with that measured in observations collected under optimal weather. In the present analysis, we do not include the epochs when data were highly affected, and only 5 additional epochs to the seven reported by Loinard et al. (2008) were included. Hence, a total of 12 epochs from 2005 September to 2007 September are considered in our analysis.

Unlike the GOBELINS observations, projects BL128 and BT093 did not include geodetic-like scans, and therefore no DELZN correction was applied to those projects. On the other hand, the secondary calibrators J1633−2557 and J1634−2058 were detected and used only in projects BT093CD and BT093CE, for which an improvement in the image quality and the rms error position was found when using the multi-calibrator strategy.

Projects BL128 and BT093 observed J1625−2527 (located 1 degree south of DoAr 21) as the main phase calibrator, while GOBELINS observed J1627−2427, which is only 0.2 degrees away from the science target. Before combining data from the three projects, it was neces-

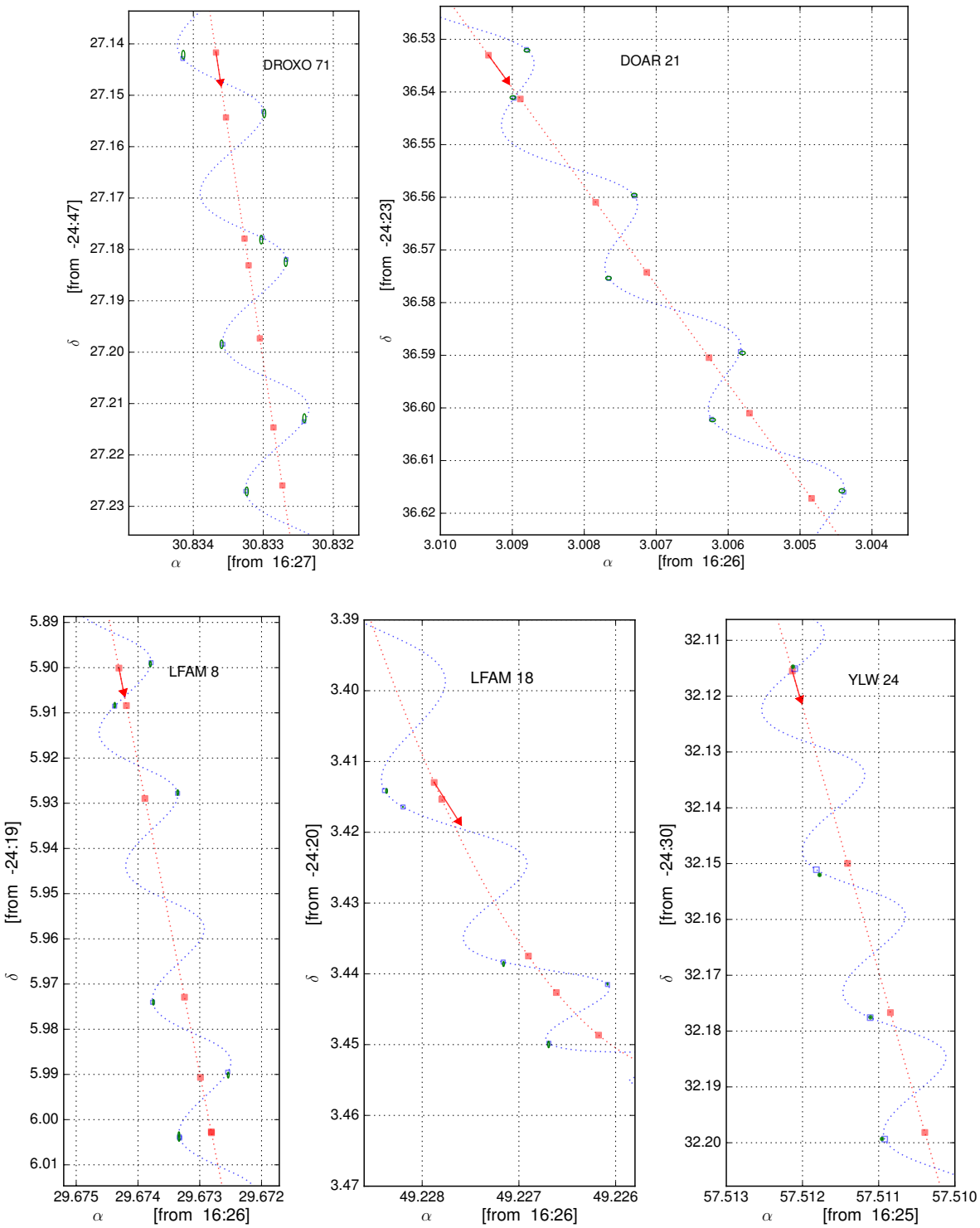

Figure 2. Observed positions and best fit for single sources. Measured positions are shown as green ellipses, the size of which represents the magnitude of the errors. The expected positions from the fit are shown as blue open squares. The blue dotted line is the full model, and the red line is the model with the parallax signature removed. The red squares indicate the position of the source expected from the model without parallax. When the systematic errors on source positions can be estimated from the fits, these are included in the error bars shown in the plots. The arrow shows the direction of position change with time.

sary to correct the target source positions, so that all positions were measured relative to the main calibrator J1627−2427. The mean position of J1625−2527 measured in observations from 2005 to 2007 is $\alpha_{\rm J2000.0}$= $16^{\rm h}25^{\rm m}46.891640^{\rm s}$; $\delta_{\rm J2000.0}$=−25°27′38.32684″. In the images corresponding to GOBELINS, we found

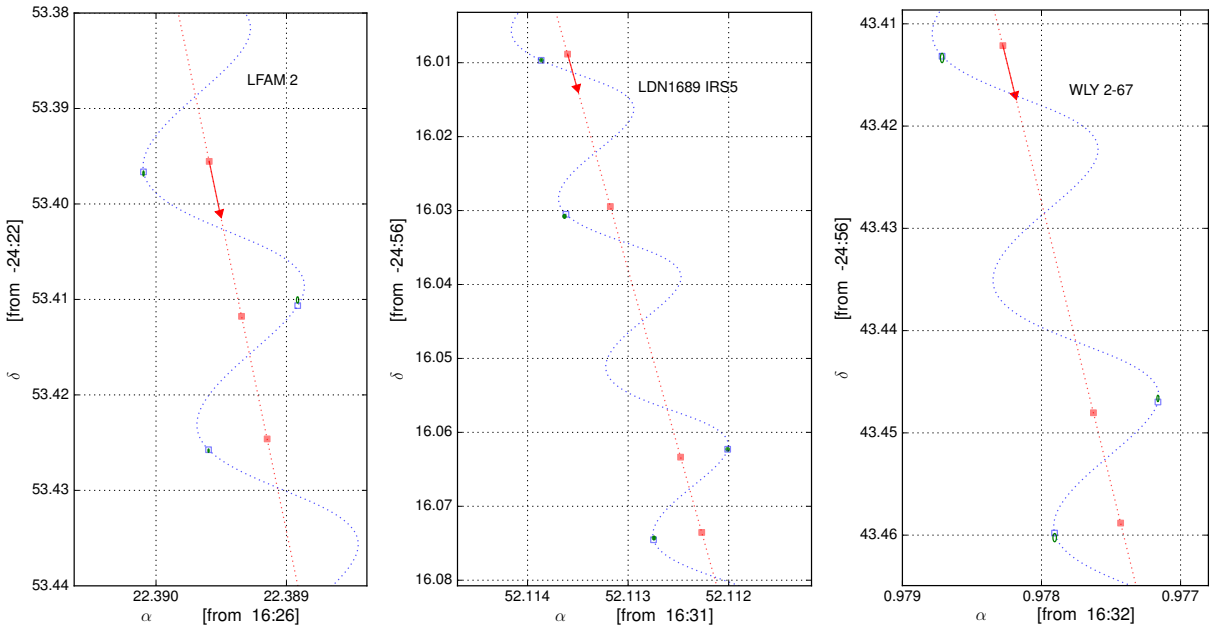

Figure 2. *Continued.*

that J1625−2527 shows a position offset relative to the phase center, as a result of a separation between the source and the main phase calibrator of 1.07 degrees. The mean position of J1625−2527 relative to J1627−2427 in those data is $\alpha_{\rm J2000.0}$= $16^{\rm h}25^{\rm m}46.891617^{\rm s}$; $\delta_{\rm J2000.0}$=$-25^{\rm o}27'38.32808''$. Thus, an offset $\Delta\alpha = -2.3 \times 10^{-5}$ s and $\Delta\delta = -0.0012''$ had to be applied to the positions of DoAr 21 measured from projects BL128 and BT093.

We fit the data from these 12 epochs from BL128 and BT093, and obtain a distance $d = 123.4^{+16.3}_{-12.9}$ pc, fully consistent with the results reported by Loinard et al. (2008) and consistent within 1 sigma with the new determination based solely on GOBELINS data. It is noteworthy, however, that the errors reported by Loinard et al. (2008) on the parallax obtained from the data corresponding to BL128 alone are significantly better than those we obtained when combining BL128 and BT093. We argue that Loinard et al. (2008) underestimated their systematic errors, which resulted in artificially small quoted errors.

When the values derived from GOBELINS data and those obtained from the older BL128+BT093 data are weighted-averaged, the resulting astrometric elements are nearly identical to those derived from GOBELINS data alone. This is expected, of course, as the accuracy of these more recent observations greatly surpass those of BL128 or BT093. In the rest of the paper, we therefore will use the results based solely on GOBELINS.

4.1.3. *LFAM 18*

LFAM 18 has been detected in 5 of 9 observations. The model assuming a linear and uniform proper motion produces a poor fit to the data. We then consider a model with an accelerated and uniform proper motion, and found that it produces a better fit to the data. Indeed, Cheetham et al. (2015) state that the source has evidence of multiplicity, and this may explain why the detected source follows an accelerated rather than a linear motion. The second component of the system is, however, not detected in our VLBA observations. We report the astrometric parameters from the latter fit, and caution that the errors may be underestimated. This is because the method we use to estimate the systematic errors that is described above can only be applied when more than 5 detections are available.

4.1.4. *YLW 24, LFAM 2, LDN 1689 IRS5 and WLY 2-67*

These four sources have been detected just in 3 to 5 epochs and the errors in astrometric parameters may be underestimated. Their corresponding fits give parallaxes that are consistent with the rest of the sources (see also Section 5). For these 4 sources, we assume a uniform and linear proper motion, since they do not show any evidence of multiplicity.

4.2. *Multiple stars*

Our VLBA observations (combined with past astrometric observations) have detected a total of 8 multiple systems (cf. Table 2). In 6 of them, the individual components have been detected at sufficient epochs

such that we can model their orbital motion, in addition to parallax and proper motion. Two different fits were performed as follows. In the first "Full model", we use all available absolute VLBA positions of individual components (including data from epochs where a single component is detected), together with relative positions, to solve for the orbital elements, center of mass at first epoch of the GOBELINS observations where the primary is detected ($\alpha_{\rm CM,0}$, $\delta_{\rm CM,0}$), parallax (ϖ), and proper motion (μ_α, μ_δ) of the system. The orbital free parameters in this model are period (P), time of periastron passage (T), eccentricity (e), angle of line of nodes (Ω), inclination (i), angle from node to periastron (ω), semimajor axis of primary (a_1), and mass ratio m_2/m_1. Combining the mass ratio with Kepler's third law (that contains the sum of masses), and because we know the distance to the system from the parallax solution, the masses of each component are also inferred. The orbital solutions are derived by minimizing χ^2, which is computed for a grid of initial guesses of model parameters. The errors in the parameters were calculated by taking the average, weighted by χ^2, of the output uncertainties over values across the entire grid.

From the VLBA images, we compute, for each system, the angular separation and position angle of the secondary relative to the primary star. In addition, we have compiled from the literature separations measured with near-infrared (NIR) observations. These data are shown in Figure 3 for each source separately. In the second "Relative astrometry model" we only use the separation and position angle of secondary relative to primary, measured at epochs when both components are detected simultaneously. We use the orbital elements determined from the "Full model" as initial parameters for the Gudehus (2001) code, the *Binary Star Combined Solution Package,*[3] to solve for P, T, e, Ω, i, ω, and a. The total mass of the system, M_T, is then obtained from Kepler's law, but we are not able to determine individual masses in this case. For this fit, the uncertainties in the orbital elements are computed from the scatter on model parameters.

The results from both fits are given in Table 6, and the resulting orbits are shown in Figure 3. We find that both fits are consistent with each other within the errors. We will comment on each system separately in the following paragraphs.

4.2.1. *LFAM 15*

The source LFAM 15 has been found to be double in 7 out of our 10 observed epochs. LFAM 15 was also observed at 4 epochs as part of project BL128 (Table 5), between 2005 June and 2006 March. We have calibrated these additional data and detected the source in three epochs, albeit always as a single component. In Figure 4, we show the measured positions for each component and the resulting best "Full model" fit that, as mentioned before, consists of the sum of orbital motion around the center of mass, proper motion, and parallax of the system.

4.2.2. *YLW 12B*

YLW 12B is found to be a hierarchical triple source formed by a close binary (separation of 4–17 milliarcseconds, equivalent to 0.6–2.4 AU), detected in 9 epochs, and a third component, located a few hundred milli-arcseconds to the southwest of the binary and detected in 7 epochs (Figure 5). Hereafter, we call the close binary YLW 12Bab and the third component, YLW 12Bc. Six archival VLBA observations, obtained between 2005 and 2006 as part of project BL128, have also been found for this source; they have been calibrated and analyzed (Table 5). One of these older epochs was discarded due to poor weather conditions during the observations. In these archival observations, both components of YLW 12Bab were detected on 2005 June 8 and 2006 June 1, while YLW 12Bc was detected on 2005 June 8 and 2006 March 24.

Given the distance to the source, the angular separation between YLW 12Bab and YLW 12Bc of ~ 140 and ~ 320 mas in 2005 and 2016, respectively, corresponds to 20 to 45 AU. This suggests that the sources form a bound multiple system, and later in this section we provide a stronger evidence that supports this conclusion. To fit the positions of the YLW 12Bab components, and to take the effect of the third companion into account, we add two more free parameters to the "Full model". These parameters are the acceleration of the center of mass of YLW 12Bab in each direction, a_α and a_δ, which we consider to be uniform. As in the case of LFAM 15, three plots were constructed to visualize the best fit solution. In the first panel of Figure 6, we show the observed positions of the compact binary and the best fit, while in the second panel, we show this fit and source positions with the effect of parallax removed. Using the solution for the mass ratio from the "Full model", we now compute the positions of the center of mass of YLW 12Bab, and plot them along with the parallax plus proper motion model in the third panel of Figure 6. It is clear that the compact binary follows a curved motion as a result of the gravitational force exerted by the third companion. Indeed, we find that the acceleration is statistically different from zero at $> 8\sigma$ in both directions.

Let us now discuss the third star of the system. The positions of YLW 12Bab relative to YLW 12Bc, as well

[3] This package is available at http://www.astro.gsu.edu/~gudehus/binary.html.

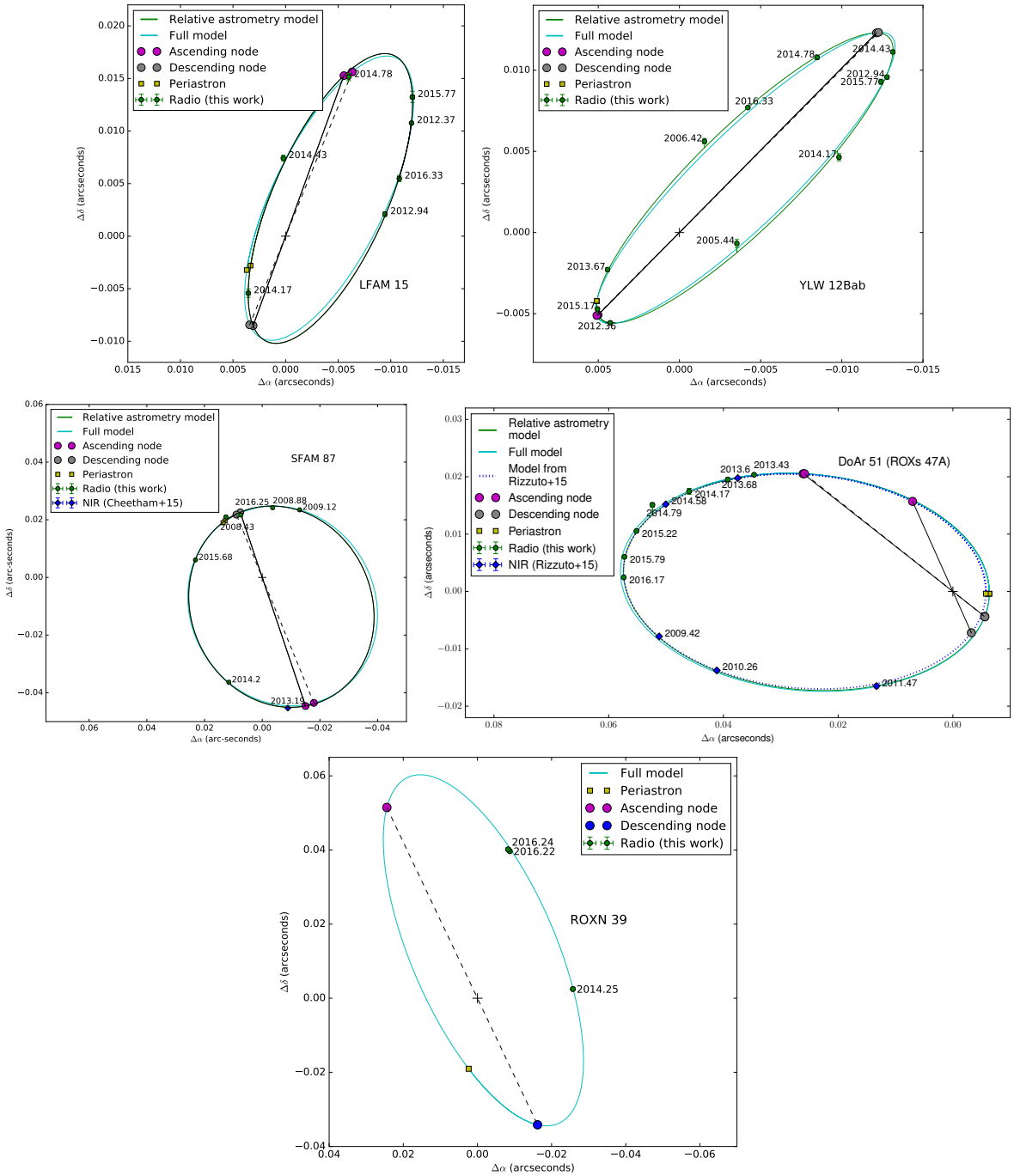

Figure 3. Relative positions of the components of the binary systems. The green points mark the detections with the VLBA, while blue points indicate the detections in the NIR by Cheetham et al. (2015) and Rizzuto et al. (2016). Green and cyan solid lines correspond to the "Relative astrometry" and "Full" model orbital fits, respectively. The blue dotted line in the fourth panel is the fit by Rizzuto et al. (2016) to NIR only data. The black solid and dashed lines trace the line of nodes of the "Relative astrometry" and "Full" model, respectively. The cross marks the position of the primary source.

as the acceleration vector of YLW 12Bab, are shown in Figure 5. We see that the acceleration vector of YLW 12Bab points toward YLW 12Bc, as would be expected of a gravitationally bound system. This plot also shows that our assumption of a uniform accelerated motion is a reasonable approximation, because our observations cover only a small fraction of the orbit expected for the wider system. We attempted to fit the orbit of this source around the center of mass of the whole system with a simultaneous distance and proper motion fit for the three stars. However, we were not able to constrain most of the orbital parameters because the VLBA

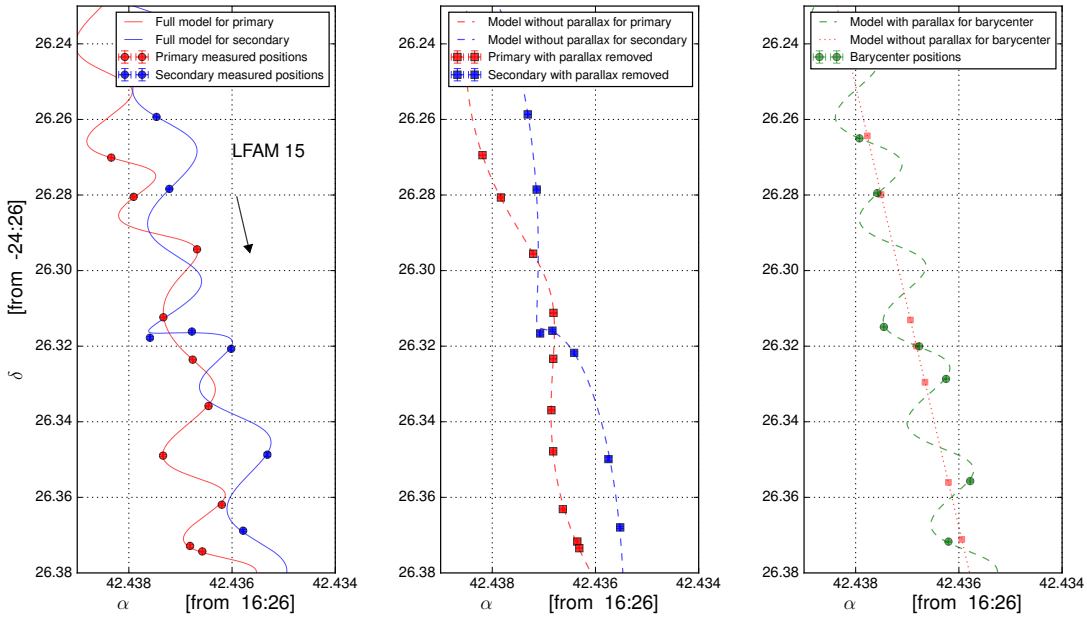

Figure 4. Observed positions and best fit for LFAM 15. *Left:* Measured positions of each component are shown as red and blue circles. The solid lines show the fit corresponding to the "Full model" described in the text. *Middle:* The squares mark the measured positions with the parallax signature removed, while the dashed lines are the fits from the "Full model", also without parallax. *Right:* Green dots mark the position of the center of mass derived using the solutions from the orbital model for the mass ratio. The green dashed line is the model for the motion of the center of mass of the system, while the red line is this same model with the parallax signature removed. The red squares indicate the position of the center of mass expected from the model without parallax. The arrow shows the direction of position change with time. Positional errors, as delivered by JMFIT, are smaller than the size of the symbols.

detections of the third companion are still insufficient. We only find solutions for the following parameters: $\Omega \sim 85^{\rm o}$, $\varpi = 7.190 \pm 0.088$ mas, $\mu_{{\rm CM},\alpha} \cos\delta = -4.55 \pm 0.03$ mas yr^{-1}, $\mu_{{\rm CM},\delta} = -24.27 \pm 0.06$ mas yr^{-1}; limits on the mass, $M_3 > 3$ M$_\odot$, period, $P \sim 300-400$ yr, and that inclination is consistent with the compact binary. Even though we do not have enough data for modeling the orbit of YLW 12Bc, we can still constrain its proper motion and acceleration using its absolute positions measured with the VLBA. In order to do so, we fit separately the third star using the astrometric code for single sources to solve solely for proper motion and acceleration terms, while fixing the parallax at the value derived for YLW 12Bab. We show this last fit in the fourth panel of Figure 6, and give the solution of the astrometric parameters in Table 4.

As we mentioned above, the trajectory of YLW 12Bab is somewhat curved. That of YLW 12Bc is, on the other hand, more linear. This results in a smaller measured acceleration for YLW 12Bc (~ 0.2 mas yr^{-2}) than for YLW 12Bab (0.64 mas yr^{-2}), and suggests that YLW 12Bc is the most massive member of the system. Indeed, we find that M_3>3 M$_\odot$, while $M_1 = 1.26$ M$_\odot$, and $M_2 = 1.40$ M$_\odot$. This is the reason why we plot the position of YLW 12Bab relative to YLW 12Bc in Figure 5, rather than the converse. We also see that, as expected, the acceleration of YLW 12Bc points, within the errors, toward YLW 12Bab (see Figure 5).

4.2.3. *SFAM 87*

SFAM 87 (also called ROX 39) has been detected in 4 epochs of GOBELINS. This source was also observed in 6 epochs from 2008 March to 2009 May as part of project BT097, but these data have not been published yet. We calibrated these additional epochs (Table 5) and combined them with our more recent data for the astrometric fits. The source is resolved into two components that are simultaneously detected in 6 out of the 10 total epochs (3 in BT097 and 3 in GOBELINS). We note that Cheetham et al. (2015) identified a companion to SFAM 87 in 2013, March, using NIR aperture masking. This source appears to be the counterpart of the secondary source detected in our VLBA images (Figure 3). We used all available VLBA and NIR data to fit jointly orbital and proper motion, as well as parallax. The resulting best fit is shown in Figure 7 in a similar fashion to LFAM 15.

4.2.4. *DoAr 51*

DoAr 51 (also called ROXs 47A) is located in the Lynds 1689 eastern streamer, 1.2$^{\rm o}$ east of the Ophiuchus core. The source has been detected in 7 epochs, and was found to be double in all of them. DoAr 51 was identi-

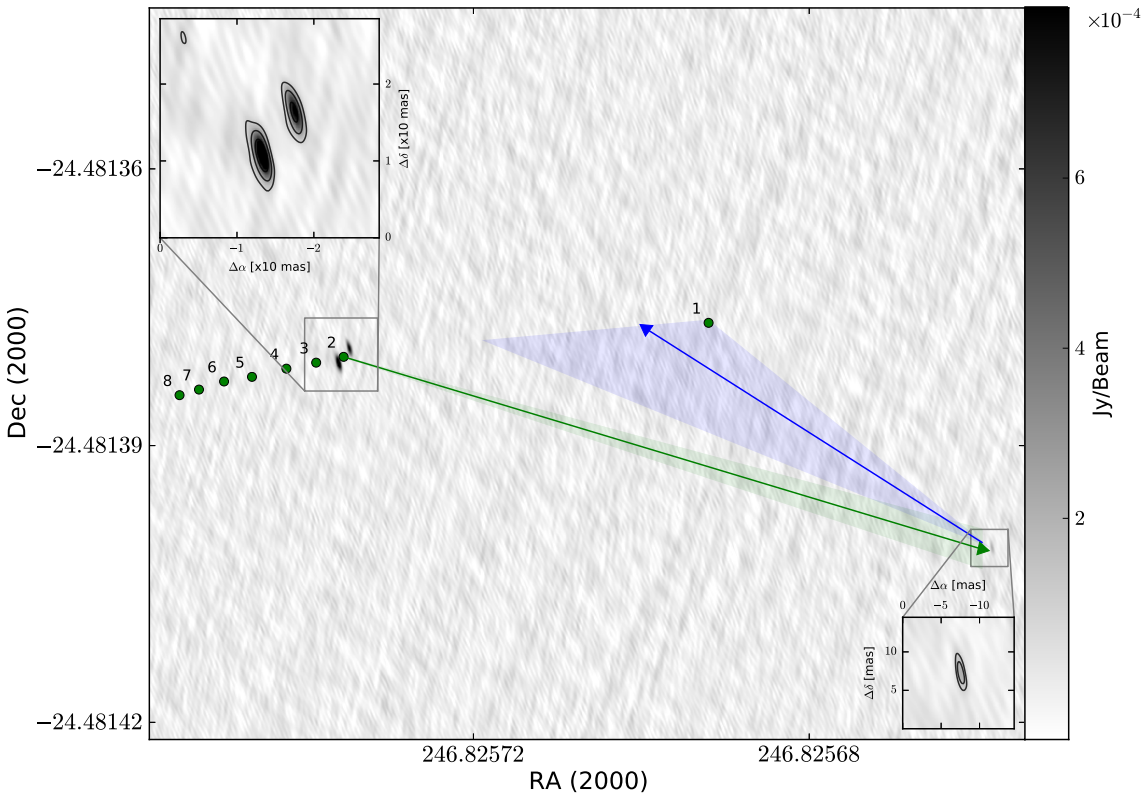

Figure 5. VLBA image of the multiple system YLW 12B, from data obtained on 2012, May 11 (first epoch observed by GOBELINS). Insets show zooms on the tight binary YLW 12Bab, top left, and the southwestern companion YLW 12Bc, bottom right. Contour levels are 3, 9 and 21 (in top left inset), and 3 and 5 (in bottom right inset) times 32μJy beam^{-1}, the rms noise in the image. The green dots mark the position of YLW 12Bab relative to YLW 12Bc at the epochs when the three sources in the system are detected. These are 8 epochs, which correspond to the Julian dates listed in Table 3 for the third component in the system, as follows: 1= 2453529.77467, 2=2456058.83738, 3=2456269.26236, etc. Notice that, at epoch with JD = 2453818.98287, the third component was detected but the compact binary was not. The arrows with their error cones show the acceleration vectors at the first epoch observed by GOBELINS.

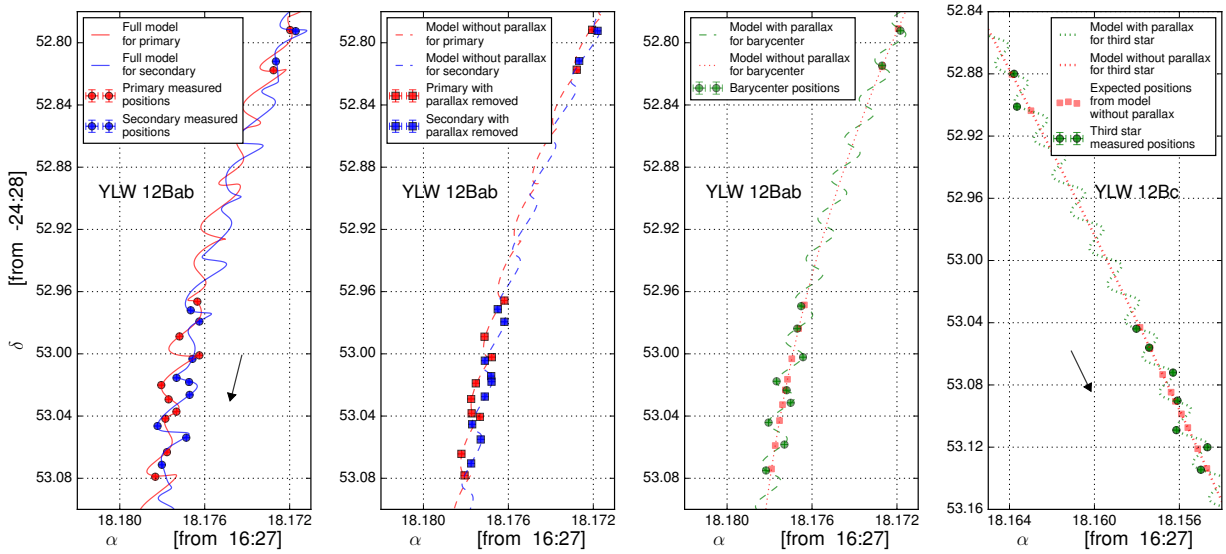

Figure 6. First to third panels are like Figure 4, but for YLW 12Bab. Fourth panel shows the observed positions and best independent fit for YLW 12Bc, with parallax fixed to the value of YLW 12Bab.

fied as a hierarchical triple system composed of a tight binary with separation of about 40 mas and a third com-

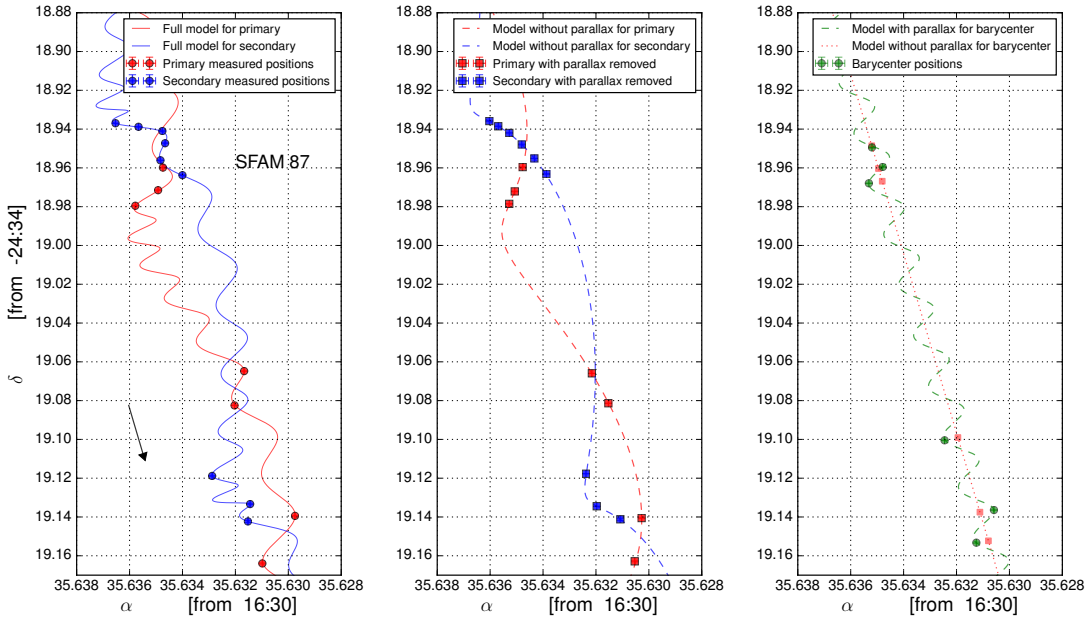

Figure 7. Same as Figure 4, but for SFAM 87.

ponent about 0.8 arcsec away by Barsony et al. (2003). Cheetham et al. (2015) confirmed the tight binary using NIR aperture masking observations. They resolved the source into two components, with an angular separation of 51.5 ± 0.20 mas in June 2009 and 43.38 ± 0.18 mas in April 2010. This is to be compared with a separation of 40 ± 30 mas reported by Barsony et al. (2003) in May 2002. More recently, Rizzuto et al. (2016) used the two positions measured by Cheetham et al. (2015) and three new detections in the NIR to model the orbit of the system. These 5 detections are shown in Figure 3, together with the positional offsets between the components of the system as seen in our VLBA images. It is clear that our radio sources are the counterparts of the NIR sources, as they lie along the orbit derived by Rizzuto et al. (2016). We model all data available from VLBA and NIR observations to better constrain the orbit of the system. The resulting best fit using the "Full model" is shown in Figure 8, and the corresponding orbit in Figure 3. For comparison, we also show in this latter figure the orbit derived by Rizzuto et al. (2016).

4.2.5. *ROXN 39*

The components of the system ROXN 39 have been detected separately in 7 and 5 epochs, respectively, and simultaneously in only 3 epochs. The "Full model" fit and measured positions of individual components are shown in Figure 9, while Figure 3 shows the same model and relative positions. We did not fit the "Relative model" to this system because of the small number of simultaneous detections of both components. Consequently, the orbital parameters are less constrained, compared to the other systems described above.

4.2.6. *S1*

This source has been detected in a total of 8 epochs, and was also observed at 14 epochs as part of projects BL128 and BT093 (Table 5). The distance estimate by Loinard et al. (2008) of $d = 116.9^{+7.2}_{-6.4}$ pc, based on the data from the first 6 of these old epochs, is significantly different from the distance obtained here for others sources in Lynds 1688 (which range from 130 to 140 pc), and hence requieres a careful inspection. We recalibrated the data used in Loinard et al. (2008), as well as the additional 8 unpublished observations obtained as part of BL128 and BT093. Similarly to DoAr 21, source positions measured at these 14 older epochs were corrected, before fitting the data, by the positional offset of the calibrator J1625−2527 relative to its old position.

A second source was detected in four epochs of the archival data, at an angular separation of about 20-30 mas from S1 (Figure 10). The detections are, however, only evident by self-calibrating the images, and the source is not present in the most recent epochs, so they should be taken somewhat cautiously. It is interesting, however, that Richichi et al. (1994) did report on the detection, using the lunar occultation technique in the NIR, of a companion to S1, at about 20 mas. Our detections of a second source in the system would be consistent with that earlier result. If we assume that the source is double, we can fit the orbital motion of the system jointly with the astrometric parameters, and use the positions of the putative second component to estimate individual masses. To that end, we discard

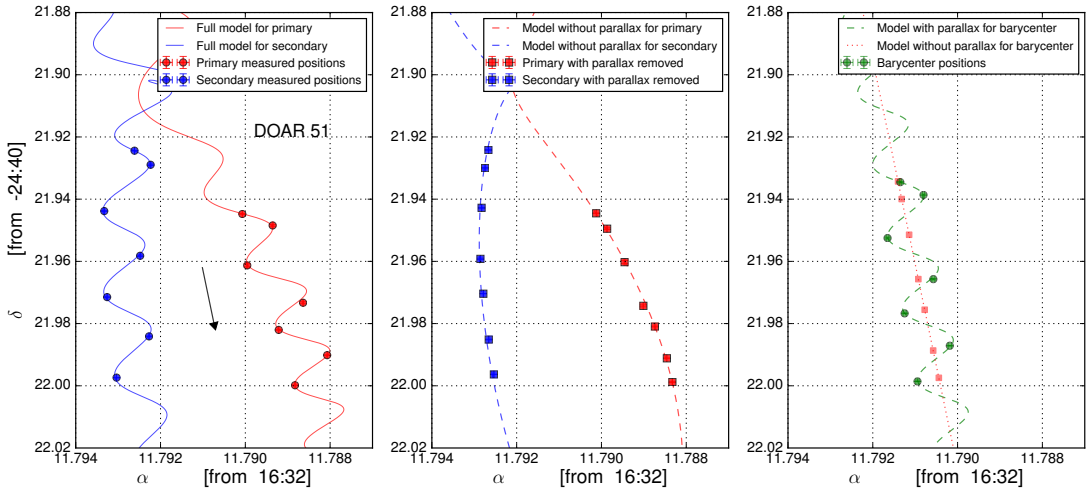

Figure 8. Same as Figure 4, but for DOAR 51.

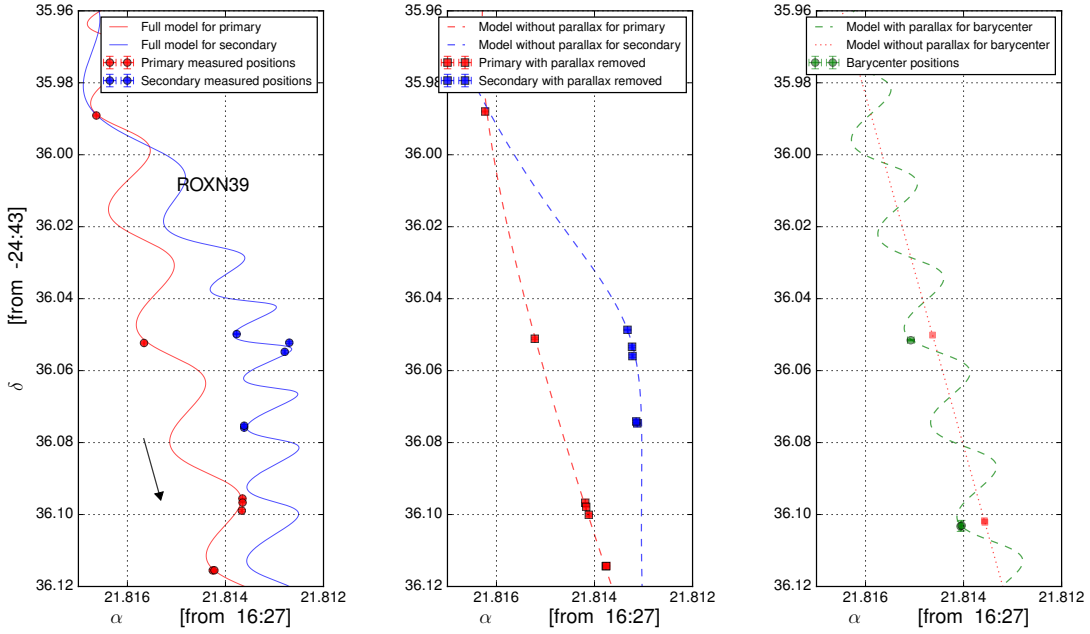

Figure 9. Same as Figure 4, but for ROXN 39.

the BL128 and 2nd BT093 secondary epochs, as well as the 2nd, 4th, and 6th BT093 primary epochs, because their corresponding images are of poor quality due to observing issues (cf. Table 5), and source positions do not match up to the best fit solution. The "Full model" fit, shown in Figure 11, yields $\varpi = 7.249 \pm 0.091$ mas and a distance of 138.0 ± 1.7 pc. The derived mass for the primary component is 5.8 $M_\odot$, which is consistent with its B4 spectral type, while for the secondary we find a mass of 1.2 $M_\odot$. When ignoring the secondary component, the purely astrometric fit to all available data of the primary source yields $\varpi = 8.335 \pm 0.522$ mas, and hence the distance derived by Loinard et al. (2008). It is clear that this discrepancy in the results from the astrometry alone and the "Full model" fits is due to the fact that the former does not take into account the multiplicity of the source. In the rest of the paper, we will use the results based on the astrometric plus orbital model, which are consistent with the distances obtained for other sources in Lynds 1688. Since the two components are detected simultaneously in only two epochs, we are not able to fit the "Relative model" to relative positions, and only provide the resulting orbital parameters from the "Full model" in Table 6.

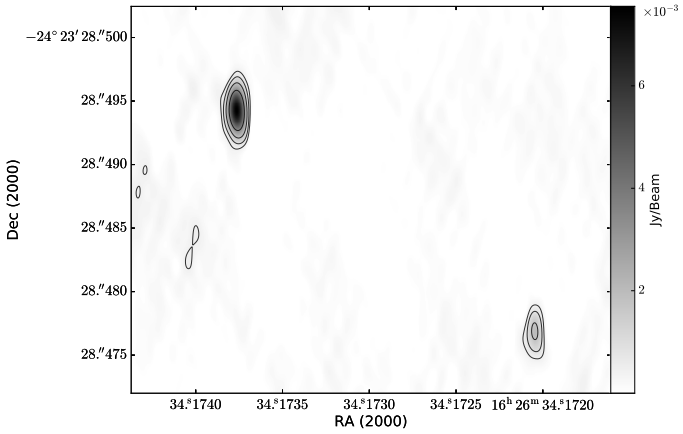

Figure 10. The two components of S1 detected on June 21, 2007. The contours are 4, 8, 16, and 32σ, where $\sigma = 1.08 \times 10^{-4}$ μJy is the rms noise of the image.

4.2.7. *VSSG 11*

VSSG 11 has been detected in 7 observed epochs, and was found to be double in the last 3. The second component is separated about 9 mas from the primary source. We perform the fits similarly to the other multiple systems discussed above. However, because our observations only cover a small fraction of the orbit, the "Full model" fit to the secondary source does not converge. This produces considerably larger errors in the astrometric and orbital parameters than those derived for the other multiple systems. Also, we were not able to reproduce the observed separations between the components of the system. We then fit solely parallax and accelerated proper motion. The resulting best fit is shown in Figure 12.

4.2.8. *WLY 2-11*

WLY2-11 has been detected in a total of 5 epochs. We resolve it into a double source in the last epoch, where the companion is detected at $> 10\sigma$. Since there are insufficient detections of primary and secondary for attempting to model the orbit, we can only fit one of the components of the system. We find that a good fit to the data is produced only when we discard the first epoch and consider for the fit the fainter component detected in the last epoch. If, instead, we take the positions of the single component as measured at the first 4 epochs and the position of the brightest component detected in the last observation, the fit does not match all the measured points, producing large errors in the astrometric parameters. Thus, the detection at the first epoch probably corresponds to the companion source, which is detected as the brightest source in the last epoch. The fit, including acceleration terms, is shown in Figure 12. Because of the few detections, we are not able to estimate systematic errors on the source positions. Nevertheless, the derived parameter uncertainties are comparable to those from the fits that do incorporate systematic errors on source positions.

4.3. *YLW 15*

We have observed the Class I protostar YLW 15 at eleven epochs, and clear detections were obtained at five. Only one source is detected in the VLBA images, and since YLW 15 is known to be a binary system (Curiel et al. 2003), it is important to determine which of the two stars is detected in our VLBA data. This can be achieved by comparing the astrometry of the present VLBA observations with that of the VLA data published by Curiel et al. (2003), which were taken between 1990 and 2002. Such a comparison is shown graphically in Figure 13. The positions of the two sources in the system (VLA 1 and VLA 2) are shown as a function of time as black and red symbols, respectively. We also calibrated and imaged the data from a VLA observation obtained in 2007 as part of project AF455. The VLBA positions are shown as blue symbols. It is clear that the source detected with the VLBA is located very near the expected position of VLA2 at the epochs of the VLBA observations, and more than half an arcsecond away from the expected position of VLA1. We conclude that the source detected with the VLBA is VLA2.

A marginal (7–9 σ) VLBI detection of YLW 15 has been reported in the past (Forbrich et al. 2007). Indeed, the authors themselves mentioned that their detection was difficult to interpret, as the position did not coincide with the expected location of any of the two protostars in the system. This can also be seen in our Figure 13, where the position of the VLBI source reported by Forbrich et al. (2007) is shown as a cyan triangle. Their observations were conducted, under project code BF083, with the High Sensitivity Array (HSA), consisting, for that run, of the Green Bank (GBT) 100-m radio telescope, the phased Very Large Array (equivalent in collecting area to a 130 m dish) as well as the VLBA. We calibrated these data following the standard procedures for incorporating non-VLBA antennas. We achieve rms noise levels between 10 and 22 μJy beam^{-1} (depending on the AIPS ROBUST parameter used for imaging), which are consistent with the value reported by Forbrich et al. (2007) of 15.4 μJy beam^{-1}. We do not detect the source, and confirm our suspicion that their detection was likely spurious.

Even though five data points are, in principle, enough to perform an astrometric fit, most of our VLBA detections of YLW15 were obtained close in time (two are separated by ~ 3 weeks and other two by only ~ 3 days). Moreover, the five detections were acquired around successive spring equinoxes, with no detection close to the fall equinox. As a result of this, the astrometric fit pro-

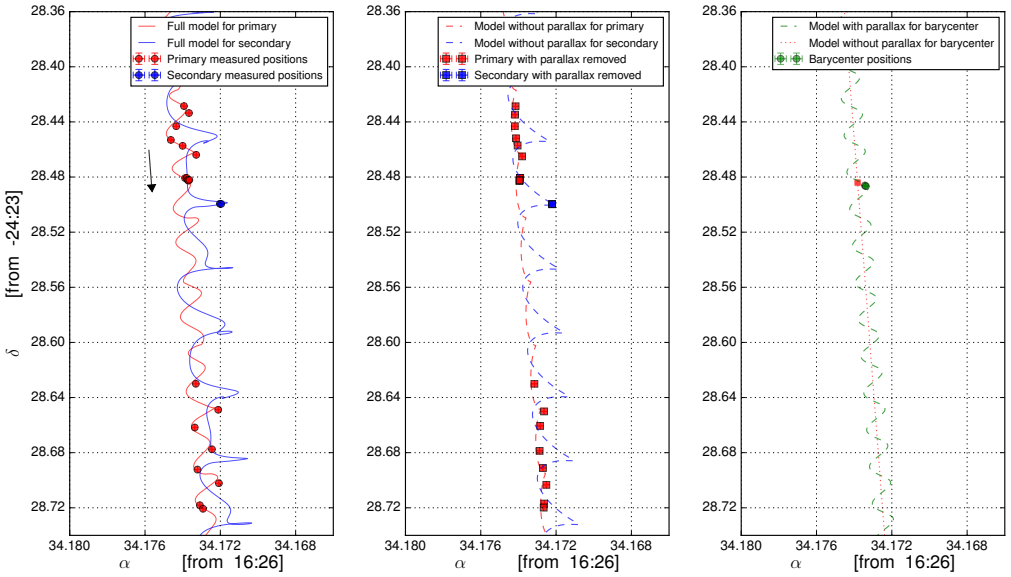

Figure 11. Same as Figure 4, but for S1.

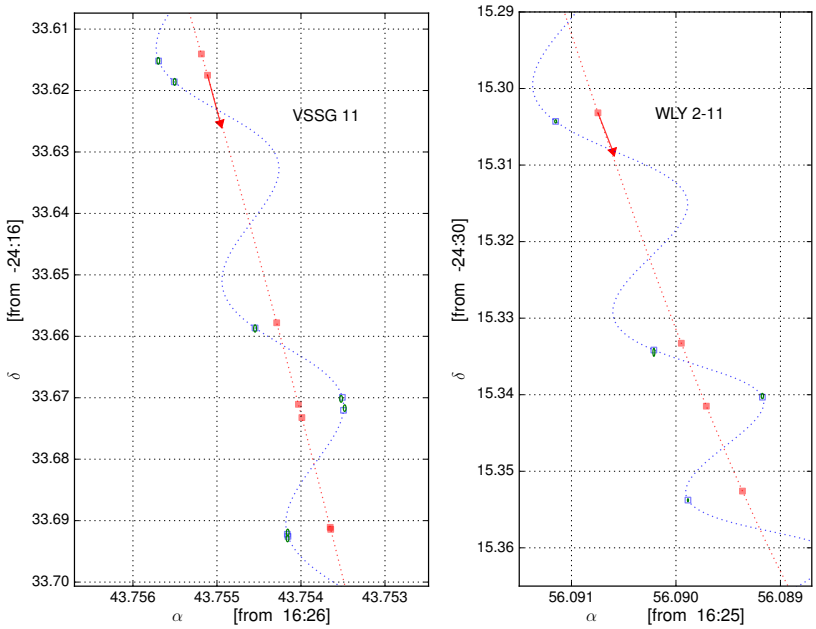

Figure 12. Same as Figure 2, but for VSSG 11 and WLY 2-11.

duces unreliable results. We will wait until we have more detections for the derivation of the astrometric parameters of this star.

5. THE DISTANCE TO OPHIUCHUS

In this paper, we report on 16 independent trigonometric parallax measurements. These results are listed in Table 4 and summarized graphically in Figure 14. They largely surpass all previously published distance measurements for Ophiuchus.

Out of these 16 measurements, 12 are for YSOs in the Ophiuchus core (Lynds 1688). The parallaxes for these 12 sources are highly consistent (Figure 14), and yield a weighted mean value $\varpi = 7.28$ mas, with a weighted standard deviation $\sigma_{\varpi} = 0.06$ mas. In terms of distance, this corresponds to $d = 137.3$ pc, with a standard devi-

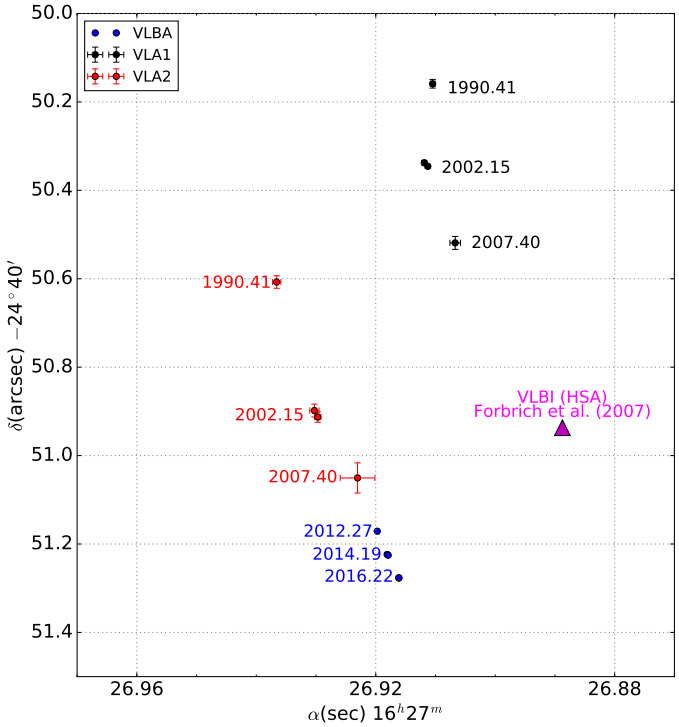

Figure 13. Observed positions of the components of YLW 15. Red and black circles mark positions measured with the VLA at the indicated epochs. The blue circles show the positions obtained from our VLBA observations. The triangle marks the position reported by Forbrich et al. (2007) from HSA observations.

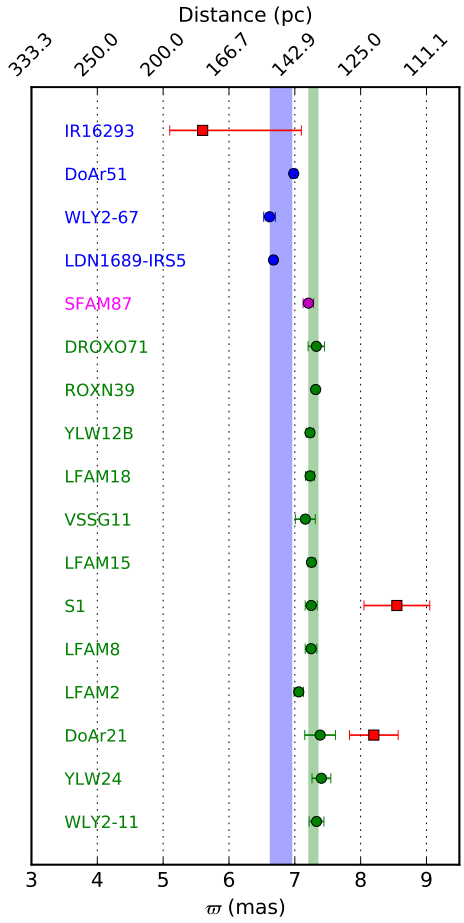

Figure 14. Summary of the parallax measurements reported here. Green circles and characters are for sources in the core (Lynds 1688), while blue circles and characters are for sources in the eastern streamer (Lynds 1689). SFAM 87 is shown with a different color because it lies neither within the core nor within the boundaries of Lynds 1689. The red squares are for previously published parallaxes (Loinard et al. 2008; Imai et al. 2007). The green vertical bar shows the mean parallax value for sources in the core, and its standard deviation (see text).

ation $\sigma_d = 1.2$ pc. In principle, the standard deviation around the mean value could reflect both the uncertainties in our distance measurements, and the true depth of the complex. Since our uncertainties on individual parallax measurements are typically larger than 0.06 mas, we argue that the measured weighted standard deviation is completely dominated by the uncertainties on individual parallaxes rather than by the true depth of the core. We will, therefore, adopt this value as our final uncertainty on the distance to the core. We note that Lynds 1688 is about 0.75 degree across (Figure 15), corresponding to 1.8 pc. Thus, our results indicate that it is not significantly more elongated along the line of sight than on the plane of the sky.

We currently can only provide limited information on the location of the streamers relative to the core, since we only have measured parallaxes in the eastern streamer (Lynds 1689), and have just three independent measurements there (the parallaxes of LDN1689 IRS5, WLY 2-67, and DoAr51). The weighted mean value of these three measurements is $\varpi = 6.79 \pm 0.16$ mas, corresponding to $d = 147.3 \pm 3.4$ pc. This suggests that the eastern streamer is about 10 pc farther than the core, although more parallax measurements of sources in Lynds 1689 would be required to confirm this. Interestingly, Imai et al. (2007) have measured the parallax of water masers in the protostar IRAS 16293–2422, located in the northern part of Lynds 1689, and found a value $\varpi = 6.5^{+1.5}_{-0.5}$ mas, which is consistent within 1 sigma with our parallax estimate for Lynds 1689 (Figure 14). Notice that we have not considered SFAM 87 in the previous analysis. It certainly lies somewhat outside of Lynds 1688 (Figure 15), and was considered as belonging to the Lynds 1689 "fringe" by McClure et al. (2010). These latter authors, however, do not explain how they arrived to such a conclusion, and we note that SFAM 87 does not formally lie within the boundaries of Lynds 1689. We find that its parallax is more consistent with the mean weighted parallax of the Ophiuchus core, suggesting that it is not part of Lynds 1689. This will be

confirmed also when the distance to stars in the central parts of this cloud become available.

The typical distance to Ophiuchus that is generally used in the pre-main sequence literature is 125–130 pc. Our new distance is about 12% larger, which translates to a luminosity increase of $\sim 25\%$, and makes young stellar objects slightly younger with respect to evolutionary tracks.

Finally, we should mention that the stellar population of Ophiuchus could be contaminated by stars from the Upper Sco association, which is located at a similar distance (∼140 pc; de Zeeuw et al. 1999) and overlaps the Ophiuchus region on the sky. The YSOs in Ophiuchus show extinctions in the range $3 \leq A_V \leq 26$ mag (Table 2), whereas the associated members of Upper Sco typically have $A_V \lesssim 2$ mag (Walter et al. 1994). The fact that our detected YSOs have larger extinctions than Upper Sco ensures that these objects are part of the Ophiuchus Complex.

5.1. *Proper Motions*

Figure 15 shows the distribution of the 16 individual sources with astrometric parameters measured in this paper. In order to calculate the motion of each source relative to its local environment, we need to remove the contribution of the solar peculiar motion. For this correction, we use the formulation of Abad & Vieira (2005), and the solar motion relative to the LSR derived by Schönrich et al. (2010). They obtained rectangular components of the solar motion $(u_\odot, v_\odot, w_\odot) = (11.1 \pm 0.7, 12.2 \pm 0.47, 7.25 \pm 0.37)$ km s^{-1}, directed towards the Galactic center, the direction of Galactic rotation, and the Galactic north pole, respectively. Corrected proper motions were transformed to tangential velocities (Table 7) and overlaid on Figure 15. It is clear that, with the exception of a few objects that may belong to a different substructure of the complex, all sources share similar motions. The derived one-dimensional velocity dispersion in R.A. and DEC. of sources in Lynds 1688 are 2.8 and 3.0 km s^{-1}, respectively. These are larger than the values found in other studies, which range from ∼1 to 2 km s^{-1} (Makarov 2007; Wilking et al. 2015). However, our sample size is small and our results need to be confirmed with additional proper motions and parallaxes. In addition, we estimate that the associated errors of the velocity dispersions (assumed to be Gaussian distributed) are 1.8 and 2.0 km s^{-1}, in R.A. and DEC., respectively. Thus, within the errors, our results are still consistent with past measurements.

6. SUMMARY

We have presented the first results from GOBELINS toward the region of Ophiuchus. We observed a total of 50 YSOs with the VLBA, and detected 26 of them. Most of our VLBA-detected YSOs are Class II-III, but three Class I sources have also been detected. The YSOs detected here are clearly non-thermal emitters (otherwise they would not be detected with the VLBA), so our observations have revealed the existence of a large population of non-thermal YSOs in Ophiuchus. About 30% of our the VLBA-detected YSOs belong to tight multiple systems with angular separations from 0.6 to 44 AU. While this fraction appears to be consistent with the binarity fraction in Ophiuchus measured in a recent infrared multiplicity survey, we note that most of the binaries detected with the VLBA are very tight systems with separations below 10 AU.

The astrometry of 16 young stellar systems was presented. Absolute positions of single sources were modelled to derive parallaxes and proper motions, and source distances were then obtained with a few percent accuracy. For sources in multiple systems, we use individual positions and, in most cases, angular separations to model jointly orbital and astrometric parameters. For these sources, the distance was measured with $0.3 - 2\%$ accuracy. Because the VLBA delivers absolute positions for each component, we were able to determine the individual masses in 6 of the 8 total multiple systems; masses range from ~ 1 to 7 $M_\odot$.

Twelve sources are associated with the Ophiuchus core (Lynds 1688). They yield a mean distance of 137.3±1.2 pc, and no indication of a detectable depth. Three sources for which the astrometric elements could be measured are located in the eastern streamer (Lynds 1689); the measurements imply a distance of 147.3±3.4 pc for this cloud. This result suggests that the eastern streamer is 10 pc more distant than the core, but this needs to be confirmed when more parallaxes become available.

The measured proper motions of young stars in the core yield one-dimensional velocity dispersions in R.A. and DEC. of 2.8±1.8 and 3.0±2.0 km s^{-1}, respectively. This result may indicate that our sources belong to different substructures of the complex. However, our result may suffer from small-number statistics, and the associated errors are large. Indeed, our values are consistent within 1σ with velocity dispersions of $1 - 2$ km s^{-1}, which have been measured in the past.

Finally, we note that 6 YSOs have been detected only 2 or 3 times with the VLBA in the observations presented here. For these sources, no meaningful astrometric fit could yet be performed, but this will become possible once a few additional detections are obtained in the coming few years. Thus, we anticipate that we will soon be able to increase the number of individual trigonometric parallaxes in Ophiuchus.

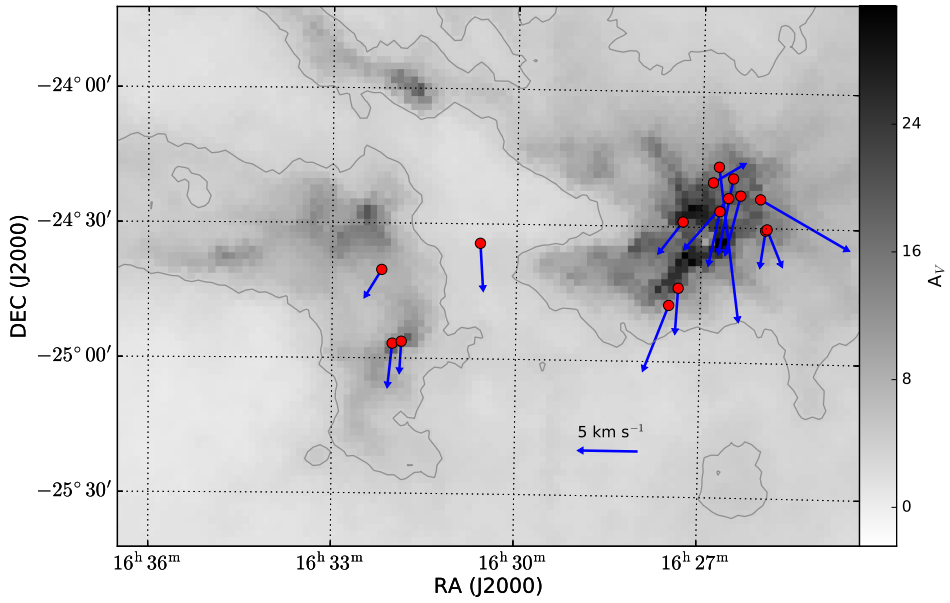

Figure 15. Spatial distribution of YSOs in Ophiuchus with astrometric parameters derived in this work. The grey scale represents the extinction map obtained as part of the COMPLETE project (Ridge et al. 2006), based on 2MASS data (Skrutskie et al. 2006). The grey contour indicates an A_V of 4. The arrows correspond to the tangential velocity corrected by the solar motion.

G.N.O.-L., L.L., L.F.R., R.A.G.-L., G.P., and J.L.R. acknowledge CONACyT, Mexico for financial support through grants 339802, 104497, 153522 and I0017-151671. L.L. and R.A.G.-L. were supported by DGAPA, UNAM grant PAPIIT IG100913. L.L. and G.N.O.-L. also acknowledge support from the von Humboldt Stiftung. N.J.E. was supported by NSF grant AST-1109116 to the University of Texas at Austin. P.A.B.G. acknowledges financial support from FAPESP. The National Radio Astronomy Observatory is operated by Associated Universities, Inc., under cooperative agreement with the National Science Foundation. This work made use of the Swinburne University of Technology software correlator, developed as part of the Australian Major National Research Facilities Programme and operated under licence.

Table 1. Observed epochs

Project code	Observation Date	Observed fields centers R.A. (α_{2000})	Decl. (δ_{2000})	Observed band
BL175B0	13 mar 2012	16 27 55.92	-24 47 24.82	X
BL175B1	25 mar 2012	16 27 30.82	-24 47 27.21	X
BL175B2	09 apr 2012	16 27 24.36	-24 42 13.39	X
BL175B3	21 apr 2012	16 25 49.10	-24 38 31.00	X
BL175B4	24 apr 2012	16 27 15.70	-24 38 45.68	X
BL175B5	29 apr 2012	16 28 04.65	-24 34 56.66	X
BL175B6	01 may 2012	16 25 56.80	-24 30 23.76	X
BL175B7	05 may 2012	16 26 07.63	-24 27 41.73	X
BL175B8	09 may 2012	16 27 32.68	-24 33 24.54	X
BL175B9	11 may 2012	16 27 18.17	-24 28 52.96	X
BL175BA	12 may 2012	16 26 42.44	-24 26 26.12	X
BL175BB	19 aug 2012	16 26 03.01	-24 23 36.42	X
BL175BC	01 sep 2012	16 27 30.83	-24 47 27.14	X
BL175C0	03 sep 2012	16 36 17.50	-24 25 55.44	X
BL175BD	09 sep 2012	16 26 29.67	-24 19 05.85	X
BL175BE	20 oct 2012	16 25 49.10	-24 38 31.00	X
BL175BF	30 oct 2012	16 27 15.70	-24 38 45.71	X
BL175BG	01 nov 2012	16 26 51.70	-24 14 41.50	X
BL175BH	26 nov 2012	16 25 56.80	-24 30 23.76	X
BL175BI	28 nov 2012	16 26 07.63	-24 27 41.73	X
BL175BJ	30 nov 2012	16 27 32.68	-24 33 24.54	X
BL175BK	07 dec 2012	16 27 18.17	-24 28 52.96	X
BL175BL	08 dec 2012	16 26 42.44	-24 26 26.12	X
BL175BM	09 dec 2012	16 26 03.01	-24 23 36.42	X
BL175BN	16 dec 2012	16 26 26.01	-24 23 41.26	X
BL175BO	21 dec 2012	16 26 29.67	-24 19 05.85	X
BL175BP	28 dec 2012	16 27 05.16	-24 20 07.82	X
BL175ZQ	25 jan 2013	16 26 49.23	-24 20 03.35	X
BL175BR	01 feb 2013	16 26 51.70	-24 14 41.50	X
BL175BS	27 apr 2013	16 31 57.16	-24 56 43.77	X
BL175A9	01 may 2013	16 27 55.92	-24 47 24.82	X
BL175BT	21 may 2013	16 31 38.57	-25 32 20.08	X
BL175BU	29 may 2013	16 31 17.60	-24 32 02.46	X
BL175BV	06 jun 2013	16 32 11.80	-24 40 21.89	X
BL175BW	15 jun 2013	16 32 45.24	-24 36 47.42	X
BL175BX	23 jun 2013	16 30 32.21	-24 33 17.86	X
BL175AA	28 jun 2013	16 27 30.82	-24 47 27.21	X
BL175BY	16 jul 2013	16 34 21.10	-23 56 25.19	X
BL175BZ	07 aug 2013	16 31 40.68	-24 15 16.49	X
BL175E0	01 sep 2013	16 27 30.82	-24 47 27.21	C
		16 26 16.31	-24 22 14.00	
BL175E1	02 sep 2013	16 27 18.18	-24 28 52.99	C
		16 26 42.44	-24 26 26.27	
BL175E2	03 sep 2013	16 32 11.79	-24 40 21.92	C
		16 36 17.50	-24 25 55.41	
BL175E3	05 sep 2013	16 31 38.58	-25 32 20.08	C
		16 32 45.24	-24 36 47.33	

Table 1 continued

Table 1 *(continued)*

Project code	Observation Date	Observed fields centers R.A. (α_{2000})	Decl. (δ_{2000})	Observed band
BL175E4	07 sep 2013	16 27 32.68	-24 33 24.54	X
BL175E5	19 sep 2013	16 27 20.03	-24 40 29.53	C
		16 27 22.96	-24 22 36.60	
BL175E7	24 sep 2013	16 30 32.21	-24 33 17.86	C
		16 31 17.60	-24 32 02.46	
BL175G0	01 mar 2014	16 27 30.82	-24 47 27.21	C
		16 26 16.31	-24 22 14.00	
BL175G1	03 mar 2014	16 27 18.18	-24 28 52.99	C
		16 26 42.44	-24 26 26.27	
BL175G2	04 mar 2014	16 32 11.79	-24 40 21.92	C
		16 36 17.50	-24 25 55.41	
BL175GB	05 mar 2014	16 26 47.73	-24 15 37.45	C
BL175G3	06 mar 2014	16 31 38.58	-25 32 20.08	C
		16 32 45.24	-24 36 47.33	
BL175G4	09 mar 2014	16 27 32.68	-24 33 24.54	X
BL175G5	10 mar 2014	16 27 20.03	-24 40 29.53	C
		16 27 22.96	-24 22 36.60	
BL175G6	13 mar 2014	16 27 55.92	-24 47 24.82	C
		16 28 04.65	-24 34 56.66	
BL175G7	14 mar 2014	16 30 32.21	-24 33 17.86	C
		16 31 17.60	-24 32 02.46	
BL175G8	24 mar 2014	16 31 40.68	-24 15 16.49	C
		16 31 57.16	-24 56 43.77	
BL175G9	25 mar 2014	16 34 21.10	-23 56 25.19	C
		16 25 49.10	-24 38 31.00	
BL175GA	08 apr 2014	16 26 02.22	-24 29 02.76	C
		16 26 57.20	-24 20 05.59	
BL175GC	01 apr 2014	16 27 19.49	-24 41 40.74	C
BL175GR	05 jun 2014	16 26 42.44	-24 26 26.27	C
		16 27 18.18	-24 28 52.99	
BL175DY	29 aug 2014	16 27 20.03	-24 40 29.53	C
		16 27 22.96	-24 22 36.6	
BL175CR	07 oct 2014	16 27 30.82	-24 47 27.21	C
		16 26 16.31	-24 22 14.00	
BL175CS	12 oct 2014	16 27 18.18	-24 28 52.99	C
		16 26 42.44	-24 26 26.27	
BL175CT	15 oct 2014	16 32 11.79	-24 40 21.92	C
		16 36 17.50	-24 25 55.41	
BL175EX	27 feb 2015	16 27 30.82	-24 47 27.21	C
		16 26 16.31	-24 22 14.00	
BL175EY	02 mar 2015	16 27 18.18	-24 28 52.99	C
		16 26 42.438	-24 26 26.27	
BL175EZ	20 mar 2015	16 32 11.79	-24 40 21.92	C
		16 36 17.50	-24 25 55.41	
BL175F3	15 mar 2015	16 27 20.03	-24 40 29.53	C
		16 27 22.96	-24 22 36.60	
BL175F7	29 apr 2015	16 26 02.22	-24 29 02.76	C
		16 26 57.20	-24 20 05.59	
BL175FY	30 aug 2015	16 26 02.22	-24 29 02.76	C

Table 1 continued

Table 1 *(continued)*

Project code	Observation Date	Observed fields centers R.A. (α_{2000})	Decl. (δ_{2000})	Observed band
		16 26 57.20	-24 20 05.59	
BL175FZ	03 sep 2015	16 27 05.16	-24 20 07.80	C
		16 27 20.03	-24 40 29.53	
BL175GS	04 sep 2015	16 30 35.64	-24 34 19.00	C
		16 31 20.19	-24 30 01.06	
BL175GT	15 sep 2015	16 27 19.49	-24 41 40.74	X
BL175GU	19 sep 2015	16 26 47.73	-24 15 37.45	C
		16 31 57.16	-24 56 43.77	
BL175GW	04 oct 2015	16 26 29.67	-24 19 05.85	C
		16 27 21.82	-24 43 35.99	
BL175GX	06 oct 2015	16 26 42.44	-24 26 26.27	C
		16 27 18.18	-24 28 52.99	
BL175GV	11 oct 2015	16 28 04.65	-24 34 56.66	C
BL175GY	13 oct 2015	16 31 38.58	-25 32 20.08	C
		16 32 11.79	-24 40 21.92	
BL175CU	29 feb 2016	16 28 04.65	-24 34 56.66	C
		16 32 11.793	-24 40 21.92	
BL175F0	01 mar 2016	16 26 43.76	-24 16 33.40	C
		16 31 57.16	-24 56 43.77	
BL175F1	04 mar 2016	16 25 57.512	-24 30 32.11	C
		16 26 49.215	-24 20 03.06	
BL175F2	17 mar 2016	16 27 05.16	-24 20 07.80	C
		16 27 30.00	-24 38 20.00	
BL175F4	20 mar 2016	16 27 19.493	-24 41 40.74	X
BL175F5	26 mar 2016	16 26 25.620	-24 24 29.21	C
		16 27 21.82	-24 43 35.99	
BL175F6	30 mar 2016	16 30 35.64	-24 34 19.00	C
		16 31 20.19	-24 30 01.06	
BL175F8	28 apr 2016	16 26 42.44	-24 26 26.27	C
		16 27 18.18	-24 28 52.99	

Table 2. Detected YSOs

GBS-VLA name[1] (1)	Other identifier (2)	Minimum flux at 5 GHz (mJy) (3)	Maximum flux at 5 GHz (mJy) (4)	Minimum flux at 8 GHz (mJy) (5)	Maximum flux at 8 GHz (mJy) (6)	log [T_b (K)] (7)	SED Class (8)	Num. of detc./obs. (9)	A_V (10)
J162556.09-243015.3	WLY2-11a	0.13±0.05	0.27±0.06	–		>7.0	Class III	4/5	13
J162556.09-243015.3	WLY2-11b	0.86±0.05		0.60±0.09		7.9		2/5	
J162557.51-243032.1	YLW24	0.21±0.05	1.35±0.06	0.25±0.06		8.0	Class III	4/5	13
J162603.01-242336.4	DOAR21	1.98±0.11	14.97±0.14	4.13±0.07	5.66±0.07	9.2	Class III	7/7	12
J162616.84-242223.5	LFAMP1	0.15±0.06	0.47±0.04	–		6.8	Class II	2/6	20
J162622.38-242253.3	LFAM2	0.30±0.05	0.38±0.07	<0.09		>6.7	Class II	3/7	20
J162625.62-242429.2	LFAM4	0.66±0.12		<0.12		>6.9	Class I	1/14	17
J162629.67-241905.8	LFAM8	0.37±0.06	1.18±0.13	0.26±0.07	0.30±0.05	7.3	Class III	7/9	19
J162634.17-242328.4	S1[2]	5.56±0.15	7.58±0.07	3.27±0.14		9.2	Class III	8/8	18
J162642.44-242626.1	LFAM15a	0.28±0.05	0.93±0.06	0.25±0.06	1.50±0.06	7.8	Class III	10/10	18
J162642.44-242626.1	LFAM15b	0.15±0.05	0.35±0.07	0.18±0.05	1.13±0.05	6.8		7/10	
J162643.76-241633.4	VSGG11a	0.95±0.04	1.53±0.20	–		8.9	Class III	7/7	14
J162643.76-241633.4	VSGG11b	0.58±0.06	0.82±0.05	–		7.7		3/7	
J162649.23-242003.3	LFAM18	0.12±0.03	1.23±0.07	<0.09		7.6	Class III	5/9	18
J162651.69-241441.5	VSSG10	0.53±0.07		<0.06		7.1	–	1/5	12
J162705.16-242007.8	VSSG21	3.69±0.07		<0.09		8.4	Class III	1/11	19
J162718.17-242852.9	YLW12Ba	0.70±0.06	1.49±0.05	0.84±0.05	4.10±0.08	8.7	Class III	9/9	26
J162718.17-242852.9	YLW12Bb	0.42±0.06	9.89±0.11	1.19±0.08	1.33±0.05	8.9		9/9	
J162718.17-242852.9	YLW12Bc	0.45±0.06	1.16±0.09	0.17±0.04	0.74±0.08	7.8		7/9	
J162719.50-244140.3	YLW13A	0.35±0.05		0.31±0.08	0.71±0.07	7.0	Class III	3/11	22
J162721.81-244335.9	ROXN39a	0.22±0.07	1.44±0.07	0.24±0.06	0.44±0.08	7.9	Class III	7/15	20
J162721.81-244335.9	ROXN39b	0.22±0.05	0.81±0.06	0.57±0.09		7.6		5/15	
J162724.19-242929.8	GY257	0.97±0.06		<0.09		>7.0	Class III	1/8	13
J162726.90-244050.8	YLW15	0.18±0.04	0.25±0.08	0.23±0.08	0.33±0.06	7.1	Class I	5/11	25
J162730.82-244727.2	DROXO71	0.30±0.05	0.91±0.05	0.60±0.07	1.15±0.09	8.0	Class III	8/9	8
J162804.65-243456.6	ROXN78	0.38±0.04		<0.12		>6.6	Class II	1/4	20
J163035.63-243418.9	SFAM87a	0.48±0.05	2.64±0.09	–		8.1	CTTS	4/4	3
J163035.63-243418.9	SFAM87b	0.28±0.06	1.35±0.06	–		7.8		3/4	
J163115.01-243243.9	ROX42B	0.21±0.06	0.38±0.08	<0.12		7.0	WTTS	2/5	3
J163120.18-243001.0	ROX43B	0.20±0.05	1.20±0.08	<0.12		>7.1	WTTS	3/5	3
J163152.10-245615.7	LDN1689IRS5	0.23±0.05	3.17±0.08	0.64±0.07		8.3	FS	4/4	18
J163200.97-245643.3	WLY2-67	0.18±0.05	0.41±0.07	–		>6.6	Class I	3/3	14
J163211.79-244021.8	DOAR51a	0.40±0.07	3.14±0.06	0.69±0.08		8.5	WTTS/Class II	7/7	8
J163211.79-244021.8	DOAR51b	0.24±0.06	0.68±0.07	0.47±0.08		7.6		7/7	

NOTE—Reported sources have flux densities above 6σ and 5σ in the cases of one or several detections, respectively. Non-detections are indicated by giving an upper flux density limit of 3σ.

[1] GBS-VLA stands for the Gould's Belt Very Large Array Survey (Dzib et al. 2013).

[2] This star is resolved into a double source in past VLBA observations.

Table 3. Measured source positions

Julian Day	α (J2000.0)	σ_α	δ (J2000.0)	σ_δ
		DROXO71		
2456011.96538	16 27 30.83414340	0.00000470	-24 47 27.142107	0.000161
2456172.52613	16 27 30.83298666	0.00000234	-24 47 27.153542	0.000071
2456471.70936	16 27 30.83302924	0.00000177	-24 47 27.178102	0.000063
2456537.53271	16 27 30.83267868	0.00000191	-24 47 27.182477	0.000065
2456718.03765	16 27 30.83359624	0.00000260	-24 47 27.198462	0.000085
2456937.93345	16 27 30.83241321	0.00000472	-24 47 27.212846	0.000216
2457081.04343	16 27 30.83323569	0.00000437	-24 47 27.227091	0.000170
2457473.99603	16 27 30.83275199	0.00000469	-24 47 27.256316	0.000188
		YLW13A		
2456026.92477	16 27 19.49265640	0.00000349	-24 41 40.735293	0.000105
2457097.02778	16 27 19.50365400	0.00001071	-24 41 40.786841	0.000421
2457281.47003	16 27 19.49036366	0.00000974	-24 41 40.828186	0.000183
		ROXN39		
First source:				
2456026.92477	16 27 21.81663353	0.00000626	-24 43 35.989095	0.000146
2456748.92808	16 27 21.81566119	0.00000699	-24 43 36.052317	0.000246
2457269.55653	16 27 21.81365382	0.00000174	-24 43 36.095543	0.000068
2457281.47003	16 27 21.81365131	0.00000380	-24 43 36.096674	0.000110
2457300.44295	16 27 21.81366628	0.00001385	-24 43 36.098921	0.000329
2457467.95944	16 27 21.81426003	0.00000653	-24 43 36.115527	0.000252
2457473.99603	16 27 21.81422633	0.00000534	-24 43 36.115494	0.000195
Second source:				
2456748.92808	16 27 21.81377141	0.00000373	-24 43 36.049837	0.000135
2456899.06892	16 27 21.81269783	0.00000865	-24 43 36.052231	0.000272
2456937.93345	16 27 21.81279168	0.00001167	-24 43 36.054796	0.000340
2457467.95944	16 27 21.81361924	0.00000366	-24 43 36.075851	0.000106
2457473.99603	16 27 21.81361906	0.00000654	-24 43 36.075317	0.000348
		YLW15		
2456026.92477	16 27 26.91975530	0.00000512	-24 40 51.171077	0.000169
2456727.04112	16 27 26.91809446	0.00000928	-24 40 51.223581	0.000233
2456748.92808	16 27 26.91792129	0.00001583	-24 40 51.225402	0.000707
2457465.02060	16 27 26.91614817	0.00000759	-24 40 51.276500	0.000342
2457467.95944	16 27 26.91612508	0.00000712	-24 40 51.276834	0.000241
		GBS-VLA J162547.68−243735.7		
2456038.89200	16 25 47.68461899	0.00000324	-24 37 35.718454	0.000151
2456221.39490	16 25 47.68461690	0.00000795	-24 37 35.718318	0.000258
2456742.00017	16 25 47.68465538	0.00000741	-24 37 35.718683	0.000312

Table 3 continued

Table 3 *(continued)*

Julian Day	α (J2000.0)	σ_α	δ (J2000.0)	σ_δ
		ROXN78		
2456730.03293	16 28 04.64323318	0.00000338	-24 34 56.574659	0.000153
		YLW12B		
First source:				
2453529.77467	16 27 18.17199790	0.00000343	-24 28 52.790647	0.000136
2453887.79448	16 27 18.17278283	0.00000290	-24 28 52.816450	0.000123
2456058.83738	16 27 18.17634770	0.00000188	-24 28 52.966427	0.000074
2456269.26236	16 27 18.17718912	0.00000086	-24 28 52.988798	0.000037
2456538.52830	16 27 18.17625293	0.00000233	-24 28 53.000965	0.000096
2456720.03219	16 27 18.17804747	0.00000520	-24 28 53.020088	0.000168
2456813.77622	16 27 18.17770160	0.00000143	-24 28 53.029251	0.000049
2456943.42054	16 27 18.17733336	0.00000136	-24 28 53.037170	0.000051
2457084.03523	16 27 18.17785280	0.00000290	-24 28 53.041694	0.000105
2457302.43748	16 27 18.17777858	0.00000244	-24 28 53.063201	0.000093
2457506.87788	16 27 18.17832802	0.00000112	-24 28 53.079027	0.000040
Second source:				
2453529.77467	16 27 18.17173883	0.00000540	-24 28 52.791325	0.000204
2453887.79448	16 27 18.17266976	0.00000411	-24 28 52.810830	0.000122
2456058.83738	16 27 18.17665980	0.00000125	-24 28 52.971988	0.000050
2456269.26236	16 27 18.17625269	0.00000295	-24 28 52.979221	0.000124
2456538.52830	16 27 18.17657726	0.00000150	-24 28 53.003249	0.000053
2456720.03219	16 27 18.17732771	0.00000412	-24 28 53.015451	0.000142
2456813.77622	16 27 18.17673865	0.00000274	-24 28 53.018125	0.000099
2456943.42054	16 27 18.17671228	0.00000435	-24 28 53.026377	0.000135
2457084.03523	16 27 18.17822254	0.00000035	-24 28 53.046405	0.000013
2457302.43748	16 27 18.17686941	0.00000315	-24 28 53.053913	0.000128
2457506.87788	16 27 18.17801911	0.00000161	-24 28 53.071326	0.000059
Third source:				
2453529.77467	16 27 18.16380766	0.00000229	-24 28 52.878764	0.000071
2453818.98287	16 27 18.16367158	0.00000473	-24 28 52.899861	0.000168
2456058.83738	16 27 18.15802440	0.00000540	-24 28 53.043846	0.000282
2456269.26236	16 27 18.15742392	0.00000451	-24 28 53.055984	0.000204
2456538.52830	16 27 18.15629959	0.00000497	-24 28 53.072046	0.000126
2456813.77622	16 27 18.15608788	0.00000692	-24 28 53.090076	0.000206
2457084.03523	16 27 18.15614139	0.00000292	-24 28 53.109045	0.000096
2457302.43748	16 27 18.15467809	0.00000502	-24 28 53.120030	0.000143
2457506.87788	16 27 18.15498736	0.00000543	-24 28 53.134508	0.000170
		GY257		
2457506.87788	16 27 24.19599570	0.00000199	-24 29 29.992344	0.000075
		LFAM15		
First source:				
2453617.53443	16 26 42.44072639	0.00000589	-24 26 26.085858	0.000142
2453714.26955	16 26 42.44106573	0.00000587	-24 26 26.090142	0.000259
2453796.04568	16 26 42.44134043	0.00000399	-24 26 26.096076	0.000106

Table 3 continued

Table 3 *(continued)*

Julian Day	α (J2000.0)	σ_α	δ (J2000.0)	σ_δ
2456059.83431	16 26 42.43834146	0.00000119	-24 26 26.270103	0.000040
2456270.25963	16 26 42.43790745	0.00000641	-24 26 26.280485	0.000161
2456538.52830	16 26 42.43667908	0.00000321	-24 26 26.294376	0.000107
2456720.03219	16 26 42.43733099	0.00000340	-24 26 26.312356	0.000119
2456813.77622	16 26 42.43676227	0.00000259	-24 26 26.323559	0.000087
2456943.42054	16 26 42.43645660	0.00000488	-24 26 26.335835	0.000178
2457084.03523	16 26 42.43733727	0.00000560	-24 26 26.348959	0.000259
2457302.43748	16 26 42.43619859	0.00000350	-24 26 26.361949	0.000215
2457473.99603	16 26 42.43681431	0.00000819	-24 26 26.372860	0.000381
2457506.87788	16 26 42.43657742	0.00000354	-24 26 26.374173	0.000146
Second source:				
2456059.83431	16 26 42.43746443	0.00000139	-24 26 26.259340	0.000047
2456270.25963	16 26 42.43721529	0.00000590	-24 26 26.278386	0.000163
2456720.03219	16 26 42.43759083	0.00001060	-24 26 26.317776	0.000382
2456813.77622	16 26 42.43677820	0.00000775	-24 26 26.316132	0.000259
2456943.42054	16 26 42.43601697	0.00000783	-24 26 26.320697	0.000297
2457302.43748	16 26 42.43531577	0.00001382	-24 26 26.348716	0.000510
2457506.87788	16 26 42.43578894	0.00001213	-24 26 26.368869	0.000282
		DOAR21		
2453621.52350	16 26 03.01891197	0.00000724	-24 23 36.343197	0.000148
2453691.33229	16 26 03.01889886	0.00000304	-24 23 36.349153	0.000063
2453744.18763	16 26 03.01910860	0.00000745	-24 23 36.355709	0.000207
2453755.15740	16 26 03.01918629	0.00000284	-24 23 36.355807	0.000115
2453822.97193	16 26 03.01896398	0.00000511	-24 23 36.361907	0.000138
2453890.78627	16 26 03.01818785	0.00000166	-24 23 36.364290	0.000075
2453971.56511	16 26 03.01698794	0.00000267	-24 23 36.369931	0.000114
2454092.23452	16 26 03.01768929	0.00000161	-24 23 36.380009	0.000052
2454321.60671	16 26 03.01610693	0.00000490	-24 23 36.395975	0.000109
2454331.07942	16 26 03.01612164	0.00000175	-24 23 36.395067	0.000052
2454353.51917	16 26 03.01600351	0.00000262	-24 23 36.398021	0.000057
2454365.48657	16 26 03.01588946	0.00000202	-24 23 36.398070	0.000067
2456158.56345	16 26 03.00879650	0.00000023	-24 23 36.532098	0.000008
2456271.25813	16 26 03.00899222	0.00000045	-24 23 36.541056	0.000014
2456537.53271	16 26 03.00730547	0.00000110	-24 23 36.559579	0.000037
2456718.03765	16 26 03.00766323	0.00000030	-24 23 36.575357	0.000010
2456937.93345	16 26 03.00579982	0.00000097	-24 23 36.589569	0.000036
2457081.04343	16 26 03.00621579	0.00000166	-24 23 36.602285	0.000058
2457300.44295	16 26 03.00441795	0.00000725	-24 23 36.615740	0.000215
		LFAM8		
2456180.50470	16 26 29.67379969	0.00000658	-24 19 05.899181	0.000225
2456283.22537	16 26 29.67437563	0.00000298	-24 19 05.908297	0.000094
2456537.53271	16 26 29.67335645	0.00000458	-24 19 05.927633	0.000138
2457081.04343	16 26 29.67375046	0.00000292	-24 19 05.974041	0.000131
2457300.44295	16 26 29.67253899	0.00000614	-24 19 05.990153	0.000254
2457449.06429	16 26 29.67333716	0.00000274	-24 19 06.003299	0.000093
2457452.05609	16 26 29.67333731	0.00000416	-24 19 06.004169	0.000133

Table 3 continued

Table 3 *(continued)*

Julian Day	α (J2000.0)	σ_α	δ (J2000.0)	σ_δ
		VSSG10		
2457449.06429	16 26 51.69086628	0.00000458	-24 14 41.978736	0.000196
		YLW24		
2456258.29307	16 25 57.51212530	0.00000469	-24 30 32.114725	0.000187
2456755.96194	16 25 57.51177560	0.00000627	-24 30 32.152014	0.000205
2457141.90491	16 25 57.51110685	0.00000164	-24 30 32.177539	0.000068
2457452.05609	16 25 57.51095598	0.00000448	-24 30 32.199319	0.000150
		WLY2-11		
First source:				
2456755.96194	16 25 56.09115161	0.00000906	-24 30 15.304290	0.000213
2457141.90491	16 25 56.09021133	0.00000936	-24 30 15.334454	0.000522
2457265.56761	16 25 56.08917305	0.00001081	-24 30 15.340167	0.000341
2457452.05609	16 25 56.08988393	0.00000486	-24 30 15.353840	0.000178
Second source:				
2456258.29307	16 25 56.09091678	0.00000596	-24 30 15.259179	0.000122
2457452.05609	16 25 56.09085688	0.00000182	-24 30 15.339724	0.000071
		S1		
First source:				
2453545.73099	16 26 34.17395362	0.00000172	-24 23 28.427300	0.000057
2453628.50402	16 26 34.17368732	0.00000218	-24 23 28.432353	0.000096
2453722.24761	16 26 34.17436628	0.00000096	-24 23 28.441953	0.000041
2453810.00745	16 26 34.17465184	0.00000263	-24 23 28.451876	0.000080
2453889.78900	16 26 34.17402527	0.00000117	-24 23 28.456156	0.000046
2453969.57055	16 26 34.17330377	0.00000147	-24 23 28.462699	0.000057
2454256.78420	16 26 34.17389517	0.00000046	-24 23 28.479576	0.000016
2454260.77321	16 26 34.17405536	0.00000056	-24 23 28.476906	0.000019
2454264.76220	16 26 34.17381615	0.00000041	-24 23 28.479414	0.000014
2454268.75117	16 26 34.17387600	0.00000102	-24 23 28.479414	0.000027
2454272.74050	16 26 34.17376304	0.00000050	-24 23 28.480753	0.000018
2454276.72950	16 26 34.17380110	0.00000045	-24 23 28.482369	0.000013
2454280.71866	16 26 34.17371870	0.00000069	-24 23 28.481435	0.000025
2454284.70775	16 26 34.17367060	0.00000047	-24 23 28.480848	0.000015
2456278.23902	16 26 34.17330156	0.00000072	-24 23 28.630001	0.000022
2456537.53271	16 26 34.17211016	0.00000072	-24 23 28.648873	0.000024
2456718.03765	16 26 34.17335985	0.00000064	-24 23 28.661727	0.000022
2456937.93345	16 26 34.17244477	0.00000091	-24 23 28.677542	0.000031
2457081.04343	16 26 34.17321517	0.00000070	-24 23 28.692245	0.000023
2457300.44295	16 26 34.17207637	0.00000093	-24 23 28.702186	0.000032
2457473.99603	16 26 34.17308895	0.00000032	-24 23 28.718119	0.000012
2457506.87788	16 26 34.17292128	0.00000050	-24 23 28.720701	0.000016
Second source:				
2453889.78900	16 26 34.17355935	0.00000304	-24 23 28.458375	0.000076
2454272.74050	16 26 34.17202332	0.00000178	-24 23 28.499403	0.000067

Table 3 continued

Table 3 *(continued)*

Julian Day	α (J2000.0)	σ_α	δ (J2000.0)	σ_δ
2454276.72950	16 26 34.17205479	0.00000249	-24 23 28.500747	0.000087
2454280.71866	16 26 34.17195583	0.00000592	-24 23 28.499485	0.000245
	LFAM4			
2456538.52830	16 26 25.62311834	0.00000460	-24 24 29.340081	0.000167
	LFAM2			
2457081.04343	16 26 22.39009598	0.00000517	-24 22 53.396808	0.000267
2457300.44295	16 26 22.38891477	0.00000858	-24 22 53.410054	0.000331
2457473.99603	16 26 22.38959724	0.00000460	-24 22 53.425842	0.000181
	VSSG21			
2456755.96194	16 27 05.16439110	0.00000056	-24 20 08.102812	0.000024
	GBS-VLA J163151.93−245617.4			
2456409.87863	16 31 51.92835399	0.00000519	-24 56 17.490313	0.000168
2456741.00290	16 31 51.92788684	0.00001420	-24 56 17.512182	0.000360
2457449.06429	16 31 51.92686645	0.00000519	-24 56 17.565067	0.000192
	GBS-VLA J163202.39−245710.0			
2456409.87863	16 32 02.39822000	0.00000432	-24 57 10.343815	0.000154
2456741.00290	16 32 02.39823221	0.00002166	-24 57 10.344630	0.000553
	LDN1689IRS5			
2456409.87863	16 31 52.11386300	0.00000351	-24 56 16.009652	0.000093
2456741.00290	16 31 52.11363279	0.00000864	-24 56 16.030780	0.000269
2457285.48390	16 31 52.11201000	0.00000095	-24 56 16.062292	0.000034
2457449.06429	16 31 52.11274267	0.00000786	-24 56 16.074290	0.000235
	GBS-VLA J163138.57−253220.0			
2456433.81310	16 31 38.57911827	0.00000420	-25 32 20.078468	0.000158
2456541.52018	16 31 38.57910247	0.00001600	-25 32 20.080138	0.000563
2456723.02399	16 31 38.57913786	0.00000345	-25 32 20.076607	0.000137
2457309.41870	16 31 38.57913003	0.00000375	-25 32 20.077101	0.000121
	ROX42B			
2456560.49689	16 31 15.01221991	0.00001035	-24 32 44.039658	0.000379
2457477.98511	16 31 15.01218127	0.00001539	-24 32 44.101781	0.000549
	ROX43B			
2456560.49689	16 31 20.18111995	0.00000200	-24 30 01.018464	0.000076
2456731.03020	16 31 20.18256906	0.00000752	-24 30 01.028170	0.000365
2457477.98511	16 31 20.18076137	0.00001494	-24 30 01.082333	0.000455

Table 3 continued

Table 3 *(continued)*

Julian Day	α (J2000.0)	σ_α	δ (J2000.0)	σ_δ
		DOAR51		
First source:				
2456449.77302	16 32 11.79261358	0.00000197	-24 40 21.924420	0.000089
2456539.52565	16 32 11.79223385	0.00000579	-24 40 21.928946	0.000216
2456721.02946	16 32 11.79332766	0.00000435	-24 40 21.943832	0.000148
2456946.41259	16 32 11.79248077	0.00000489	-24 40 21.958212	0.000215
2457102.07550	16 32 11.79325983	0.00000059	-24 40 21.971486	0.000023
2457309.41870	16 32 11.79227112	0.00000290	-24 40 21.984119	0.000103
2457448.12863	16 32 11.79303712	0.00000227	-24 40 21.997374	0.000079
Second source:				
2456449.77302	16 32 11.79007110	0.00000269	-24 40 21.944770	0.000109
2456539.52565	16 32 11.78935516	0.00001089	-24 40 21.948446	0.000263
2456721.02946	16 32 11.78995501	0.00001231	-24 40 21.961295	0.000497
2456946.41259	16 32 11.78863803	0.00000746	-24 40 21.973309	0.000310
2457102.07550	16 32 11.78921243	0.00000357	-24 40 21.982029	0.000146
2457309.41870	16 32 11.78806957	0.00000361	-24 40 21.990150	0.000124
2457448.12863	16 32 11.78882778	0.00000293	-24 40 21.999831	0.000118
		SFAM200		
2456458.74485	16 32 45.23630782	0.00000791	-24 36 47.331480	0.000179
2456541.52018	16 32 45.23628708	0.00001362	-24 36 47.332569	0.000400
2456723.02399	16 32 45.23630881	0.00000937	-24 36 47.331435	0.000298
		SSTc2d J163027.7−243300		
2456731.03020	16 30 27.69715982	0.00000740	-24 33 00.166706	0.000227
2457270.55380	16 30 27.69716395	0.00000719	-24 33 00.166547	0.000347
		SFAM212		
2456174.52068	16 36 17.50047169	0.00000084	-24 25 55.410771	0.000027
2456539.52565	16 36 17.50048182	0.00000235	-24 25 55.411813	0.000080
2456721.02946	16 36 17.50043917	0.00000329	-24 25 55.411946	0.000108
2456946.41259	16 36 17.50048274	0.00000525	-24 25 55.412111	0.000178
2457102.07550	16 36 17.50047251	0.00000116	-24 25 55.411264	0.000047
		LFAMP1		
2456718.03765	16 26 16.84931422	0.00000236	-24 22 23.537591	0.000088
2456937.93345	16 26 16.84846826	0.00001253	-24 22 23.550740	0.000517
		LFAM13		
2456720.03219	16 26 35.33007904	0.00001742	-24 24 05.378855	0.000554
2456937.93345	16 26 35.33016006	0.00001436	-24 24 05.378401	0.000281
2456943.42054	16 26 35.33013612	0.00000787	-24 24 05.376639	0.000298
2457302.43748	16 26 35.33013402	0.00001301	-24 24 05.377817	0.000371

Table 3 continued

Table 3 *(continued)*

Julian Day	α (J2000.0)	σ_α	δ (J2000.0)	σ_δ
GBS-VLA J162718.25−243334.8				
2457084.03523	16 27 18.23431162	0.00000882	-24 33 34.951660	0.000347
SFAM130				
2456721.02946	16 32 10.77123123	0.00000769	-24 38 27.498627	0.000233
2456946.41259	16 32 10.77132165	0.00001042	-24 38 27.496690	0.000383
2457102.07550	16 32 10.77128863	0.00001343	-24 38 27.497429	0.000317
2457309.41870	16 32 10.77126826	0.00000644	-24 38 27.497571	0.000250
SSTc2d J163211.1−243651				
2456539.52565	16 32 11.08492873	0.00000804	-24 36 50.916471	0.000549
2456721.02946	16 32 11.08495049	0.00000963	-24 36 50.915528	0.000274
2456946.41259	16 32 11.08491744	0.00000818	-24 36 50.917097	0.000224
2457102.07550	16 32 11.08494017	0.00000383	-24 36 50.915872	0.000177
2457309.41870	16 32 11.08495182	0.00000556	-24 36 50.915556	0.000282
GBS-VLA J163212.25−243643.7				
2457102.07550	16 32 12.24716110	0.00000524	-24 36 43.555532	0.000196
2457309.41870	16 32 12.24719840	0.00001393	-24 36 43.555066	0.000612
GBS-VLA J163213.92−244407.8				
2457309.41870	16 32 13.92922573	0.00000974	-24 44 07.782062	0.000186
SSTc2d J163227.4−243951				
2456721.02946	16 32 27.40769338	0.00002030	-24 39 51.454135	0.000725
2457102.07550	16 32 27.40765118	0.00000920	-24 39 51.456859	0.000382
2457309.41870	16 32 27.40762110	0.00001175	-24 39 51.455911	0.000659
SSTc2d J163231.2−244014				
2457102.07550	16 32 31.16848721	0.00000770	-24 40 14.638470	0.000295
2457309.41870	16 32 31.16851261	0.00000859	-24 40 14.639088	0.000376
GBS-VLA J162713.06−241817.0				
2457269.55653	16 27 13.06069106	0.00000787	-24 18 17.090808	0.000338
2457465.02060	16 27 13.06072912	0.00001137	-24 18 17.092477	0.000381
ROC25				
2456555.51075	16 27 29.23368916	0.00000582	-24 17 55.411620	0.000156
2456727.04112	16 27 29.23368444	0.00000273	-24 17 55.411606	0.000073
2456899.06892	16 27 29.23371052	0.00000246	-24 17 55.411246	0.000075
2457097.02778	16 27 29.23368684	0.00000476	-24 17 55.411581	0.000139
2457269.55653	16 27 29.23368353	0.00000548	-24 17 55.411757	0.000137

Table 3 continued

Table 3 *(continued)*

Julian Day	α (J2000.0)	σ_α	δ (J2000.0)	σ_δ
		ROC26		
2456555.51075	16 27 34.55992198	0.00000920	-24 20 20.725049	0.000281
2456727.04112	16 27 34.55990816	0.00000510	-24 20 20.724976	0.000176
2456899.06892	16 27 34.55991988	0.00000299	-24 20 20.725208	0.000104
2457097.02778	16 27 34.55991770	0.00000610	-24 20 20.725197	0.000177
2457269.55653	16 27 34.55988071	0.00000902	-24 20 20.725929	0.000350
		SSTc2d J163032.3−243128		
2456560.49689	16 30 32.26027376	0.00000447	-24 31 28.011713	0.000186
2456731.03020	16 30 32.26025039	0.00000216	-24 31 28.012042	0.000067
2457270.55380	16 30 32.26027063	0.00000352	-24 31 28.012434	0.000131
		ROC49		
2456560.49689	16 31 09.78490899	0.00000944	-24 30 08.324997	0.000282
2456731.03020	16 31 09.78489672	0.00000537	-24 30 08.325067	0.000171
2457270.55380	16 31 09.78491218	0.00000441	-24 30 08.324410	0.000184
		SSTc2d J163033.2−243039		
2456731.03020	16 30 33.25165317	0.00000638	-24 30 38.884059	0.000206
		GBS-VLA J163115.25−243313.8		
2456731.03020	16 31 15.25452244	0.00000545	-24 33 13.781612	0.000281
2457477.98511	16 31 15.25455673	0.00002498	-24 33 13.781713	0.000755
		ROC52		
2456560.49689	16 31 20.13897283	0.00000266	-24 29 28.542211	0.000089
2456731.03020	16 31 20.13896190	0.00000060	-24 29 28.542334	0.000023
2457270.55380	16 31 20.13897246	0.00000075	-24 29 28.541947	0.000026
		SFAM87		
First source:				
2454620.78761	16 30 35.63476219	0.00000484	-24 34 18.958646	0.000167
2454785.33715	16 30 35.63494522	0.00000500	-24 34 18.970301	0.000172
2454877.08587	16 30 35.63580491	0.00000407	-24 34 18.978334	0.000165
2456560.49689	16 30 35.63166911	0.00000102	-24 34 19.064773	0.000040
2456731.03020	16 30 35.63203197	0.00000362	-24 34 19.082480	0.000121
2457270.55380	16 30 35.62974397	0.00000151	-24 34 19.139299	0.000050
2457477.98511	16 30 35.63098169	0.00000835	-24 34 19.163958	0.000267
Second source:				
2454540.00885	16 30 35.63655437	0.00000135	-24 34 18.935779	0.000053
2454620.78761	16 30 35.63568452	0.00000435	-24 34 18.937621	0.000148
2454698.57472	16 30 35.63478278	0.00000464	-24 34 18.939787	0.000147
2454785.33715	16 30 35.63468005	0.00000557	-24 34 18.946096	0.000212
2454877.08587	16 30 35.63485533	0.00000211	-24 34 18.954888	0.000079
2454967.83741	16 30 35.63402510	0.00000481	-24 34 18.962548	0.000165

Table 3 continued

Table 3 *(continued)*

Julian Day	α (J2000.0)	σ_α	δ (J2000.0)	σ_δ
2456731.03020	16 30 35.63287869	0.00000291	-24 34 19.118843	0.000116
2457270.55380	16 30 35.63143895	0.00000147	-24 34 19.133256	0.000054
2457477.98511	16 30 35.63152547	0.00001503	-24 34 19.142294	0.000522
SSTc2d J163130.6−243352				
2456560.49689	16 31 30.62178183	0.00001008	-24 33 51.512104	0.000239
2456731.03020	16 31 30.62181139	0.00000426	-24 33 51.512137	0.000167
2457270.55380	16 31 30.62177163	0.00000812	-24 33 51.511820	0.000319
GBS-VLA J163036.26−243135.3				
2456560.49689	16 30 36.26501151	0.00000629	-24 31 35.400645	0.000275
2456731.03020	16 30 36.26500965	0.00000206	-24 31 35.401147	0.000078
2457270.55380	16 30 36.26502326	0.00000408	-24 31 35.401258	0.000142
VSGG11				
First source:				
2456722.00179	16 26 43.75569790	0.00000130	-24 16 33.615170	0.000060
2456755.96194	16 26 43.75550380	0.00000342	-24 16 33.618593	0.000139
2457141.90491	16 26 43.75454490	0.00000505	-24 16 33.658504	0.000212
2457265.56761	16 26 43.75352207	0.00000313	-24 16 33.670179	0.000132
2457285.48390	16 26 43.75347972	0.00000172	-24 16 33.671690	0.000055
2457449.06429	16 26 43.75415819	0.00000107	-24 16 33.691930	0.000043
2457452.05609	16 26 43.75415976	0.00000210	-24 16 33.692895	0.000076
Second source:				
2457285.48390	16 26 43.75384015	0.00000355	-24 16 33.678776	0.000123
2457449.06429	16 26 43.75459284	0.00000210	-24 16 33.689691	0.000089
2457452.05609	16 26 43.75456000	0.00000788	-24 16 33.689666	0.000349
SSTc2d J163154.5−245217				
2456741.00290	16 31 54.49445738	0.00001834	-24 52 17.136283	0.000774
2457449.06429	16 31 54.49438170	0.00001014	-24 52 17.138334	0.000276
WLY2-67				
2456741.00290	16 32 00.97871474	0.00001192	-24 56 43.413340	0.000456
2457285.48390	16 32 00.97716307	0.00000733	-24 56 43.446632	0.000312
2457449.06429	16 32 00.97790521	0.00001256	-24 56 43.460244	0.000403
LFAM18				
2456722.00179	16 26 49.22836555	0.00000789	-24 20 03.414117	0.000375
2456755.96194	16 26 49.22819914	0.00000199	-24 20 03.416423	0.000071
2457141.90491	16 26 49.22715919	0.00000817	-24 20 03.438613	0.000336
2457265.56761	16 26 49.22608389	0.00000392	-24 20 03.441434	0.000147
2457452.05609	16 26 49.22669248	0.00000861	-24 20 03.449981	0.000452
LFAM17				

Table 3 continued

Table 3 *(continued)*

Julian Day	α (J2000.0)	σ_α	δ (J2000.0)	σ_δ
2456722.00179	16 26 46.36011062	0.00001632	-24 20 02.188965	0.000342
2456755.96194	16 26 46.36010779	0.00001240	-24 20 02.191625	0.000382
2457141.90491	16 26 46.36005985	0.00001738	-24 20 02.191462	0.000423
2457265.56761	16 26 46.35994120	0.00001558	-24 20 02.192545	0.000467
2457452.05609	16 26 46.36005050	0.00001543	-24 20 02.192970	0.000480
GDS J162702.1−241928				
2456755.96194	16 27 02.15242055	0.00001218	-24 19 27.915618	0.000350
2457141.90491	16 27 02.15241390	0.00000876	-24 19 27.915343	0.000447
2457265.56761	16 27 02.15242622	0.00001325	-24 19 27.915196	0.000502
2457452.05609	16 27 02.15240463	0.00000675	-24 19 27.915947	0.000298
SFAM127				
2456741.00290	16 31 59.36475311	0.00000244	-24 56 39.800373	0.000088
2457285.48390	16 31 59.36476531	0.00000360	-24 56 39.800194	0.000124
SSTc2d J162540.9−244147				
2456742.00017	16 25 40.94715532	0.00001533	-24 41 47.337014	0.000538
SFAM12				
2456722.00179	16 26 33.48487742	0.00001057	-24 12 16.100168	0.000479
2457285.48390	16 26 33.48605313	0.00001170	-24 12 16.124239	0.000455

Table 4. Parallaxes and proper motions

GBS-VLA name (1)	Other identifier (2)	Parallax (mas) (3)	$\mu_\alpha \cos\delta$ (mas yr^{-1}) (4)	μ_δ (mas yr^{-1}) (5)	$a_\alpha \cos\delta$ (mas yr^{-2}) (6)	a_δ (mas yr^{-2}) (7)	Distance (pc) (8)
J162556.09-243015.3	WLY2-11	7.330 ± 0.112	-9.78 ± 0.09	-25.11 ± 0.20	0.94 ± 0.38	6.02 ± 0.83	136.4 ± 2.1
J162557.51-243032.1	YLW24	7.404 ± 0.143	-7.26 ± 0.04	-25.29 ± 0.07	–	–	135.1 ± 2.6
J162603.01-242336.4	DoAr21	7.385 ± 0.234	-19.63 ± 0.19	-26.92 ± 0.13	–	–	135.4 ± 4.3
J162622.38-242253.3	LFAM2	7.060 ± 0.072	-5.64 ± 0.09	-27.02 ± 0.30	–	–	141.6 ± 1.5
J162629.67-241905.8	LFAM8	7.246 ± 0.088	-5.89 ± 0.06	-29.54 ± 0.16	–	–	138.0 ± 1.7
J162634.17-242328.4	S1	7.249 ± 0.091	-2.05 ± 0.02	-26.72 ± 0.04	–	–	138.0 ± 1.7
J162642.44-242626.1	LFAM15	7.253 ± 0.054	-6.31 ± 0.02	-26.95 ± 0.05	–	–	137.9 ± 1.0
J162643.76-241633.4	VSSG11	7.160 ± 0.152	-10.48 ± 0.16	-38.99 ± 0.35	0.31 ± 0.65	-1.54 ± 1.09	139.7 ± 3.0
J162649.23-242003.3	LFAM18	7.232 ± 0.068	-11.62 ± 0.06	-18.30 ± 0.15	-0.10 ± 0.32	8.17 ± 0.84	138.3 ± 1.3
J162718.17-242852.9	YLW 12Bab	7.230 ± 0.057	6.56 ± 0.02	-26.26 ± 0.04	-0.62 ± 0.01	-0.17 ± 0.02	138.3 ± 1.1
J162718.17-242852.9	YLW 12Bc[1]	7.230 ± 0.057	-11.23 ± 0.07	-23.10 ± 0.10	0.19 ± 0.03	0.11 ± 0.05	138.3 ± 1.1
J162721.81-244335.9	ROXN39	7.317 ± 0.021	-7.32 ± 0.31	-26.21 ± 0.73	–	–	136.7 ± 0.4
J162730.82-244727.2	DROXO71	7.327 ± 0.125	-4.41 ± 0.11	-28.79 ± 0.33	–	–	136.5 ± 2.3
J163035.63-243418.9	SFAM 87	7.206 ± 0.080	-7.69 ± 0.02	-26.04 ± 0.04	–	–	138.8 ± 1.5

Table 4 continued

Table 4 *(continued)*

GBS-VLA name (1)	Other identifier (2)	Parallax (mas) (3)	$\mu_\alpha \cos\delta$ (mas yr^{-1}) (4)	μ_δ (mas yr^{-1}) (5)	$a_\alpha \cos\delta$ (mas yr^{-2}) (6)	a_δ (mas yr^{-2}) (7)	Distance (pc) (8)
J163152.10-245615.7	LDN1689IRS5	6.676 ± 0.046	-6.38 ± 0.03	-22.74 ± 0.04	–	–	149.8 ± 1.0
J163200.97-245643.3	WLY2-67	6.616 ± 0.088	-5.94 ± 0.12	-24.08 ± 0.30	–	–	151.2 ± 2.0
J163211.79-244021.8	DoAr51	6.983 ± 0.050	-4.80 ± 0.08	-23.11 ± 0.11	–	–	143.2 ± 1.0

[1] Parallax is fixed at the value obtained for YLW 12Bab when solving for the other astrometric parameters.

Table 5. Archive VLBA data

Project code	Date of observation	Source	Relevant entries from the observing log
BL128 FA	2005 Jun 07	LFAM 15	
BL128 FB	2005 Sep 03	LFAM 15	
BL128 FC	2005 Dec 09	LFAM 15	
BL128 FD	2006 Mar 01	LFAM 15	
BL128 FG[1]	2006 Dec 20	DOAR 21	PT may have some residual snow in the dish.
			Cloudy at NL,LA, and PT.
			LA weather: overcast and snowing. 2 inches of snow.
			NL precipitation.
BL128 FF	2006 Dec 22	DOAR 21	
BT093 CA[1]	2007 Jul 10	DOAR 21	Rain at NL, overcast SC, HN.
BT093 CB[1]	2007 Jul 20	DOAR 21	SC out due to bad HVAC in vertex rm. LA raining.
			KP 35+ mph wind caution.
BT093 CC[1]	2007 Jul 31	DOAR 21	HN and BR unavailable for observing due to
			scheduled maintenance visits. Raining at SC and FD.
BT093 CD	2007 Aug 09	DOAR 21	
BT093 CE	2007 Aug 18	DOAR 21	
BT093 CF[1,2]	2007 Aug 29	DOAR 21	SC, NL cloudy. NL, OV windy.
BT093 CG	2007 Sep 09	DOAR 21	
BT093 CH	2007 Sep 21	DOAR 21	
BL128 DA	2005 jun 08	YLW 12B	
BL128 DG	2005 sep 11	YLW 12B	
BL128 DC	2005 dec 05	YLW 12B	BR: not fringing, data not usable.
			NL: slow to get on source.
BL128 DD	2006 mar 24	YLW 12B	
BL128 DE	2006 jun 01	YLW 12B	
BL128 DF[1]	2006 aug 27	YLW 12B	Raining at FD, MK and HN.
BL128 GA	2005 jun 24	S1	
BL128 GB	2005 sep 15	S1	
BL128 GC	2005 dec 17	S1	
BL128 GD	2006 mar 15	S1	
BL128 GE	2006 jun 03	S1	Raining at HN.
			KP subreflector not moving to any position in ROTATION.
			KP antenna is removed from observing.
			HN disabled ROTATION axis, subreflector is
			about 6 counts off in ROTATION position.

Table 5 continued

Table 5 *(continued)*

Project code	Date of observation	Source	Relevant entries from the observing log
BL128 GF	2006 aug 22	S1	
BT093 BA	2007 jun 05	S1	
BT093 BB	2007 jun 09	S1	FD is on generator power, not in observation.
			PT HC2 FIFO error.
BT093 BC	2007 jun 13	S1	
BT093 BD	2007 jun 17	S1	SC, HN, NL overcast.
			SC precipitation.
BT093 BE	2007 jun 21	S1	
BT093 BF	2007 jun 25	S1	NL dense fog.
			NL precipitation.
BT093 BG	2007 jun 29	S1	
BT093 BH	2007 jul 03	S1	
BT097 A	2008 mar 14	SFAM 87	
BT097 B	2008 jun 03	SFAM 87	
BT097 C	2008 ago 19	SFAM 87	
BT097 D	2008 nov 14	SFAM 87	
BT097 E	2009 feb 14	SFAM 87	
BT097 F	2009 may 16	SFAM 87	

[1] Epoch was discarded.

[2] Data shows low amplitudes for IFs 3-4.

Table 6. Orbital elements

Name	a	P	T_0	e	Ω	i	ω	M_1	M_2	M_T
	(mas)	(yr)			(^{o})	(^{o})	(^{o})	($M_\odot$)	($M_\odot$)	($M_\odot$)
(1)	(2)	(3)	(4)	(5)	(6)	(7)	(8)	(9)	(10)	(11)
LFAM 15										
Full	16.40±0.13	3.591±0.0183	2007.008±0.039	0.528±0.005	337.93±0.81	110.30±0.49	235.54±1.02	0.4687 ±0.0146	0.421 ±0.010	0.89 ±0.01
Rel. astr.	16.98±0.16	3.598±0.0099	2010.626±0.011	0.561±0.007	340.05±0.49	109.77±0.27	239.60±0.64	–	–	0.99 ±0.03
YLW 12Bab										
Full	12.70±0.09	1.425±0.0012	2005.174±0.009	0.444±0.003	135.15±1.03	75.60±1.25	158.69±1.47	1.3969 ±0.0194	1.258 ±0.006	2.66 ±0.02
Rel. astr.	12.54±0.06	1.424±0.0005	2013.720±0.003	0.442±0.003	135.38±0.32	74.32±0.48	160.11±0.99	–	–	2.58 ±0.07
SFAM 87										
Full	35.58±0.31	7.691±0.007	2023.781±0.006	0.343±0.001	22.36±8.57	-162.66±2.84	346.19±8.83	1.0207 ±0.0224	0.999 ±0.038	2.02 ±0.04
Rel. astr.	35.79±0.30	7.719±0.019	2008.404±0.015	0.341±0.005	18.62±4.32	-157.95±2.59	344.25±4.91	–	–	2.06 ±0.09
DoAr 51										

Table 6 continued

Table 6 *(continued)*

Name	a	P	T_0	e	Ω	i	ω	M_1	M_2	M_T
	(mas)	(yr)			(^{o})	(^{o})	(^{o})	($M_\odot$)	($M_\odot$)	($M_\odot$)
(1)	(2)	(3)	(4)	(5)	(6)	(7)	(8)	(9)	(10)	(11)
Full	32.83±0.45	8.102±0.063	2012.025±0.044	0.802±0.004	51.56±6.31	18.95±1.75	216.41±6.42	0.7909 ±0.0140	0.781 ±0.042	1.57 ±0.05
Rel. astr.	32.47±0.39	8.070±0.035	2012.020±0.029	0.801±0.005	51.81±9.66	17.80±4.36	215.81±10.20	–	–	1.54 ±0.07
Rizzuto+16	32.69±0.35	8.233±0.117	2012.009±0.010	0.818±0.009	24.1±11.0	16.3±2.0	243.0±10.9	–	–	1.57 ±0.03(±0.29)
ROXN 39										
Full	54.3±3.9	11.2±1.5	2056.1±1.2	0.40±0.12	25.4±2.9	68.4±3.3	120.0±12.9	2.31 ±1.04	0.97 ±0.50	3.3 ±1.2
S1										
Full	19.99±0.20	1.734±0.003	2017.089±0.020	0.745±0.010	118.9±17.7	36.2±6.1	294.6±15.8	5.78 ±0.15	1.18 ±0.10	6.95 ±0.18

Table 7. Corrected proper motions and tangential velocities

Name	$\mu_{\alpha\cos\delta}^{\rm corr}$	$\mu_\delta^{\rm corr}$	$v_\alpha^{\rm t}$	$v_\delta^{\rm t}$
	(mas yr^{-1})	(mas yr^{-1})	(km s^{-1})	(km s^{-1})
(1)	(2)	(3)	(4)	(5)
WLY2-11	-1.96 ± 0.72	-4.2 ± 0.75	-1.26 ± 0.46	-2.72 ± 0.49
YLW24	0.63 ± 0.83	-4.17 ± 0.84	0.41 ± 0.53	-2.67 ± 0.54
DoAr21	-11.74 ± 0.89	-5.91 ± 0.86	-7.54 ± 0.57	-3.79 ± 0.55
LFAM2	1.87 ± 0.87	-6.94 ± 0.73	1.26 ± 0.58	-4.66 ± 0.49
LFAM8	1.82 ± 0.83	-8.96 ± 0.76	1.19 ± 0.54	-5.86 ± 0.5
S1	5.65 ± 0.88	-6.1 ± 0.77	3.69 ± 0.57	-3.99 ± 0.51
LFAM15	1.37 ± 0.74	-6.29 ± 0.71	0.9 ± 0.49	-4.11 ± 0.46
VSSG11	-2.88 ± 0.92	-18.67 ± 0.9	-1.9 ± 0.61	-12.36 ± 0.59
LFAM18	-3.96 ± 0.82	2.25 ± 0.71	-2.59 ± 0.53	1.47 ± 0.46
YLW12B	3.05 ± 0.77	-3.66 ± 0.7	2.0 ± 0.5	-2.4 ± 0.46
ROXN39	0.33 ± 0.91	-5.25 ± 0.83	0.21 ± 0.59	-3.4 ± 0.54
DROXO71	3.22 ± 0.81	-7.77 ± 0.72	2.09 ± 0.52	-5.03 ± 0.47
SFAM87	-0.41 ± 0.86	-5.48 ± 0.76	-0.27 ± 0.56	-3.6 ± 0.5
LIRS5	0.21 ± 0.71	-3.55 ± 0.69	0.15 ± 0.5	-2.52 ± 0.49
WLY2-67	0.58 ± 0.79	-5.06 ± 0.67	0.41 ± 0.57	-3.63 ± 0.48
DoAr51	2.1 ± 0.84	-3.15 ± 0.72	1.43 ± 0.57	-2.14 ± 0.49

APPENDIX

A. NON-THERMAL RADIO EMISSION IN YOUNG STARS AND GOBELINS DETECTION STATISTICS

A.1. *Introduction*

YSOs are often detectable radio sources due to a variety of mechanisms. One common radio emission process in YSOs is thermal bremsstrahlung (free-free) continuum emission, either from photo-ionized gas around massive stars

(e.g., Churchwell 2002) or from shock-ionized gas in supersonic jets and outflows (e.g., Rodríguez 1997). The brightness temperature corresponding to thermal bremsstrahlung emission, however, is typically only 10^4 K, much too small to be detectable in VLBI observations. The situation with thermal dust continuum emission, which can be detected up to centimeter wavelengths from circumstellar disks (e.g., Pérez et al. 2015), is even worse, as such emission has brightness temperatures of at most several hundred K. Thermal line emission, from molecules or atoms, is similarly limited to brightness temperatures smaller than several hundred K. Thus, to find emission that could be detected in VLBI observations, one must turn to non-thermal mechanisms. For line emission, this implies focusing on strongly amplified maser lines, like those of water (H_2O), methanol (CH_3OH), formaldehyde (H_2CO), silicon monoxide (SiO), or hydroxyl (OH). Those lines (particularly those of water and methanol) are widespread in regions of high-mass star-formation, and can be detected and studied with VLBI observations up to distances of several kpc. Indeed, the BeSSeL project (Brunthaler et al. 2009) takes advantage of these lines to measure the parallax and proper motions of high-mass star-forming regions distributed across the entire Milky Way disk. In the Gould's Belt star-forming regions, however, only a handful of maser sources are known (e.g., Moscadelli et al. 2006).

Non-thermal *continuum* emission also exists, and broadly corresponds to the situation where electrons gyrate in a magnetic field. This type of radiation is called cyclotron, gyro-synchrotron, or synchrotron emission depending on whether the electrons are non-relativistic (with a γ Lorentz factor about 1), mildly relativistic (γ of a few), or ultra-relativistic ($\gamma \gg 1$), respectively (Dulk 1985). Such continuum non-thermal emission has been detected around a number of low-mass young stars (e.g., Forbrich et al. 2011, and references therein), and has been interpreted as coronal emission from active stellar magnetospheres. The most common mechanism appears to be gyro-synchrotron, although maser-amplified cyclotron emission (Smith et al. 2003) as well as synchrotron emission (Massi et al. 2006) have also been reported in rare instances. The magnetic field in which the electrons are gyrating is generated through the dynamo mechanism, which requires convection in the outer layers of the stellar interior (e.g., Dormy et al. 2013). As a consequence, non-thermal coronal emission should occur only in low-mass stars, because intermediate and high-mass stars are fully radiative. This is true both for main sequence and pre-main sequence stars: while low-mass T Tauri stars approach the main sequence on fully convective Hayashi tracks, stars more massive than about 3 $M_\odot$ follow radiative Henyey tracks (e.g., Palla & Stahler 1993). It is noteworthy, however, that a few intermediate-mass young stars have been found to exhibit non-thermal coronal emission (Andre et al. 1991; Dzib et al. 2010). The electrons gyrating in the magnetic field are thought to be accelerated to mildly relativistic speeds during energetic reconnection processes (Parker 1957), so the emission is often produced in flares (e.g., Bower et al. 2003) and is therefore highly variable. Once again, there are some exceptions to this general behavior (e.g., Andre et al. 1991). Finally, it should be mentioned that most of the low-mass young stars where non-thermal emission has been reported are T Tauri stars (particularly Weak Line T Tauri stars), although a few younger Class I protostars have also been detected (Forbrich et al. 2006; Deller et al. 2013).

Coronal non-thermal radio continuum emission usually remains unresolved at the milli-arcsecond resolution of VLBI observations (e.g., Loinard et al. 2007; but see Andre et al. 1991). Theoretically, the emission is expected to be confined to the magnetosphere of the YSO, which extends to only a few stellar radii (Bouvier et al. 2007). This is indeed very small: for instance, 10 $R_\odot$ corresponds to about 0.5 mas at 100 pc.

A.2. *Statistics*

As mentioned in the main text, we have firmly detected a total of 26 YSOs, corresponding to roughly half of the 50 YSOs targeted in our observations. This confirms the claim by Dzib et al. (2013), that about 50% of the radio-bright YSOs in Ophiuchus are non-thermal emitters. We searched the literature and found that only 6 of these YSOs had previously been detected in VLBI experiments. These sources (DoAr 21, S1, LFAM 15, VSSG 11, YLW 12 B, and SFAM 87) were known to be magnetically active stars, with centimetric non-thermal radio emission, before our observations (e.g. Andre et al. 1992; Loinard et al. 2008). We note that Forbrich et al. (2007) reported on the detection, with the HSA, of one of the components of the binary class 0/I source YLW 15 (a target that we also detect here). However, our analysis of the proper motions of the system components (see Section 4.3) suggests that the detection by Forbrich et al. (2007) was likely spurious. The 26 detected YSOs correspond to a total of 34 individual young stars, because five detections are found to be tight binary systems, while one corresponds to a triple system (see Table 2).

Dzib et al. (2013) also published a list of YSOc detected in their VLA observations. They reported as YSOc those radio sources that are not associated with known young stars, but that show high VLA flux variations, a negative spectral index, or circular polarization. Four of these sources were also detected in our VLBA observations, as well as another 27 (presumably background) sources. We analyze the astrometry of these 31 objects in Section B and find that, as expected, most of them are extragalactic sources.

In order to establish the nature of the emission, we have measured the brightness temperature (T_b) of the VLBA-detected sources, according to

$$T_b = \frac{2c^2}{k_B \nu^2} \frac{S_{\rm total}}{\pi \theta_{\rm maj} \theta_{\rm min}}, \tag{A1}$$

where $\theta_{\rm maj}$ and $\theta_{\rm min}$ are the deconvolved sizes of the major and minor axes diameter, and $S_{\rm total}$ is the total flux density measured in the VLBA images. Since most of the sources have been detected at several epochs, we are reporting the highest measured brightness temperature. For unresolved sources, we give a lower limit to T_b obtained using the corresponding beam size as an upper limit for the source size. Brightness temperatures are given in columns (7) and (5) of Tables 2 and B1, respectively. All of the VLBA-detected YSOs have $T_b > 10^6$ K, which is larger than the brightness temperature expected for thermal bremsstrahlung radiation ($T_b \lesssim 10^4$ K), and consistent with the brightness temperature expected for non-thermal emission. Our study has, therefore, found a population of non-thermal YSOs larger than previously reported. It is noteworthy that non-thermal emission is detected in sources in the Class I to Class III stages.

A.3. *Non-thermal emission as a function of evolutionary stage and multiplicity*

In Figure A1, we plot the VLBA flux density at 5 GHz of the detected YSOs as a function of their evolutionary phase, as measured from their infrared/millimeter spectral energy distribution (SED). It appears, at first sight, that older objects have, on average, stronger non-thermal radio emission. The significance of this correlation can be assessed by a Kolmogorov-Smirnov test on the three YSOs classes. The p values derived from such a test are > 0.08, so we cannot reject the null hypothesis that different classes are taken from the same distribution function. The relation is, therefore, not statistically significant. We also perform the Wilcoxon rank-sum statistic finding similar results. Thus, our conclusion about the significance of the correlation does not depend on the statistical test that we use.

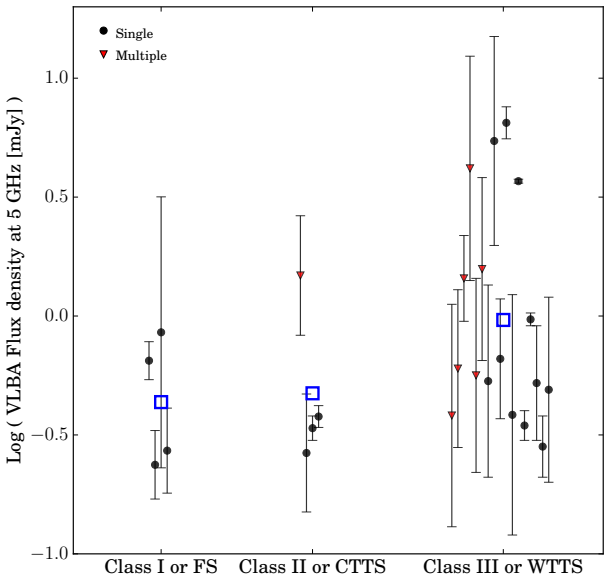

Figure A1. VLBA flux density at 5 GHz, as a function of evolutionary phase. The error bars represent the range in flux density from the maximum to the minimum measured values for variable sources, and measured flux uncertainties for sources with constant flux. Black circles correspond to single sources, while red triangles to multiple systems. We adopt for the VLBA flux density of multiple systems the sum of the flux densities of individual components. The black points are the mean VLBA flux density for each individual object, whereas the open blue squares are mean values for each object type. Here and in the rest of the paper, FS stands for Flat Spectrum, CTTS for classical T Tauri, and WTTS for weak-lined T Tauri.

From Table 2, it is clear that Class II and III sources are the most common types of YSOs with non-thermal radio emission. Past studies had only found two cases of Class I protostars with non-thermal emission detectable in VLBI observations. These sources are CrA IRS 5 (Deller et al. 2013) and EC 95 (Dzib et al. 2010). Here we have detected non-thermal emission from three other Class I objects, namely LFAM 4, YLW 15,[2] and WLY 2-67. We have, therefore,

[2] As we mentioned earlier, a VLBI detection was reported by

more than doubled the number of protostars with confirmed non-thermal emission. In a recent study, Heiderman & Evans (2015) investigated whether the Class 0+I and Flat SED sources identified in the c2d (Evans et al. 2009) and Gould Belt (Dunham et al. 2015) surveys are in the embedded phase. These authors used the detection of the HCO^+ $J = 3 \rightarrow 2$ as a good indicator of the Stage 0+1, which corresponds to "a star and a disk embedded in a dense, infalling envelope" van Kempen et al. (2009). Our 3 Class I objects with non-thermal radio emission meet the criterion to be in this embedded stage. Non-thermal emission has not been detected in Class 0 sources and at this point it is unclear if this results from a lack of such emission or if such young systems always contain thermal radio jets that systematically absorb underlying active coronas.

Magnetic activity is known to occur throughout the early evolution of low-mass stars, so protostellar sources could easily produce non-thermal emission. On the other hand, accretion and outflow activity is also present in this protostellar stage. In order for the observer to see the radio emission from the stellar corona, the line of sight cannot cross regions where optically thick radio emission is present –i.e. the central portions of disks or wind/outflow systems. This might occur only for some privileged relative orientation of the system, and naturally explains the low fraction of detected protostars in our observations, in comparison with the larger number of detections of more evolved objects.

There does seem to exist a correlation between non-thermal radio emission in young stellar objects and multiplicity. Perhaps the best documented case is that of the V773 Tau system (Massi et al. 2002; Torres et al. 2012), where the radio flux increases by more than one order of magnitude when the system passes periastron. We have found here that a significant fraction of the VLBA-detected young stars belong to very tight binary or multiple systems (with a separation of a few tens of mas – a few AU; Table 2). Multiplicity may help to clear out the surrounding material, and result in non-thermal emission that is statistically less affected by free-free absorption, but the exact mechanisms behind this remains unclear. The flux from thermal jets becomes transparent at frequencies above a few GHz (Reynolds 1986). Thus, coronal non-thermal emission from protostars with thermal emission should be detectable at higher frequencies.

In our VLBA observations, we found that 7 YSOs form multiple systems, and one more has evidence of multiplicity (See Table 2). This represents $\sim 30\%$ of the total number of YSOs detected with the VLBA. The angular separations of the components in these systems range from 4 to 315 mas, corresponding to 0.6 to 44 AU at the distance of Ophiuchus. In order to investigate if this fraction is expected from the known population of multiple systems in Ophiuchus, or if it indicates that tight multiple systems are more likely to be non-thermal radio emitters than single stars or wider multiple systems, we compared it with the binary fraction reported in the literature. Recently, Cheetham et al. (2015) compiled high-resolution multiplicity data and combined them with their results from an aperture masking survey; they obtained a binary fraction of $35 \pm 6\%$ for spatial scales from $1.3 - 41.6$ AU. Taken at face value, our VLBA detection of 30% of binaries with separations between 0.6 and 44 AU appears to be consistent with the binary fraction derived from the multiplicity survey by Cheetham et al. (2015). However, we still favor the idea that very tight binaries are more often radio sources than single stars or more separated binary systems, because 7 of our 8 detected binaries have separations of a few AU, whereas only one has a separation larger than 10 AU. Thus, for separations below 10 AU, there does appear to be an excess of radio bright binaries. Our interpretation will be tested by considering the whole sample of multiple stars seen in the five regions observed by GOBELINS, and comparing with multiplicity studies in the infrared, where aperture masking observations can explore angular separations similar to those attained with the VLBA.

A.4. *Radio luminosity function of non-thermal YSOs*

We show in Figure A2 the number of objects versus the radio luminosity at 5 GHz, i.e., the luminosity function, of the 26 YSOs detected with the VLBA. The number of objects appears to decrease with increasing luminosity, following roughly a linear trend (in logarithmic luminosity). Assuming that the trend is valid for lower luminosities, we can infer that deeper observations with an improved sensitivity by an order of magnitude will detect ~ 20 more YSOs with non-thermal radio emission, i.e., will double the number of sources. It will be interesting to construct the luminosity function for the other regions considered in GOBELINS, and see if this is a general trend.

B. OTHER SOURCES

In this section, we analyze the astrometry of 27 sources detected in our VLBA observations that are not classified as YSOs in the literature. These sources are listed in Table B1. Column 6 in that table provides a proposed classification

Forbrich et al. (2007) toward YLW 15, but that detection was most likely spurious (see 4.3).

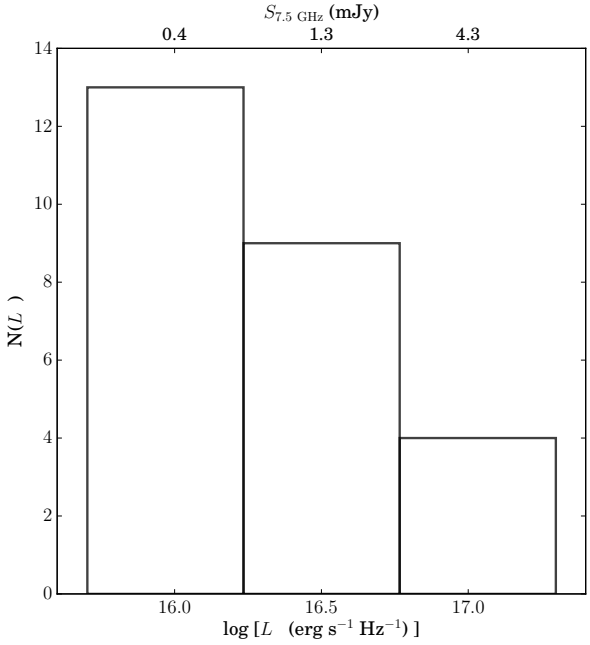

Figure A2. Luminosity function for the YSOs detected with the VLBA at 5 GHz.

based on the radio emission properties in the VLA observations of Dzib et al. (2013). Out of the 31 sources that are not known YSOs in that list, 18 are proposed to be extragalactic (E), 4 are YSO candidates (YSOc), and 9 have no proposed identifications. Many of these sources have been detected in several of our VLBA observations, so we can analyze their changes in position as a function of time to constrain their location along the line of sight. Extragalactic sources are expected to remain practically fixed on the celestial sphere, so any measured change in their positions should be of the order of or less than the rms astrometric errors. These errors are given by the systematic errors found in the astrometric fits, and are $\lesssim 1.2$ mas for YSOs in the core, while for sources located in the L1689 streamer, we obtain systematic errors $\lesssim 2.4$ mas. These larger errors in L1689 result from the larger separation between the main phase calibrator and the targets there. Galactic sources, on other hand, should show an appreciable parallax and a proper motion signature, particularly if they are within a few kpc.

For each source in Table B1 that has been observed in at least two epochs (that is, 56 out of the 64 sources in Table B1), we measured the shift in position ($\sqrt{\Delta\alpha\cos\delta^2 + \Delta\delta^2}$) between consecutive epochs, normalized it to one year, and averaged over all consecutive pairs of epochs. For instance, for a source with three detections, we averaged two displacements: that between epoch 1 and epoch 2, and that between epoch 2 and epoch 3. We will call this quantity the *position change rate* in the rest of this section. This position change rate should be zero (within the errors) for extragalactic sources and non-zero for (nearby) Galactic objects. However, since the position change rate contains information on both the parallax and the proper motions, and is based on a varying number of detections for different sources (from 2 to 5 detections), a non-zero value cannot be easily interpreted in terms of distance along the line of sight. Sources for which a non-zero value is found should be analyzed in more detail.

The results are shown in the form of a histogram in Figure B3, where we separate known YSOs from other sources. The two histograms are markedly different. For known YSOs, the histogram is roughly Gaussian and centered around a position change rate of ~ 36 mas yr^{-1}. For the rest of the sources, on the other hand, the distribution is dominated by a peak around a position change rate of zero, to within a few mas yr^{-1}. Specifically, the first four bins in the histogram (23 sources) correspond to sources that do not show appreciable motion on the celestial sphere (i.e., they have position changes between consecutive epochs smaller on average than the astrometric noise), and we identify them as extragalactic. This new classification is shown in Column 6 of Table 2. Of course, for the four unclassified sources that have only been detected once in our VLBA observations, the position change rate cannot be measured, and we classify these sources as "?" in Column 6 of Table B1.

There are three sources, however, that do show a non-zero position change rate, and we now discuss them in turn. The source with the largest position change rate (~ 27 mas yr^{-1}) is GBS-VLA J163151.93-245617.4, and has been

detected three times. However, as in the case of YLW15, the three detections occurred around the spring equinoxes. Thus, it is impossible to obtain any meaningful information on its parallax. We note, however, that its position change rate places it squarely within the range covered by the YSOs in Ophiuchus. In addition, because the detections occurred only on spring equinoxes (April 2013, March 2014 and March 2016), the displacement is dominated by proper motions, with only a small contribution from parallax. The fact that the measured displacement (~ 27 mas yr^{-1}) is so similar to the proper motion of sources in Ophiuchus suggests that GBS-VLA J163151.93-245617.4 is not only Galactic, but indeed an Ophiuchus member. Interestingly, this source had been classified as a YSO candidate by Dzib et al. (2013) on the basis of the variability and spectral slope of the radio emission. Additional detections will be necessary to confirm this and obtain a trigonometric parallax but, for the time being, we classify GBS-VLA J163151.93-245617.4 as an "Oph" member in Column 6 of Table B1.

The source with the second largest position change rate (~ 19 mas yr^{-1}) is SFAM12, which was detected only twice. In this case, the two detections occurred around the spring equinox of 2015 and the fall equinox of 2015, respectively. Thus, the displacement results from the combination of both parallax and proper motion. This makes it unlikely that SFAM12 is an Ophiuchus member, since for sources in Ophiuchus, a larger position change rate would be expected (roughly 25 mas yr^{-1} due to proper motion, and an additional 15 mas due to parallax, since the observations were obtained at opposite equinoxes). Thus, we classify SFAM12 as a Galactic source ("G" in Column 6 of Table 2), but unlikely to be associated with Ophiuchus itself. We note that SFAM12 was previously believed to be extragalactic. Finally, the third source with a definite non-zero position change rate (~ 10 mas yr^{-1}) is LFAM17. Since there were 5 detections of this target, an astrometric fit could be attempted. Formally, it suggests a parallax $\varpi = 0.87 \pm 0.14$ mas (corresponding to $d = 1.2 \pm 0.2$ kpc), but the fit is poor. Certainly, however, this source is Galactic but much farther away than Ophiuchus. Thus, we classify it as "G" in Column 6 of Table 2. We note that Dzib et al. (2013) had classified it as a YSO on the basis of its radio properties. Both SFAM12 and LFAM17 are likely to be active stars (possibly, but not necessarily, young ones) located behind Ophiuchus.

To finish this section, we should mention source GBS-VLA J163138.57-253220.0, which is the sole member of the fifth red histogram bin in Figure B3. Its position change rate is formally above the astrometric uncertainty. It was detected four times, so an astrometric fit could again be attempted. As in the case of LFAM17, the fit is poor; it results in a parallax $\varpi = 0.17 \pm 0.05$ mas (corresponding to $d = 5.9^{+2.4}_{-1.3}$ kpc). This might suggest that GBS-VLA J163138.57-253220.0 is a Galactic source at several kpc, but given the large errors and poor quality of the fit, we cannot completely discard that it be extragalactic. Thus, we classify it as "G?" in Column 6 of Table B1. In general, the identification proposed by Dzib et al. (2013) for sources in Table B1 matches well our new classification based on VLBA observations.

REFERENCES

Abad, C., & Vieira, K. 2005, A&A, 442, 745

Andre, P., Deeney, B. D., Phillips, R. B., & Lestrade, J.-F. 1992, ApJ, 401, 667

Andre, P., Phillips, R. B., Lestrade, J.-F., & Klein, K.-L. 1991, ApJ, 376, 630

André, P., Men'shchikov, A., Bontemps, S., et al. 2010, A&A, 518, L102

Barsony, M., Koresko, C., & Matthews, K. 2003, ApJ, 591, 1064

Benz, A. O., & Guedel, M. 1994, A&A, 285, 621

Bertiau, F. C. 1958, ApJ, 128, 533

Bertout, C., Robichon, N., & Arenou, F. 1999, A&A, 352, 574

Bouvier, J., Alencar, S. H. P., Harries, T. J., Johns-Krull, C. M., & Romanova, M. M. 2007, Protostars and Planets V, 479

Bouy, H., & Alves, J. 2015, A&A, 584, A26

Bower, G. C., Plambeck, R. L., Bolatto, A., et al. 2003, ApJ, 598, 1140

Brunthaler, A., Reid, M. J., Menten, K. M., et al. 2009, ApJ, 693, 424

Cambrésy, L. 1999, A&A, 345, 965

Cheetham, A. C., Kraus, A. L., Ireland, M. J., et al. 2015, ApJ, 813, 83

Chini, R. 1981, A&A, 99, 346

Churchwell, E. 2002, ARA&A, 40, 27

Curiel, S., Girart, J. M., Rodríguez, L. F., & Cantó, J. 2003, ApJL, 582, L109

David, T. J., Conroy, K. E., Hillenbrand, L. A., et al. 2016, AJ, 151, 112

de Bruijne, J. H. J. 2012, Ap&SS, 341, 31

de Geus, E. J., de Zeeuw, P. T., & Lub, J. 1989, A&A, 216, 44

de Grijs, R. 2011, An Introduction to distance measurement in Astronomy (John Wiley & Sons Ltd.)

de Zeeuw, P. T., Hoogerwerf, R., de Bruijne, J. H. J., Brown, A. G. A., & Blaauw, A. 1999, AJ, 117, 354

Deller, A. T., Forbrich, J., & Loinard, L. 2013, A&A, 552, A51

Deller, A. T., Brisken, W. F., Phillips, C. J., et al. 2011, PASP, 123, 275

Dormy, E., Petitdemange, L., & Schrinner, M. 2013, in IAU Symposium, Vol. 294, Solar and Astrophysical Dynamos and Magnetic Activity, ed. A. G. Kosovichev, E. de Gouveia Dal Pino, & Y. Yan, 163–173

Dulk, G. A. 1985, ARA&A, 23, 169

Dunham, M. M., Allen, L. E., Evans, II, N. J., et al. 2015, ApJS, 220, 11

Dzib, S., Loinard, L., Mioduszewski, A. J., et al. 2010, ApJ, 718, 610

—. 2011, RMxAC, 40, 231

Dzib, S. A., Ortiz-León, G. N., Loinard, L., et al. 2016, ApJ, 826, 201

Dzib, S. A., Loinard, L., Mioduszewski, A. J., et al. 2013, ApJ, 775, 63

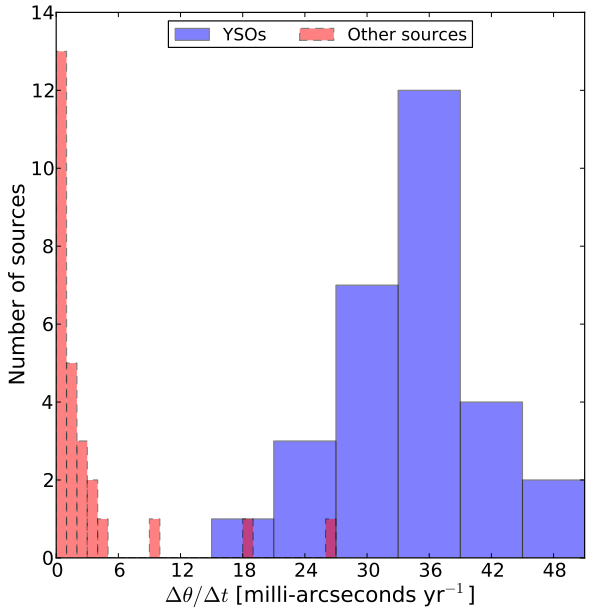

Figure B3. Histogram of position change rate for all sources detected at least twice toward Ophiuchus. The sources previously identified as YSOs are shown as a blue histogram, whereas the other sources are shown as a red histogram.

Dzib, S. A., Loinard, L., Rodríguez, L. F., et al. 2015, ApJ, 801, 91

Evans, II, N. J., Dunham, M. M., Jørgensen, J. K., et al. 2009, ApJS, 181, 321

Forbrich, J., Massi, M., Ros, E., Brunthaler, A., & Menten, K. M. 2007, A&A, 469, 985

Forbrich, J., Osten, R. A., & Wolk, S. J. 2011, ApJ, 736, 25

Forbrich, J., Preibisch, T., & Menten, K. M. 2006, A&A, 446, 155

Greisen, E. W. 2003, ASSL, 285, 109

Gudehus, D. H. 2001, BAAS, 33, 850

Guedel, M., & Benz, A. O. 1993, ApJL, 405, L63

Heiderman, A., & Evans, II, N. J. 2015, ApJ, 806, 231

Imai, H., Nakashima, K., Bushimata, T., et al. 2007, PASJ, 59, 1107

Knude, J., & Hog, E. 1998, A&A, 338, 897

Kounkel, M., Hartmann, L., Loinard, L., et al. 2014, ApJ, 790, 49

Le Bouquin, J.-B., Monin, J.-L., Berger, J.-P., et al. 2014, A&A, 561, A101

Loinard, L., Mioduszewski, A. J., Rodríguez, L. F., et al. 2005, ApJL, 619, L179

Loinard, L., Torres, R. M., Mioduszewski, A. J., & Rodríguez, L. F. 2008, ApJL, 675, L29

Loinard, L., Torres, R. M., Mioduszewski, A. J., et al. 2007, ApJ, 671, 546

Lombardi, M., Lada, C. J., & Alves, J. 2008, A&A, 480, 785

Makarov, V. V. 2007, ApJ, 670, 1225

Mamajek, E. E. 2008, AN, 329, 10

Massi, M., Forbrich, J., Menten, K. M., et al. 2006, A&A, 453, 959

Massi, M., Menten, K., & Neidhöfer, J. 2002, A&A, 382, 152

McClure, M. K., Furlan, E., Manoj, P., et al. 2010, ApJS, 188, 75

Melis, C., Reid, M. J., Mioduszewski, A. J., Stauffer, J. R., & Bower, G. C. 2014, Science, 345, 1029

Menten, K. M., Reid, M. J., Forbrich, J., & Brunthaler, A. 2007, A&A, 474, 515

Moscadelli, L., Testi, L., Furuya, R. S., et al. 2006, A&A, 446, 985

Napier, P. J., Bagri, D. S., Clark, B. G., et al. 1994, IEEE Proceedings, 82, 658

Ortiz-León, G. N., Loinard, L., Mioduszewski, A. J., et al. 2015, ApJ, 805, 9

Palla, F., & Stahler, S. W. 1993, ApJ, 418, 414

Parker, E. N. 1957, PhRv, 107, 830

Pech, G., Loinard, L., Dzib, S. A., et al. 2016, ApJ, 818, 116

Pérez, L. M., Chandler, C. J., Isella, A., et al. 2015, ApJ, 813, 41

Perrot, C. A., & Grenier, I. A. 2003, A&A, 404, 519

Perryman, M. A. C., Lindegren, L., Kovalevsky, J., et al. 1997, A&A, 323, L49

Poppel, W. 1997, FCPh, 18, 1

Pradel, N., Charlot, P., & Lestrade, J.-F. 2006, A&A, 452, 1099

Reid, M. J., & Brunthaler, A. 2004, ApJ, 616, 872

Reid, M. J., & Honma, M. 2014, ARA&A, 52, 339

Reynolds, S. P. 1986, ApJ, 304, 713

Richichi, A., Leinert, C., Jameson, R., & Zinnecker, H. 1994, A&A, 287, 145

Ridge, N. A., Di Francesco, J., Kirk, H., et al. 2006, AJ, 131, 2921

Rivera, J. L., Loinard, L., Dzib, S. A., et al. 2015, ApJ, 807, 119

Rizzuto, A. C., Ireland, M. J., Dupuy, T. J., & Kraus, A. L. 2016, ApJ, 817, 164

Rodríguez, L. F. 1997, in IAU Symposium, Vol. 182, Herbig-Haro Flows and the Birth of Stars, ed. B. Reipurth & C. Bertout, 83–92

Schaefer, G. H., Simon, M., Prato, L., & Barman, T. 2008, AJ, 135, 1659

Schönrich, R., Binney, J., & Dehnen, W. 2010, MNRAS, 403, 1829

Skrutskie, M. F., Cutri, R. M., Stiening, R., et al. 2006, AJ, 131, 1163

Smith, K., Pestalozzi, M., Güdel, M., Conway, J., & Benz, A. O. 2003, A&A, 406, 957

Stothers, R., & Frogel, J. A. 1974, AJ, 79, 456
Thompson, A. R., Moran, J. M., & Swenson, G. W. 2007, Interferometry and Synthesis in Radio Astronomy, John Wiley & Sons, 2007.
Torres, R. M., Loinard, L., Mioduszewski, A. J., et al. 2012, ApJ, 747, 18
Torres, R. M., Loinard, L., Mioduszewski, A. J., & Rodríguez, L. F. 2007, ApJ, 671, 1813
—. 2009, ApJ, 698, 242
van Kempen, T. A., van Dishoeck, E. F., Salter, D. M., et al. 2009, A&A, 498, 167
Walter, F. M., Vrba, F. J., Mathieu, R. D., Brown, A., & Myers, P. C. 1994, AJ, 107, 692
Ward-Thompson, D., Di Francesco, J., Hatchell, J., et al. 2007, PASP, 119, 855
Whittet, D. C. B. 1974, MNRAS, 168, 371
Wilking, B. A., Gagné, M., & Allen, L. E. 2008, Star Formation in the ρ Ophiuchi Molecular Cloud, ed. B. Reipurth, 351
Wilking, B. A., Vrba, F. J., & Sullivan, T. 2015, ApJ, 815, 2

Table B1. Other detected sources

GBS-VLA name (1)	Other identifier (2)	Maximum flux at 5 GHz (mJy) (3)	Maximum flux at 8 GHz (mJy) (4)	log [T_b (K)] (5)	Type[1] of source (6)		Number of detections/observations (7)
J162540.94-244147.2	SSTc2d J162540.9−244147	0.39	<0.06	0.08	E	?	1/1
J162547.68-243735.7	–	0.45	0.37	0.05	?	E	3/3
J162633.48-241215.9	SFAM12	0.39	<0.06	0.05	E	G	2/2
J162635.33-242405.2	LFAM13	0.79	<0.09	0.07	E	E	4/10
J162646.36-242002.0	LFAM17	0.64	<0.06	0.08	YSOc	G	5/6
J162702.15-241927.8	GDS J162702.1−241928	0.48	<0.06	0.07	E	E	4/4
J162713.06-241817.0	–	0.21	<0.06	0.05	?	E	2/9
J162718.25-243334.8	–	0.52	<0.06	0.16	?	?	1/6
J162729.23-241755.3	ROC25	2.74	<0.18	0.06	E	E	5/5
J162734.55-242020.7	ROC26	1.25	<0.18	0.06	E	E	5/5
J163027.69-243300.2	SSTc2d J163027.7−243300	0.25	<0.06	0.05	E	E	2/4
J163032.26-243127.9	SSTc2d J163032.3−243128	0.90	<0.06	0.06	YSOc	E	3/3
J163033.26-243038.7	SSTc2d J163033.2−243039	0.40	<0.06	0.06	YSOc	?	1/3
J163036.26-243135.3	–	0.80	<0.06	0.07	?	E	3/3
J163109.79-243008.4	ROC49	0.73	<0.06	0.07	E	E	3/3
J163115.25-243313.8	–	0.29	<0.06	0.04	?	E	2/4
J163120.14-242928.5	ROC52	4.38	<0.06	0.14	E	E	3/3
J163130.62-243351.6	SSTc2d J163130.6−243352	0.64	<0.06	0.06	E	E	3/3
J163138.57-253220.0	–	0.56	1.00	0.07	?	G?	4/4
J163151.93-245617.4	–	0.34	0.28	0.06	YSOc	Oph	3/4
J163154.49-245217.1	SSTc2d J163154.5−245217	0.35	<0.06	0.05	E	E	2/3
J163159.36-245639.7	SFAM127	1.72	<0.06	0.09	E	E	2/2
J163202.39-245710.0	–	0.18	0.34	0.06	?	E	2/3
J163210.77-243827.6	SFAM130	0.42	<0.09	0.07	E	E	4/5
J163211.08-243651.1	SSTc2d J163211.1−243651	0.80	<0.09	0.08	E	E	5/5
J163212.25-243643.7	–	0.37	<0.06	0.07	?	E	2/5
J163213.92-244407.8	–	0.36	<0.05	0.06	?	?	1/6
J163227.41-243951.4	SSTc2d J163227.4−243951	0.51	<0.06	0.06	E	E	3/5
J163231.17-244014.6	SSTc2d J163231.2−244014	0.51	<0.06	0.05	E	E	2/5
J163245.23-243647.4	SFAM200	0.47	0.26	0.07	E	E	3/3
J163617.50-242555.4	SFAM212	1.82	2.50	0.09	E	E	5/5

NOTE—Reported sources have flux densities above 6σ and 5σ in the cases of one or several detections, respectively. Non-detections are indicated by giving an upper flux density limit of 3σ.

[1] The first entry indicates the classification given by Dzib et al. (2013) from VLA observations. The second entry indicates the classification given in this work by comparing the shift in source positions against the rms astrometric errors. Here *E* stands for extragalactic and *G*, for Galactic objects.

Capítulo 4

La distancia hacia la región de formación estelar Serpens/Aquila

Las nube de Serpens y los cúmulos estelares W40 y Serpens Sur en la Grieta del Aquila son regiones con copiosa actividad de formación estelar. Numerosas estimaciones de la distancia hacia estas regiones se han reportado en la literatura, las cuales van desde 245 ± 30 pc (Chavarria-K. *et al.*, 1988) hasta 650 ± 180 pc (Zhang *et al.*, 1988) para Serpens y de 455 a 600 pc para W40 (Kolesnik y Iurevich, 1983; Shuping *et al.*, 2012). La discrepancia de casi 400 pc en las estimaciones de la distancia hacia Serpens nos impide aseverar con certeza si las tres regiones son parte o no del mismo complejo de nubes moleculares. Por ésta y las razones que expusimos en el capítulo 2, es necesario obtener nuevas paralajes trigonométricas hacia objetos en las tres regiones. Las observaciones de radio realizadas con el VLA hacia Serpens, W40 y Serpens Sur, y que presentamos en el capítulo 2, detectaron un total de ~ 150 fuentes en las tres regiones. Analizando las características de la emisión detectada, identificamos 18 objetos que posiblemente están asociados con estrellas jóvenes con emisión no térmica suficientemente intensa para detectarse usando VLBI.

En este capítulo, presentamos observaciones obtenidas con el VLBA hacia Serpens, W40 y Serpens Sur entre septiembre de 2013 y abril de 2016 como parte del proyecto

GOBELINS. Además, analizamos datos de observaciones realizadas específicamente para monitorear a la estrella binaria EC 95, en el núcleo de Serpens, y que comprenden un periodo de 8 años. De manera similar a Ofiuco, derivamos los parámetros astrométricos de aquellos objetos que han sido detectados en al menos 3 épocas en equinoccios alternos, esto es, 3 objetos en Serpens y 4 en W40. Para EC 95 obtenemos, además, los parámetros orbitales así como las masas de sus componentes y discutimos sobre la detección de una tercera componente en el sistema.

4.1. Observaciones y calibración de datos

Los apuntados del VLBA se acomodaron para observar 18 objetos estelares jóvenes con posible emisión de radio no térmica identificados con el VLA. Sin embargo, también incluimos otras 63 fuentes que caen dentro de los campos de visión hacia estas 18 fuentes, con el propósito de investigar su desplazamiento en el plano del cielo y especular sobre su naturaleza. Entonces, un total de 81 fuentes fueron observadas. Veintidós y 5 épocas se obtuvieron a 5 y 8 GHz, respectivamente, siendo las fuentes que se observaron a 8 GHz aquellos objetos con un índice espectral muy positivo (Ortiz-León *et al.*, 2015), que podrían no detectarse a frecuencias bajas. Asimismo, las observaciones dedicadas EC 95 que no son parte de GOBELINS se obtuvieron a 8 GHz. Finalmente, la calibración de datos y construcción de imágenes se realizaron siguiendo el procedimiento descrito en el Capítulo 3.

4.2. Detecciones

En total, 30 objetos se han detectado a la fecha. Hemos identificado que 20 de ellos son objetos de fondo que no pertenecen a Serpens o La Grieta del Aquila, ya que su desplazamiento en el plano del cielo es considerablemente menor al esperado para los objetos que pertenecen a estas regiones. De hecho, las fuentes extragalácticas muestran desplazamientos iguales a cero entre épocas consecutivas (dentro de la precisión astrométrica de

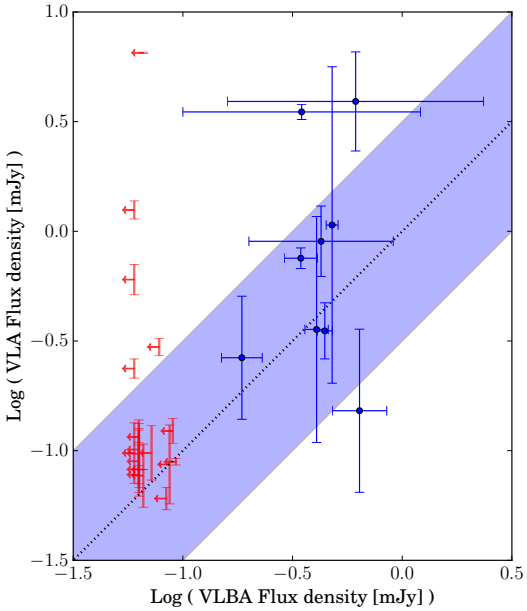

Figura 4-1 Gráfica similar a la Figura 3-2 pero para las fuentes detectadas en las regiones de Serpens y la Grieta del Aquila. Los flujos VLA se tomaron de Ortiz-León *et al.* (2015, c.f. Capítulo 2).

las observaciones).

La temperatura de brillo de las fuentes detectadas con el VLBA es $\gtrsim 10^6$ K, consistente con emisión no térmica. De manera similar al análisis presentado para las fuentes en Ofiuco, mostramos en la Figura 4-1 la relación entre el flujo VLA reportado en Ortiz-León *et al.* (2015) y el flujo medido con el VLBA. Una vez más encontramos que, dentro de las barras de error, las estrellas jóvenes detectadas con el VLBA caen cerca de la línea $S_{\rm VLA} = S_{\rm VLBA}$. Esto quiere decir que el flujo de radio total de los objetos a los que el VLBA es sensitivo es enteramente no térmico, pues si hubiera una contibución térmica, los objetos se ubicarían por arriba la linea de identidad.

Los objetos estelares jóvenes que se han observado pero no detectado con el VLBA

Table 4-1. Objetos estelares jóvenes en Serpens/Aquila no detectados con el VLBA

Fuente (1)	Flujo máx.[1] (VLA) a 5 GHz (mJy) (2)	Variabilidad[1] (%) (3)	Lím. sup. de flujo a 5 GHz (mJy) (4)	Num. de obs. (5)	Clase evolutiva (6)
J182929.78+012158.1	0.0855	–	<0.063	5	Class II
J182951.17+011640.4	0.138	$> 51 \pm 16$	<0.063	5	Class I
J182952.22+011547.4	0.126	16 ± 23	<0.063	6	Class I
J182956.96+011247.6	0.1072	–	<0.066	1	Class II
J182957.60+011300.2	0.134	47 ± 20	<0.06	1	Class I
J182957.85+011251.1	0.109	$> 43 \pm 19$	<0.063	1	Class I
J182959.55+011158.1	0.124	$> 48 \pm 12$	<0.063	1	Class I
J182959.94+011311.3	0.133	42 ± 20	<0.063	6	Class I
J182940.34-015127.9	<0.08	–	<0.066	1	Flat
J183105.01-020247.6	0.131	$> 56 \pm 10$	<0.087	1	Class III
J183120.65-020943.6	0.13	$> 44 \pm 12$	<0.072	1	Class III
J183122.81-020930.7	0.092	7 ± 35	<0.093	1	Class III
J183124.56-020231.9	0.068	$> 21 \pm 28$	<0.084	1	Class III
J183127.78-020449.5	0.14	23 ± 22	<0.09	1	Class III
J183127.80-020521.9	1.377	17 ± 9	<0.06	5	HAeBe
J183128.01-020517.9	0.706	27 ± 10	<0.06	5	Class II/III
J183128.65-020529.8	6.56	–	<0.066	5	Class II
J183128.67-020522.2	0.325	17 ± 14	<0.078	5	Class II/III
J183130.54-020530.7	0.262	18 ± 27	<0.06	4	Class III

[1]El flujo medido por el VLA y su variabilidad a 5 GHz se tomaron de Ortiz-León *et al.* (2015). Las incertidumbres asociadas a la variabilidad corresponden a una desviación de 1σ.

se listan en la Tabla 4-1. Una fracción considerable de ellos tienen flujos medidos con el VLA que caen por debajo del límite de detección del VLBA (~ 150 μJy), lo que explica por qué han permanecido sin detectarse. Por otro lado, 5 objetos son fuentes de radio suficientemente brillantes y su no detección con el VLBA sugiere que el flujo observado con el VLA es térmico. Sin embargo, casi todos estos objetos se han clasificado en la literatura como estrellas de Clase II/III, y es de esperarse que ya hayan despejado su material circunestelar. Por consiguiente, no es clara la razón por la que estos objetos se mantienen como fuentes de radio térmicas.

4.3. Astrometría

A diferencia de las fuentes en Ofiuco, los ajustes astrométricos para las fuentes en Serpens y el Aquila se realizaron minimizando por separado la χ^2 asociada a la ascensión recta y a la declinación. Esto es, los parámetros α_0, $\mu_\alpha \cos\delta$ y ϖ_α se obtienen al minimizar $\chi^2_\alpha = \sum_i^n \left[\frac{\alpha_i - \alpha(t_i)}{\sigma_{\alpha,i}}\right]^2$, mientras que δ_0, μ_δ y ϖ_δ al minimizar $\chi^2_\delta = \sum_i^n \left[\frac{\delta_i - \delta(t_i)}{\sigma_{\delta,i}}\right]^2$. El valor final de ϖ resulta de tomar el promedio pesado entre ϖ_α y ϖ_δ. Después, los valores finales de la posición en la época de referencia y de los movimientos propios se derivan repitiendo los ajustes por separado pero manteniendo el valor de la paralaje constante e igual a ϖ. Verificamos que este método produce parámetros astrométricos esencialmente idénticos a los que se obtienen si los 5 parámetros se ajustan simultáneamente, como en el caso de las fuentes de Ofiuco. Sin embargo, las incertidumbres de los elementos astrométricos obtenidos en el ajuste simultáneo serán siempre menores a las incertidumbres que se obtienen del ajuste por separado, porque el número de parámetros libres se reduce de 5 a 3.

Las distancias individuales obtenidas hacia las 3 fuentes en Serpens son consistentes con las distancias que derivamos para las fuentes en W40 y el promedio de las 7 fuentes da 436.0 ± 9.2 pc. Las velocidades tangenciales de los dos cúmulos tambien son similares y apuntan hacia una misma dirección. Entonces, nuestras observaciones sugieren que las regiones de Serpens y W40 están asociadas físicamente y pertenecen a una sola gran estructura de nubes moleculares. Ningún objeto estelar joven perteneciente a Serpens Sur se ha detectado con el VLBA, y por tanto no ha sido posible realizar mediciones astrométricas hacia este cúmulo. Existen, sin embargo, mediciones de la velocidad de Serpens Sur, con respecto al sistema local de reposo, obtenidas a partir de observaciones de líneas moleculares (Gutermuth *et al.*, 2008; Bontemps *et al.*, 2010). Estas mediciones arrojan valores similares a la velocidad medida para Serpens y W40, lo cual apunta a que los tres cúmulos se mueven similarmente, por lo que Serpens Sur posiblemente también está asociado con Serpens y W40.

La estimación de 225 ± 55 pc obtenida por Straižys *et al.* (2003) es probablemente

correcta para el complejo de nubes localizado enfrente de las regiones de formación estelar en Serpens y W40. Estos autores utilizaron ∼ 500 estrellas pertenecientes a Serpens, con una magnitud de hasta $V \sim 13$, para estimar la extinción en el visible A_V y la distancia hacia la pared de extinción en la dirección de Serpens. Sugirieron, además, que la profundidad del complejo de nubes es aproximadamente 80 pc. Suponiendo que su estimación es correcta, y considerando una desviación de $3\sigma = 165$ pc, encontramos que el extremo lejano del complejo se encuentra a 470 pc, lo cual es totalmente consistente con la nueva determinación dada aquí.

4.4. EC 95

EC 95 es un objeto protoestelar localizado en el núcleo de Serpens. Los primeros en identificarla como un sistema binario fueron Dzib *et al.* (2010), quienes sugirieron que sus componentes se encuentran en una órbita con un periodo de aproximadamente 17 años. Utilizando 11 épocas de observaciones con el VLBA, estos autores también derivaron la paralaje trigonométrica del sistema al modelar las posiciones de la componente secundaria con un movimiento uniformemente acelerado. GOBELINS ha arrojado nuevos datos astrométricos de esta fuente que, en conjunto con los previamente publicados por Dzib *et al.* (2010) y Dzib *et al.* (2011), cubren una escala temporal de ∼ 8 años. En estas observaciones, hemos detectado las dos componentes del sistema en un número suficiente de veces tal que podemos llevar a cabo un análisis más complejo para modelar la órbita del sistema. Para ello, utilizamos los modelos de ajuste de parámetros astrométricos y orbitales que fueron introducidos en el Capítulo 3. Derivamos un periodo orbital de 21.5 ± 1.5 años y masas individuales de 2.0 ± 0.2 y $2.3 \pm 0.1\ M_\odot$, resultando en una masa total de $4.3 \pm 0.2\ M_\odot$, lo cual es consistente con la estimación previa de Preibisch (1999).

Durante dos épocas observadas con el VLBA detectamos una tercera fuente de radio localizada a ∼ 140 mas de EC 95 con ángulo de posición ∼ 50º. Esta fuente también fue detectada en observaciones en el cercano infrarrojo realizadas en Mayo de 2005 con

el Telescopio Muy Grande (VLT por *Very Large Telescope*) a una separación y ángulo de posición similares a los de la fuente de radio. Dada su proximidad con respecto a la binaria ($\sim$ 65 UA a la distancia de Serpens), es posible que esta tercera componente esté ligada gravitacionalmente a EC 95. Sin embargo, el número limitado de detecciones que hemos colectado para esta componente nos impide intentar modelar su órbita para corroborar esta asociación. Es interesante, y a la vez desafortunado, el hecho de que la tercera compañera permanezca sin detectarse con el VLBA desde 2012, lo que indica que posiblemente se encuentra en un estado bajo de actividad magnética.

El artículo que contiene los resultados aquí discutidos ha sido aceptado para su publicación en el ApJ y se incluyen eseguida.

Draft version October 10, 2016
Preprint typeset using LaTeX style AASTeX6 v. 1.0

THE GOULD'S BELT DISTANCES SURVEY (GOBELINS) III. THE DISTANCE TO THE SERPENS/AQUILA MOLECULAR COMPLEX

Gisela N. Ortiz-León[1], Sergio A. Dzib[2], Marina A. Kounkel[3], Laurent Loinard[1,2], Amy J. Mioduszewski[4], Luis F. Rodríguez[1], Rosa M. Torres[5], Gerardo Pech[1], Juana L. Rivera[1], Lee Hartmann[3], Andrew F. Boden[6], Neal J. Evans II[7], Cesar Briceño[8], John J. Tobin[9,10], and Phillip A. B. Galli[11,12]

[1]Instituto de Radioastronomía y Astrofísica, Universidad Nacional Autónoma de México, Morelia 58089, México

[2]Max Planck Institut für Radioastronomie, Auf dem Hügel 69, D-53121 Bonn, Germany

[3]Department of Astronomy, University of Michigan, 500 Church Street, Ann Arbor, MI 48105, USA

[4]National Radio Astronomy Observatory, Domenici Science Operations Center, 1003 Lopezville Road, Socorro, NM 87801, USA

[5]Centro Universitario de Tonalá, Universidad de Guadalajara, Avenida Nuevo Periférico No. 555, Ejido San José Tatepozco, C.P. 48525, Tonalá, Jalisco, México.

[6]Division of Physics, Math and Astronomy, California Institute of Technology, 1200 East California Boulevard, Pasadena, CA 91125, USA

[7]Department of Astronomy, The University of Texas at Austin, 2515 Speedway, Stop C1400, Austin, TX 78712-1205, USA

[8]Cerro Tololo Interamerican Observatory, Casilla 603, La Serena, Chile

[9]Homer L. Dodge Department of Physics and Astronomy, University of Oklahoma, 440 W. Brooks Street, Norman, OK 73019, USA

[10]Leiden Observatory, PO Box 9513, NL-2300 RA, Leiden, The Netherlands

[11]Instituto de Astronomia, Geofísica e Ciências Atmosféricas, Universidade de São Paulo, Rua do Matão 1226, Cidade Universitária, São Paulo, Brazil

[12]Univ. Grenoble Alpes, IPAG, 38000, Grenoble, France

ABSTRACT

We report on new distances and proper motions to seven stars across the Serpens/Aquila complex. The observations were obtained as part of the Gould's Belt Distances Survey (GOBELINS) project between September 2013 and April 2016 with the Very Long Baseline Array (VLBA). One of our targets is the proto-Herbig AeBe object EC 95, which is a binary system embedded in the Serpens Core. For this system, we combined the GOBELINS observations with previous VLBA data to cover a total period of 8 years, and derive the orbital elements and an updated source distance. The individual distances to sources in the complex are fully consistent with each other, and the mean value corresponds to a distance of 436.0 ± 9.2 pc for the Serpens/W40 complex. Given this new evidence, we argue that Serpens Main, W40 and Serpens South are physically associated and form a single cloud structure.

Keywords: astrometry - radiation mechanisms: non-thermal - radio continuum: stars - techniques: interferometric

1. INTRODUCTION

The Serpens molecular cloud is a region rich in low-mass star formation selected for observations as part of the Gould's Belt Distances Survey (GOBELINS; Ortiz-León et al. 2016). There are two smaller regions, of ~ 1 deg^2 in size, associated with this cloud: Serpens Main and Serpens South. Serpens Main (centered on R.A. $18^{\rm h}29^{\rm m}00^{\rm s}$, Dec. $+00^{\rm o}30'00''$; Eiroa et al. 2008) consists of three prominent sub-regions; namely the Serpens core, Serpens G3-G6 and VV Serpentis. Its northernmost sub-region is the Serpens core (also called Serpens North or Cluster A; Harvey et al. 2006), a cluster of YSOs deeply embedded with extinction exceeding 40 mag in the visual. This sub-region has numerous observations from X-rays to the submillimeter that have revealed a large population of protostars (e.g., Kaas et al. 2004; Eiroa et al. 2005; Harvey et al. 2006, 2007; Winston et al. 2007, 2009; Oliveira et al. 2010). Serpens G3-G6 Cohen & Kuhi (1979), also referred to as Cluster B, was identified by Harvey et al. (2006) as a cluster of star formation harboring many previously unknown young stellar objects (YSOs). Finally, VV Serpentis is the southernmost sub-

g.ortiz@crya.unam.mx

region associated to the eponymous star. Presently, the most extensive study of the young stellar population in Serpens Main was conducted by the Spitzer Legacy Program "From Molecular Cores to Planet-Forming Disks" (c2d; Evans et al. 2003), where more than two hundred Class 0 to Class III YSOs associated with IR excess were identified in an area of 0.85 deg^2 (Dunham et al. 2015). Serpens South (centered on R.A. $18^{\rm h}30^{\rm m}00^{\rm s}$, Dec. $-02^{\rm o}02'00''$, i.e. at an angular distance of $\sim 3^{\rm o}$ to the south of Serpens Main) was discovered by Gutermuth et al. (2008). Since then, it has received a lot of attention because of the large number of extremely young objects that it contains. It shows an unusually large fraction of protostars (Gutermuth et al. 2008), presenting an excellent laboratory to study the earliest stages of star formation.

To the east of Serpens South, at R.A. $\sim 18^{\rm h}31^{\rm m}29^{\rm s}$, Dec. $-02^{\rm o}05'24''$, lies the W40 complex, named after the H II region, also known as Sharpless 2-64 (Smith et al. 1985; Vallee 1987). This complex shows evidence for ongoing star formation, since it contains dense molecular cores (Dobashi et al. 2005), millimeter-wave sources (Molinari et al. 1996; Maury et al. 2011), and YSOs (Kuhn et al. 2010; Rodríguez et al. 2010; Mallick et al. 2013). There is also a cluster of massive stars which ionizes the H II region (Smith et al. 1985; Shuping et al. 2012). Both Serpens South and W40 belong to a larger complex of molecular clouds collectively known as the *Aquila Rift*, a large elongated feature seen in 2MASS extinction maps (Bontemps et al. 2010). The Aquila Rift was one of the clouds targeted by the *Herschel* (André et al. 2010; Könyves et al. 2015) and *Spitzer* (Dunham et al. 2015) Gould Belt Surveys, which revealed hundreds of YSOs all across the complex. Figure 1 shows the location of the Serpens Main region, as well as the position of W40 and Serpens South within the Aquila Complex. We note that, although Serpens and the Aquila Rift do not formally belong to the Gould's Belt, they are usually included in Gould Belt Surveys because of their star-formation activity, and because they were previously thought to be closer to the Sun.

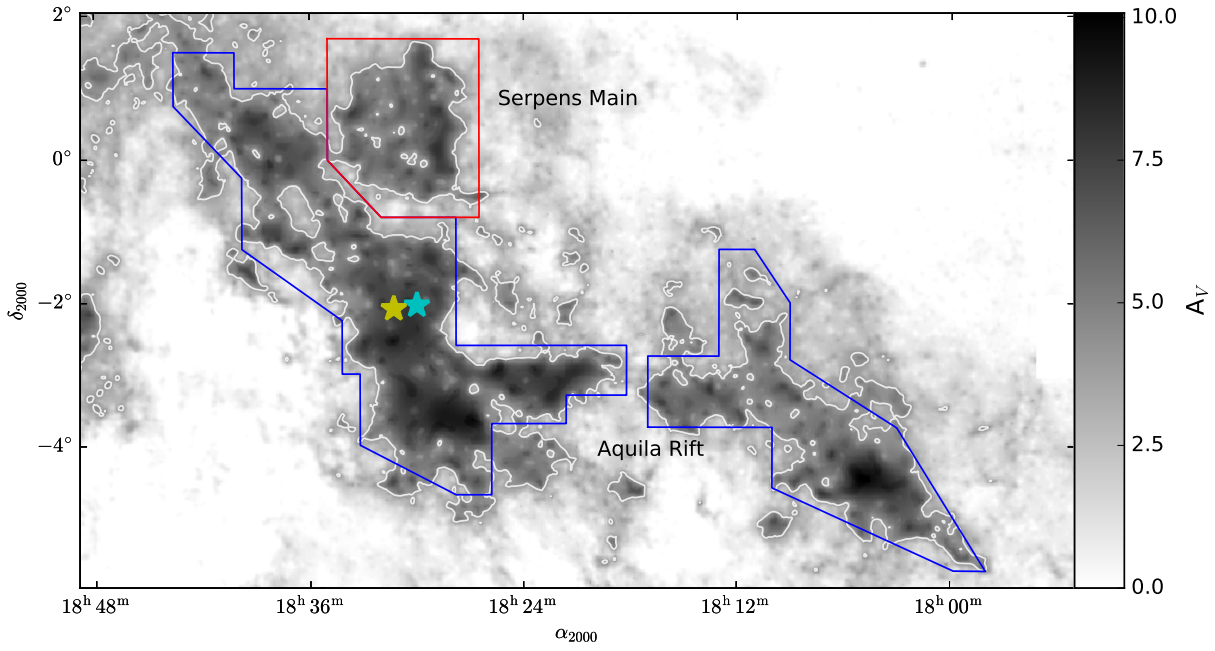

Figure 1. Extinction map of the Serpens and Aquila star-forming regions obtained as part of the COMPLETE project, based on the STScI Digitized Sky Survey data (Cambrésy 1999). Red and blue polygons mark the structures corresponding to Serpens Main and the Aquila Rift, respectively, while cyan and yellow stars indicate the center of the W40 and Serpens South regions. The white contour indicates an A_V of 4.

1.1. *The distance to the clouds in Serpens/Aquila*

The distances to the different regions in the Serpens/Aquila Complex have been a matter of controversy. For Serpens Main, there is an ample range of distances reported in the literature, from 245 ± 30 pc (Chavarria-K. et al. 1988) to 650 ± 180 pc (Zhang et al. 1988). Most of these estimates are indirect, since they are often based on spectroscopic parallaxes and extinction measurements. Winston et al. (2010) constructed the X-ray luminosity function of the Serpens cluster using different distances to calculate the X-ray luminosity, and fitted the data with the distribution

determined by Feigelson & Getman (2005) for Orion, IC 348 and NGC 1333. The best fit to the data was found to be at a distance to Serpens of 360^{+22}_{-13} pc. The only direct measurement of the distance to Serpens Main has been obtained by Dzib et al. (2010) and Dzib et al. (2011) from Very Long Baseline Interferometry (VLBI) trigonometric parallax of the YSO EC 95 associated with the Serpens Core. These authors derived a distance to the Serpens Core of 415 ± 5 pc and a mean distance to the Serpens cloud of 415 ± 25 pc. Later, they updated the distance to the Core to 429 ± 2 pc. However, the usually adopted distance for Serpens Main and the Aquila Rift as well is 259 ± 37 pc, which was derived by Straižys et al. (1996) from photometry of ~ 100 optically visible stars, 18 of which belong to Serpens Main. In a more recent paper, Straižys et al. (2003) used 80 stars from their original sample, as well as 400 other stars, to measure the distance to the front edge of the dark clouds (the extinction wall) in the Serpens/Aquila complex. They placed this wall at 225 ± 55 pc, and suggested that the cloud is about 80 pc deep.

As we mentioned earlier, W40 and Serpens South are embedded within the Aquila Rift. Estimates of the distance to W40 seem to favor values between 455 and 600 pc (Kolesnik & Iurevich 1983; Shuping et al. 2012), which suggests this cloud lies somewhat further away than the extinction wall of the Aquila Rift. So far, there are no distance measurements to sources in Serpens South, but many authors argue that the region is at the same distance as Serpens Main, and adopt either 260 or 429 pc (e.g., Gutermuth et al. 2008; Maury et al. 2011; Plunkett et al. 2015; Kern et al. 2016; Heiderman & Evans 2015). It has also been argued that W40 and Serpens South belong to the same continuous extinction feature and should be part of the same complex, likely at the same distance (Maury et al. 2011).

In this paper, we report on the distance to 3 stars in the Serpens cloud core and 4 objects in the W40 cluster. The observations were obtained as part of the GOBELINS project (Ortiz-León et al. 2016) with the Very Long Baseline Array (VLBA). We describe our targets and observations in Section 2. The astrometry of our sources is given in Section 3. Finally, we discuss our findings in Section 4 and provide a summary in Section 5.

2. TARGET SELECTION AND OBSERVATIONS

While both thermal and non-thermal processes produce radio emission in young stars, only brightness temperatures $\gtrsim 10^6$ K will be detectable on VLBI baselines (Thompson et al. 2007), which limits VLBI observations to non-thermal radiation. Thus, our targets consist of young stars with potentially non-thermal radio emission. This kind of emission is expected to be produced in the coronae of magnetically active stars by energetic electrons gyrating around the magnetic field lines (Feigelson & Montmerle 1999).

In Ortiz-León et al. (2015), we reported on deep radio observations carried out with the Karl Jansky Very Large Array (VLA) of three of the most prominent regions in the Serpens/Aquila Complex, namely, the Serpens Core, W40 and Serpens South. A total of 18 possible targets (known or candidate YSOs) for VLBA astrometry were identified across these three regions, based on their compactness, negative spectral index and/or variability. The VLBA was pointed at the positions of the 18 candidates, however we also correlated (i.e., changed the phase center of the correlation) at the positions of other sources which lay in the primary beam of the individual VLBA telescopes (of $10'$ in size at 5 GHz). This provided an additional 63 sources, of which 3 turned out to be YSOs with detectable non-thermal radio emission.

We refer the reader to Ortiz-León et al. (2016) for a detailed description of our observing approach. Briefly, the VLBA observations of GOBELINS were taken between 2013 September and 2016 April at $\nu = 4.9$ or 8.3 GHz (C- and X-band, respectively). The data were recorded in dual polarization mode with 256 MHz of bandwidth in each polarization, covered by 8 separate 32-MHz intermediate frequency (IF) channels. VLBA project codes, observing dates, pointing positions, and corresponding observing bands are given in Table 1. Several sets of phase calibrators were chosen according to their angular separations relative to target positions and used for multi-source phase referencing. The corresponding sets of calibrators for each pointing position (target) are listed in Table 2. One or two targets were observed in each observing session. These consisted of cycles alternating between the target(s) and the main phase calibrator: {target — calibrator} for single-target sessions, and {target 1 — calibrator — target 2 — calibrator} for those sessions where two targets were observed simultaneously. The secondary calibrators were observed every $\sim$ 50 minutes. The total integration time for each target was $\sim$ 1.6 hours in projects that observed at 8.3 GHz, and $\sim$ 1 hour at 4.9 GHz. Geodetic-like blocks, consisting of observations of many calibrators over a wide range of elevations, were taken before and after each session. These were observed with 512 MHz total bandwidth covered by 16 IFs and centered at $\nu = 4.6$ and 8.1 GHz for projects observing at C- and X-band, respectively.

Data reduction was performed using AIPS (Greisen 2003), following the strategy described in Ortiz-León et al. (2016). Calibrated visibilities were imaged using a pixel size of 50–100 μas and pure natural weighting. Typical angular resolutions were 4 mas $\times$ 2 mas ($\sim$ 1.3 AU at a distance of 429 pc) at 4.9 GHz and 3 mas $\times$ 0.9 mas ($\sim$ 0.8 AU) at 8.3 GHz. Noise levels were typically 30 and 38 μJy beam^{-1} at C- and X-band, respectively.

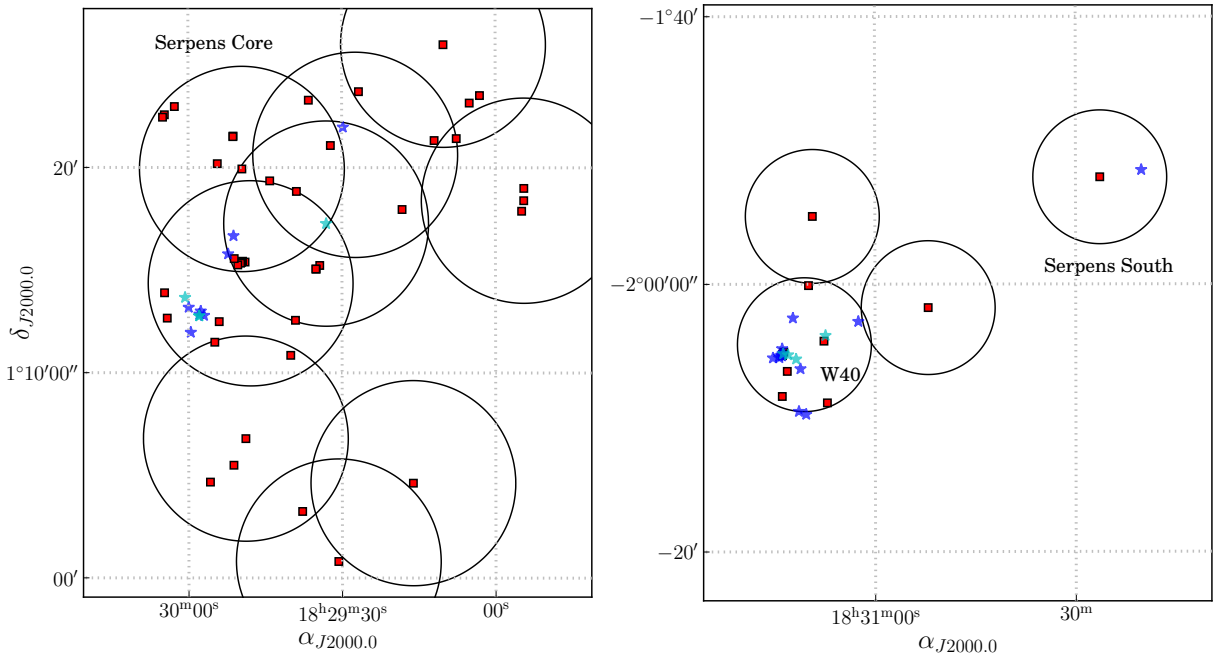

Figure 2. Spatial distribution of observed sources in the Serpens Core (left) and W40/Serpens South (Right). Blue and cyan stars correspond to known YSOs and YSOs with a distance estimation provided in this paper, respectively. Red squares mark the positions of other unclassified observed sources.

In addition, we will use of data from VLBA projects BL155 and BL160 (P.I.: L. Loinard) and BD155 (P.I.: S. Dzib) which were designed to only observe the source EC 95 between 2007, December and 2016, January at $\nu = 8.4$ GHz. The images corresponding to these old observations have noise levels of 76 μJy beam^{-1}.

3. RESULTS

As mentioned earlier, we observed a total of 81 sources in the Serpens/Aquila region. Their spatial distribution is shown in Figure 2, while source VLA coordinates, names, source types, fluxes and brightness temperatures, T_b, are given in the first eight columns in Table 3. Out of the total observed sources, 30 have been firmly detected. These are sources detected in several epochs, with at least one detection at 5σ, or sources detected just in one epoch but at 6σ, where σ is the *rms* noise measured in the images. All sources show $T_b > 10^6$ K, consistent with the brightness temperature expected for non-thermal emission.

3.1. *Individual distances: Single stars*

Source positions at individual epochs were extracted by performing two-dimensional Gaussian fits with the AIPS task JMFIT. These and the associated uncertainties provided by JMFIT, which are based on the expected theoretical astrometric precision of an interferometer (Condon 1997), are listed in Table 7. We analyze the motion of all objects detected in at least 2 epochs. A total of 20 objects, which do not have a firm classification in the literature, show a motion consistent with that expected for background sources, i.e., their positions remain systematically unchanged within the positional errors, or even if they move, their derived parallaxes correspond to distances larger than 1 kpc. This can be seen grapically in Figure 3. The horizontal axis of this plot corresponds to the *position change rate* in milli-arcseconds (mas) per year, which we define as the shift in position between consecutive epochs, normalized to one year, and averaged over all consecutive pairs of epochs. The 20 unclassified objects have position change rates below 3 mas yr^{-1}, while objects that belong to Serpens or W40 clearly show larger values because of the significant contribution of their parallax and proper motion. We identify these 20 objects as background sources and give a "B" flag in Column 3 of Table 3. Note that not all these sources are necessarily extragalactic. Some might be Galactic objects located behind the Serpens/Aquila complex. For example, the fit to the positions of the source PMN 1829+0101 yields a distance of $4.025^{+0.854}_{-0.600}$ kpc (Section 3.3). The large number of background sources detected here with the VLBA is not surprising. Oliveira et al. (2009) determined that 25% of the YSO candidates with IR excess in the Serpens/Aquila complex are actually background giants. As stated by these authors, this is consistent

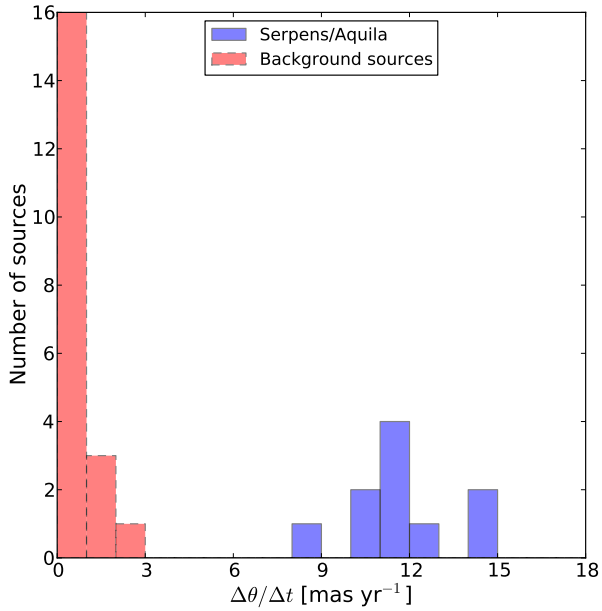

Figure 3. Histogram of position change rate for all sources detected at least twice toward Serpens/Aquila. The sources previously identified as members of the complex are shown as a blue histogram. These are 10 sources: 5 single YSOs, the 4 components of the two binary systems and the B1V star. The source KGF 138 is not shown because it has been detected only once. Other sources, whose classification is unknown in the literature, are shown as a red histogram.

with the location of the regions being close to the Galactic plane.

Only 8 VLBA-detected objects are previously known YSOs, and one more object is a B1V star. Out of these 9 objects, two are resolved into double components in the GOBELINS data, while 7 are single stars. This gives a total of 11 individual objects. The astrometry of 5 single stars is given in the present section; the other two single objects will be presented in a later paper because they were not detected often enough to do astrometric fits. The two binaries are discussed in Section 3.2.

Parallax, ϖ, position at median epoch, (α_0, δ_0), and proper motions μ_α, and μ_δ are derived by fitting the equations

$$\alpha(t) = \alpha_0 + (\mu_\alpha \cos\delta)t + \varpi_\alpha f_\alpha(t), \quad (1)$$

$$\delta(t) = \delta_0 + \mu_\delta t + \varpi_\delta f_\delta(t), \quad (2)$$

to the measured positions and minimizing separately χ^2_α and χ^2_δ along the right ascension and declination directions, respectively. Here, f_α and f_δ are the projections of the parallactic ellipse over α and δ, respectively. The values of the parallax determined in right ascension (ϖ_α) and declination (ϖ_δ) were then weighted-averaged to produce a single parallax value. The fit is then repeated to solve for the remaining parameters while holding the best fit parallax solution constant. We show the resulting best fits in Figure 4, and summarize the derived astrometric parameters in Table 5. Errors in the model parameters depend on the positional uncertainties of all the individual detections as measured by JMFIT. However, systematic offsets in positions could be introduced by errors in station coordinates, Earth rotation parameters, reference source coordinates, and tropospheric zenith delays (Pradel et al. 2006). When data from many epochs are available, these systematic offsets can be estimated by scaling the positional errors provided by JMFIT until the reduced χ^2 of the fit becomes equal to 1 (e.g., Menten et al. 2007). Here we are not able to apply this approach given that we have typically 3–4 epochs available for each source. We thus estimate systematic errors by using the empirical relations found by Pradel et al. (2006), according to which the VLBA astrometric accuracy scales linearly with the target to reference source angular separation. We obtain $\Delta\alpha\cos\delta = 0.052 - 0.070$ mas and $\Delta\delta = 0.124 - 0.182$ mas by extrapolating the astrometric errors given in Tables 3 and 4 in Pradel et al. (2006) for a source at a declination of 0° (the range in errors corresponds to the different source to calibrator angular separations). In order to estimate the offsets introduced by ionospheric phase delays, we follow the approach outlined in Kounkel et. al. (2016, submitted). Source positions were referenced to a secondary phase calibrator by adding offsets such

that the position of this secondary calibrator remains fixed in all epochs. We repeat the astrometric fits to the re-referenced target positions obtaining a different solution to that derived when all positions are referenced to the main phase calibrator. We take the difference in the distance solutions divided by the angular separation between the two phase calibrators as the phase gradient across the sky introduced by ionospheric delays. On average, this yields additional systematic offsets of $\Delta\alpha\cos\delta = 0.026$ mas and $\Delta\delta = 0.042$ mas in declination. In total, systematic errors of $\Delta\alpha\cos\delta = 0.058 - 0.075$ mas and $\Delta\delta = 0.130 - 0.187$ mas were added quadratically to the statistical errors provided by JMFIT at each individual epoch and used in the last iteration of the fits.

We discuss separately the properties of these objects in the following sections. Sources names come from the X-ray surveys by Giardino et al. (2007, GFM) and Kuhn et al. (2010, KGF).

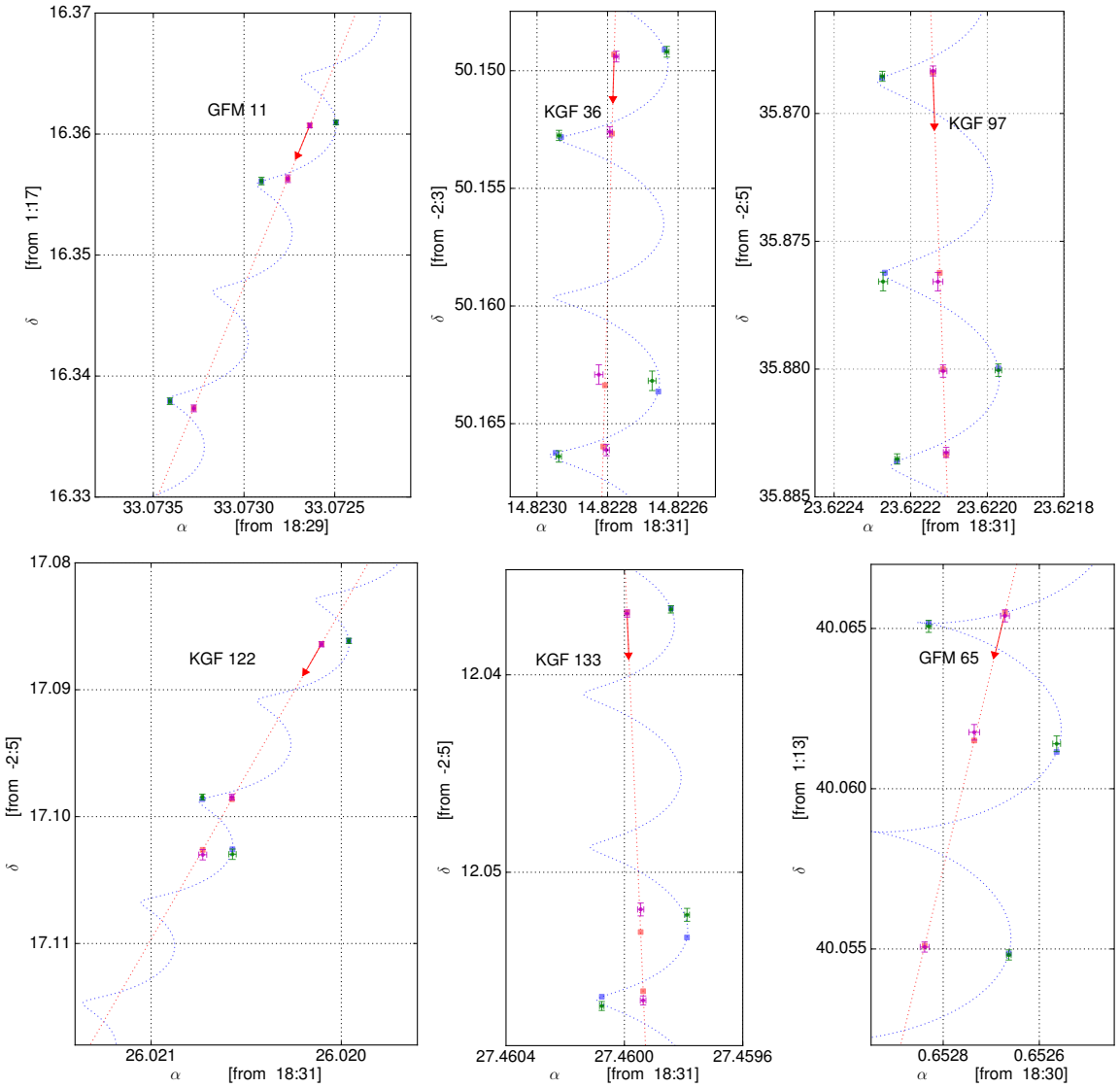

Figure 4. Observed positions and best fits for six sources. Measured positions are shown as green dots, and expected positions from the fits as blue squares. The blue dotted line is the full model, and the red line is the model with the parallax signature removed. The red squares indicate the position of the source expected from the model without parallax, while magenta dots are measured positions with parallax signature removed. The arrow indicates the direction of position change with time.

3.1.1. *GFM 11 = GBS-VLA J182933.07+011716.3*

GFM 11 is a Class III YSO (Giardino et al. 2007). Its spectral type remains somewhat uncertain: between G2.5 (Winston et al. 2010) and K0 (Erickson et al. 2015). The source has a spectral index[1] of $+0.3 \pm 0.2$, and shows high levels of variability in both VLA ($> 73\%$; Ortiz-León et al. 2015) and VLBA observations. Based on optical spectroscopy, Erickson et al. (2015) estimated a mass of 2.0 $M_\odot$ for the source.

3.1.2. *KGF 36 = GBS-VLA J183114.82-020350.1*

This source, identified as a main sequence star of B1 spectral type by Shuping et al. (2012), is located in the W40 cluster. Its radio flux as measured by the VLA shows variations of $44 \pm 9\%$ on time scales of months at 4.5 GHz, and it has a spectral index of $+0.3 \pm 0.2$. Shuping et al. (2012) also suggested that KGF 36 is probably a binary source due to the presence of strong He I 1.083 μm absorption in the star spectra. However, our VLBA observations have detected a single source with no sign of a close companion in the parallax fit. Non-thermal emission has been confirmed in other early-type B stars. The source S1 in Ophiuchus (Andre et al. 1988) is perhaps the most documented case. Kuhn et al. (2010) derived a photometric mass of 17 $M_\odot$ from a color–magnitude J vs. J–H diagram assuming distance of 600 pc and age of 1 Myr.

3.1.3. *KGF 97 = GBS-VLA J183123.62-020535.8*

KGF 97, whose spectral type is unknown, is also a YSO also located in the W40 cluster. Since the source does not show excess in the infrared K_s-Band, it is classified as a Class III object, with a mass of 3.3 ± 1.0 $M_\odot$ (Kuhn et al. 2010, reduced by a factor of ~ 2 given a distance of 436 pc). The source is found to be very variable in our VLBA observations by a factor > 10. Additionally, it is one of the few sources of the cluster detected in circular polarization (Ortiz-León et al. 2015), a strong signature of gyrosynchrotron radiation. The spectral index is -0.1 ± 0.1.

3.1.4. *KGF 122 = GBS-VLA J183126.02-020517.0*

This source was classified as a low-mass Class II YSO by Shuping et al. (2012) based on the analysis of infrared data. It shows high flux variations in both VLA ($52 \pm 5\%$ at 4.5 GHz) and VLBA observations, and has a negative spectral index of -0.6 ± 0.2. Kuhn et al. (2010) estimated a photometric mass of 16 $M_\odot$ for the source, and a bolometric luminosity of $2.9 \times 10^4 L_\odot$, assuming 600 pc as the distance to the cluster (a lower distance of 436 pc reduces the luminosity and mass by a factor of ~ 2). Thus, the source may be associated to an early-type source. We discard the last measured source position for the derivation of the astrometric parameters because it significantly deteriorates the quality of the fit and, since we ignore the source of any positional error that may be introduced in this particular epoch, we cannot correct the source position.

3.1.5. *KGF 133 = GBS-VLA J183127.45-020512.0*

KGF 133 was identified as a Class II/III YSO by Mallick et al. (2013) based on *Spitzer* and near-IR data. Like the rest of the VLBA-detected YSOs, the source is very variable in radio, with fluctuations of $96 \pm 1\%$ at 4.5 GHz (Ortiz-León et al. 2015). The spectral index of the source is $+0.3 \pm 0.2$. The mass of the source is not yet well constrained. Kuhn et al. (2010) derived a photometric mass of 24 $M_\odot$ (reduced to ~ 12 $M_\odot$ for a distance of 436 pc), but the associated error is uncertain and not provided by these authors.

3.2. *Multiple systems*

3.2.1. *GFM 65 = GBS-VLA J183000.65+011340.0*

This source is a M0.5, 0.96 $M_\odot$ star (Winston et al. 2010) located in the Serpens Core. It was classified as a Class III object by Giardino et al. (2007). Based on multi-epoch VLA observations, Ortiz-León et al. (2015) found that the source shows large flux variations ($> 75\%$) on time scales of months, and measured a spectral index of -0.9 ± 0.4. Both properties of the radio emission are fully consistent with its non-thermal nature. Because of this variability, the source has been detected with the VLBA just in 3 of the 6 observed epochs. Another source, possible a gravitationally bound companion, was detecetd in two epochs separated by $\sim$5 mas from the primary. We are not able to constrain the orbit of the system using our present small number of detections. We perform the parallax fit for only one component following the procedure described in Section 3.1.

[1] From VLA measurements published in Ortiz-León et al. (2015). The spectral index was taken between 4.5 and 7.5 GHz.

3.2.2. *EC 95 = GBS-VLA J182957.89+011246.0*

EC 95 is located in the Serpens core. The system is formed by two close components first observed by Dzib et al. (2010). Early estimations of its spectral type (∼K2 star), age (∼ 10^5 yr) and mass (∼4 $M_\odot$) indicated that the source is a proto-Herbig AeBe star (Preibisch 1999). Dzib et al. (2011) reported observations from 11 epochs taken with the VLBA at 8 GHz and reported a distance to the source of 429 ± 2 pc. Earlier, Dzib et al. (2010) performed a circular Keplerian orbit fit to the data from 8 of these 11 epochs, constraining the orbital period of the system to $10 - 20$ years.

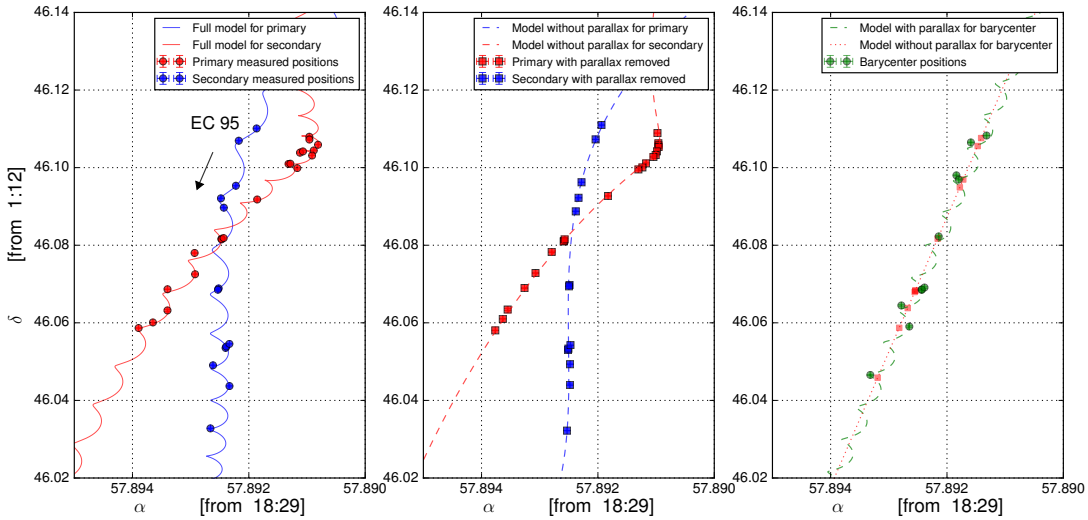

Figure 5. Observed positions of EC 95 and best astrometric fits. *Left:* Measured positions of each component are shown as red and blue circles. The solid lines show the fit corresponding to the "Full model" described in the text. The arrow indicates the direction of position change with time. *Middle:* The squares mark the measured positions with the parallax signature removed, while the dashed lines are the fits from the "Full model", also without parallax. *Right:* Green dots mark the position of the center of mass derived using the solutions from the orbital model for the mass ratio. The green dashed line is the model for the motion of the center of mass of the system, while the red line is this same model with the parallax signature removed. The red squares indicate the position of the center of mass expected from the model without parallax.

In order to derive the full orbital parameters of EC 95, we carried out follow-up VLBA observations as part of the project coded BD155, which observed the system at 8 GHz in 5 new epochs. The source has also been monitored with GOBELINS at 5 GHz, and 6 additional epochs are available. The new observations together with those previously reported by Dzib et al. (2011) cover a baseline timescale of ∼ 8 years, i.e. a significant fraction of the orbit. Old data were recalibrated homogeneously applying the same calibration strategy as for the new data, and combined with the GOBELINS observations to form a single data set. The data were fitted with two models. In the first "Full model", we fit the orbital and astrometric parameters of the system simultaneously. Orbital elements in this model are period (P), time of periastron passage (T), eccentricity (e), angle of line of nodes (Ω), inclination (i), angle from node to periastron (ω), semimajor axis (a_1) of the primary, and mass ratio (m_2/m_1). Astrometric parameters include center of mass at first epoch of the GOBELINS observations where the primary is detected ($\alpha_{\rm CM,0}$, $\delta_{\rm CM,0}$), parallax (ϖ), and proper motion (μ_α, μ_δ) of the system. For this fit, a grid of initial guesses of P, e, T, and ω is explored. The final values of these parameters are fine-tuned by the code, and the remaining model parameters are fitted directly. The first panel of Figure 5 shows the resulting best-fit curve and the measured positions of both components of the system, while the second panel shows the same fit without parallax and measured positions with parallax signature removed. Finally, the motion of the barycenter is shown in the last panel of the same figure.

In the second "Relative Model", we use the *Binary Star Combined Solution Package* to fit the positions of the secondary relative to the primary component and solve for P, T, e, Ω, i, ω, and a. The total mass of the system is then derived from Kepler's law. The solutions found by the "Full model" are used as initial guesses for this fit. Uncertainties in the orbital elements are computed from the scatter on model parameters. The best-fit solution is shown in Figure 6, and compared with the solution found by the "Full model". Solutions for the orbital elements from both models are given in Table 6. Dzib et al. (2010) argued that one of the system components should be considerably more massive than the other, however, their reported observations only covered a small fraction of the complete orbit. Here, based on a larger number of observations, we have derived a similar mass for both components, while the total

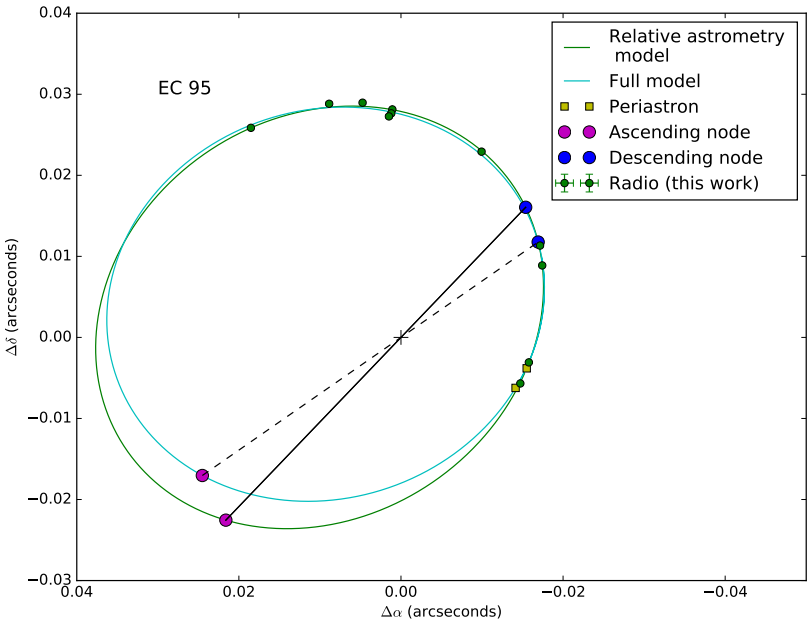

Figure 6. Relative positions of the components of the young binary system EC 95. The green points mark the detections with the VLBA. Green and cyan solid lines correspond to the "Relative astrometry" and "Full model" orbital fits, respectively. The black solid and dashed lines trace the line of nodes of the "Relative astrometry" and "Full model", respectively.

mass of $\sim 4 M_\odot$ is consistent with that estimated in past works (Preibisch 1999; Pontoppidan et al. 2004), and with the spectral type of the source.

A third source is detected in the EC95 system at two epochs at 8 and 61σ, respectively. This source was located ~ 145 mas to the North-east of the barycenter of the close binary, at a position angle of 48.3° on 2008 September 15, and ~ 138 mas in the same direction, at a position angle of 52.4° on 2012 January 9 (See Table 4). The third source was also detected in near-IR (NIR) observations taken at the VLT on 2005, May 11 and 22 (Duchêne et al. 2007). A map of the system as seen in NIR emission is shown in the first panel of Figure 7. The northernmost source is EC 92, a young ($\sim 10^5$ yr), Class I (Pontoppidan et al. 2004) and low-mass ($\sim 0.5\ M_\odot$; Preibisch 1999) star. EC 95 is the brightest source to the south in the map. While the two close components of EC 95 are unresolved, the third component is clearly visible, at a position angle of 47.2°, and separation of 152 mas from the close binary, i.e. at a position similar to that of the radio source seen in our VLBA images (Figure 7, right). Given the short angular separation of the third component relative to the close binary, it is possible that the three sources form a bound system. To investigate this possibility, we include two more free parameters in the "Full model", corresponding to the acceleration terms in right ascension, a_α, and declination, a_δ. We find that these acceleration terms are zero within the errors, and that the motion of the barycenter of the close binary remains linear during the timescale covered by our observations. This suggests that the third source may be much less massive than the close binary and following a very long period orbit. Actually, if we assume that the total mass of the system is 4.2 $M_\odot$, i.e. that the mass of the third source is negligible, we estimate an orbital period ~ 260 yr. The change in angular separation of the third companion (detected first in the NIR and then in the VLBA images) relative to the barycenter of the close binary is ~ 20 mas in 6.7 yr, while the position angle only changes ~ 5 degrees over this time scale. This is consistent, within the errors, with the expected motion of the companion on a circular orbit that has the period estimated above. Unfortunately, the third companion has remained undetectable in the radio since 2012. If there were more detections, we would constrain its astrometric parameters and investigate a possible acceleration induced by its orbital motion around the close binary.

Finally, we note that Dzib et al. (2011) estimated a distance to EC 95 of 429 ± 2 pc by modeling separately the source motion of each component as a superposition of parallax and uniform accelerated proper motion. The derived distance from the "Full model" is 435.2 ± 6.0 pc, which is consistent within 1σ with the previous determination.

3.3. *Comments on other sources: PMN 1829+0101*

PMN 1829+0101 = GBS VLA J182930.71+010048.3 is a strong radio source with reported VLA fluxes of 196.0 ± 5.9 mJy at 1.4 GHz (Ofek & Frail 2011) and 32.10 ± 5.60 mJy at 4.5 GHz (Ortiz-León et al. 2015). The source

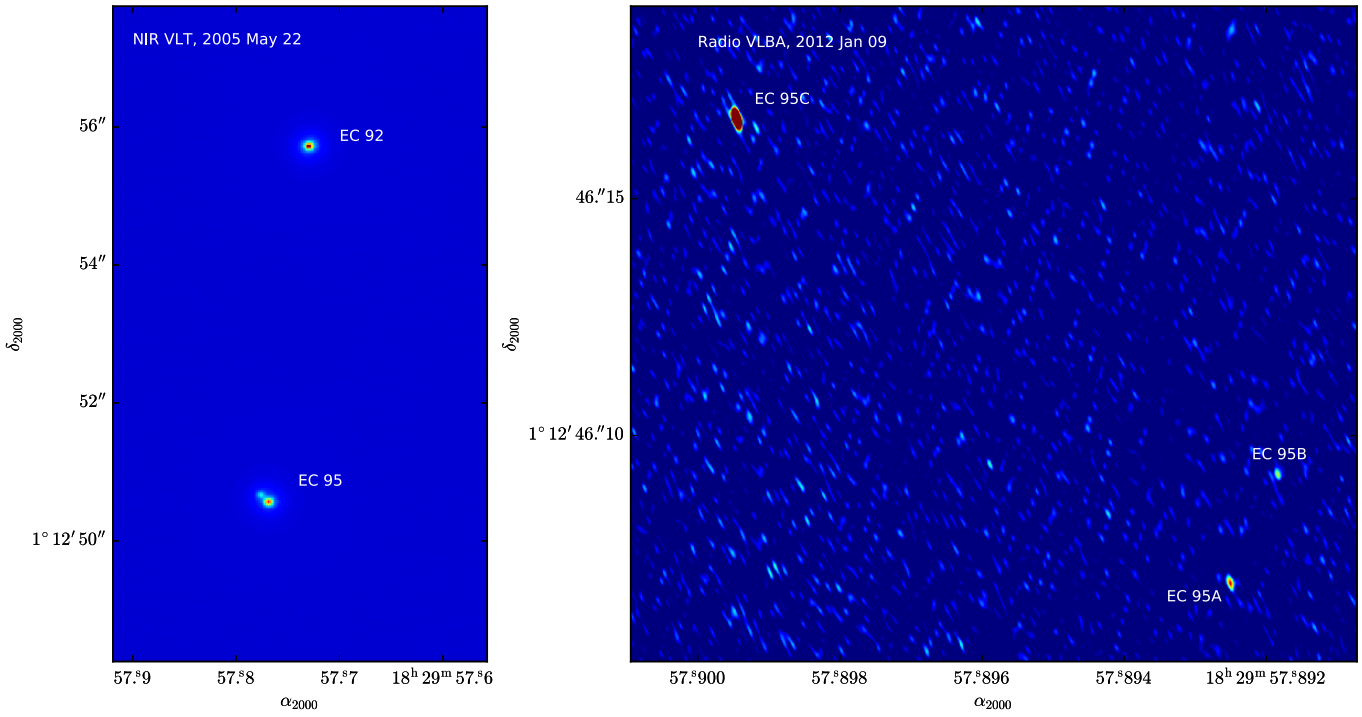

Figure 7. *Left*: NIR image of EC 92 and EC 95 taken with the VLT. *Right*: Radio image of the system EC 95 corresponding to one of the two epochs when the three sources are detected simultaneously with the VLBA.

shows an extended structure of $\sim 1.4''$ in the 4.5 GHz VLA images, but this emission is filtered out by the VLBA. There is a counterpart in X-ray emission at $\sim 1.3''$ (Xmm-Newton Survey Science Centre 2013), and in the IRAC 3.6 μm-band (Evans et al. 2003) at $\sim 1.7''$ from the radio peak. The fit to the data yields $\varpi = 0.248 \pm 0.044$ mas, corresponding to a distance of $d = 4025^{+854}_{-600}$ pc. Using this distance we derive the location (x, y, z) of the source in the Milky Way. This position is expressed in the rectangular frame centered on the location of the Sun, with the (Ox) axis pointing toward the Galactic Center, the (Oy) axis perpendicular to (Ox) and pointing in the direction of the Galactic rotation, and (Oz) pointing toward the Galactic North Pole. The source coordinates in this system are $(x, y, z) = (3443, 2096, 377)$ pc: it is located in the direction of the Scutum arm, which hosts newly formed OB-type stars, but at 377 pc above the Galactic mid-plane.

4. DISCUSSION

We have derived the distance to 7 objects in the Serpens/Aquila complex. The parallaxes for these objects are shown graphically in Figure 8, where we see clearly that sources in Serpens and Aquila share similar values. Proper motions, on the other hand, show a large spread, but this is expected as Serpens and W40 are different clusters. The weighted mean value of the 7 parallaxes is $\varpi = 2.32$ mas, with a weighted standard deviation of $\sigma_\varpi = 0.10$ mas. Only the source GMF 65, for which we derive 379.1 ± 17.0 pc, differs from the rest by more than 1 sigma. As discussed in Section 3.2.1, this source seems to be a binary system, whose orbital motion remains unmodelled because of the low number of detections. Ignoring this source yields a mean weighted parallax of $\varpi = 2.29 \pm 0.05$ mas. This corresponds to a weighted mean distance of $d = 436.0$ pc, with a standard deviation of $\sigma_d = 9.2$ pc. The standard deviation on the mean reflects only the uncertainties in the distance measurements because typical errors on individual distances are larger than 10 pc.

Note that Straižys et al. (2003) determined the near edge of the Aquila/Serpens cloud complex to be at 225 ± 55 pc, with a depth of 80 pc. Therefore, according to their estimates, the far edge of the complex lies at a distance (assuming a $+1\sigma$ deviation) of $225 + 55 + 80 = 360$ pc (Winston et al. 2010). Assuming a $+3\sigma$ deviation, we place the far edge of the cloud at a maximum distance of 470 pc, which is consistent with the mean distance to the cloud obtained here from parallax measurements.

Our measurements not only confirm the early estimation by Dzib et al. (2010) of a larger distance to Serpens than previously thought, but also show that Serpens and W40 are part of the same complex, lying at the same distance

along the line of sight. Earlier estimates based on indirect methods, e.g. by Kuhn et al. (2010) and Shuping et al. (2012), suggested a mean distance to W40 of $\sim 500 \pm 50$ pc. Based on these measurements, W40 and the Serpens region have been treated in the literature as separated objects, as such works used the value obtained by Straižys et al. (1996) of ∼260 pc for the Serpens/Aquila Rift (see e.g. Straižys et al. 2003; Gutermuth et al. 2008). When it was first discovered, Serpens South was associated with Serpens Main because both regions share similar local standard of rest (LSR) velocities (∼6–11 km s^{-1}; White et al. 1995; Gutermuth et al. 2008; Bontemps et al. 2010), indicating that they are comoving. Until recently, it has become more common to consider that Serpens South and W40 form a single cloud structure. This is because the LSR velocities measured by molecular line observations in the entire W40/Serpens South region are 4–10 km s^{-1} (Zeilik & Lada 1978; Maury et al. 2011), which are in the range of the LSR velocities measured in Serpens Main. We do not have any astrometric measurement to sources in Serpens South (because known YSOs in the cluster are intrinsically radio weak, Ortiz-León et al. 2015; Kern et al. 2016), but given its proximity and similarity in LSR velocities to W40, we speculate that these two clusters are physically associated. If this last statement is confirmed, it would represent a meaningful evidence for an association between Serpens Main, W40, and Serpens South.

Proper motions are plotted in Figure 8 after the correction for the solar peculiar motion is applied. Mean values are ($\mu_\alpha \cos\delta = 8.0 \pm 2.2$ mas yr^{-1}, $\mu_\delta = -11.6 \pm 2.9$ mas yr^{-1}) for Serpens sources, and ($\mu_\alpha \cos\delta = 3.8 \pm 4.1$ mas yr^{-1}, $\mu_\delta = -10.2 \pm 0.9$ mas yr^{-1}) for W40 sources. Uncertainties in the mean values correspond to the standard deviation of individual measurements in each cluster. It appears that the clusters are moving in similar directions, which is an additional support for our interpretation of Serpens Main and W40 being part of the same cloud complex.

Finally, we note that a larger distance to the Serpens and Aquila regions imply luminosities and dust masses larger by a factor of ~ 2.8 relative to those derived assuming 260 pc, and makes young stellar objects younger with respect to evolutionary tracks. This implies that the physical interpretation of the stellar and core population in the regions needs to be revised.

5. SUMMARY

We have analyzed multi-epoch VLBA observations taken as part of the GOBELINS project toward young stars in the Serpens and W40 regions in the Aquila complex. The astrometric fits to 7 sources, including one confirmed binary (posible triple) system, provide us with parallaxes and proper motions for single sources, as well as with the orbital parameters for the multiple system. Since individual parallaxes of sources in Serpens are consistent with those of W40 sources, we conclude that both Serpens and W40 are located at the same distance. The mean parallax value yields 436.0 ± 9.2 pc, confirming the early distance estimation obtained solely for the source EC 95 in the Serpens Core, which was also derived from a parallax measurement with the VLBA. The other 20 sources detected during the survey resulted to be background sources, not associated with the Aquila Rift.

G.N.O.-L., L.L., L.F.R., G.P., and J.L.R. acknowledge DGAPA, UNAM, CONACyT, Mexico for financial support. L.L. and G.N.O.-L. also acknowledge support from von Humboldt Stiftung. N.J.E. was supported by NSF grant AST-1109116 to the University of Texas at Austin. P.A.B.G. acknowledges financial support from FAPESP. The National Radio Astronomy Observatory is operated by Associated Universities, Inc., under cooperative agreement with the National Science Foundation.

REFERENCES

Andre, P., Montmerle, T., Feigelson, E. D., Stine, P. C., & Klein, K.-L. 1988, ApJ, 335, 940
André, P., Men'shchikov, A., Bontemps, S., et al. 2010, A&A, 518, L102
Bobylev, V. V. 2016, Astronomy Letters, 42, 544
Bontemps, S., André, P., Könyves, V., et al. 2010, A&A, 518, L85
Cambrésy, L. 1999, A&A, 345, 965
Chavarria-K., C., de Lara, E., Finkenzeller, U., Mendoza, E. E., & Ocegueda, J. 1988, A&A, 197, 151
Cohen, M., & Kuhi, L. V. 1979, ApJS, 41, 743
Condon, J. J. 1997, PASP, 109, 166
Dobashi, K., Uehara, H., Kandori, R., et al. 2005, PASJ, 57, S1
Duchêne, G., Bontemps, S., Bouvier, J., et al. 2007, A&A, 476, 229
Dunham, M. M., Allen, L. E., Evans, II, N. J., et al. 2015, ApJS, 220, 11
Dzib, S., Loinard, L., Mioduszewski, A. J., et al. 2010, ApJ, 718, 610
—. 2011, RMxAC, 40, 231
Eiroa, C., & Casali, M. M. 1995, A&A, 303, 87
Eiroa, C., Djupvik, A. A., & Casali, M. M. 2008, The Serpens Molecular Cloud, ed. B. Reipurth, 693
Eiroa, C., Torrelles, J. M., Curiel, S., & Djupvik, A. A. 2005, AJ, 130, 643
Erickson, K. L., Wilking, B. A., Meyer, M. R., et al. 2015, ApJ, 149, 103
Evans, II, N. J., Allen, L. E., Blake, G. A., et al. 2003, PASP, 115, 965

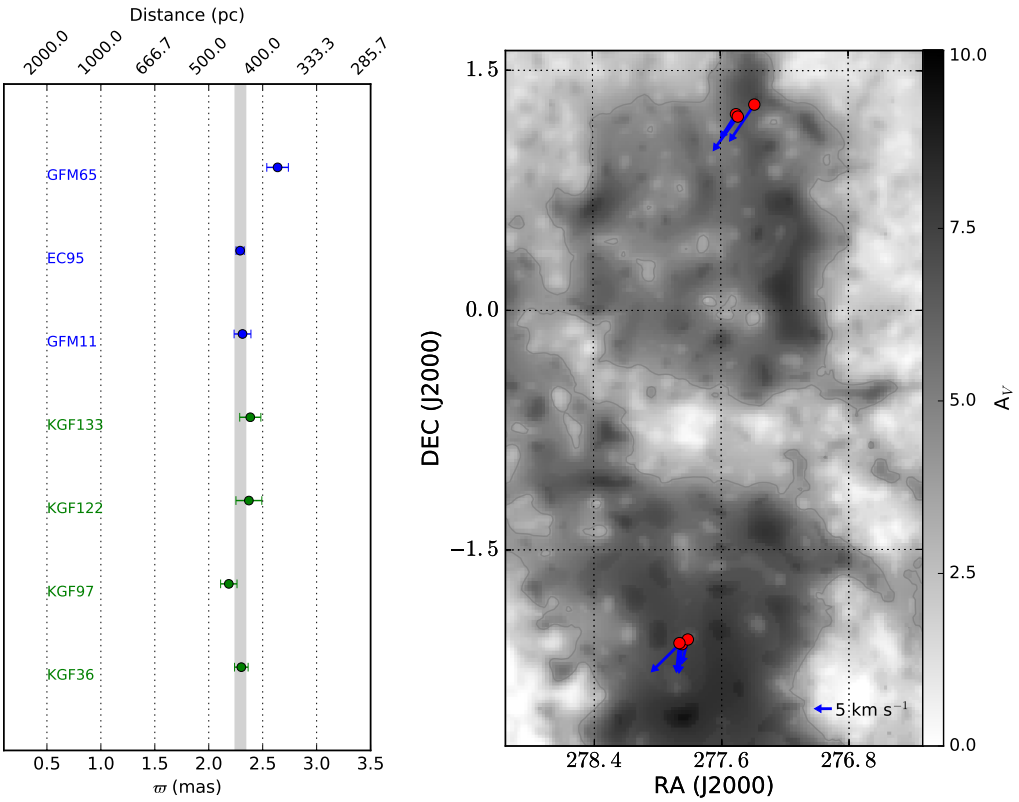

Figure 8. *Left:* Parallax results for the Serpens/Aquila complex. Blue circles and characters are for sources in the Serpens Core, while green circles and characters are for sources W40. The grey vertical bar shows the mean parallax value for all sources but GFM 65 (a binary source for which we are not able to model its orbital motion based on the data collected so far), and its standard deviation (see text). *Right:* Enlargement of Figure 1 showing the spatial distribution of the YSOs in Serpens and W40 with astrometric parameters derived in this work. The arrows represent the source tangential velocity corrected by the solar motion.

Feigelson, E. D., & Getman, K. V. 2005, ArXiv:astro-ph/0501207
Feigelson, E. D., & Montmerle, T. 1999, ARA&A, 37, 363
Giardino, G., Favata, F., Micela, G., Sciortino, S., & Winston, E. 2007, A&A, 463, 275
Greisen, E. W. 2003, Information Handling in Astronomy - Historical Vistas, 285, 109
Gutermuth, R. A., Bourke, T. L., Allen, L. E., et al. 2008, ApJL, 673, L151
Harvey, P., Merín, B., Huard, T. L., et al. 2007, ApJ, 663, 1149
Harvey, P. M., Chapman, N., Lai, S.-P., et al. 2006, ApJ, 644, 307
Heiderman, A., & Evans, II, N. J. 2015, ApJ, 806, 231
Kaas, A. A., Olofsson, G., Bontemps, S., et al. 2004, A&A, 421, 623
Kern, N. S., Keown, J. A., Tobin, J. J., Mead, A., & Gutermuth, R. A. 2016, AJ, 151, 42
Kolesnik, I. G., & Iurevich, L. V. 1983, Astrofizika, 19, 761
Könyves, V., André, P., Men'shchikov, A., et al. 2015, A&A, 584, A91
Kuhn, M. A., Getman, K. V., Feigelson, E. D., et al. 2010, ApJ, 725, 2485
Mallick, K. K., Kumar, M. S. N., Ojha, D. K., et al. 2013, ApJ, 779, 113
Maury, A. J., André, P., Men'shchikov, A., Könyves, V., & Bontemps, S. 2011, A&A, 535, A77
Menten, K. M., Reid, M. J., Forbrich, J., & Brunthaler, A. 2007, A&A, 474, 515
Molinari, S., Brand, J., Cesaroni, R., & Palla, F. 1996, A&A, 308, 573
Ofek, E. O., & Frail, D. A. 2011, ApJ, 737, 45
Oliveira, I., Mern, B., Pontoppidan, K. M., et al. 2009, ApJ, 691, 672
Oliveira, I., Pontoppidan, K. M., Merín, B., et al. 2010, ApJ, 714, 778
Ortiz-León, G. N., Loinard, L., Mioduszewski, A. J., et al. 2015, ApJ, 805, 9
Plunkett, A. L., Arce, H. G., Corder, S. A., et al. 2015, ApJ, 803, 22
Pontoppidan, K. M., van Dishoeck, E. F., & Dartois, E. 2004, A&A, 426, 925
Pradel, N., Charlot, P., & Lestrade, J.-F. 2006, A&A, 452, 1099
Preibisch, T. 1999, A&A, 345, 583
Rodríguez, L. F., Rodney, S. A., & Reipurth, B. 2010, AJ, 140, 968
Shuping, R. Y., Vacca, W. D., Kassis, M., & Yu, K. C. 2012, AJ, 144, 116
Smith, J., Bentley, A., Castelaz, M., et al. 1985, ApJ, 291, 571
Straižys, V., Černis, K., & Bartašiute, S. 1996, BaltA, 5, 125
Straižys, V., Černis, K., & Bartašiute, S. 2003, A&A, 405, 585
Thompson, A. R., Moran, J. M., & Swenson, G. W. 2007, Interferometry and Synthesis in Radio Astronomy, John Wiley & Sons, 2007.
Vallee, J. P. 1987, A&A, 178, 237
White, G. J., Casali, M. M., & Eiroa, C. 1995, A&A, 298, 594

Winston, E., Megeath, S. T., Wolk, S. J., et al. 2007, ApJ, 669, 493
—. 2009, AJ, 137, 4777
—. 2010, AJ, 140, 266
Xmm-Newton Survey Science Centre, C. 2013, VizieR Online Data Catalog, 9044
Zeilik, II, M., & Lada, C. J. 1978, ApJ, 222, 896
Zhang, C. Y., Laureijs, R. J., Wesselius, P. R., & Clark, F. O. 1988, A&A, 199, 170

Table 1. Observed epochs

Project code	Observation Date	VLBA pointing positions R.A. (α_{2000})	Decl. (δ_{2000})	Observed band
BL175E0	01 sep 2013	18:29:10.178	+01:25:59.56	C
		18:29:27.366	+01:20:37.43	
BL175E1	02 sep 2013	18:29:30.714	+01:00:48.31	C
		18:29:47.838	+01:14:21.66	
BL175E2	03 sep 2013	18:30:44.115	–02:01:45.66	C
		18:31:21.969	–02:04:52.54	
BL175E3	05 sep 2013	18:29:49.507	+01:19:55.88	C
		18:29:52.736	–01:51:59.93	
BL175E4	07 sep 2013	18:31:21.141	–02:04:31.08	X
		18:29:16.120	+01:04:37.58	
		18:29:33.073	+01:17:16.39	
BL175DX	17 feb 2014	18:31:18.685	–01:54:55.99	X
BL175G0	01 mar 2014	18:29:10.178	+01:25:59.56	C
		18:29:27.366	+01:20:37.43	
BL175G1	03 mar 2014	18:29:30.714	+01:00:48.31	C
		18:29:47.838	+01:14:21.66	
BL175G2	04 mar 2014	18:31:21.969	–02:04:52.54	C
		18:30:44.115	–02:01:45.66	
BL175G3	06 mar 2014	18:29:49.507	+01:19:55.88	C
		18:29:52.736	–01:51:59.93	
BL175G4	09 mar 2014	18:29:16.120	+01:04:37.58	X
		18:29:33.073	+01:17:16.39	
BL175GC	01 apr 2014	18:28:54.46	+01:18:23.78	C
		18:29:48.83	+01:06:47.46	
BL175CR	07 oct 2014	18:29:10.178	+01:25:59.56	C
		18:29:27.366	+01:20:37.43	
BL175CS	12 oct 2014	18:29:30.714	+01:00:48.31	C
		18:29:47.838	+01:14:21.66	
BL175CT	15 oct 2014	18:31:21.969	–02:04:52.54	C
		18:30:44.115	–02:01:45.66	
BL175EX	27 feb 2015	18:29:10.178	+01:25:59.56	C
		18:29:27.366	+01:20:37.43	
BL175EY	02 mar 2015	18:29:47.838	+01:14:21.66	C
		18:31:18.685	–01:54:55.99	
BL175EZ	20 mar 2015	18:31:21.969	–02:04:52.54	C
		18:30:44.115	–02:01:45.66	
BL175GT	15 sep 2015	18:28:54.46	+01:18:23.78	X
		18:29:48.83	+01:06:47.46	
BL175GU	19 sep 2015	18:31:21.969	–02:04:52.54	C
		18:30:44.115	–02:01:45.66	
BL175GW	04 oct 2015	18:29:10.178	+01:25:59.56	C
		18:29:27.366	+01:20:37.43	
BL175GX	06 oct 2015	18:29:47.838	+01:14:21.66	C
		18:31:18.685	–01:54:55.99	
BL175GV	11 oct 2015	18:31:21.141	–02:04:31.08	C
		18:29:16.120	+01:04:37.58	
		18:29:33.073	+01:17:16.39	

Table 1 continued on next page

Table 1 *(continued)*

Project code	Observation Date	VLBA pointing positions R.A. (α_{2000})	Decl. (δ_{2000})	Observed band
BL175GY	13 oct 2015	18:29:49.507	+01:19:55.88	C
		18:29:52.736	–01:51:59.93	
BL175CU	29 feb 2016	18:29:52.736	–01:51:59.93	C
		18:31:21.141	–02:04:31.08	
BL175F4	20 mar 2016	18:29:33.073	+01:17:16.39	X
BL175F8	28 apr 2016	18:29:47.838	+01:14:21.66	C

Table 2. Calibrators setup

R.A. (J2000)	DEC. (J2000)	Calibrators[1]
18:29:52.736	–01:51:59.93	J1834–0301, J1833+0115, J1824+0119, J1821–0502
18:31:21.141	–02:04:31.08	
18:29:47.838	+01:14:21.66	J1833+0115, J1826+0149, J1824+0119, J1832+0118
18:29:30.714	+01:00:48.31	
18:28:54.460	+01:18:23.78	J1832+0118, J1833+0115, J1826+0149, J1824+0119
18:29:48.830	+01:06:47.46	
18:31:21.969	–02:04:52.54	J1834–0301, J1833+0115, J1824+0119, J1821–0502
18:30:44.115	–02:01:45.66	
18:29:16.120	+01:04:37.58	J1826+0149, J1833+0115, J1824+0119, J1832+0118
18:29:33.073	+01:17:16.39	
18:29:10.178	+01:25:59.56	
18:29:27.366	+01:20:37.43	
18:29:33.073	+01:17:16.39	
18:31:18.685	–01:54:55.99	J1834–0301, J1824+0119, J1819–0258, J1833+0115
18:29:49.507	+01:19:55.88	J1826+0149, J1832+0118, J1833+0115, J1824+0119

[1] First source in the list corresponds to main phase calibrator.

Table 3. Detected sources

GBS-VLA name[1]	Other identifier	Type of source	Minimum flux at 5 GHz (mJy)	Maximum flux at 5 GHz (mJy)	Minimum flux at 8 GHz (mJy)	Maximum flux at 8 GHz (mJy)	log [T_b (K)][3]	SED Class
(1)	(2)	(3)	(4)	(5)	(6)	(7)	(8)	(9)
Serpens Main								
J182854.44+011859.7	–	?	–		0.26±0.05		>6.4	–
J182854.46+011823.7	–	B	3.88±0.05		6.04±0.07		8.5	–
J182854.87+011753.0	–	B	0.21±0.04		0.24±0.07		7.2	–
J182903.06+012331.0	–	B	0.49±0.05	0.76±0.07	–		7.5	–
J182905.07+012309.0	–	B	0.26±0.04	0.31±0.05	–		>6.5	–
J182910.17+012559.5	SSTc2d J182910.2+012560	B	2.70±0.05	3.45±0.05	–		9.3	–
J182911.94+012119.4	–	B	0.36±0.03	0.51±0.06	–		7.7	–
J182916.11+010437.5	SSTSL2 J182916.10+010438.6	B	0.33±0.06		0.24±0.05	0.26±0.08	8.0	–
J182918.23+011757.7	SSTc2d J182918.2+011758	B	0.19±0.05	0.25±0.05	–		7.3	–
J182926.71+012342.1	SSTSL2 J182926.72+012342.4	B	0.17±0.05	0.25±0.06	–		6.6	–
J182930.71+010048.3	PMN 1829+0101	B	3.87±0.05	7.44±0.10	–		8.7	–
J182933.07+011716.3	GFM 11	YSO	0.19±0.04		0.27±0.05	0.33±0.06	>6.6	Class III
J182935.02+011503.2	DCE08-210 5	B	0.14±0.05	0.20±0.04	–		>6.3	–
J182936.50+012317.0	SSTc2d J182936.5+012317	B	0.14±0.04	0.26±0.05	–		>6.4	–
J182944.07+011921.1	NVSS 182944+011920	B	1.41±0.04	1.74±0.04	–		>7.2	–
J182948.83+010647.4	SSTc2d J182948.8+010648	B	0.35±0.05		0.63±0.07		7.5	–
J182949.50+011955.8	–	B	1.96±0.07	2.40±0.07	–		7.6	–
J182951.04+011533.8	ETC 8	B	0.35±0.06	0.59±0.05	–		8.0	–
J182957.89+011246.0	EC 95A	YSO	0.26±0.05	1.18±0.04	–		8.3	P-HAeBe
J182957.89+011246.0	EC 95B		0.16±0.04	1.17±0.04	–		8.4	
J182957.89+011246.0	EC 95C[2]		–	–	0.86±0.19	3.68±0.10	>7.4	
J183000.65+011340.0	GFM 65A	YSO	0.26±0.05	0.50±0.04	–		>6.7	Class III
J183000.65+011340.0	GFM 65B		0.22±0.05	0.57±0.11	–		6.4	
J183004.62+012234.1	GFM 70	B	0.41±0.05	0.42±0.05	–		>6.6	–
J182952.73-015159.9	–	B	0.20±0.05	0.26±0.07	–		6.6	–
W40								
J183044.11-020145.6	2M18304408–0201458	B	1.65±0.06	2.15±0.06	–		7.9	–
J183114.82-020350.1	KGF 36	Star	0.41±0.08	0.48±0.05	0.36±0.09	0.48±0.08	7.3	–
J183118.68-015455.9	–	B	0.43±0.10	0.52±0.06	1.14±0.18		7.0	–
J183122.32-020619.6	KGF 82	YSO	0.41±0.05		0.26±0.06		7.6	Class III
J183123.62-020535.8	KGF 97	YSO	0.10±0.05	1.21±0.05	–		7.9	Class III
J183126.02-020517.0	KGF 122	YSO	0.20±0.05	0.91±0.06	–		8.0	Class II
J183127.45-020512.0	KGF 133	YSO	0.45±0.07	0.51±0.06	2.40±0.11		7.7	Class II/III
J183127.65-020509.7	KGF 138	YSO	0.35±0.06		–		>6.5	HAeBe

[1] GBS-VLA stands for Gould's Belt Very Large Array Survey (Ortiz-León et al. 2015).

[2] Data corresponding to EC 95c were taken as part of projects BL160 and BD155, and are shown here for completeness.

[3] Because most of the sources show significant flux variations, this value correspond to the maximum brightness temperature

Table 4. Measured positions of EC 95

Julian Day	Project[1]	α (J2000.0)	σ_α	δ (J2000.0)	σ_δ
EC 95A					
2454800.39885	BL160	18 29 57.89186638	0.00000180	1 12 46.110101	0.000069
2454890.14136	BL160	18 29 57.89217322	0.00000048	1 12 46.106940	0.000018
2455171.38315	BL160	18 29 57.89222331	0.00000098	1 12 46.095333	0.000041
2455268.11855	BL160	18 29 57.89247995	0.00000202	1 12 46.092081	0.000067
2455356.87555	BL160	18 29 57.89242962	0.00000117	1 12 46.089683	0.000054
2455936.29042	BD155	18 29 57.89251865	0.00000457	1 12 46.068868	0.000150
2455937.28769	BD155	18 29 57.89253227	0.00000298	1 12 46.068531	0.000082
2456522.68545	BD155	18 29 57.89239849	0.00000095	1 12 46.053528	0.000034
2456524.67999	BD155	18 29 57.89238944	0.00000228	1 12 46.053868	0.000114
2456538.70634	BL175	18 29 57.89232999	0.00000204	1 12 46.054528	0.000066
2456720.20849	BL175	18 29 57.89263275	0.00000445	1 12 46.049701	0.000122
2456943.59865	BL175	18 29 57.89233271	0.00000528	1 12 46.043694	0.000186
2457507.02912	BL175	18 29 57.89266020	0.00000104	1 12 46.032795	0.000036
EC 95B					
2454457.31822	BL156	18 29 57.89095609	0.00000120	1 12 46.107905	0.000038
2454646.81935	BL160	18 29 57.89095848	0.00000481	1 12 46.107242	0.000186
2454724.60637	BL160	18 29 57.89080948	0.00000083	1 12 46.105900	0.000029
2454800.39885	BL160	18 29 57.89088405	0.00000217	1 12 46.104416	0.000089
2454890.14136	BL160	18 29 57.89112095	0.00000388	1 12 46.103859	0.000138
2454985.89100	BL160	18 29 57.89106970	0.00000414	1 12 46.104177	0.000240
2455074.64800	BL160	18 29 57.89091190	0.00000082	1 12 46.103134	0.000032
2455268.11855	BL160	18 29 57.89131814	0.00000402	1 12 46.100962	0.000162
2455356.87555	BL160	18 29 57.89128563	0.00000363	1 12 46.101013	0.000176
2455442.64072	BL160	18 29 57.89116731	0.00000472	1 12 46.099877	0.000202
2455936.29042	BD155	18 29 57.89185545	0.00000614	1 12 46.091786	0.000156
2456522.68545	BD155	18 29 57.89246953	0.00000063	1 12 46.081657	0.000023
2456524.67999	BD155	18 29 57.89246863	0.00000421	1 12 46.081514	0.000137
2456538.70634	BL175	18 29 57.89244323	0.00000760	1 12 46.081859	0.000200
2456720.20849	BL175	18 29 57.89295395	0.00000877	1 12 46.078949	0.000243
2456943.59865	BL175	18 29 57.89292358	0.00000378	1 12 46.072521	0.000108
2457084.21205	BL175	18 29 57.89339762	0.00000179	1 12 46.068654	0.000071
2457302.61352	BL175	18 29 57.89339468	0.00000865	1 12 46.063242	0.000279
2457391.30720	BD155	18 29 57.89364862	0.00000016	1 12 46.060099	0.000006
2457507.02912	BL175	18 29 57.89389465	0.00000108	1 12 46.058656	0.000036
EC 95C					
2454724.60637	BL160	18 29 57.89856745	0.00000305	1 12 46.205651	0.000108
2455936.29042	BD155	18 29 57.89945356	0.00000060	1 12 46.166823	0.000019

[1] VLBA project code.

Table 5. Parallaxes and proper motions

GBS-VLA name (1)	Other identifier[1] (2)	Parallax (mas) (3)	$\mu_\alpha \cos\delta$ (mas yr^{-1}) (4)	μ_δ (mas yr^{-1}) (5)	Distance (pc) (6)
J182933.07+011716.3	GFM 11	2.313 ± 0.078	3.634 ± 0.050	-8.864 ± 0.127	432.3 ± 14.6
J182957.89+011246.0	EC 95	2.291 ± 0.038	3.599 ± 0.026	-8.336 ± 0.030	436.4 ± 7.1
J183000.65+011340.0	GFM 65[2]	2.638 ± 0.118	1.573 ± 0.070	-6.513 ± 0.152	379.1 ± 17.0
J183114.82-020350.1	KGF 36	2.302 ± 0.063	0.186 ± 0.053	-6.726 ± 0.121	434.5 ± 11.8
J183123.62-020535.8	KGF 97	2.186 ± 0.076	-0.258 ± 0.058	-7.514 ± 0.135	457.5 ± 16.0
J183126.02-020517.0	KGF 122	2.372 ± 0.120	4.586 ± 0.074	-7.946 ± 0.167	421.5 ± 21.4
J183127.45-020512.0	KGF 133	2.385 ± 0.098	-0.330 ± 0.049	-7.746 ± 0.111	419.3 ± 17.3

[1] GFM = Giardino et al. (2007); EC= Eiroa & Casali (1995), KGF = Kuhn et al. (2010).

[2] Parallax solution could be affected by unmodelled binary motion.

Table 6. Orbital elements of EC 95

Model	a	P	T_0	e	Ω	i	ω	M_1	M_2	M_T
	(mas)	(yr)			(^{o})	(^{o})	(^{o})	($M_\odot$)	($M_\odot$)	($M_\odot$)
(1)	(2)	(3)	(4)	(5)	(6)	(7)	(8)	(9)	(10)	(11)
Full	28.9 ± 0.4	21.5 ± 1.5	2008.85 ± 2.0	0.397 ± 0.001	124.8 ± 2.1	31.6 ± 0.9	477.5 ± 1.8	2.0 ± 0.2	2.3 ± 0.1	4.3 ± 0.2
Rel. astr.	30.7 ± 1.4	23.1 ± 1.4	2009.08 ± 0.14	0.393 ± 0.011	136.2 ± 2.5	34.8 ± 2.0	475.3 ± 2.8	–	–	4.5 ± 0.2

Table 7. Measured source positions

Julian Day	α (J2000.0)	σ_α	δ (J2000.0)	σ_δ
SSTc2d J182910.2+012560				
2456537.71083	18 29 10.18111439	0.00000048	1 25 59.593986	0.000016
2456718.21396	18 29 10.18111515	0.00000048	1 25 59.593964	0.000016
2456938.61153	18 29 10.18111964	0.00000046	1 25 59.594012	0.000016
2457081.21921	18 29 10.18110324	0.00000063	1 25 59.594051	0.000020
2457300.62039	18 29 10.18110850	0.00000051	1 25 59.594058	0.000017
SSTc2d J182918.2+011758				
2456537.71083	18 29 18.23057894	0.00000623	1 17 57.783157	0.000237
2456718.21396	18 29 18.23057676	0.00000432	1 17 57.782977	0.000165
2456938.61153	18 29 18.23060031	0.00000827	1 17 57.783177	0.000266
2457081.21921	18 29 18.23056481	0.00000605	1 17 57.782967	0.000199
2457300.62039	18 29 18.23058354	0.00000919	1 17 57.783323	0.000305
GBS-VLA J182903.06+012331.0				
2456537.71083	18 29 03.06984956	0.00000319	1 23 31.087749	0.000103
2456718.21396	18 29 03.06986038	0.00000339	1 23 31.087530	0.000110
2456938.61153	18 29 03.06986699	0.00000383	1 23 31.087498	0.000101
2457081.21921	18 29 03.06987411	0.00000425	1 23 31.087780	0.000116
2457300.62039	18 29 03.06987273	0.00000382	1 23 31.087686	0.000132
SSTc2d J182936.5+012317				
2456537.71083	18 29 36.50110691	0.00000859	1 23 17.076353	0.000169
2456718.21396	18 29 36.50114312	0.00000627	1 23 17.075662	0.000226
2456938.61153	18 29 36.50113297	0.00000496	1 23 17.076045	0.000161
2457081.21921	18 29 36.50112373	0.00001097	1 23 17.075484	0.000410
2457300.62039	18 29 36.50110998	0.00000771	1 23 17.076210	0.000196
GBS-VLA J182905.07+012309.0				
2456537.71083	18 29 05.08095263	0.00000445	1 23 09.149373	0.000137
2456718.21396	18 29 05.08096153	0.00000384	1 23 09.149402	0.000155
2457081.21921	18 29 05.08094750	0.00000559	1 23 09.149718	0.000160
2457300.62039	18 29 05.08094627	0.00000762	1 23 09.150555	0.000146
SSTSL2 J182926.72+012342.4				
2456537.71083	18 29 26.71049982	0.00000918	1 23 42.131201	0.000268
2456718.21396	18 29 26.71050367	0.00001050	1 23 42.130807	0.000385
GBS-VLA J182911.94+012119.4				
2456537.71083	18 29 11.94832584	0.00000362	1 21 19.484862	0.000107
2456718.21396	18 29 11.94830530	0.00000283	1 21 19.485004	0.000112
2456938.61153	18 29 11.94832429	0.00000313	1 21 19.484997	0.000106

Table 7 continued on next page

Table 7 *(continued)*

Julian Day	α (J2000.0)	σ_α	δ (J2000.0)	σ_δ
2457081.21921	18 29 11.94830236	0.00000478	1 21 19.485052	0.000132
2457300.62039	18 29 11.94833353	0.00000291	1 21 19.484955	0.000089
	NVSS 182944+011920			
2456537.71083	18 29 44.07658313	0.00000075	1 19 21.164119	0.000025
2456718.21396	18 29 44.07657402	0.00000085	1 19 21.164280	0.000028
2456938.61153	18 29 44.07659031	0.00000068	1 19 21.164227	0.000023
2457081.21921	18 29 44.07657708	0.00000112	1 19 21.164286	0.000035
2457300.62039	18 29 44.07655805	0.00000085	1 19 21.164512	0.000029
	PMN 1829+0101			
2456538.70634	18 29 30.72388371	0.00000033	1 0 48.005138	0.000010
2456720.20849	18 29 30.72391467	0.00000085	1 0 48.005243	0.000022
2456943.59865	18 29 30.72388420	0.00000045	1 0 48.004833	0.000016
	DCE08-210 5			
2456538.70634	18 29 35.02394353	0.00001739	1 15 03.254608	0.000371
2456720.20849	18 29 35.02397943	0.00001364	1 15 03.252858	0.000403
2457507.02912	18 29 35.02401622	0.00000701	1 15 03.253580	0.000198
	GFM 65			
2456720.20849	18 30 00.65283020	0.00000429	1 13 40.065067	0.000136
2456943.59865	18 30 00.65256389	0.00000712	1 13 40.061403	0.000205
2457302.61352	18 30 00.65266340	0.00000277	1 13 40.054815	0.000088
second source:				
2456720.20849	18 30 00.65296360	0.00002331	1 13 40.066599	0.000638
2456943.59865	18 30 00.65289182	0.00000696	1 13 40.061476	0.000276
	ETC 8			
2456720.20849	18 29 51.04143717	0.00000565	1 15 33.871396	0.000160
2456943.59865	18 29 51.04141126	0.00000725	1 15 33.870733	0.000178
2457084.21205	18 29 51.04142997	0.00000353	1 15 33.870437	0.000131
2457302.61352	18 29 51.04141829	0.00000270	1 15 33.870371	0.000080
2457507.02912	18 29 51.04142929	0.00000406	1 15 33.870259	0.000106
	KGF 122			
2456539.70380	18 31 26.01996029	0.00000276	-2 5 17.086151	0.000086
2457102.16179	18 31 26.02073064	0.00000306	-2 5 17.098461	0.000137
2457285.66188	18 31 26.02057197	0.00001863	-2 5 17.102963	0.000368
2457448.21552	18 31 26.02087306	0.00001310	-2 5 17.105731	0.000405
	2M18304408–0201458			
2456539.70380	18 30 44.11485642	0.00000199	-2 1 45.688322	0.000051
2456721.20565	18 30 44.11487547	0.00000271	-2 1 45.689938	0.000071

Table 7 continued on next page

Table 7 *(continued)*

Julian Day	α (J2000.0)	σ_α	δ (J2000.0)	σ_δ
2456946.58954	18 30 44.11484733	0.00000336	-2 1 45.688604	0.000087
2457102.16179	18 30 44.11486486	0.00000140	-2 1 45.688221	0.000038
2457285.66188	18 30 44.11485685	0.00000236	-2 1 45.688281	0.000057
		KGF 138		
2457102.16179	18 31 27.65620135	0.00000709	-2 5 09.799495	0.000178
		KGF 97		
2456721.20565	18 31 23.62227407	0.00000250	-2 5 35.868544	0.000074
2456946.58954	18 31 23.62203557	0.00002812	-2 5 35.873472	0.000761
2457102.16179	18 31 23.62227217	0.00001073	-2 5 35.876576	0.000314
2457285.66188	18 31 23.62197113	0.00000699	-2 5 35.880042	0.000161
2457448.21552	18 31 23.62223545	0.00000309	-2 5 35.883516	0.000086
		KGF 36		
2456543.60141	18 31 14.82263201	0.00000386	-2 3 50.149196	0.000131
2456726.05521	18 31 14.82293762	0.00000369	-2 3 50.152750	0.000106
2457306.96324	18 31 14.82267359	0.00000980	-2 3 50.163179	0.000371
2457448.21552	18 31 14.82293818	0.00000571	-2 3 50.166392	0.000155
		GBS-VLA J182952.73–015159.9		
2456541.69591	18 29 52.73464125	0.00001627	-1 51 59.925315	0.000561
2456723.19777	18 29 52.73465607	0.00002462	-1 51 59.926572	0.000665
2457309.09678	18 29 52.73469573	0.00001149	-1 51 59.925989	0.000363
		KGF 82		
2456543.60141	18 31 22.32975638	0.00000485	-2 6 19.633463	0.000140
2457306.96324	18 31 22.32894475	0.00000404	-2 6 19.660373	0.000166
		KGF 133		
2456543.60141	18 31 27.45984260	0.00000137	-2 5 12.036684	0.000039
2457306.96324	18 31 27.45978832	0.00000657	-2 5 12.052156	0.000273
2457448.21552	18 31 27.46007650	0.00000568	-2 5 12.056771	0.000139
		GBS-VLA J183118.68–015455.9		
2456706.16961	18 31 18.68250486	0.00001724	-1 54 56.073788	0.000262
2457084.21205	18 31 18.68250948	0.00001509	-1 54 56.073322	0.000371
2457302.61352	18 31 18.68249661	0.00000858	-1 54 56.072971	0.000207
		GBS-VLA J182949.50+011955.8		
2456541.69877	18 29 49.50633251	0.00000273	1 19 55.885107	0.000090
2456723.20062	18 29 49.50632851	0.00000189	1 19 55.885721	0.000123
2457309.09678	18 29 49.50633154	0.00000120	1 19 55.885384	0.000068

Table 7 continued on next page

Table 7 *(continued)*

Julian Day	α (J2000.0)	σ_α	δ (J2000.0)	σ_δ
		GFM 70		
2456723.20062	18 30 04.62941667	0.00000502	1 22 34.131415	0.000132
2457309.09678	18 30 04.62940928	0.00000397	1 22 34.131168	0.000121
		GFM 11		
2456543.69416	18 29 33.07249309	0.00000229	1 17 16.360959	0.000098
2456726.19504	18 29 33.07290417	0.00000527	1 17 16.356120	0.000275
2457507.02912	18 29 33.07340833	0.00000593	1 17 16.337928	0.000238
		SSTSL2 J182916.10+010438.6		
2456543.69416	18 29 16.11947301	0.00000517	1 4 37.589379	0.000201
2456726.19504	18 29 16.11946492	0.00000667	1 4 37.589438	0.000220
2457307.60223	18 29 16.11947017	0.00000623	1 4 37.589495	0.000238
		GBS-VLA J182854.46+011823.7		
2456749.07794	18 28 54.46499411	0.00000049	1 18 23.813820	0.000015
2457281.61856	18 28 54.46500889	0.00000023	1 18 23.813619	0.000008
		GBS-VLA J182854.44+011859.7		
2457281.61856	18 28 54.44344643	0.00000226	1 18 59.737811	0.000112
		GBS-VLA J182854.87+011753.0		
2456749.07794	18 28 54.87254346	0.00000603	1 17 53.051049	0.000192
2457281.61856	18 28 54.87253760	0.00000534	1 17 53.051239	0.000208
		SSTc2d J182948.8+010648		
2456749.09635	18 29 48.82981795	0.00000628	1 6 47.450268	0.000181
2457281.61856	18 29 48.82980672	0.00000240	1 6 47.450032	0.000084

Parte II

Observaciones hacia el centro Galáctico con VLBI milimétrica

Capítulo 5

La estructura intrínseca de Sgr A* a 3.5 mm

En el trabajo desarrollado en los capítulos anteriores, utilizamos la VLBI en el centimétrico para estudiar estructuras cercanas ($d \lesssim 500$ pc) cuyas escalas se extienden hasta algunas decenas de parsecs. La medición precisa de la paralaje trigonométrica hacia fuentes más lejanas que ~ 1 kpc requiere utilizar VLBI a longitudes de onda milimétricas. Por ejemplo, distancias con incertidumbres $\lesssim 10\%$ se han obtenido hacia fuentes de emisión máser localizadas a unos cuantos kiloparsecs del Sol a partir de observaciones a $\lambda = 7$ mm (Zhang *et al.* 2012). La VLBI milimétrica representa entonces una herramienta única con la cual es posible investigar estructuras a escala Galáctica. También, gracias a la alta resolución espacial que se puede alcanzar con líneas de base muy extensas, la VLBI milimétrica es la única técnica disponible para obtener imágenes de las partes más centrales en núcleos activos de galaxias. La VLBI a longitudes de onda corta puede además ver através de estas regiones centrales que generalmente son opacas a longitudes de onda larga.

El desarrollo de la VLBI milimétrica depende en gran medida de la adición de telescopios, que no necesariamente se construyeron para tal objetivo, a la red de arreglos VLBI existentes. El GTM, siendo el telescopio más grande en el mundo que opera en las bandas

del milimétrico y submilimétrico, puede entonces jugar un papel importante en proyectos VLBI que requieren de mucha sensitividad y gran cobertura del plano *uv*. En el presente capítulo, presentamos el trabajo que dió inicio al uso del GTM en experimentos VLBI. Como parte de este proyecto, uno de los objetivos originales fue el de realizar observaciones astrométricas hacia el centro Galáctico a $\lambda = 3.5$ mm utilizando el GTM y el VLBA. Sin embargo, veremos que diferentes factores dificultan este tipo de observaciones a esta corta longitud de onda. Por tanto, y con el propósito de demostrar el alcance del uso del GTM en experimentos VLBI, decidimos concentrarnos en la obtención de observaciones sensitivas y de alta resolución angular para investigar la estructura de la fuente asociada al centro Galáctico.

5.1. Observaciones astrométricas de Sgr A*

Un parámetro fundamental en el campo de la dinámica Galáctica, y sustancial para los modelos de la estructura y rotación de la Vía Láctea, es la distancia hacia el centro Galáctico, R_0. Estimaciones indirectas de R_0 se han obtenido mediante diferentes métodos. Reid *et al.* (2014), por ejemplo, realizaron observaciones VLBI de emisión máser asociada a regiones de formación estelar masiva y derivaron un valor de $R_0 = 8.34 \pm 0.16$ kpc a partir de un modelo de rotación Galáctico. Ghez *et al.* (2008) y Gillessen *et al.* (2009), por otro lado, obtuvieron un resultado similar, $R_0 = 8.33 \pm 0.11$ kpc, al utilizar velocidades tridimensionales determinadas a partir del monitoreo en el infrarrojo hacia varias estrellas que orbitan el centro Galáctico dentro de ~ 0.01 pc. Si bien estas estimaciones son precisas y consistentes entre ellas, podrían incluir errores sistemáticos relacionados con incertidumbres en los modelos utilizados. Es claro que una determinación directa y puramente geométrica de R_0, a partir de paralaje trigonométrica, se requiere para descartar esta posibilidad.

Uno de los objetivos originales del trabajo presentado en este capítulo fue la medición de la paralaje de Sgr A* (para la cual $\varpi = 0.12$ mas a una distancia de 8.3 kpc) mediante observaciones conjuntas con 7 antenas del VLBA y el GTM a una longitud de onda de

3.5 mm. Para este experimento, programamos dos épocas de observaciones de referenciado de fase en Abril de 2014 y 2015 con el propósito de derivar la posición de Sgr A* respecto a dos fuentes extragalácticas, J1745-283 y J1748-291, las cuales están proyectadas en el plano del cielo dentro de 1º de Sgr A*. Las observaciones involucraron apuntados alternando entre Sgr A* y los cuásares, siguiendo un procedimiento semejante al de las observaciones astrométricas del proyecto GOBELINS, pero usando intervalos de tan sólo ∼15 segundos de duración entre cada cambio de fuente. La calibración en fase de estos datos también se efectuó de manera semejante a los datos de GOBELINS con la única diferencia de que utilizamos los datos mismos de Sgr A* para la determinación de las soluciones de retraso, tasa de retraso y fase (c.f. Apéndice A). La razón de esto es que el flujo esperado de Sgr A* a $\lambda = 3.5$ mm es ~ 2 Jy, mientras que los cuásares poseen un flujo $\lesssim 0.1$ Jy (Broderick *et al.*, 2011), por lo que el cociente de señal a ruido en los cortos tiempo de integración empleados es significativamente menor para estas fuentes deébiles. La calibración en amplitud consistió en utilizar el espectro del máser VX Sgr observado con el GTM, para definir la escala absoluta de flujo y derivar las curvas de ganancia como función de la elevación al comparar este espectro con el observado en el resto de las antenas del arreglo.

Mientras que observaciones astrométricas similares han sido obtenidas con éxito a $\lambda = 7$ mm (Reid *et al.* 1999 y Reid y Brunthaler 2004), varios obstáculos nos impidieron la detección de las fuentes extragalácticas a $\lambda = 3.5$ mm. Primero, el tiempo empleado por las antenas para desplazarse de una fuente a otra disminuye los tiempos de integración en fuente a ~ 8 segundos. Esto reduce el cociente señal a ruido de las visibilidades, lo que a su vez introduce una dispersión grande en las soluciones de retraso, tasa de retraso y fase. La fase interpolada a las fuentes débiles muestra también una dispersión alta, haciendo imposible una reconstrucción correcta de las imágenes de los cuásares a partir de las visibilidades. Nótese que utilizar tiempos de integración mayores imposibilitaría seguir las variaciones rápidas de la fase introducidas por cambios de densidad en las capas turbulentas de la atmósfera.

Vista desde el hemisferio Norte, Sgr A* se observa en el cielo a elevaciones relativamente bajas. A estas bajas elevaciones, la variación de la ganancia de antena y temperatura del sistema y los errores de apuntado de las antena son significativos y difíciles de corregir, sobre todo cuando las condiciones de clima no son las óptimas como ocurrió en nuestras observaciones. En este caso, una calibración de amplitud imprecisa introduce ruido a las imágenes haciendo difícil la detección de fuentes débiles.

Es claro que observaciones astrométricas a $\lambda = 3.5$ mm requieren de una ejecución cuidadosa pero éstas podrían efectuarse con éxito a corto plazo si se toman en cuenta los dos siguientes aspectos. Para incrementar el cociente señal a ruido de las visibilidades en cortos tiempos de integración se puede recurrir a incluir antenas más sensitivas (e.g. GBT, ALMA, IRAM) además del GTM o bien buscar un incremento de ancho de banda. Finalmente, las observaciones deben realizarse en óptimas condiciones climáticas para reducir los efectos introducidos por la atmósfera y obtener una calibración de amplitud apropiada.

5.2. El agujero negro supermasivo en el centro Galáctico

El centro de nuestra Galaxia alberga al candidato de un agujero negro supermasivo que mejor se ha caracterizado. Su masa de $4.3\ (\pm 0.4) \times 10^6\ M_\odot$ se ha medido de manera muy precisa mediante el monitoreo de órbitas estelares en la vecindad inmediata ($\lesssim 1$ pc) del centro Galáctico (Ghez *et al.*, 2008; Gillessen *et al.*, 2009). La distancia hacia Sgr A* también se conoce con bastante precisión gracias a observaciones astrométricas con el VLBA de máseres distribuidos en la Galaxia, que han resultado en $D = 8.35\ (\pm 0.15)$ kpc (Reid *et al.*, 2014).

Debido a su cercanía, las propiedades físicas de Sgr A* se pueden determinar con un grado de detalle que no es posible lograr en otras galaxias cercanas. Por ejemplo, suponiendo una distribución de brillo dada por una gaussiana circular, Doeleman *et al.* (2008) determinaron que el diámetro íntrinseco de Sgr A*, a una longitud de onda de

1.3 mm, es igual a 37^{+16}_{-10} μas. Tomando el límite superior de 3σ de esta determinación para el tamaño de la fuente y combinando con la masa de Sgr A*, se deriva un límite inferior para la densidad de masa de $\sim 2\times10^{23}$ $M_\odot$ pc^{-3}. Dicho valor de la densidad descarta esencialmente a la mayoría de los posibles escenarios, excepto el de un agujero negro supermasivo, que se han propuesto para explicar la naturaleza de la gran concentración de masa en el centro Galáctico.

Finalmente, la evidencia para la asociación de esta masa oscura con Sgr A* viene de la medición con VLBI del movimiento propio de la fuente de radio. Reid y Brunthaler (2004) determinaron que este movimiento propio se debe al efecto del movimiento orbital del Sol alrededor del centro Galáctico. El movimiento residual, en la dirección perpendicular al plano Galáctico, resulta ser $< 0.4 \pm 0.9$ km s^{-1}, un valor que es consistente con cero e implica que Sgr A* se encuentra en el centro dinámico de la Galaxia.

5.3. Tamaño y estructura de Sgr A*

Décadas después de su descubrimiento en 1974 por Balick y Brown, se encontró que el diámetro de Sgr A* cambia con la longitud de onda siguiendo una ley de potencias cuadrática. La forma y tamaño de la emisión de radio centimétrica observada hacia Sgr A* no es intrínceca a la fuente, sino el resultado de la dispersión de la radiación por el medio interestelar ionizado que se encuentra en la dirección hacia el centro Galáctico. La radiación proveniente de Sgr A* se propaga por este medio, cuyas fluctuaciones de densidad introducen fases estocásticas a las visibilidades medidas con arreglos VLBI. El efecto dominante de la dispersión es el *ensanchamiento* de la imagen de la fuente, cuando los tiempos de integración se realizan sobre varias épocas. La imagen dispersada de Sgr A*, observada a una longitud de onda entre 0.7 y 25 cm, es una distribución gaussiana elíptica con eje mayor (e.g. , Bower *et al.*, 2006),

$$\phi_{\rm scatt} = (1.36 \pm 0.02)\ {\rm mas} \times (\lambda/{\rm cm})^2, \tag{5-1}$$

orientada en la dirección este-oeste y con un cociente de ejes ~2:1.

La escala característica de un agujero negro sin rotación está dada por el radio de Schwarzschild, $R_S = 2GM/c^2$, que corresponde al radio de su horizonte de eventos (a la distancia de Sgr A*, 1 R_S subtiende un ángulo de $\simeq 10$ μas). Con la idea emergente de que el agujero negro en Sgr A* está probablemente rodeado por un disco de acreción, muchos trabajos se han dedicado a investigar la forma y apariencia de un agujero negro iluminado por una región con emisión ópticamente delgada. Falcke *et al.* (2000) identificaron que la imagen del agujero negro consiste en una "sombra", de diámetro ~ 50 μas, producida por el efecto de lente gravitacional que desvía las órbitas de fotones hacia el horizonte de eventos, creándose un déficit de radiación en la región más cercana al agujero negro.

Hasta $\lambda = 1$ cm, el ensanchamiento por la dispersión del medio interestelar domina totalmente sobre el tamaño de la sombra. Sin embargo, este efecto decrece con la longitud de onda, por lo que observaciones en el milimétrico y sub-milimétrico con VLBI son necesarias para detectar la forma y orientación de la emisión originada a escalas comparables al horizonte de eventos.

5.4. VLBI milimétrica con el GTM

En años recientes ha habido un gran desarrollo tecnológico muy enfocado a la VLBI milimétrica y en particular al Telescopio del Horizonte de Eventos[1] (EHT por el inglés *Event Horizon Telescope*). El EHT es un arreglo de radiotelescopios que realizará observaciones interferométricas a $\lambda = 0.8 - 1.3$ mm con el objetivo de obtener imágenes del agujero negro en Sgr A* con una resolución angular sin precedentes. Una versión temprana del arreglo consistió de tan solo tres elementos situados en Hawaii, Arizona y California, que ya ha proporcionado importantes pistas sobre la estrutura de la emisión milimétrica y la presencia de campos magnéticos ordenados a escalas de algunos R_S en Sgr A* (Doeleman *et al.*, 2008; Johnson *et al.*, 2015). Tales resultados se han basado solo en el análisis de

[1] http://www.eventhorizontelescope.org/

visibilidades interferométricas, porque tres elementos son insuficientes para reconstruir un mapa de la fuente. En su transición hacia un arreglo idóneo para la obtención de imágenes, se han añadido más estaciones incluyendo al GTM, situado en la cima del volcán Sierra Negra en el estado de Puebla, y al Gran Arreglo Milimétrico de Atacama (ALMA) localizado en el desierto en Chile.

El GTM presenta una de las superficies de mayor tamaño (solo por debajo de ALMA) dentro de los elementos que integran al EHT. Los primeros trabajos de integración y verificación del sistema VLBI en el sitio del GTM se realizaron a $\lambda = 3.5$ mm e involucró su acoplamiento con el VLBA[2]. Dichos trabajos finalizaron con observaciones de ciencia hacia Sgr A*.

A $\lambda = 1.3$ mm, la emisión de Sgr A* refleja los efectos del campo gravitacional intenso alrededor del agujero negro, y su forma puede utilizarse para investigar predicciones de la Teoría de Relatividad General de Einstein. Por otro lado, a $\lambda = 3.5$ mm la emisión se origina en regiones más alejadas al agujero negro, y su tamaño y estructura representan un importante observable para los diferentes modelos que investigan qué regiones en el flujo de acreción forman la fuente de radiación que recibimos. En el presente capítulo, utilizamos observaciones VLBI a $\lambda = 3.5$ mm obtenidas en Abril 27 y 28 de 2015 con el GTM+VLBA, para modelar la estructura intrínseca de la emisión asociada a Sgr A*. Trabajamos directamente con cerraduras de fase: la suma de fases interferométricas alrededor de un triángulo de líneas de base y cerraduras de amplitud: definidas como un cociente de amplitudes interferométricas alrededor de un cuadrilátero. En el Apéndice A, mostramos que estas cantidades son inmunes a errores introducidos por la atmósfera, instrumentación, variaciones en la ganancia de antena y cualquier otro error asociado a estaciones individuales, y por tanto contienen información intrínseca a la estructura de la fuente.

[2]El VLBA es un arreglo homogéneo optimizado para observaciones VLBI en el centimétrico. La longitud de onda más corta a la que puede operar es 3.5 mm.

5.5. Detección de la forma intrínseca y subestructura en Sgr A*

Encontramos que la distribución de las cerraduras de fase, construidas para todos los triángulos presentes en cada una de las dos épocas observadas, tiene la forma de una distribución Gaussiana alrededor de cero, que es consistente con una estructura elíptica para la distribución de brillo. Entonces, las cerraduras de amplitud fueron ajustadas con un modelo, donde los parámetros libres son el eje mayor, el eje menor y el ángulo de posición de una Gaussiana elíptica. Este ajuste nos proporcionó el tamaño y orientación de Sgr A*, ensanchado por la dispersión del medio interestelar, en cada una de las dos épocas que incluyeron al GTM. Contrario a intentos realizados en años anteriores para determinar la forma bidimensional de Sgr A*, hemos sido capaces de determinar, por primera vez y de manera robusta, el tamaño del eje menor a $\lambda = 3.5$ mm en épocas individuales. Este resultado no es sorprendente, pues los arreglos usados con anterioridad carecían tanto de resolución angular como de suficientes líneas de base sensitivas a lo largo de la dirección norte-sur. Es claro que la posición geográfica del GTM ha resultado favorable para el estudio de la estructura milimétrica de Sgr A*.

De la ecuación 5-1 se sigue que, a $\lambda = 3.5$ mm, Sgr A* tiene un tamaño por dispersión del medio interestelar igual a $159.2^{+3.6}_{-3.6}$ μas $\times$ $77.8^{+4.9}_{-6.1}$ μas. Este valor es mayor al tamaño derivado en el ajuste de las cerraduras de amplitud debido a la contribución del tamaño intrínseco de la fuente. Después de remover la contribución por la dispersión del medio interestelar y transformar distancias angulares a escalas físicas, obtenemos que la estructura intrínseca tiene, en promedio, dimensiones de $14.4^{+0.6}_{-0.6}$ $R_S \times 11.8^{+1.0}_{-1.3}$ R_S, donde R_S es el radio de Schwarzschild.

Por otro lado, las cerraduras de fase en varios triángulos que incluyen al GTM muestran valores que son estadísticamente diferentes de cero. Para investigar la naturaleza de estas desviaciones, realizamos una simulación numérica donde generamos una pantalla de dispersión que introduce fases aleatorias a las visibilidades de una fuente con simetría circular y tamaño igual a 130 μas. Estimamos el ruido en las cerraduras de fase por la

adición de estas fases aleatorias y lo comparamos con nuestros datos observacionales. La simulación reproduce muy bien a los datos, sugiriendo que las cerraduras de fase distintas de cero corresponden a subestructura en la imagen de Sgr A* que son introducidas por el medio ionizado en la dirección del centro Galáctico. Sin embargo, no podemos descartar que tal subestructura sea por asimetrías intrínsecas de la emisión.

A continuación incluimos el artículo correspondiente, el cual fue publicado en el ApJ en el presente año.

The Astrophysical Journal, 824:40 (10pp), 2016 June 10 doi:10.3847/0004-637X/824/1/40

THE INTRINSIC SHAPE OF SAGITTARIUS A* AT 3.5 mm WAVELENGTH

Gisela N. Ortiz-León[1], Michael D. Johnson[2], Sheperd S. Doeleman[2,3], Lindy Blackburn[2], Vincent L. Fish[3], Laurent Loinard[1,4], Mark J. Reid[2], Edgar Castillo[5,9], Andrew A. Chael[2], Antonio Hernández-Gómez[1], David H. Hughes[5], Jonathan León-Tavares[5,6], Ru-Sen Lu[4], Alfredo Montaña[5,9], Gopal Narayanan[7], Katherine Rosenfeld[2], David Sánchez[5], F. Peter Schloerb[7], Zhi-qiang Shen[8], Hotaka Shiokawa[2], Jason SooHoo[3], and Laura Vertatschitsch[2]

[1] Instituto de Radioastronomía y Astrofísica, Universidad Nacional Autónoma de México, Morelia 58089, México; g.ortiz@crya.unam.mx
[2] Harvard-Smithsonian Center for Astrophysics, 60 Garden Street, Cambridge, MA 02138, USA
[3] Massachusetts Institute of Technology, Haystack Observatory, Route 40, Westford, MA 01886, USA
[4] Max Planck Institut für Radioastronomie, Auf dem Hügel 69, D-53121 Bonn, Germany
[5] Instituto Nacional de Astrofísica Óptica y Electrónica, Apartado Postal 51 y 216, 72000 Puebla, México
[6] Sterrenkundig Observatorium, Universiteit Gent, Krijgslaan 281-S9, B-9000 Gent, Belgium
[7] Department of Astronomy, University of Massachusetts, Amherst, MA 01002, USA
[8] Shanghai Astronomical Observatory, 80 Nandan Road, Shanghai 200030, China
Received 2016 January 25; accepted 2016 March 14; published 2016 June 8

ABSTRACT

The radio emission from Sgr A* is thought to be powered by accretion onto a supermassive black hole of $\sim 4 \times 10^6\,M_\odot$ at the Galactic Center. At millimeter wavelengths, Very Long Baseline Interferometry (VLBI) observations can directly resolve the bright innermost accretion region of Sgr A*. Motivated by the addition of many sensitive long baselines in the north–south direction, we developed a full VLBI capability at the Large Millimeter Telescope Alfonso Serrano (LMT). We successfully detected Sgr A* at 3.5 mm with an array consisting of six Very Long Baseline Array telescopes and the LMT. We model the source as an elliptical Gaussian brightness distribution and estimate the scattered size and orientation of the source from closure amplitude and self-calibration analysis, obtaining consistent results between methods and epochs. We then use the known scattering kernel to determine the intrinsic two-dimensional source size at 3.5 mm: $(147 \pm 7\ \mu\text{as}) \times (120 \pm 12\ \mu\text{as})$, at position angle $88^\circ \pm 7^\circ$ east of north. Finally, we detect non-zero closure phases on some baseline triangles, but we show that these are consistent with being introduced by refractive scattering in the interstellar medium and do not require intrinsic source asymmetry to explain.

Key words: accretion, accretion disks – galaxies: active – galaxies: individual (Sgr A*) – Galaxy: center – techniques: interferometric

1. INTRODUCTION

The compact radio source Sagittarius A* (Sgr A*) at the center of the Galaxy is associated with a supermassive black hole of $\sim 4 \times 10^6\,M_\odot$ (Ghez et al. 2008; Gillessen et al. 2009). The mechanism responsible for the radio emission is thought to be synchrotron from a jet-like outflow (Markoff et al. 2007; Falcke et al. 2009), a radiatively inefficient accretion flow (RIAF) onto the black hole (e.g., Narayan et al. 1995; Yuan et al. 2003; Broderick et al. 2009), or an almost isothermal jet coupled to an accretion flow (Mościbrodzka & Falcke 2013). Different jet and accretion disk models can be tested by modeling the radio through the submillimeter spectrum of Sgr A* (e.g., Markoff et al. 2007), the frequency-dependent source size (e.g., Bower et al. 2004; Mościbrodzka & Falcke 2013; Chan et al. 2015), and data from millimeter Very Long Baseline Interferometry (VLBI) observations (Broderick et al. 2011; Dexter et al. 2012).

At wavelengths longer than a few centimeters, the image of Sgr A* is heavily scattered by the intervening ionized interstellar medium, and the scattering determines the size of the measured image. The effect of this scattering decreases at shorter wavelengths, with a λ^2 dependence, and VLBI observations at wavelengths shorter than a centimeter have found deviations from the λ^2 law, suggesting that intrinsic source structure contributes to the apparent image at these wavelengths (Doeleman et al. 2001; Bower et al. 2004, 2006; Shen et al. 2005; Krichbaum et al. 2006). The intrinsic two-dimensional (2D) source size can then be estimated by extrapolating the scattering properties from longer wavelengths and then deconvolving the scattering ellipse from the observed size. At a wavelength of one millimeter or less, the scatter broadening is subdominant to intrinsic structure in the image (Doeleman et al. 2008; Fish et al. 2011; Johnson et al. 2015).

Because of the lack of good north–south baselines in existing VLBI arrays, efforts to study the intrinsic structure of Sgr A* at 3.5 mm have been mostly limited to the east–west direction. To unambiguously determine the intrinsic 2D structure of Sgr A*, VLBI observations with higher angular resolution in the north–south direction are needed. In this paper we describe such observations of Sgr A* obtained at $\lambda = 3.5$ mm with the National Radio Astronomy Observatory[10] Very Long Baseline Array (VLBA) and the Large Millimeter Telescope Alfonso Serrano (LMT) located in Central Mexico, operated in concert as a single VLBI array. This required that the LMT be equipped as a VLBI station as we now describe.

[9] Consejo Nacional de Ciencia y Tecnología Research Fellow.

[10] The National Radio Astronomy Observatory (NRAO) is a facility of the National Science Foundation operated under cooperative agreement by Associated Universities, Inc.

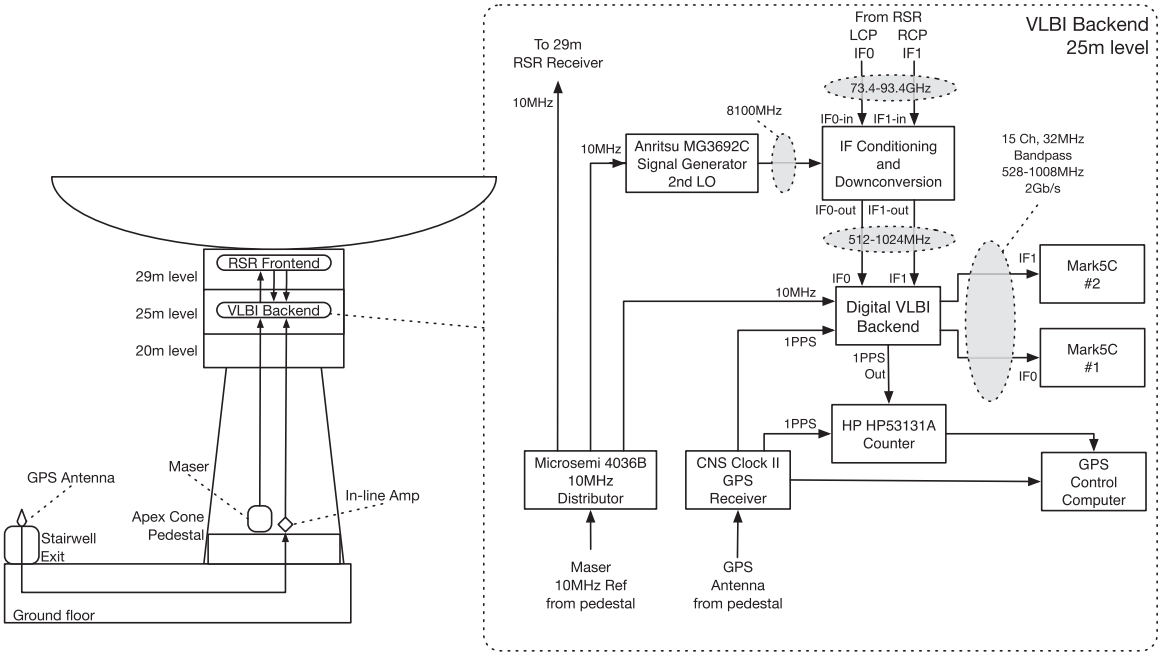

Figure 1. Block diagram of VLBI instrumentation setup at the LMT for the 2015 April observations.

2. VLBI AT THE LMT

Situated at an altitude of 4600 m at the summit of Volcán Sierra Negra in Central Mexico, the LMT has a large collecting area (32 m circular aperture currently operational, extending to the full 50 m diameter by 2017) and geographical location that make it particularly useful for mm-wavelength VLBI observations. Technical work leading to development of VLBI capability at the LMT was the product of a multi-year collaboration between Instituto Nacional de Astrofísica, Óptica y Electrónica, the University of Massachusetts, the Smithsonian Astrophysical Observatory, the Massachusetts Institute of Technology Haystack Observatory, the Universidad Nacional Autónoma de México (UNAM), and the NRAO. Recognizing the importance of LMT participation in 3.5 mm VLBI networks (e.g., the VLBA or the Global Millimeter VLBI Array—GMVA) and in the Event Horizon Telescope (EHT) project at 1.3 mm wavelength, these groups began planning VLBI tests in 2012. First 3.5 mm observations were scheduled in 2013 April, for which a full VLBI recording system was installed. This included integration at the Sierra Negra site of

1. a GPS receiver (model CNS) to enable synchronization with other VLBI sites;
2. a custom-built radio frequency downconverter to shift the output of the facility Redshift Search Receiver (RSR) to a standard VLBI intermediate frequency (IF) range of 512-1024 MHz;
3. a digital backend to digitize and format data for VLBI recording (Whitney et al. 2013); and
4. two high-speed hard-disk Mark5c VLBI recorders.[11]

The RSR is one of the two instruments currently available at the LMT. The RSR has two H and V linear polarization receivers that instantaneously cover a wide frequency range of 73–111 GHz and has a dedicated backend spectrometer that covers the entire band with a spectral resolution of 31 MHz (Erickson et al. 2007). The receivers are chopped between the ON and OFF source positions (beam 1 and 0, respectively) separated by 76″. Sources are tracked on beam 1 during VLBI observations. The RSR has two fixed first local oscillators at 93.4 and 112.3 GHz, which are used to downconvert the frontend band into two 0–20 GHz IF bands. For this VLBI experiment we used the 73–93.4 GHz band (see Figure 1) for further down-conversion and processing.

A hydrogen maser, typically used to provide a stable frequency reference for VLBI, was not available for the 2013 observations, so an ultra-stable quartz crystal oscillator loaned by the Applied Physics Laboratories of Johns Hopkins University was used. This unit has an Allan Deviation of $<10^{-13}$ over integration times from 1 to 10 s, resulting in coherence losses of $<25\%$ at 3.5 mm wavelength. This crystal was thus sufficient for initial tests but not for scientific observations. To convert the Linear Polarization natively received by the RSR to Circular Polarization, a quarter-wave plate made of grooved dielectric was inserted into the telescope optics, and for subsequent observations Left Circular Polarization was selected.

Using this test setup (see Figure 1), several SiO maser sources ($v = 1$, $J = 2 - 1$) and bright active galactic nucleus were detected on baselines from the LMT to the VLBA, confirming the stability of the LMT RSR and VLBI system performance. In 2014, this same setup was augmented by the installation and integration of a hydrogen maser frequency standard (manufactured by Microsemi), which is housed in the pedestal room of the telescope. A custom-built enclosure provides a temperature stable environment for the maser and a low-noise distribution system installed near the VLBI equipment routes the maser reference to phase lock all VLBI instrumentation.

Commissioning observations in 2014 were conducted over the course of four nights between the VLBA and the LMT. A precise

[11] http://www.haystack.edu/tech/vlbi/mark5/mark5_memos/057.pdf. Unlike nominal operations of the VLBA, the LMT did not record dual polarization on the same disk set.

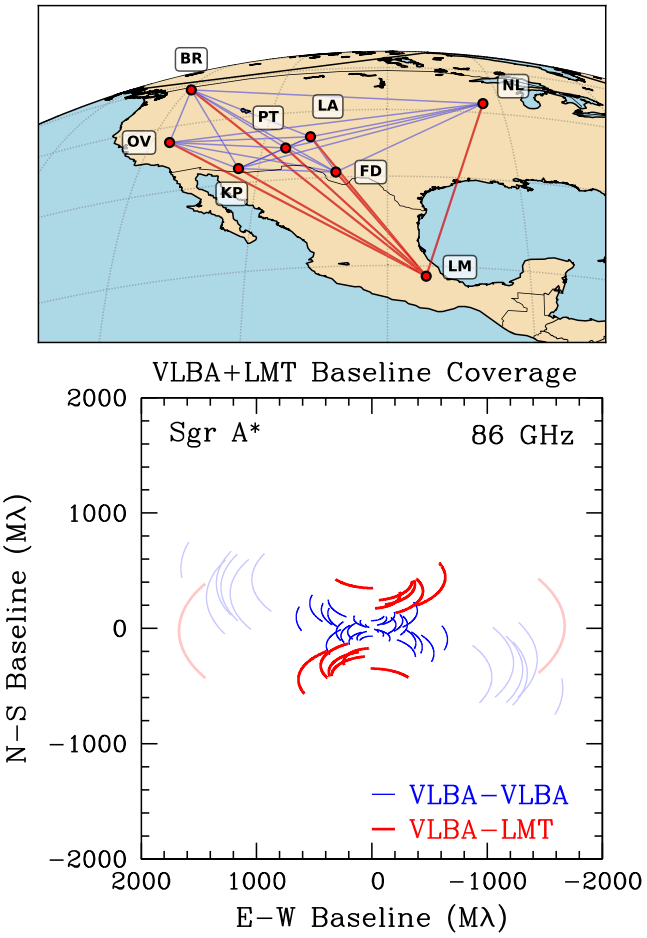

Figure 2. Top: the 3.5 mm stations of the VLBA and the LMT. Bottom: the corresponding *u–v* coverage; the faint tracks denote baselines to Mauna Kea, on which we do not detect Sgr A*.

position for the LMT was measured by modeling the delays and rates of VLBI detections on strong quasars over a wide range of elevation. The operational location of the LMT in the International Terrestrial Reference Frame geocentric coordinates is $(X, Y, Z) = (-7.687156(2) \times 10^5\,\mathrm{m}, \quad -5.9885071(2) \times 10^6\,\mathrm{m}, 2.0633549(5) \times 10^6\,\mathrm{m})$. This location corresponds to the projection point of the horizontal axis onto the vertical axis. Figure 2 shows the VLBA and LMT as seen by Sgr A* and the corresponding baseline coverage.

3. OBSERVATIONS AND DATA CALIBRATION

The observations reported here (project code BD183) were obtained in 2015 by operating the eight VLBA antennas equipped with 3.5 mm receivers and the LMT as a single VLBI array. The central frequency was 86.068 GHz. A total of 27 hr of telescope time were allocated to the project, which were covered in three epochs of 9 hr each on 2015 April 24, 27, and 28 (codes A, C, and D, respectively). Because scans for pointing and calibration were also included in each observation, only about 3.6 hr were actually spent on-source in each epoch. Observations were triggered at all sites based on expected weather conditions at LMT and North Liberty, the key stations of the project. Data were recorded at a rate of 2 Gb s^{-1} and taken in left circular polarization, with 480 MHz of bandwidth covered by 15 32 MHz IF channels.

In the first epoch, the LMT RSR tracked on the wrong beam (beam 0) and this was caught just before finalizing observations. On the second epoch, the station at Pie Town (PT) experienced precipitation during most of the observing run, so data were highly affected. On the third epoch, the Los Alamos (LA) recording system corrupted the data due to timing issues. Thus, the data taken at the LMT on first epoch, at PT on the second epoch, and at LA on the third epoch were discarded. Because the longest VLBI baselines between Mauna Kea and the rest of the array resolve out the emission from Sgr A*, the source was not detected on these baselines. Fringe detections on Sgr A* were therefore obtained with an array consisting of seven stations in the North American continent in each of the three epochs.

For the remainder of the paper we will focus on the last two epochs (BD183C and BD183D) because our goal of constraining the intrinsic size of Sgr A* at 3 mm relies heavily on the north–south baselines provided by the LMT.

The initial data reduction was done using the Astronomical Image Processing System (AIPS; Greisen 2003). Phase calibration was performed as follows. Corrections for the antenna axis offset at the LMT and for voltage offsets in the samplers at all stations were first applied to the data. Single-band delays were determined by fringe-fitting on a strong calibrator (3C279 for BD183C and 3C454.3 for BD183D) and the solutions were applied to all scans in the corresponding observing night. Sgr A* was then fringe-fitted, producing rate and delay solutions every 1 minute. These solutions were smoothed using a median window filter smoothing function with a six-minute filter time and then applied to the data. A single bandpass solution was derived from the autocorrelations on the continuum sources and applied to the data after fringe-fitting. At this point, all scans with non-detections were flagged. Also, the outer 4.5 MHz from the edge of each IF were discarded because these are adversely affected by the bandpass response function.

To optimize the coherent averaging of visibilities, we estimated the atmospheric coherence time of our data by examining the ratios of debiased coherent to incoherent averages[12] as a function of time using a scan on 3C279. For every baseline we found that the fractional amplitude loss is $<0.7\%$ for $t_{\mathrm{avg}} = 10$ s (see Figure 3). Considering the fractional amplitude loss scales with the line of sight optical depth and because Sgr A* is at lower elevation, we estimated the loss increases to $<4\%$ in the worst case. To ensure that closure relationships (discussed below) were not affected by coherence losses, we then utilized 10 s coherent averages. For this segment of time, the losses can be considered negligible in all of our data. After this coherent averaging in time and across the full bandwidth, these phase-only calibrated data were exported as FITS files for further analysis outside of AIPS.

4. ANALYSIS

VLBI visibilities were analyzed via two standard pathways: the first analysis used only "closure" quantities, which provide immunity to station-based calibration errors, and the second

[12] A coherent average takes the vector-average of complex visibilities, preserving the coherence of phase over time and frequency (Thompson et al. 2007). An incoherent average takes the scalar-average of complex visibilities segmented at short-length times. A debiased average corrects visibility amplitudes by the noise bias introduced because of the inherently positive nature of amplitudes.

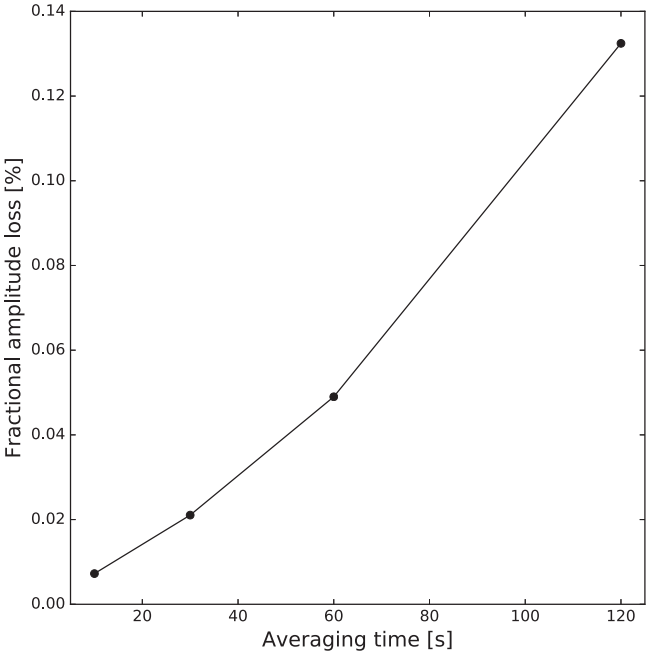

Figure 3. Fractional amplitude loss as a function of averaging time for a scan on 3C279 taken in the first epoch. We estimated this fraction for each baseline and took the maximum values to show in the plot.

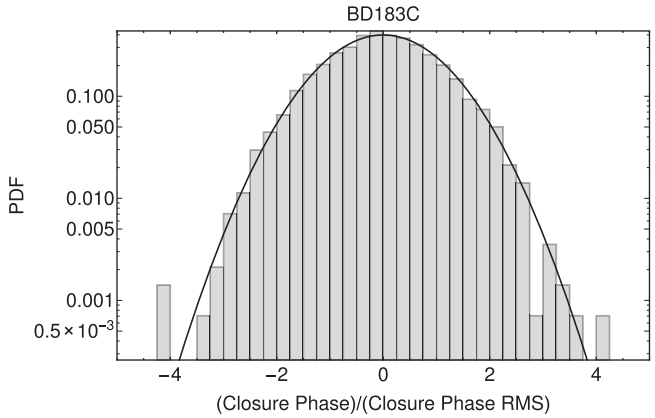

Figure 4. Probability density function (PDF) of the standardized closure phases on all triangles with baselines shorter than 250 $M\lambda$. The solid line shows a fitted Gaussian, representing zero intrinsic closure phase and non-zero measurements entirely due to thermal noise. We use this Gaussian fit to estimate the scaling factor relating each "weight" reported by AIPS for a complex visibility to the thermal noise.

analysis used "self-calibration," which attempts to simultaneously solve for source structure and complex, time-dependent station gains.

4.1. Fitting an Elliptical Gaussian Using Closure Amplitudes

For a closed triangle of interferometric baselines, the phase of the bispectrum (the directed product $V_{12}V_{23}V_{31}$ of the three complex visibilities V_{ij} around the triangle) is immune to any station-based phase errors. This quantity is known as a "closure phase." Likewise, closure amplitudes, such as $|(V_{12}V_{34})/(V_{13}V_{24})|$, can be constructed for any quadrangle of sites and provide immunity to station-based gain amplitude errors (Thompson et al. 2007). We constructed closure amplitudes and phases from the phase-only calibrated data for each 10 s time segment.

Measured closure phases from both days are consistent with a zero-mean Gaussian distribution (see Figure 4). We then fit the distribution of closure phases to calculate a single coefficient that converts AIPS weights w_i to thermal noise $\sigma_i \propto 1/\sqrt{w_i}$ for each measurement. Because the atmospheric coherence time at $\lambda = 3.5$ mm is only tens of seconds and because coherent averages must be done over even shorter timescales to preserve the closure relationships discussed below, most of our measurements have only moderate signal-to-noise. For example, the median signal-to-noise ratio (S/N) in our two observing epochs was 8.3 and 7.2, respectively, for all detections, but ∼10% of detections have S/N < 3. Both closure amplitudes and phases have markedly non-Gaussian errors in this regime, and closure amplitudes suffer a noise bias. For example, for a closure amplitude constructed from four visibilities that each have an S/N of 3, the average will be biased upward by 30%, and estimates of the closure amplitude uncertainty using high-S/N properties will be incorrect. For this reason, we derived the conversion between AIPS weights and thermal noise using closure phases with S/N > 3, and we used Monte Carlo simulations to estimate the bias and uncertainties in our closure quantities.

Even after averaging our closure phases over each epoch, they are still close to zero, which is consistent with an elliptical Gaussian structure. Consequently, for both epochs BD183C and BD183D, we performed a least-squares fit of elliptical Gaussian source models to the closure amplitudes (see Figure 5). To avoid errors that were significantly non-Gaussian and the associated bias, we only used closure amplitudes constructed from visibilities that had S/N > 3 in their 10 s coherent average for these fits.

The best-fit solutions have a reduced χ^2 of 1.50 for BD183C and 1.25 for BD183D. These values are greater than unity at high significance, so to determine whether the excess can be entirely accounted for by the non-Gaussian closure amplitude errors we generated synthetic data sets for each epoch using the best-fit elliptical Gaussian model for the source. We sampled the model on each baseline for which there was a detection and added the expected amount of thermal noise to each sample. Finally, we calculated closure amplitudes for these synthetic data and used them to find the best-fit elliptical Gaussian. This procedure successfully reproduced the input model within the derived uncertainties and found a corresponding reduced χ^2 of ∼1.25 in both epochs. Thus, the excess in our reduced χ^2 is comparable to what is expected from the non-Gaussian errors on the closure amplitudes.

Unlike previous efforts (e.g., Bower et al. 2004, 2014b; Shen et al. 2005), we did not use the χ^2 hypersurface to estimate parameter uncertainties in the fits to closure amplitudes. Several problems in this approach have been noted by Doeleman et al. (2001). Namely, because the closure amplitudes are not independent, a fixed increase $\Delta\chi^2$ does not accurately represent an expected confidence interval. As a trivial example of this, duplicating a data set will double the $\Delta\chi^2$ but obviously does not constrain model parameters better. Because there are nominally $\sim N^4$ closure amplitudes for N stations but only $\sim N^2$ visibilities and independent closure amplitudes, the redundant information can be substantial. Non-Gaussian noise, especially the high tail in the closure amplitude distribution, can also invalidate a standard χ^2 approach.

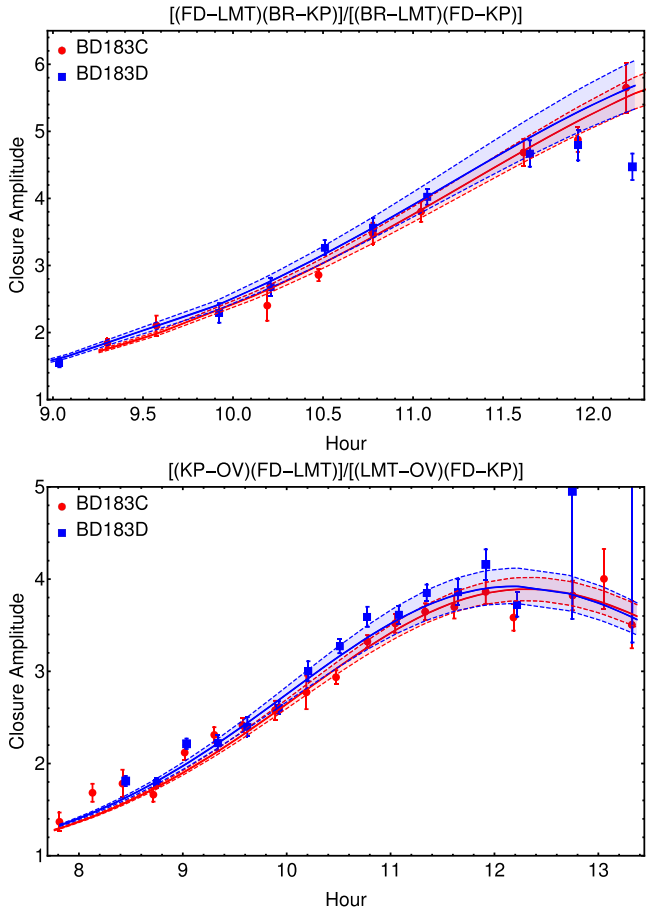

Figure 5. Examples of closure amplitudes on two quadrangles. The points show scan-averaged closure amplitudes. The lines and shaded regions show the best-fit model from self-calibration in each epoch and $\pm 1\sigma$ uncertainty.

Instead, we estimated the uncertainty of the Gaussian parameters using a Monte Carlo simulation, independently fitting elliptical Gaussians to 20 different new data sets that each added additional thermal noise to the original complex visibilities with equal standard deviation to their original thermal noise before constructing the closure amplitudes for each set. We then report uncertainties given by the scatter in the fitted parameters. Note that because this procedure decreases the S/N of each measurement by a factor of $1/\sqrt{2}$, it conservatively estimates the parameter uncertainties. Table 1 gives our best-fit model and its associated uncertainty in each epoch.

4.2. Fitting an Elliptical Gaussian Using Self-calibration

We also fit an elliptical Gaussian to the complex visibilities using "self-calibration." This approach fits the Gaussian model simultaneously with time-dependent complex station gains. In this case, measurement uncertainties are described simply as additive complex Gaussian noise, and so there is neither bias nor non-Gaussian noise to contend with, even when the S/N is low. Thus, self-calibration can reliably utilize weaker detections than the closure-only analysis.

A concern for self-calibration is that the derived model can be heavily biased by the input self-calibration model (the initial guess for the source structure), especially if the minimization is not permitted to iteratively converge (Bower et al. 2014b illustrates this unsurprising bias for self-calibration with a single iteration). A second concern is that parameters reported for self-calibration are often computed without accounting for the uncertainties in the self-calibration parameters—the $\Delta\chi^2$ is explored over the space of model parameters while holding the best-fit self-calibration solution constant. Such estimates can significantly underestimate model parameter uncertainties.

We self-calibrated our data by independently deriving gain solutions for every 10 s integration. We confirmed that the self-calibration (iteratively) converged to the same solution regardless of the initially specified model. Specifically, we checked convergence by comparing the results with two initial models: a point source and a 500 μas circular Gaussian source.

We then use the χ^2 hypersurface of both the self-calibration and elliptical Gaussian parameters to evaluate uncertainties in the model. We only included points with S/N > 3 to avoid potentially spurious or corrupted detections. This restriction eliminates $\approx$10% of our data but only $<$2% of the LMT detections because of their higher S/N. The best-fit model in each epoch and the corresponding model uncertainties are given in Table 1.

We also repeated the estimate of uncertainties in the Gaussian model parameters while holding the self-calibration solution constant and equal to the best-fit self-calibration solution (this is the most straightforward self-calibration approach in AIPS, for instance). The derived Gaussian parameter uncertainties were a factor of $\sim$6 smaller for the major and minor axes, and were a factor of $\sim$10 smaller for the position angle, showing that the self-calibration uncertainties are a critical part of the error budget even when the self-calibration is allowed to iteratively converge.

4.3. Self-calibration Versus Closure-only Analysis

There has been considerable discussion in the literature about whether self-calibration or closure-only analysis is preferable for fitting Gaussian models to Sgr A* (e.g., Doeleman et al. 2001; Bower et al. 2004, 2014b; Shen et al. 2005). We have performed both analyses and found consistent results both in the best-fit models and for their associated parameter uncertainties when the self-calibration model uncertainties are properly taken into account. We do find that the self-calibration uncertainties are still smaller by a factor of $\sim$2, even after accounting for uncertainties in the self-calibration solution. Overall, our data suggest that both approaches should be used and checked for consistent results; differences may highlight problems in the assumptions for deriving the uncertainties of either model.

4.4. The Role of the LMT

Prior attempts to constrain the minor (NS) axis size of Sgr A* have met with varied success. Shen et al. (2005), who analyzed closure amplitudes, could only determine an upper bound for the minor axis size; likewise, Lu et al. (2011), who self-calibrated to an elliptical Gaussian model, found that in 2 out of 10 observing epochs the elliptical model is underdetermined. When LMT baselines are excluded from the analysis presented here, the results are similar. Specifically, even when including weak detections, self-calibration to the BD183C data without the LMT gave a minor axis size of 153 ± 15 μas. However, in BD183D, the self-calibration finds a best-fit minor axis of 67^{+40}_{-67} μas (i.e., a size of zero is

Table 1
Summary of Elliptical Gaussian Fits to 3 mm VLBI of Sgr A*

	BD183C		BD183D		Doeleman+(′01)	Shen+(′05)	Lu+(′11)
	Closure Amp.	Self-Calibration	Closure Amp.	Self-Calibration	Self-Calibration	Closure Amp.	Self-Calibration
Major axis	214.9 ± 4.0 μas	212.7 ± 2.3 μas	217.7 ± 5.0 μas	221.7 ± 3.6 μas	180 ± 20 μas	210^{+20}_{-10} μas	210 ± 10 μas
Minor axis	139.0 ± 8.1 μas	138.5 ± 3.5 μas	147.3 ± 8.0 μas	145.6 ± 4.0 μas	⋯	130^{+50}_{-130} μas	130 ± 10 μas
P.A.	$80.^{\circ}8 \pm 3.^{\circ}2$	$81.^{\circ}1 \pm 1.^{\circ}8$	$80.^{\circ}2 \pm 4.^{\circ}8$	$75.^{\circ}2 \pm 2.^{\circ}5$	⋯	$79^{+12\circ}_{-33}$	$83.^{\circ}2 \pm 1.^{\circ}5$
Axial ratio	1.55 ± 0.08	1.54 ± 0.04	1.48 ± 0.07	1.52 ± 0.05	⋯	$1.62^{+20}_{-0.6}$	1.62 ± 0.11

Note. Our elliptical Gaussian fits to the scattered image of Sgr A* at $\lambda = 3.5$ mm and previously published values. Major and minor axes are given as the FWHM. Doeleman et al. (2001) found that their data did not warrant an elliptical Gaussian model rather than a circular Gaussian; their quoted uncertainties include the effects from uncertainties in the self-calibration solution and from thermal noise. Shen et al. (2005) only placed upper limits on the minor axis and did not measure anisotropy at high statistical significance. Lu et al. (2011) reported fits and uncertainties from self-calibration and used the spread of fitted size among different epochs to estimate the overall uncertainty. However, their reported spread in fitted values from epoch to epoch did not include the two epochs for which an elliptical model is underdetermined. Consequently, the uncertainties reported by Lu et al. (2011) in minor axis size are likely too small by a factor of ∼2–3. Note that the axial ratio and its corresponding uncertainty was not reported in Shen et al. (2005) or Lu et al. (2011); we derived these quantities using a skew normal distribution for the Shen et al. (2005) results and a normal distribution for Lu et al. (2011), each with uncorrelated errors on the major and minor axes.

Table 2
Summary of Intrinsic Sizes of Sgr A*at 3.5 mm

	BD183C		BD183D		Doeleman+(′01)	Shen+(′05)	Lu+(′11)
	Closure Amp.	Self-Calibration	Closure Amp.	Self-Calibration	Self-Calibration	Closure Amp.	Self-Calibration
Major axis	145 ± 9 μas	142 ± 7 μas	149 ± 9 μas	155 ± 8 μas	82 ± 46 μas	136^{+32}_{-18} μas	139 ± 17 μas
Minor axis	114^{+14}_{-19} μas	113^{+11}_{-17} μas	124^{+13}_{-17} μas	122^{+11}_{-16} μas	⋯	104^{+65}_{-164} μas	102 ± 21 μas
P.A.	$88^{\circ+9}_{-4}$	$89^{\circ+10}_{-4}$	$87^{\circ+13}_{-4}$	$69^{\circ+3}_{-5}$	⋯	$82^{+15\circ}_{-34\circ}$	$95^{\circ} \pm 10^{\circ}$
Axial ratio	$1.27^{+0.26}_{-0.15}$	$1.25^{+0.22}_{-0.12}$	$1.20^{+0.21}_{-0.12}$	$1.27^{+0.19}_{-0.12}$	⋯	$1.31^{+0.87}_{-2.07}$	1.36 ± 0.33

Note. We apply the same deconvolution scheme to the measured sizes by Doeleman et al. (2008), Shen et al. (2005), and Lu et al. (2011) to arrive at the values listed in this table. Notice that the measurement by Lu et al. (2011) resulted from an average over eight epochs, while here we are able to determine the intrinsic size and orientation at individual epochs.

excluded at a significance of $<1\sigma$). Likewise, in both epochs, fits using only closure amplitudes could only estimate an upper bound for the minor axis size, so the self-calibration solutions must be interpreted with caution. We then conclude that past measurements could only confidently measure an upper bound for the minor axis size of the scattered image of Sgr A* at $\lambda = 3.5$ mm in individual observing epochs. This analysis confirms that inclusion of the LMT baselines is essential to the robust determination of the intrinsic size in the north–south direction. This result is unsurprising because the geographical location and size of the LMT significantly improves the north–south coverage and sensitivity of the VLBI array.

5. THE INTRINSIC SIZE OF SGR A*

The size of the scattering ellipse can be estimated based on the wavelength-dependent size of Sgr A* at wavelengths longer than a few cm. Bower et al. (2006) determined the normalization of the scattering law to be given according to 1.31×0.64 mas cm^{-2} at 78° east of north. The uncertainties in these values are ±0.03 mas in major axis size, +0.04 and −0.05 mas in minor axis size and ±1° in position angle. At 3.5 mm, this law gives scattering sizes of 159.2 ± 3.6 μas and $77.8^{+4.9}_{-6.1}$ μas for major and minor axis, respectively. This ellipse is smaller that the ellipse measured at both epochs from closure quantities and self-calibration, which means that we are detecting the intrinsic structure of the source. However, Psaltis et al. (2015) have also analyzed the set of measured sizes of Sgr A* and suggest that there are large systematic errors in the minor axis size. Indeed, our comparison of self-calibration and closure-only results reinforces the suspicion that uncertainties derived in previous experiments may be systematically low.

We deconvolve the measured ellipse with the scattering ellipse to determine the intrinsic size and orientation of Sgr A*. To properly account for the errors, we perform a Monte Carlo simulation. For this simulation we create 10,000 realizations of the observed ellipse by taking independently a major axis size, a minor axis size, and a position angle from Gaussian distributions with standard deviations equal to the errors given in Table 1. For each of these realizations we similarly create a realization of the scattering ellipse, with parameters taken from Gaussian distributions that have a variance equal to the quadratic sum of the errors reported by Bower et al. (2006) and the systematic errors by Psaltis et al. (2015). These systematic errors are 3% in the major axis, 25% in the minor axis, and 12% in the position angle. We then take the deconvolution with the observed ellipse for each realization and compute the ratio of major to minor axis, $A_{\rm int}$. The resulting distributions are symmetric Gaussians for the intrinsic major axes with means and standard deviations given in Table 2. The distributions for minor axis, position angle, and axial ratio are non-Gaussian, so we give for those the median and the 15.87th and 84.13th percentiles ($-\sigma$ and $+\sigma$) in Table 2. We note that errors estimated using this approach are comparable to those derived by standard error propagation. Within the accuracy of our measurements, we do not see significant variations from one epoch to other in the intrinsic sizes of major and minor axis, and in position angle. For our two observations, we performed a weighted average of the closure and self-calibrated intrinsic size estimates to arrive at an intrinsic ellipse of 147 ± 6 μas $\times$ 120^{+10}_{-13} μas, at $88^{\circ+7}_{-3}$ for the

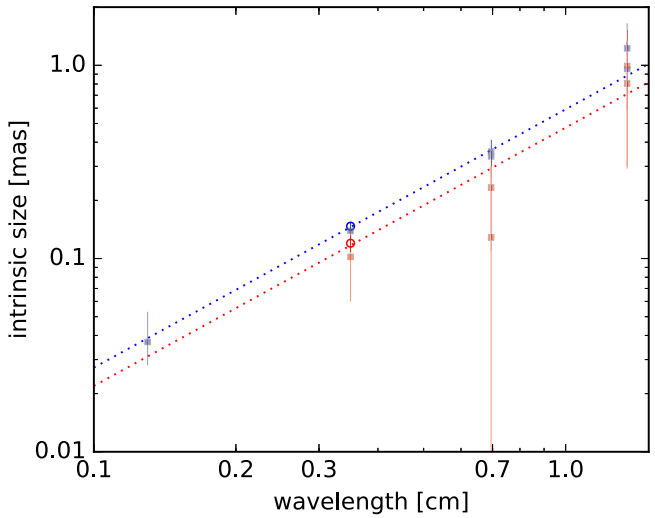

Figure 6. Plot of intrinsic major (blue) and minor (red) axis size vs. wavelength. The open circles at 3.5 mm correspond to the measurements reported in this work from closure approach. The squares at 1.3, 3.5, 7, and 13.5 mm were obtained by reanalyzing the measurements from Doeleman et al. (2008), Bower et al. (2004, 2014b), and Lu et al. (2011). The dotted lines represent a fit to a power-law trend with common index of 1.34 ± 0.13 for both major and minor axes.

closure approach and $148 \pm 5\ \mu$as $\times\ 118^{+8}_{-10}\ \mu$as, at $81° \pm 3°$ for the self-calibration approach. The corresponding axial ratios of major to minor intrinsic size are $1.23^{+0.16}_{-0.09}$ and $1.26^{+0.14}_{-0.08}$, respectively. Considering that the Schwarzschild radius ($R_{\rm sch}$) for a black hole of mass $4.3 \times 10^6\ M_\odot$ (Gillessen et al. 2009) at a distance of 8.34 kpc (Reid et al. 2014) is 10.2 μas, the intrinsic angular sizes can be translated into physical sizes. The resulting values are $14.4 \pm 0.6\ R_{\rm sch} \times 11.8^{+1.0}_{-1.3}\ R_{\rm sch}$ for the closure approach and $14.5 \pm 0.5\ R_{\rm sch} \times 11.6^{+0.8}_{-1.0}\ R_{\rm sch}$ for the self-calibration approach.

We now use past measurements of the scattered image at 1.3, 7, and 13.5 mm to study the dependence of the intrinsic size as a function of wavelength. We again use the kernel from Bower et al. (2006) to remove the effects of scattering and determine the intrinsic size of major and minor axis at these wavelengths.

At 7 mm, the scattered 2D image has been reported by Bower et al. (2014b), Lu et al. (2011), and Shen et al. (2005). At 13.5 mm, there are measurements by Bower et al. (2004) and Lu et al. (2011). We follow the approach described above for deconvolution of these five size measurements with the scattering ellipse. At 1.3 mm, the (NS) apparent size is not well-constrained (Doeleman et al. 2008), so the scattered source at this wavelength is assumed to be given by a circular Gaussian distribution. We find that intrinsic sizes at a given wavelength from measurements by different authors are consistent within the errors.

We note that when the uncertainties reported by Psaltis et al. (2015) are included in the error budget of the scattering kernel, the axial ratio of intrinsic sizes at 7 mm is not statistically significant. Specifically, an axial ratio of $2.78^{+4.79}_{-4.94}$ is found and then this measurement should be treated with caution.

To investigate if the axial ratio scales with wavelength, we show in Figure 6 the intrinsic sizes derived from the measurements by Doeleman et al. (2008) at 1.3 mm, Bower et al. (2014b) at 7 mm, Bower et al. (2004) at 13.5 mm, as well as the measurements from Lu et al. (2011) at 3.5, 7 and 13.5 mm, where we have multiplied the minor axis uncertainty at 3.5 mm by a factor of two. Our weighted averages of sizes derived from the closure approach at 3.5 mm using the new observations presented here are also shown as open circles.

Assuming that the data can be represented by a λ^β law, we performed a weighted least-squares linear fit to all measurements obtaining $\beta = 1.34 \pm 0.13$. If the power-law indices for the major and minor axes are allowed to differ, the respective fits give $\beta = 1.35 \pm 0.14$ and $\beta = 1.26 \pm 0.38$. The errors in the power-law indices are taken from the diagonal entries of the covariance matrix constructed for the fits. Hence, within the errors of the measurements, the intrinsic size of the major and minor axes follow the same power law. More precise measurements at wavelengths other than 3.5 mm are necessary to enable a robust fit from the minor axis data alone and an investigation of the dependence of the intrinsic shape on wavelength.

The observed size at 3.5 mm also gives an absolute upper limit on the scatter broadening along the minor axis. Our measurements at both epochs are only 1.4–1.7σ above the minor axis suggested by Psaltis et al. (2015) at 3.5 mm, significantly constraining the scattering kernel.

6. DISCUSSION

6.1. Effects from Refractive Scattering

The "blurring" from interstellar scattering that causes the λ^2 scaling of the scattered image of Sgr A* at wavelengths longer than a few centimeters is an ensemble-average effect and so only strictly applies when the scattered image is averaged over a long period of time. Diffractive scattering of the intrinsic image with an elliptical Gaussian kernel does not affect closure phase (Fish et al. 2014). However, within individual observing epochs, refractive scattering causes the image to become fragmented and it does introduce stochastic non-zero closure phase variations (Johnson & Gwinn 2015). The imprint of these stochastic fluctuations can then be used to constrain properties of both the intrinsic source and the turbulence in the scattering material (Gwinn et al. 2014).

Refractive scattering causes flux modulation and positional variation (image wander) at scales smaller than the scattered size (Rickett et al. 1984; Blandford & Narayan 1985; Cordes et al. 1986; Narayan 1992). On baselines that are long enough to resolve the ensemble-average image, the refractive scattering introduces small-scale power from substructure that affects interferometric visibilities and which can be estimated analytically (Goodman & Narayan 1989; Narayan & Goodman 1989; Johnson & Gwinn 2015). However, effects from refractive scattering on closure amplitudes and closure phases for baselines that weakly or moderately resolve the image are difficult to estimate analytically. For this reason, we use numerical simulations of the refractive scattering to estimate the expected effects on our measurements.

Following the methodology outlined in Johnson & Gwinn (2015), we generated an ensemble of 500 scattered images of a circular Gaussian source with an intrinsic FWHM of 130 μas. For each image, we generated a scattering screen with $2^{13} \times 2^{13}$ correlated random phases corresponding to a Kolmogorov spectrum for the turbulence and we determined the strength of the scattering by extrapolating the frequency-dependent angular size from longer wavelength measurements (Bower et al. 2006). We assumed a scattering screen, placed at a distance of 5.8 kpc from the Galactic Center, as inferred by the

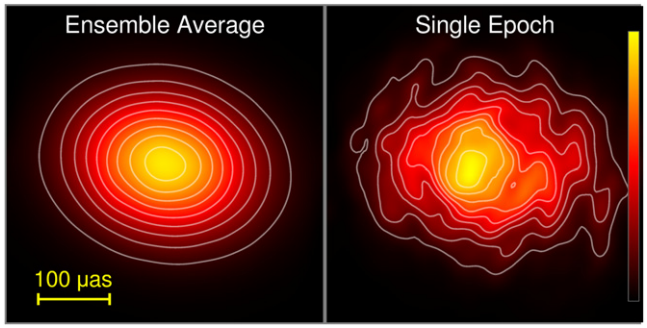

Figure 7. Simulated scattered images of Sgr A* at $\lambda = 3.5$ mm; color denotes brightness on a linear scale, shown at the far right and image contours are 10% to 90% of the peak brightness, in steps of 10%. The intrinsic source is modeled as a circular Gaussian with a FWHM of 130 μas; the ensemble-average scattered image has a FWHM of (206 μas) × (151 μas). The left image shows an approximation of the ensemble-average image, obtained by averaging 500 different scattering realizations. This image illustrates the "blurring" effects of scattering when averaged over time. The right image shows the appearance for a single epoch, which exhibits scattering-induced asymmetries that would persist over a characteristic timescale of approximately one week. Each image has been convolved with a 20 μas restoring beam to emphasize the features that are potentially detectable at $\lambda = 3.5$ mm.

combination of angular and temporal broadening from the Galactic Center magnetar (Bower et al. 2014a; Spitler et al. 2014). Refractive effects are, however, rather insensitive to the placement of the screen, with their strength scaling with $D^{-1/6}$, where D is the observer-screen distance (Johnson & Gwinn 2015). Figure 7 shows an example image from these scattering simulations.

Each screen phase "pixel" had a linear dimension of approximately 0.5 μas corresponding to 2×10^5 km, which is still insufficient to resolve the phase coherence length, r_0, of the scattering screen, which is (1200 km) × (2400 km) as determined by the angular size, $\theta_{\rm scatt}$ of the scattering kernel ($r_0 \sim \lambda/\theta_{\rm scatt}$). Because of this limitation, we set the inner scale, $r_{\rm in}$, of the scattering to be equal to the pixel resolution to ensure that the unresolved phase variations were smooth. For this reason, our simulations have slightly more refractive noise than expected, by a factor of $\approx(r_{\rm in}/r_0)^{1/6} \sim 1.6$, where r_0 is the phase coherence length of the scattering along the major axis. We divide the fluctuations of our simulations by this correction factor to derive comparisons with data.

Our simulations gave a root mean square flux modulation of 6.6%, which is reasonably close to the result from analytic calculations of 5.6%. They also predict fractional modulation of the major and minor axes of the measured image of 3.1% and 1.5%, respectively, or about 7 μas for the major axis and 2 μas for the minor axis. The expected fluctuation in the position angle of the scattered image is 2°.0. These fluctuations are potentially detectable among a set of multiple epochs when the LMT participates in VLBI with the VLBA. However, because our two observing epochs with the LMT are on consecutive days and the scattering likely evolves on a timescale of a week, the inter-epoch consistency in our measured parameters (see Table 1) is expected. The timescale for the stochastic fluctuations to evolve is approximately given by the transverse size of the scatter-broadened image at the location of the scattering material divided by the transverse velocity of the scattering material (Johnson & Gwinn 2015). Assuming a transverse velocity of 50 km s^{-1}, we derive a characteristic timescale of approximately two weeks for the refractive scattering to evolve.

The fluctuations in visibility phase on each baseline are primarily determined by the visibility amplitude on that baseline. For an ensemble-average normalized visibility amplitude of $0.1 \lesssim |V| \lesssim 0.5$, the phase fluctuations in our numerical simulations are approximately $0.05/|V|$ (radians) for long east–west baselines and $0.03/|V|$ (radians) for long north–south baselines. However, because the phase fluctuations are correlated on similar baselines, the closure phase fluctuations are not well-approximated by the quadrature sum of these fluctuations. For example, phase fluctuations from image wander are entirely canceled in closure phase.

Figure 8 compares our measured closure phases as a function of time on three representative baseline triangles with the root mean square fluctuations expected from refractive scattering. Our data exhibit some non-zero closure phases at high statistical significance ($\gtrsim 4\sigma$), but these values are consistent with being introduced by the scattering. Thus, while we find evidence for non-zero closure phases, we do not find evidence for intrinsic non-zero closure phases. With additional observing epochs, the level of closure phase fluctuations could be used to constrain the scattering kernel and intrinsic structure of Sgr A* without relying on extrapolating the scattering kernel from longer wavelengths.

6.2. Constraints on the Stratified Emission Structure of Sgr A*

Our measurement of intrinsic source size at 3.5 mm and the λ^β intrinsic size scaling provides a crucial constraint for any model of the emission from Sgr A*. Models that successfully reproduce the radio properties of Sgr A* usually separate outflow from accretion inflow for the emission. On the one hand, RIAF models (e.g., Yuan et al. 2003; Broderick et al. 2009) suggest that the submillimeter emission stems from thermal electrons in the inner parts of the accretion flow. The intrinsic intensity profile, however, cannot be well described by a Gaussian distribution (Yuan et al. 2006). In the semi analytical jet model of Falcke & Markoff (2000), on the other hand, the intrinsic structure is comprised of two components, the jet and the nozzle, whose length and width at 3.5 mm are ~160 μas (15.7 $R_{\rm sch}$) and ~48 μas (4.7 $R_{\rm sch}$), respectively. At this frequency the nozzle dominates the millimeter emission. In this model the jet length scales as λ^m, with $m \sim 1$, and the axial ratio of major to minor axis of the jet is ~3 at 3.5 mm. While our results support a power-law dependence of the intrinsic size close to 1, we have found a somewhat symmetric deconvolved size, which does not agree with the intrinsic anisotropic structure predicted by such jet model.

More sophisticated models in which jets are coupled to a RIAF, are equally successful in explaining the spectrum of Sgr A*. Mościbrodzka et al. (2014) conclude that the radio appearance is dominated by the outflowing plasma; however, the geometry of the emitting region depends on model parameters such as electron temperature in the jet and accretion disk, the inclination angle of the jet, and the position angle of the black hole spin axis. Nevertheless, their best (bright jet) models are within the size constraint imposed by our measurements at 3.5 mm.

To unambiguously distinguish between the various models more accurate closure phase measurements are needed. In addition, multi-epoch observations will be essential to unambiguously distinguish between intrinsic structure and refractive substructure from interstellar scattering. The LMT has recently joined the EHT for 1.3 mm VLBI observations of

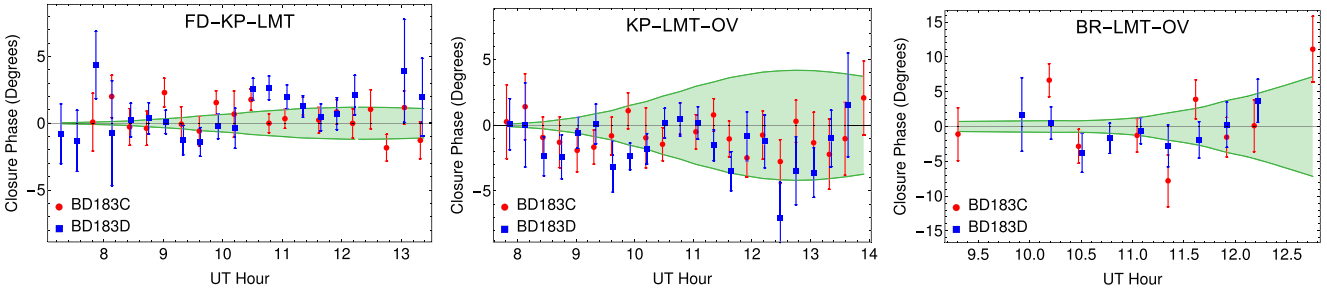

Figure 8. Measured closure phases in each observing epoch as a function of time on three representative baseline triangles. The $\pm 1\sigma$ range of closure phase expected from refractive scattering of a 130 μas circular Gaussian source is shown as the green shaded region of each plot. When the two epochs are combined, the average closure phases of the FD-KP-LMT ($0^{\circ}67 \pm 0^{\circ}17$) and KP-LMT-OV ($-1^{\circ}02 \pm 0^{\circ}24$) triangles are each non-zero at a significance of $\sim 4\sigma$. However, these values are consistent with the expected closure phase excursions introduced by refractive scattering. Note that the scattering-introduced closure phases are largest when the visibility amplitudes are smallest, so the largest non-zero closure phases are also the most difficult to detect.

Sgr A* and ALMA is planned to do so in the near term. Because at 1.3 mm the source structure is less contaminated by scattering, the EHT (Doeleman et al. 2009) operating in its full configuration will enable image reconstruction of Sgr A*, and the first direct images of this nearest supermassive black hole.

7. SUMMARY

We have used VLBI to study Sgr A* at 3.5 mm wavelength. Our results are the first to use the LMT as part of a VLBI network, providing significant improvements to the VLBA, especially in the north–south array coverage. We find that the image of Sgr A* at this wavelength is well characterized as an elliptical Gaussian and we determine a robust measurement of the intrinsic size at this wavelength separately in two observing epochs. When our data are analyzed without including the LMT, we are unable to meaningfully constrain the intrinsic north–south structure because the LMT adds the critical north–south baseline coverage. We also find that previous experiments reported significantly underestimated uncertainties in the minor axis size, principally because they did not consider the systematic errors in the scattering kernel. Our data show non-zero closure phases in Sgr A*, but we demonstrate that these values are consistent with being introduced by refractive scattering in the ionized interstellar medium; they do not yet provide evidence for asymmetric intrinsic structure at 3.5 mm wavelength. Our measurements provide guidance for simulations and theories that describe the energetic accretion and outflow from Sgr A* and they highlight the importance of refractive interstellar scattering for understanding the intrinsic structure of Sgr A* with short-wavelength VLBI imaging.

G.N.O-L., L.L., J.L-T., and A.H. acknowledge the financial support of Consejo Nacional de Ciencia y Tecnología, Mexico. G.N.O-L., L.L., and A.H. also acknowledge DGAPA, UNAM, for financial support. M.J. and S.D. acknowledge the Gordon and Betty Moore Foundation for financial support of this work through grant GBMF-3561. This work was supported by US National Science Foundation grants AST-1310896, AST-1211539, and AST-1337663. V.L.F. acknowledges support from the National Science Foundation. The authors gratefully acknowledge expert assistance from Mark Claussen and Vivek Dhawan in coordinating the joint LMT-VLBA observations. G.N.O-L. is grateful to L.F. Rodríguez for sharing his deconvolution script and for assistance with its use. We thank the Electronics and Telecommunications Engineering Department of Universidad Politècnica de Puebla (UPP) for providing us with the Anritsu synthesizer that served as second local oscillator at the LMT VLBI station.

Facilities: VLBA, LMT.

REFERENCES

Blandford, R., & Narayan, R. 1985, MNRAS, 213, 591
Bower, G. C., Deller, A., Demorest, P., et al. 2014a, ApJL, 780, L2
Bower, G. C., Falcke, H., Herrnstein, R. M., et al. 2004, Sci, 304, 704
Bower, G. C., Goss, W. M., Falcke, H., Backer, D. C., & Lithwick, Y. 2006, ApJL, 648, L127
Bower, G. C., Markoff, S., Brunthaler, A., et al. 2014b, ApJ, 790, 1
Broderick, A. E., Fish, V. L., Doeleman, S. S., & Loeb, A. 2009, ApJ, 697, 45
Broderick, A. E., Fish, V. L., Doeleman, S. S., & Loeb, A. 2011, ApJ, 738, 38
Chan, C.-K., Psaltis, D., Özel, F., Narayan, R., & Sad¸owski, A. 2015, ApJ, 799, 1
Cordes, J. M., Pidwerbetsky, A., & Lovelace, R. V. E. 1986, ApJ, 310, 737
Dexter, J., Agol, E., Fragile, P. C., & McKinney, J. C. 2012, JPhCS, 372, 012023
Doeleman, S., Agol, E., Backer, D., et al. 2009, The Astronomy and Astrophysics Decadal Survey. Science White Papers, 68
Doeleman, S. S., Shen, Z.-Q., Rogers, A. E. E., et al. 2001, AJ, 121, 2610
Doeleman, S. S., Weintroub, J., Rogers, A. E. E., et al. 2008, Natur, 455, 78
Erickson, N., Narayanan, G., Goeller, R., & Grosslein, R. 2007, in ASP Conf. Ser. 375, From Z-Machines to ALMA: (Sub)Millimeter Spectroscopy of Galaxies, ed. A. J. Baker et al. (San Francisco, CA: ASP), 71
Falcke, H., & Markoff, S. 2000, A&A, 362, 113
Falcke, H., Markoff, S., & Bower, G. C. 2009, A&A, 496, 77
Fish, V. L., Doeleman, S. S., Beaudoin, C., et al. 2011, ApJL, 727, L36
Fish, V. L., Johnson, M. D., Lu, R.-S., et al. 2014, ApJ, 795, 134
Ghez, A. M., Salim, S., Weinberg, N. N., et al. 2008, ApJ, 689, 1044
Gillessen, S., Eisenhauer, F., Trippe, S., et al. 2009, ApJ, 692, 1075
Goodman, J., & Narayan, R. 1989, MNRAS, 238, 995
Greisen, E. W. 2003, in Information Handling in Astronomy—Historical Vistas, Vol. 285, ed. A. Heck (Dordrecht: Kluwer Academic Publishers), 109
Gwinn, C. R., Kovalev, Y. Y., Johnson, M. D., & Soglasnov, V. A. 2014, ApJL, 794, L14
Johnson, M. D., Fish, V. L., Doeleman, S. S., et al. 2015, Sci, 350, 1242
Johnson, M. D., & Gwinn, C. R. 2015, ApJ, 805, 180
Krichbaum, T. P., Graham, D. A., Bremer, M., et al. 2006, JPhCS, 54, 328
Lu, R.-S., Krichbaum, T. P., Eckart, A., et al. 2011, A&A, 525, A76
Markoff, S., Bower, G. C., & Falcke, H. 2007, MNRAS, 379, 1519
Mościbrodzka, M., & Falcke, H. 2013, A&A, 559, L3
Mościbrodzka, M., Falcke, H., Shiokawa, H., & Gammie, C. F. 2014, A&A, 570, A7
Narayan, R. 1992, RSPTA, 341, 151
Narayan, R., & Goodman, J. 1989, MNRAS, 238, 963
Narayan, R., Yi, I., & Mahadevan, R. 1995, Natur, 374, 623
Psaltis, D., Özel, F., Chan, C.-K., & Marrone, D. P. 2015, ApJ, 814, 115

Reid, M. J., Menten, K. M., Brunthaler, A., et al. 2014, ApJ, 783, 130
Rickett, B. J., Coles, W. A., & Bourgois, G. 1984, A&A, 134, 390
Shen, Z.-Q., Lo, K. Y., Liang, M.-C., Ho, P. T. P., & Zhao, J.-H. 2005, Natur, 438, 62
Spitler, L. G., Lee, K. J., Eatough, R. P., et al. 2014, ApJL, 780, L3
Thompson, A. R., Moran, J. M., & Swenson, G. W. 2007, Interferometry and Synthesis in Radio Astronomy (New York: Wiley)
Whitney, A. R., Beaudoin, C. J., Cappallo, R. J., et al. 2013, PASP, 125, 196
Yuan, F., Quataert, E., & Narayan, R. 2003, ApJ, 598, 301
Yuan, F., Shen, Z.-Q., & Huang, L. 2006, ApJL, 642, L45

Capítulo 6

Conclusiones

El trabajo desarrollado en esta tesis ha demostrado que la VLBI es una herramienta muy poderosa con múltiples aplicaciones en diferentes campos de la astronomía Galáctica. Por ejemplo, la VLBI se ha utilizado aquí para investigar fuentes con una resolución angular inigualable a la de otros instrumentos que operan desde tierra a cualquier longitud de onda. Esto nos ha permitido hacer estudios astrométricos precisos hacia regiones de formación estelar, para derivar paralajes trigonométricas y movimientos propios de objetos muy embebidos e invisibles en el óptico. Aún cuando los resultados aquí presentados se basan en una muestra pequeña de estrellas (debido a que las observaciones VLBI de estrellas individuales deben cubrir típicamente un periodo de 2–3 años para producir resultados significativos), hemos derivado varias conclusiones sobre la población estelar joven en las regiones de Ofiuco, Serpens y la Grieta del Aquila, así como sobre su estructura.

Con las observaciones obtenidas con el VLA hacia Serpens/Aquila, por otro lado, identificamos fuentes adecuadas para la astrometría. Además, el análisis conjunto de éstas y las observaciones hacia las otras regiones del Cinturón de Gould, nos permitió determinar cómo cambian las propiedades de la emisión de radiocontinuo en estrellas jóvenes (índice espectral y variabilidad) como función del estado evolutivo. Las observaciones realizadas con el VLA también revelaron que la fracción de estrellas jóvenes con emisión de radio-

continuo en Serpens y el Aquila es pequeña en comparación con otras regiones tal como Ofiuco o Tauro. Esta baja tasa de detección podría estar relacionada con el estado evolutivo de los objetos en la nube y con la etapa durante la cual se inician los procesos de emisión de radio en dichos objetos.

A partir de la medición de la paralaje trigonométrica de 12 sistemas estelares, derivamos una distancia promedio igual a 137.3 ± 1.2 pc para L1688 en Ofiuco. La precisión de esta nueva medición es ~1 % y representa una mejora por un factor de ~ 8 respecto a mediciones reportadas anteriormente en la literatura (~ 130 ± 10 pc). Además, los resultados de la astrometría hacia 3 estrellas pertenecientes a L1689 sugieren que esta nube se encuentra 10 pc más lejos que L1688, revelando que el complejo de nubes en Ofiuco posee estructura a lo largo de la línea de visión.

Varias estrellas detectadas en esta región se han resuelto en sistemas binarios y debido a que se conocen las posiciones absolutas de ambas componentes y la distancia hacia el sistema, se ha modelado la órbita y derivado la masa de cada componente individual. Las masas estelares y parámetros orbitales son de gran importancia para investigar modelos de formación estelar a través de la comparación con predicciones que estos modelos proveen sobre las propiedades de sistemas múltiples. Una vez finalizadas, las observaciones del proyecto GOBELINS van a jugar un papel crucial en esta dirección, pues mientras que otros censos de multiplicidad realizados en el infrarrojo pueden llegar a tener resoluciones angulares comparables a la del VLBA, éstos no pueden desligar las masas individuales de las soluciones orbitales. Otro resultado interesante es que las escalas físicas para casi todas las binarias detectadas aquí son menores a 10 UA, lo cual podría implicar que los sistemas binarios, con componentes muy cercanas entre ellas, son más propensos a ser fuentes de emisión de radio no térmica.

La astrometría hacia fuentes en las regiones de Serpens y W40 en la grieta del Aquila nos ha permitido dar una solución al debate sobre una posible asociación entre estas estructuras, ya que hemos determinado que las dos nubes se encuentran a una distancia

promedio de 436.0 ± 9.2 pc. Esta nueva estimación representa un incremento del $\sim 68\,\%$ con respecto al valor de 260 pc más utilizado en la literatura. Esto implica que los objetos embebidos en las regiones son $\sim 180\,\%$ más brillantes y $\sim 79\,\%$ más jóvenes de lo estimado en base a la medición previa de la distancia.

Con los movimientos propios medidos en Ofiuco, Serpens y W40 se ha determinado el desplazamiento bidimensional de las estrellas con respecto a su nube anfitriona. Las velocidades radiales de estos objetos, una vez colectadas, nos permitirán determinar los vectores de velocidad tridimensional. Esta información nos será de utilidad para determinar el estado dinámico y la cinemática interna de las nubes e investigar modelos de formación de nubes moleculares. Por otro lado, los movimientos relativos entre las 5 regiones nos ayudarán a explorar diferentes modelos sobre el origen del cinturón de Gould.

Anticipamos que las observaciones correspondientes al proyecto GOBELINS finalizarán en 2017, por lo que se colectarán al menos 3 temporadas adicionales a las ya analizadas a la fecha. Los primeros resultados de la astrometría hacia estrellas jóvenes en Orión se han publicado en Kounkel *et al.* (2016) casi de manera paralela a las publicaciones II y III contenidas en la presente tesis. Por otro lado, los datos obtenidos hacia las regiones de Tauro y Perseo se encuentran en proceso de reducción y análisis y serán publicados en Galli *et al.* (en preparación).

Es importante mencionar aquí que hemos buscado en el primer catálogo de *Gaia*, publicado en septiembre de este año[1], aquellas fuentes observadas con el VLBA por GOBELINS y que ya cuentan con soluciones astrométricas. Como bien habíamos anticipado, fuentes muy embebidas han permanecido inalcanzables por el telescopio óptico y solamente 2 fuentes en Orión y 5 en Tauro han sido observadas por los dos programas, mientras que ninguna de nuestras fuentes en las regiones de Ofiuco y Serpens se ha observado con *Gaia*. En la Figura 6-1, comparamos las dos soluciones de la paralaje para estos 7 objetos y la

[1] http://gea.esac.esa.int/archive/

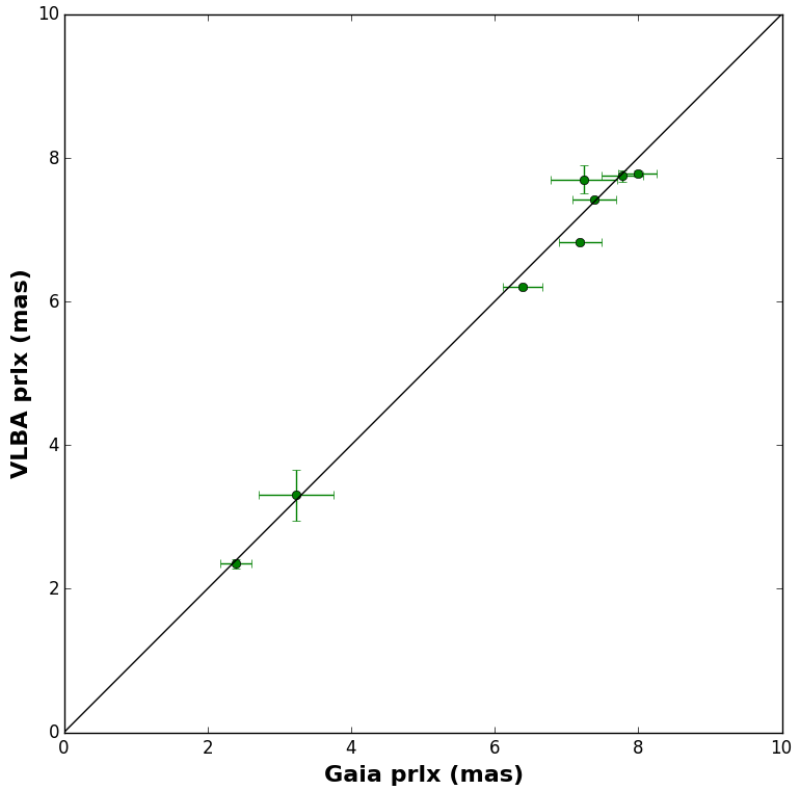

Figura 6-1 Comparación entre las paralajes medidas por el VLBA y *Gaia* hacia 8 objetos observados por los dos instrumentos. La línea corresponde a la relación de identidad.

fuente HII 174 en el cúmulo de las Pléyades (Melis *et al.*, 2014). La gráfica muestra que 7 estrellas caen sobre la línea identidad, indicando que la paralaje derivada con el VLBA es correcta. El sistema triple T Tau es el único objeto cuya paralaje obtenida con el VLBA se desvía significativamente de la identidad. Sin embargo, sus componentes no son resueltas por *Gaia*, por lo que el no considerar su multiplicidad pudiera estar introduciendo errores sistemáticos en la paralaje. La Figura 6-1 también muestra que las incertidumbres asociadas a las paralajes obtenidas con VLBI son menores que aquellas derivadas por *Gaia*, a partir de los datos que ha colectado a la fecha.

Finalmente, estudiamos con observaciones VLBI el caso de la emisión milimétrica

asociada al agujero negro en el centro Galáctico, Sgr A*. Para ello, trabajamos en el montaje de un sistema VLBI en el sitio del GTM para operar a 1.3 mm como parte del EHT y a 3.5 mm en observaciones conjuntas con el VLBA. La adición de líneas de base sensitivas en la dirección norte-sur por la incorporación del GTM nos permitió determinar la forma y orientación intrínseca de Sgr A* en épocas individuales. Esta determinación representa una restricción importante para los modelos existentes sobre el origen de la emisión milimétrica en Sgr A*. Además, detectamos subestructura en la imagen de Sgr A* que muy posiblemente es introducida por la dispersión por el medio interestelar, pero no descartamos la posibilidad de que tal subestructura sea intrínseca a la fuente.

Apéndice A

Interferometría

En este capítulo introducimos los conceptos básicos de interferometría siguiendo la formulación dada en Doeleman (1995) y destacando los conceptos clave de la VLBI, pues es ésta la técnica inteferométrica que es ampliamente utilizada en la presente tesis. La derivación formal de las ecuaciones presentadas aquí va más allá de los objetivos planteados para esta tesis y puede ser consultada en Thompson *et al.* (2007).

A.1. Fórmulas básicas

Un interferómetro básico consta de dos elementos (antenas) que observan el mismo objeto en el cielo. Las señales registradas por cada elemento del inteferómetro se multiplican y promedian en una supercomputadora que recibe el nombre de *correlador*. En la Figura A-1 se muestra el interferómetro básico de dos elementos, el retraso temporal entre las señales recibidas en ambos elementos τ_g y la línea de base del interferómetro d.

La señal de salida del correlador es el producto promediado de dos señales de radio monocromáticas. Para una fuente puntual, la salida del correlador es la visibilidad compleja

$$\mathcal{V}_n = \exp\{-2\pi j(u\xi + v\eta)\} \tag{A-1}$$

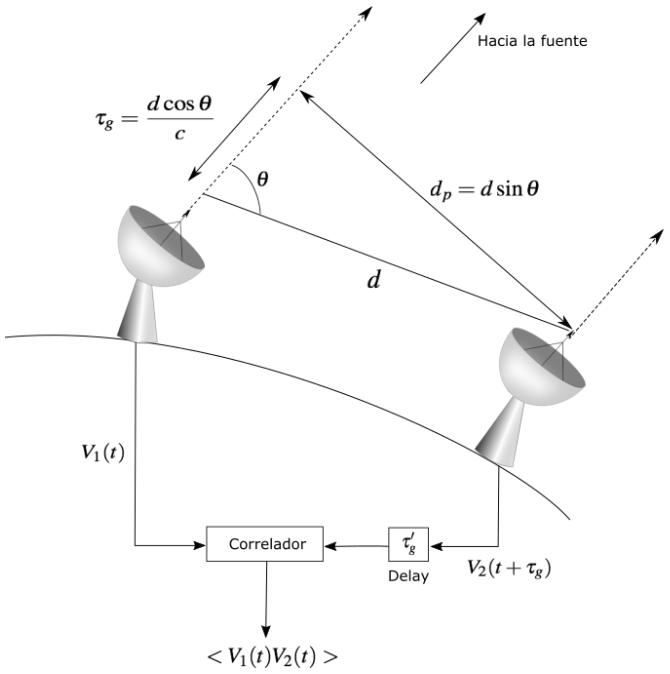

Figura A-1 Interferómetro de dos elementos.

donde la proyección en el plano del cielo del vector línea de base tiene componentes (u,v), que están expresadas en unidades de la longitud de onda observada λ. (ξ,η) son los desplazamientos en cielo con respecto al origen del plano de la imagen. Dado que $\mathcal{V}_n$ es un número complejo, comúnmente se habla de amplitudes y fases de la visibilidad. La salida del correlador para una fuente extendida es la integral sobre la distribución de brillo en el cielo $B(\xi,\eta)$ de la respuesta del interferómetro a una fuente puntual

$$\mathcal{V} = \int\int B(\xi,\eta)e^{-2\pi j(u\xi+v\eta)}d\xi d\eta. \tag{A-2}$$

Vemos que la salida del correlador y la distribución de brillo del cielo están relacionadas vía una transformada de Fourier. Entonces, las visibilidades son componentes de Fourier de la distribución de brillo que están especificadas por la longitud y orientación de una línea de base particular. Vamos ahora a suponer que tenemos un interferómetro de varios

elementos, es claro que cada par de antenas contribuyen con solamente un punto en el plano (u,v). Afortunadamente, la cobertura del plano (u,v) incrementa gracias a la rotación terrestre pues las líneas de base varían si son vistas por un observador situado en la fuente y mirando hacia la Tierra. Cada línea de base traza una elipse en el espacio (u,v), de dimensiones y excentricidad que dependen de la configuración del interferómetro y de la declinación de la fuente. En la práctica, los arreglos VLBI poseen una cobertura del plano (u,v) escasa debido al limitado número de antenas, por lo que la transformada de Fourier no está determinada de manera única.

Consideremos una vez más al interferómetro de dos elementos y un sistema coordenado derecho (X,Y,Z) donde X y Y se miden en el plano paralelo al ecuador terrestre, X en el plano del meridiano local (definido como el plano que pasa por los polos terrestres y el punto de referencia del interferómetro), Y se mide hacia el este y Z hacia el polo norte. En términos del ángulo horario H y la declinación δ, las coordenadas (X,Y,Z) de la fuente se miden en las direcciones $(H=0,\delta=0)$, $(H=-6^{\mathrm{h}},\delta=0)$ y $(\delta=90^{\mathrm{o}})$, respectivamente. La diferencia en los tiempos de arrivo del frente de onda a cada elemento del interferómetro equivale a una diferencia de camino óptico dado por

$$c\tau_g = X\cos(\delta)\cos(H) - Y\cos(\delta)\sin(H) + Z\sin(\delta) \tag{A-3}$$

Nótese que tanto τ_g como la línea de base proyectada d_p en la Figura A-1 varían con la rotación de la Tierra. La cantidad $\nu\tau_g$, donde ν es la frecuencia de observación, se conoce como la *fase de franjas*, y es una cantidad sensitiva tanto a la configuración del arreglo como a la elevación de la fuente. Su tasa de cambio, la *frecuencia o tasa de franjas*

$$\nu_f = \frac{\nu}{2\pi}\frac{d\tau_g}{dt} = -\frac{\omega_e}{2\pi}[X_\lambda\cos(\delta)\sin(H) + Y_\lambda\cos(\delta)\cos(H)], \tag{A-4}$$

donde $\omega_e = dH/dt = 7.29115\times10^{-5}$ rad s^{-1} es la rotación angular terrestre y $(X_\lambda, Y_\lambda, Z_\lambda)$ son las coordenadas de la fuente expresadas en unidades de la longitud de onda observada,

puede causar que las fases roten a frecuencias mayores a 10 kHz. Por ejemplo, para líneas de base de 2×10^9 λ, que son típicas en arreglos VLBI milimétricos, la frecuencia de franjas puede ser tan alta como ~ 25 kHz. Esta variación rápida en la salida del correlador se reduce hasta un valor casi igual a cero al introducirse un retraso de compensación τ_g' en el camino que recorre la señal de la antena 2 (Figura A-1). Un valor dado de τ_g' remueve exactamente la fase y tasa de franjas en una sóla posición en el plano del cielo – el *centro de fase*. Esta corrección no es exacta para otras posiciones en el campo de visión del interferómetro y da lugar a fases y tasas de franjas residuales.

A diferencia de los interferómetros de elementos conectados, los arreglos VLBI utilizan relojes independientes en cada estación para asociar una estampa de tiempo a los datos, los cuales se procesan en el correlador en un tiempo posterior a las observaciones. Entonces, pequeñas diferencias entre dichos relojes introducen errores de fase en la visibilidad. Además, el paso por la atmósfera situada sobre cada elemento del interferómetro del frente de onda proveniente de la fuente introduce errores en el retraso geométrico τ_g. Estos errores corrompen la fase de la visibilidad y es importante, por lo tanto, discutir las ideas básicas detrás del tratamiento de datos VLBI para entender como se recuperan las visibilidades intrínsecas a la fuente a partir de la salida del correlador. Siguiendo Beasley y Conway (1995) y Reid y Honma (2014), ahora discutimos brevemente éstas y otras fuentes de error en la fase de la visibilidad, así como la calibración en fase y amplitud de datos VLBI.

A.2. Fuentes de error de fase en VLBI

La función del correlador es multiplicar las señales de radio provenientes de la fuente que son registradas en diferentes antenas pero que corresponden a un mismo frente de onda (Walker, 1999). Las antenas se encuentran a diferentes distancias con respecto a la fuente, por lo que el frente de onda arriba a cada antena a tiempos diferentes y se habla

entonces de *retrasos*[1]. También, las antenas se mueven a distintas velocidades con respecto a la fuente e introducen diferentes tasas de retraso. Utilizando un modelo geométrico para los retrasos y sus derivadas, el correlador es capaz de remover dichos retrasos de las visibilidades. Sin embargo, el modelo tiene una precisión limitada $\Delta\tau(t)$ y, como resultado, las visibilidades generadas por el correlador contienen un error residual de fase

$$\phi_{\text{corr}}(t,\nu) = 2\pi\nu\Delta\tau(t) = 2\pi\Delta l(t)/\lambda, \tag{A-5}$$

donde $\Delta l(t) = c\Delta\tau(t)$ es el incremento en la longitud del camino óptico. Este error residual de fase se puede expresar como

$$\phi_{\text{corr}}(t,\nu) = \phi_{\text{v}}(t,\nu) + \phi_{\text{inst}}(t,\nu) + \phi_{\text{geom}}(t,\nu) + \phi_{\text{atmo}}(t,\nu) + \phi_{\text{iono}}(t,\nu), \tag{A-6}$$

donde ϕ_{v} es la fase verdadera de la visibilidad de la fuente, ϕ_{inst} es la suma de los errores de fase instrumentales en las dos antenas, ϕ_{geom} es el error residual debido a errores geométricos en el modelo de retraso y ϕ_{atmo} y ϕ_{iono} representan los efectos de la atmósfera neutra y ionosfera sobre cada antena, respectivamente.

Errores geométricos

Los errores geométricos son causados por errores tanto en las coordenadas terrestres de las antenas, como en las coordenadas celestiales de la fuente utilizadas durante la correlación. A su vez, los errores en las coordenadas de antena se originan principalmente por:

1. Posiciones de antena imprecisas (que típicamente se conocen con una presición de unos cuantos cm a m); o ambigüedades que resultan de combinar coordenadas de antena medidas en diferentes sistemas de referencia terrestres.

[1] El término utilizado en el idioma inglés es *delay*.

2. Desplazamiento de las antenas debido al movimiento tectónico de placas, que en algunos casos puede ser de hasta ~ 10 cm yr^{-1}.

3. Desplazamientos de la superficie terrestre causados por efectos de marea debido a la gravedad de la Luna y el Sol. La magnitud de este efecto puede llegar a ser de hasta ~ 50 cm.

Los errores de posición de antenas se traducen en errores de línea de base ΔB_λ, que introducen una tasa de franjas del orden de $\omega_e \Delta B_\lambda$. Por ejemplo, para un error de 1 m en la línea de base y $\lambda = 3.6$ cm, la tasa de franjas residual resulta ser ≈ 2 mHz.

Por otro lado, los errores en coordenadas celestiales se originan de:

1. Posiciones imprecisas de los calibradores de fase, si éstas se derivaron a partir de observaciones de baja resolución, u observaciones en la banda del óptico.

2. Utilizar un model inadecuado para la nutación y precesión del eje de rotación terrestre.

La tasa de franjas residual debido a un error en posición $\Delta\theta$ es del orden de $\omega_e \Delta\theta B_\lambda$. Por ejemplo, para $\Delta\theta$ =100 mas, $B_\lambda = 2000$ km, $\lambda = 3.6$ cm, la taza de franjas residual es también ≈ 2 mHz.

Errores instrumentales

Los errores de fase instrumentales son aquellos errores introducidos durante la propagación de la señal a través de la electrónica de la antena antes de que se registre con un sistema de grabado. Como se mencionó anteriormente, la principal fuente de error de fase instrumental la constituyen las diferencias en los relojes utilizados en cada antena del arreglo. Estos relojes tienen típicamente precisiones de unos cuantos microsegundos y tasas de retraso de $\approx 10^{-12} - 10^{-13}$ s s^{-1}, que a $\lambda = 3.6$ cm corresponden a tasas de franjas residuales de 0.8–8 mHz.

Efectos de la atmósfera neutra

Tanto el vapor de agua como el aire poseen índices de refracción $n \neq 1$, lo que da lugar a un incremento del camino óptico a lo largo de la línea de visión a la fuente. El índice de refracción experimenta variaciones "estables" (es decir, que varían lentamente en el tiempo) con la altitud y variaciones estocásticas, principalmente debido a variaciones en la densidad de vapor de agua. El efecto de la componente estable de la atmósfera es introducir una longitud de camino $l_z m(z)$, donde l_z es el camino en la dirección del cénit y $m(z)$ es una función que depende del ángulo de la fuente con respecto al cénit (por ejemplo, para valores moderados de z, $m(z) \approx 1/\cos(z)$). El efecto de la componente estocástica de la atmósfera da lugar a errores de fase de variación rápida. Esta componente normalmente se modela usando la aproximación de "pantalla fija", cuyo espectro de fluctuaciones está caracterizado por la función de estructura

$$D(b) =< [\phi(x) - \phi(x+b)]^2 >, \tag{A-7}$$

donde $\phi(x) - \phi(x+b)$ es la diferencia en fase de dos puntos sobre la pantalla separados por una distancia b y <> denotan el promedio sobre muchas realizaciones de la pantalla. Tanto la teoría como las observaciones sugieren que $D(b) = 1.4\left(\frac{2\pi}{\lambda}\right)^2 C_n^2 L b^{5/3}$ para $b < L$ y $D(b) = 0.9\left(\frac{2\pi}{\lambda}\right)^2 C_n^2 L^2 b^{2/3}$ para $b > L$, donde L es la escala de altura de la atmósfera y C_n es un parámetro que describe la intensidad de la turbulencia.

Efectos de la ionósfera

La ionósfera es una región compuesta de electrones y iones libres localizada a una altitud entre ~ 50 y ~ 500 km. La propagación de una onda electromagnética por la ionósfera introduce errores de fase y causa rotación del plano de polarización en una onda linealmente polarizada (rotación de Faraday). El exceso de camino en la dirección del cénit es

(Thompson *et al.*, 2007)

$$l_0 \approx 40.3\left(\frac{\nu}{\mathrm{Hz}}\right)^{-2}\left(\frac{N_{\mathrm{TEC}}}{\mathrm{m}^{-2}}\right)\mathrm{m}, \tag{A-8}$$

donde N_{TEC} es la densidad de columna del contenido total de electrones sobre la línea de visión. Nótese que el efecto de la ionósfera decrece con la frecuencia de observación y es por tanto de mayor relevancia en la VLBI centimétrica. Los valores del TEC pueden variar considerablemente dependiendo de la hora del día, época del año y ciclo solar. Durante el máximo solar, N_{TEC} varía de $1-5\times10^{17}$ m^{-2}, por lo que si $\nu = 1.6$ GHz, l_0 varía de 8 m (durante el día) a 1.6 m (durante la noche). En observaciones VLBI, tanto el tiempo local en cada antena como la elevación de los objetos astronómicos pueden variar significativamente y generar errores de fase considerables.

Existen varios métodos para estimar y reducir los efectos de la ionósfera:

1. Utilizar modelos de la ionósfera publicados en la literatura, con parámetros razonables para una época del año y hora del día dada, etc. Sin embargo, estos modelos pueden llegar a ser muy imprecisos en su predicción del comportamiento diario del contenido de electrones sobre la línea de visión.

2. Medir directamente N_{TEC} usando observaciones satelitales de la rotación de Faraday junto con modelos del campo magnético terrestre. Con datos obtenidos a través de sistemas de posicionamiento global (GPS) en varias estaciones alrededor de la Tierra se producen modelos de N_{TEC} aproximadamente cada dos horas.

3. Realizar observaciones simultáneas a dos frecuencias suficientemente separadas para estimar la tasa de cambio de fase con la frecuencia y N_{TEC}.

A.3. Ajuste de franjas

Los programas de computadora que se utilizan para el análisis de datos VLBI incorporan rutinas que permiten remover los errores de fase descritos en la sección anterior. La

aplicación de estas correcciones se denomina calibración *a priori*, pues utiliza información recolectada con anticipación sobre los parámetros de orientación de la Tierra, modelos de la ionósfera, desempeño de las antenas, etc. Después de que dichos errores son removidos de los datos, todavía existen variaciones residuales de la fase tanto en tiempo como en frecuencia. En VLBI, la determinación de tales residuos se conoce como *ajuste de franjas*.

Las fuentes de error de fase originadas en el modelo del correlador se pueden separar casi siempre en contribuciones asociadas a cada antena. Entonces, los errores para una línea de base se pueden expresar como una diferencia de los errores asociados a cada antena. El error en fase asociado a la línea de base entre las antenas i y j es (Cotton, 1995)

$$\Delta\phi_{ij} = \Delta\phi_{i0} - \Delta\phi_{j0} + \left(\left[\frac{\partial\phi_i}{\partial\nu} - \frac{\partial\phi_j}{\partial\nu}\right]\Delta\nu + \left[\frac{\partial\phi_i}{\partial t} - \frac{\partial\phi_j}{\partial t}\right]\Delta t\right), \tag{A-9}$$

donde el subíndice 0 denota errores de fase medidos a un tiempo y frecuencia de referencia.

Arreglos homogéneos como el VLBA realizan un ajuste de franjas global, donde la ecuación A-9 y todos los datos disponibles de la fuente se usan de manera conjunta para estimar los residuos tanto de la fase como de sus derivadas y que están asociados a cada antena. Por último, recordemos que el interferómetro es sensitivo solamente a diferencias de fase entre las antenas, lo que significa que los residuos no se pueden determinar de manera absoluta. Sin embargo, commúnmente se declara a una antena del interferómetro como la *antena de referencia* y para ésta se le asignan arbitrariamente residuos iguales a cero.

A.4. Referenciado de fase

Para obtener una imagen a partir de datos VLBI, es necesario primero estimar y remover los residuos de los errores en fase, de la variación de la fase con respecto a la frecuencia (retraso) y de la variación de la fase con respecto al tiempo (tasa de retraso). Cuando el objeto observado es muy brillante, se utiliza el ajuste de franjas para realizar una búsqueda

de las tres variables desconocidas, usando los datos mismos de la fuente, sobre periodos de tiempo donde la fase y sus derivadas caracterizan adecuadamente los errores de fase (~10 minutos en el centimétrico). Si nuestro objeto es débil, en lugar de usar los datos mismos de la fuente, se recurre a utilizar un objeto brillante y relativamente cercano a la fuente para la calibración de los datos de fase. Esta técnica se conoce como *referenciado de fase* y requiere de observaciones regulares del calibrador para determinar correcciones de fase que se aplicarán a las visibilidades de la fuente.

Para ilustrar como funciona esta técnica consideremos una fuente débil, cuya posición y estructura es apenas conocida, y un calibrador brillante proyectado muy cerca de la fuente. Supongamos que intercalamos las observaciones de la fuente y del calibrador, de tal manera que las observaciones de la fuente ocurren a un tiempo t_2 y las observaciones del calibrador a los tiempos t_1 y t_3. Después de promediar los datos en frecuencia, las fases medidas para el calibrador $\phi_{\rm cal}$ y la fuente $\phi_{\rm targ}$ son

$$\begin{aligned}
\phi_{\rm cal}(t_1) &= \phi_{\rm c}(t_1) + \phi^{\rm c}_{\rm inst}(t_1) + \phi^{\rm c}_{\rm pos}(t_1) + \phi^{\rm c}_{\rm ant}(t_1) + \phi^{\rm c}_{\rm atmo}(t_1) + \phi^{\rm c}_{\rm iono}(t_1) \\
\phi_{\rm targ}(t_2) &= \phi_{\rm t}(t_2) + \phi^{\rm t}_{\rm inst}(t_2) + \phi^{\rm t}_{\rm pos}(t_2) + \phi^{\rm t}_{\rm ant}(t_2) + \phi^{\rm t}_{\rm atmo}(t_2) + \phi^{\rm t}_{\rm iono}(t_2) \\
\phi_{\rm cal}(t_3) &= \phi_{\rm c}(t_3) + \phi^{\rm c}_{\rm inst}(t_3) + \phi^{\rm c}_{\rm pos}(t_3) + \phi^{\rm c}_{\rm ant}(t_3) + \phi^{\rm c}_{\rm atmo}(t_3) + \phi^{\rm c}_{\rm iono}(t_3).
\end{aligned} \tag{A-10}$$

En la expresión anterior, los errores de fase geométricos se han separado en errores en la posición de la fuente y posición de antena, es decir $\phi_{\rm geom} = \phi_{\rm pos} + \phi_{\rm ant}$, y $\phi^{\rm c}_{\rm atmo}$, $\phi^{\rm t}_{\rm atmo}$, $\phi^{\rm c}_{\rm iono}$ y $\phi^{\rm t}_{\rm iono}$ son los errores de fase introducidos por la atmósfera y ionósfera en los datos del calibrador y fuente, respectivamente. El retraso, la tasa de retraso y la fase se derivan en los tiempos correspondientes a las observaciones del calibrador t_1 y t_3 mediante el ajuste de franjas, mientras que la fase del calibrador a un tiempo t_2 se interpolan a partir de la integración de las derivadas de la fase.

La fase del calibrador interpolada al tiempo t_2 está dada por

$$\tilde{\phi}_{\rm cal}(t_2) = \tilde{\phi}_{\rm c}(t_2) + \tilde{\phi}^{\rm c}_{\rm inst}(t_2) + \tilde{\phi}^{\rm c}_{\rm pos}(t_2) + \tilde{\phi}^{\rm c}_{\rm ant}(t_2) + \tilde{\phi}^{\rm c}_{\rm atmo}(t_2) + \tilde{\phi}^{\rm c}_{\rm iono}(t_2) \tag{A-11}$$

donde las cantidades interpoladas se muestran con tilde. Tomando la diferencia entre la fase interpolada del calibrador y la fase medida de la fuente al tiempo t_2 resulta

$$\phi_{\rm targ} - \tilde{\phi}_{\rm cal} = (\phi_{\rm t} - \tilde{\phi}_{\rm c}) + (\phi^{\rm t}_{\rm inst} - \tilde{\phi}^{\rm c}_{\rm inst}) + (\phi^{\rm t}_{\rm pos} - \tilde{\phi}^{\rm c}_{\rm pos}) + (\phi^{\rm t}_{\rm ant} - \tilde{\phi}^{\rm c}_{\rm ant}) + (\phi^{\rm t}_{\rm atmo} - \tilde{\phi}^{\rm c}_{\rm atmo}) + (\phi^{\rm t}_{\rm iono} - \tilde{\phi}^{\rm c}_{\rm iono}). \tag{A-12}$$

Hay algunas aproximaciones razonables que podemos hacer en la expresión anterior: (a) los errores instrumentales afectan de la misma manera a la fuente y al calibrador, por lo que $\phi^{\rm t}_{\rm inst} \approx \tilde{\phi}^{\rm c}_{\rm inst}$; (b) dado que la fuente y el calibrador se encuentran en el plano del cielo lo suficientemente cercanos entre ellos, se puede considerar que los errores introducidos por la atmósfera y ionósfera son aproximadamente iguales en ambas líneas de visión, por lo que $\phi^{\rm t}_{\rm atmo} \approx \tilde{\phi}^{\rm c}_{\rm atmo}$ y $\phi^{\rm t}_{\rm iono} \approx \tilde{\phi}^{\rm c}_{\rm iono}$; (c) los errores de fase geométricos también serán aproximadamente iguales cuando la separación entre la fuente y el calibrador es pequeña, es decir $\phi^{\rm t}_{\rm ant} \approx \tilde{\phi}^{\rm c}_{\rm ant}$; y finalmente (d) si el calibrador es un objeto compacto, podemos asumir que $\tilde{\phi}_{\rm c} = 0$. Bajo estas aproximaciones, la ecuación A-12 se reduce a

$$\phi_{\rm targ} - \tilde{\phi}_{\rm cal} = \phi_{\rm t} + (\phi^{\rm t}_{\rm pos} - \tilde{\phi}^{\rm c}_{\rm pos}) + \text{errores de interpolación} \tag{A-13}$$

Es claro que esta diferencia de fase contiene información solamente de la estructura y posición de la fuente, así como información de la posición del calibrador. Si el calibrador no es compacto, su estructura introduce una fase adicional que se corrige aplicando auto-calibración. El proceso de transferencia de fase del calibrador a la fuente permite entonces producir una imagen del objeto observado y derivar la posición de la fuente con respecto al calibrador.

A.5. Calibración de amplitud

En VLBI, la calibración de amplitud consiste esencialmente en transformar los coeficientes de correlación a unidades de flujo (Jy) junto con una estimación apropiada de los errores asociados. La visibilidad medida en la línea de base formada por las antenas i y j es el coeficiente de correlación normalizado ρ_{ij}^{obs}. La amplitud de la visibilidad calibrada, V_{ij}^{cal}, se obtiene al multiplicar el coeficiente de correlación por un factor de ganancia g_{ij} que incluye tanto las características de antena y del sistema receptor, así como el ruido introducido por la atmósfera:

$$V_{ij}^{cal} = g_{ij}\rho_{ij}^{obs}. \tag{A-14}$$

Convenientemente, los radioastrónomos se refieren a la potencia P de las señales de radio en términos de una temperatura equivalente, T, tal que

$$P = k_{\mathrm{B}} T \Delta\nu, \tag{A-15}$$

donde k_{B} es la constante de Boltzmann y $\Delta\nu$ el ancho de banda. Las contribuciones a la potencia del ruido del receptor, pérdidas de transmisión, radiación lateral del suelo, emisión atmosférica y emisión de fondo se incluyen dentro de la *temperatura del sistema* T_{sys}. En términos de T_{sys} y del área y eficiencia de la antena A y η, respectivamente, el factor de ganancia está dado por

$$g_{ij} = 2k_{\mathrm{B}} \sqrt{\frac{T_{\mathrm{sys},i} T_{\mathrm{sys},j}}{\eta_i A_i \eta_j A_j}}. \tag{A-16}$$

Es instructivo expresar T_{sys} en términos de la densidad de flujo equivalente del sistema *SEFD*, definida como la densidad de flujo de una fuente que entregaría la misma potencia asociada a la temperatura del sistema,

$$SEFD = \frac{2k_{\mathrm{B}} T_{\mathrm{sys}}}{\eta A}. \tag{A-17}$$

Se sigue entonces que,

$$g_{ij} = \sqrt{SEFD_i \times SEFD_j}. \tag{A-18}$$

Durante una observación VLBI, la temperatura del sistema se mide y se registra constantemente en tablas que se entregan al observador junto con los datos correlacionados. Por otra parte, la información de las ganancias de antena se entregan en forma de gráficas de la eficiencia de apertura, en unidades de K/J, como función de la elevación. La caracterización de estas curvas de ganancia generalmente se realiza a partir de observaciones dedicadas para la calibración de antena en épocas diferentes a las observaciones VLBI.

A.6. Cantidades de cerradura

Siguiendo Moran y Dhawan (1995) supongamos que tenemos tres antenas que poseen errores instrumentales ϕ_1, ϕ_2 y ϕ_3, los cuales contribuyen con factores de ganancia e^{ϕ_1}, e^{ϕ_2} y e^{ϕ_3}. La fase de las visibilidades en estas tres líneas de base son (Figura A-2)

$$\begin{aligned} \phi_{12} &= \psi_{12} + \phi_1 - \phi_2 \\ \phi_{23} &= \psi_{23} + \phi_2 - \phi_3 \\ \phi_{31} &= \psi_{31} + \phi_3 - \phi_1 \end{aligned} \tag{A-19}$$

donde ψ_{ij} es la visibilidad medida en la línea de base entre el par de antenas i y j. Debido a que los errores instrumentales se cancelan, la suma de las fases alrededor del triángulo que forman estas líneas de base es

$$\Phi_{123} = \phi_{12} + \phi_{23} + \phi_{31} = \psi_{12} + \psi_{23} + \psi_{31}. \tag{A-20}$$

Obviamente, esta cancelación también ocurre para los errores en fase debido a la contribución atmosférica y a los errores geométricos discutidos en la sección A.2. Entonces,

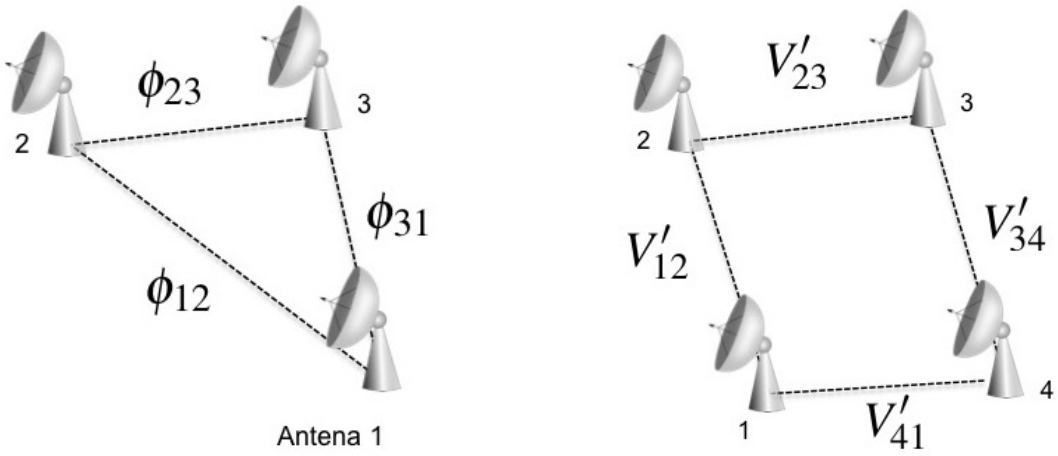

Figura A-2 *Izquierda:* Conjunto de tres líneas de base en un arreglo que forman un triángulo para generar las cerraduras de fase. *Derecha:* Conjunto de cuatro líneas de base que forman un cuadrángulo para generar las cerraduras de amplitud.

para cualquier triángulo de líneas de base, la cerradura de fase Φ_{ijk} se encuentra libre de errores instrumentales, atmosféricos y geométricos y se puede utilizar para determinar la estructura de la fuente (que está contenida en los términos ψ_{ij}). Nótese además que si la fuente es puntual, entonces $\Phi_{ijk} = 0$. La cerradura de amplitud se define para cuatro líneas de base que forman un cuadrángulo cerrado como sigue,

$$A = \frac{|V'_{12}||V'_{34}|}{|V'_{23}||V'_{41}|} = \frac{g_1 g_2 |V_{12}| g_3 g_4 |V_{34}|}{g_2 g_3 |V_{23}| g_4 g_1 |V_{41}|} = \frac{|V_{12}||V_{34}|}{|V_{23}||V_{41}|}, \tag{A-21}$$

donde V'_{ij} son visibilidades medidas, V_{ij} visibilidades verdaderas. En este cociente, las amplitudes de los factores de ganancia complejos, g_i, se cancelan. Por lo tanto, con omisión del ruido, la cerradura de amplitud observada es exactamente igual a la cerradura de amplitud verdadera. Sin embargo, es necesario mencionar que tanto la densidad total del flujo de la fuente así como su posición absoluta no se pueden recuperar a partir de las ecuaciones A-19 y A-21.

Bibliografía

Abad, C. y Vieira, K. Systematic motions in the galactic plane found in the Hipparcos catalogue using Herschel's Method. *A&A* **442**:745–755 (2005)

Anglada, G., Rodríguez, L.F., y Carrasco-Gonzalez, C. Radio Jets in Young Stellar Objects with the SKA. *Advancing Astrophysics with the Square Kilometre Array (AASKA14)* 121 (2015)

Balick, B. y Brown, R.L. Intense sub-arcsecond structure in the galactic center. *ApJ* **194**:265–270 (1974)

Beasley, A.J. y Conway, J.E. VLBI Phase-Referencing. En J.A. Zensus, P.J. Diamond, y P.J. Napier (editores), *Very Long Baseline Interferometry and the VLBA*, *Astronomical Society of the Pacific Conference Series*, tomo 82, pág. 327 (1995)

Bobylev, V.V. The system of molecular clouds in the Gould Belt. *Astronomy Letters* **42**:544–554 (2016)

Bontemps, S., André, P., Könyves, V., Men'shchikov, A., Schneider, N., Maury, A., Peretto, N., Arzoumanian, D., Attard, M., Motte, F., Minier, V., Didelon, P., Saraceno, P., Abergel, A., Baluteau, J.P., Bernard, J.P., Cambrésy, L., Cox, P., di Francesco, J., di Giorgo, A.M., Griffin, M., Hargrave, P., Huang, M., Kirk, J., Li, J., Martin, P., Merín, B., Molinari, S., Olofsson, G., Pezzuto, S., Prusti, T., Roussel, H., Russeil, D., Sauvage, M., Sibthorpe, B., Spinoglio, L., Testi, L., Vavrek, R., Ward-Thompson, D., White, G.,

Wilson, C., Woodcraft, A., y Zavagno, A. The Herschel first look at protostars in the Aquila rift. *A&A* **518**:L85 (2010)

Bower, G.C., Goss, W.M., Falcke, H., Backer, D.C., y Lithwick, Y. The Intrinsic Size of Sagittarius A* from 0.35 to 6 cm. *ApJL* **648**:L127–L130 (2006)

Broderick, A.E., Loeb, A., y Reid, M.J. Localizing Sagittarius A* and M87 on Microarcsecond Scales with Millimeter Very Long Baseline Interferometry. *ApJ* **735**:57 (2011)

Chavarria-K., C., de Lara, E., Finkenzeller, U., Mendoza, E.E., y Ocegueda, J. An observational study of the Herbig AE star VV Serpentis, and of stars with reflection nebula associated with it darks cloud. *A&A* **197**:151–160 (1988)

Cheetham, A.C., Kraus, A.L., Ireland, M.J., Cieza, L., Rizzuto, A.C., y Tuthill, P.G. Mapping the Shores of the Brown Dwarf Desert. IV. Ophiuchus. *ApJ* **813**:83 (2015)

Comeron, F. y Torra, J. The oblique impact of a high velocity cloud on the galactic disk. *A&A* **261**:94–104 (1992)

Comeron, F. y Torra, J. The origin of the Gould Belt by the impact of a high velocity cloud on the galactic disk. *A&A* **281**:35–45 (1994)

Cotton, W.D. Fringe Fitting. En J.A. Zensus, P.J. Diamond, y P.J. Napier (editores), *Very Long Baseline Interferometry and the VLBA*, *Astronomical Society of the Pacific Conference Series*, tomo 82, pág. 189 (1995)

Doeleman, S.S. *Imaging Active Galactic Nuclei with 3 mm-VLBI.* Tesis Doctoral, MASSACHUSETTS INSTITUTE OF TECHNOLOGY. (1995)

Doeleman, S.S., Weintroub, J., Rogers, A.E.E., Plambeck, R., Freund, R., Tilanus, R.P.J., Friberg, P., Ziurys, L.M., Moran, J.M., Corey, B., Young, K.H., Smythe, D.L., Titus, M., Marrone, D.P., Cappallo, R.J., Bock, D.C.J., Bower, G.C., Chamberlin, R., Davis, G.R., Krichbaum, T.P., Lamb, J., Maness, H., Niell, A.E., Roy, A., Strittmatter, P., Werthimer,

D., Whitney, A.R., y Woody, D. Event-horizon-scale structure in the supermassive black hole candidate at the Galactic Centre. *Natur* **455**:78–80 (2008)

Dulk, G.A. Radio emission from the sun and stars. *ARA&A* **23**:169–224 (1985)

Dunham, M.M., Allen, L.E., Evans, II, N.J., Broekhoven-Fiene, H., Cieza, L.A., Di Francesco, J., Gutermuth, R.A., Harvey, P.M., Hatchell, J., Heiderman, A., Huard, T.L., Johnstone, D., Kirk, J.M., Matthews, B.C., Miller, J.F., Peterson, D.E., y Young, K.E. Young Stellar Objects in the Gould Belt. *ApJS* **220**:11 (2015)

Dzib, S., Loinard, L., Mioduszewski, A.J., Boden, A.F., Rodríguez, L.F., y Torres, R.M. VLBA Determination of the Distance to Nearby Star-forming Regions. IV. A Preliminary Distance to the Proto-Herbig AeBe Star EC 95 in the Serpens Core. *ApJ* **718**:610–619 (2010)

Dzib, S., Loinard, L., Mioduszewski, A.J., Boden, A.F., Rodríguez, L.F., y Torres, R.M. VLBA astrometry of the AeBe star EC 95 in Serpens. En *Revista Mexicana de Astronomia y Astrofisica Conference Series*, *Revista Mexicana de Astronomia y Astrofisica Conference Series*, tomo 40, págs. 231–232 (2011)

Dzib, S.A. *Radio-Astrometría de alta precisión a objetos estelares jóvenes.* Tesis Doctoral, UNIVERSIDAD NACIONAL AUTÓNOMA DE MÉXICO. (2013)

Dzib, S.A., Loinard, L., Mioduszewski, A.J., Rodríguez, L.F., Ortiz-León, G.N., Pech, G., Rivera, J.L., Torres, R.M., Boden, A.F., Hartmann, L., Evans, II, N.J., Briceño, C., y Tobin, J. The Gould's Belt Very Large Array Survey. I. The Ophiuchus Complex. *ApJ* **775**:63 (2013)

Dzib, S.A., Loinard, L., Rodríguez, L.F., Mioduszewski, A.J., Ortiz-León, G.N., Kounkel, M.A., Pech, G., Rivera, J.L., Torres, R.M., Boden, A.F., Hartmann, L., Evans, II, N.J., Briceño, C., y Tobin, J. The Gould's Belt Very Large Array Survey. IV. The Taurus-Auriga Complex. *ApJ* **801**:91 (2015)

Eiroa, C., Torrelles, J.M., Curiel, S., y Djupvik, A.A. Very Large Array 3.5 cm Continuum Sources in the Serpens Cloud Core. *AJ* **130**:643–651 (2005)

Eiroa, C., Djupvik, A.A., y Casali, M.M. *The Serpens Molecular Cloud*, pág. 693 (2008)

Falcke, H., Melia, F., y Agol, E. Viewing the Shadow of the Black Hole at the Galactic Center. *ApJL* **528**:L13–L16 (2000)

Feigelson, E.D. y Montmerle, T. High-Energy Processes in Young Stellar Objects. *ARA&A* **37**:363–408 (1999)

Ghez, A.M., Salim, S., Weinberg, N.N., Lu, J.R., Do, T., Dunn, J.K., Matthews, K., Morris, M.R., Yelda, S., Becklin, E.E., Kremenek, T., Milosavljevic, M., y Naiman, J. Measuring Distance and Properties of the Milky Way's Central Supermassive Black Hole with Stellar Orbits. *ApJ* **689**:1044-1062 (2008)

Gillessen, S., Eisenhauer, F., Trippe, S., Alexander, T., Genzel, R., Martins, F., y Ott, T. Monitoring Stellar Orbits Around the Massive Black Hole in the Galactic Center. *ApJ* **692**:1075–1109 (2009)

Güdel, M. Stellar Radio Astronomy: Probing Stellar Atmospheres from Protostars to Giants. *ARA&A* **40**:217–261 (2002)

Gutermuth, R.A., Bourke, T.L., Allen, L.E., Myers, P.C., Megeath, S.T., Matthews, B.C., Jørgensen, J.K., Di Francesco, J., Ward-Thompson, D., Huard, T.L., Brooke, T.Y., Dunham, M.M., Cieza, L.A., Harvey, P.M., y Chapman, N.L. The Spitzer Gould Belt Survey of Large Nearby Interstellar Clouds: Discovery of a Dense Embedded Cluster in the Serpens-Aquila Rift. *ApJL* **673**:L151 (2008)

Hachisuka, K., Choi, Y.K., Reid, M.J., Brunthaler, A., Menten, K.M., Sanna, A., y Dame, T.M. Parallaxes of Star-forming Regions in the Outer Spiral Arm of the Milky Way. *ApJ* **800**:2 (2015)

Hayashi, M.R., Shibata, K., y Matsumoto, R. X-Ray Flares and Mass Outflows Driven by Magnetic Interaction between a Protostar and Its Surrounding Disk. *ApJL* **468**:L37 (1996)

Hirota, T., Bushimata, T., Choi, Y.K., Honma, M., Imai, H., Iwadate, K., Jike, T., Kameya, O., Kamohara, R., Kan-Ya, Y., Kawaguchi, N., Kijima, M., Kobayashi, H., Kuji, S., Kurayama, T., Manabe, S., Miyaji, T., Nagayama, T., Nakagawa, A., Oh, C.S., Omodaka, T., Oyama, T., Sakai, S., Sasao, T., Sato, K., Shibata, K.M., Tamura, Y., y Yamashita, K. Astrometry of H_2O Masers in Nearby Star-Forming Regions with VERA. II. SVS13 in NGC1333. *PASJ* **60**:37–44 (2008)

Hirota, T., Honma, M., Imai, H., Sunada, K., Ueno, Y., Kobayashi, H., y Kawaguchi, N. Astrometry of H_2O Masers in Nearby Star-Forming Regions with VERA. IV. L 1448 C. *PASJ* **63**:1–8 (2011)

Johnson, M.D., Fish, V.L., Doeleman, S.S., Marrone, D.P., Plambeck, R.L., Wardle, J.F.C., Akiyama, K., Asada, K., Beaudoin, C., Blackburn, L., Blundell, R., Bower, G.C., Brinkerink, C., Broderick, A.E., Cappallo, R., Chael, A.A., Crew, G.B., Dexter, J., Dexter, M., Freund, R., Friberg, P., Gold, R., Gurwell, M.A., Ho, P.T.P., Honma, M., Inoue, M., Kosowsky, M., Krichbaum, T.P., Lamb, J., Loeb, A., Lu, R.S., MacMahon, D., McKinney, J.C., Moran, J.M., Narayan, R., Primiani, R.A., Psaltis, D., Rogers, A.E.E., Rosenfeld, K., SooHoo, J., Tilanus, R.P.J., Titus, M., Vertatschitsch, L., Weintroub, J., Wright, M., Young, K.H., Zensus, J.A., y Ziurys, L.M. Resolved magnetic-field structure and variability near the event horizon of Sagittarius A*. *Science* **350**:1242–1245 (2015)

Kern, N.S., Keown, J.A., Tobin, J.J., Mead, A., y Gutermuth, R.A. Radio Properties of Young Stellar Objects in the Core of the Serpens South Infrared Dark Cloud. *AJ* **151**:42 (2016)

Kolesnik, I.G. y Iurevich, L.V. Determination of distances to interstellar clouds using OH absorption lines. *Astrofizika* **19**:761–777 (1983)

Kounkel, M., Hartmann, L., Loinard, L., Mioduszewski, A.J., Dzib, S.A., Ortiz-León, G.N., Rodríguez, L.F., Pech, G., Rivera, J.L., Torres, R.M., Boden, A.F., Evans, II, N.J., Briceño, C., y Tobin, J. The Gould's Belt Very Large Array Survey. III. The Orion Region. *ApJ* **790**:49 (2014)

Kounkel, M., Hartmann, L., Loinard, L., Ortiz-León, G.N., Mioduszewski, A.J., Rodríguez, L.F., Dzib, S.A., Torres, R.M., Pech, G., Galli, P.A.B., Rivera, J.L., Boden, A.F., Evans, II, N.J., Briceño, C., y Tobin, J.J. The Gould's Belt Distances Survey (GOBELINS) III. Distances and structure towards the Orion Molecular Clouds. *ArXiv e-prints* (2016)

Kraus, A.L., Ireland, M.J., Martinache, F., y Hillenbrand, L.A. Mapping the Shores of the Brown Dwarf Desert. II. Multiple Star Formation in Taurus-Auriga. *ApJ* **731**:8 (2011)

Kuhn, M.A., Getman, K.V., Feigelson, E.D., Reipurth, B., Rodney, S.A., y Garmire, G.P. A Chandra Observation of the Obscured Star-forming Complex W40. *ApJ* **725**:2485–2506 (2010)

Liu, H.B., Galván-Madrid, R., Forbrich, J., Rodríguez, L.F., Takami, M., Costigan, G., Manara, C.F., Yan, C.H., Karr, J., Chou, M.Y., Ho, P.T.P., y Zhang, Q. Time Monitoring of Radio Jets and Magnetospheres in the Nearby Young Stellar Cluster R Coronae Australis. *ApJ* **780**:155 (2014)

Loinard, L. The Gould's Belt Distances Survey. En R. de Grijs (editor), *Advancing the Physics of Cosmic Distances*, *IAU Symposium*, tomo 289, págs. 36–43 (2013)

Loinard, L., Torres, R.M., Mioduszewski, A.J., Rodríguez, L.F., González-Lópezlira, R.A., Lachaume, R., Vázquez, V., y González, E. VLBA Determination of the Distance to Nearby Star-forming Regions. I. The Distance to T Tauri with 0.4% Accuracy. *ApJ* **671**:546–554 (2007)

Loinard, L., Torres, R.M., Mioduszewski, A.J., y Rodríguez, L.F. A Preliminary VLBA Distance to the Core of Ophiuchus, with an Accuracy of 4%. *ApJL* **675**:L29 (2008)

Melis, C., Reid, M.J., Mioduszewski, A.J., Stauffer, J.R., y Bower, G.C. A VLBI resolution of the Pleiades distance controversy. *Science* **345**:1029–1032 (2014)

Moran, J.M. y Dhawan, V. Calibration techniques for VLBI. En J.A. Zensus, P.J. Diamond, y P.J. Napier (editores), *Very Long Baseline Interferometry and the VLBA*, *Astronomical Society of the Pacific Conference Series*, tomo 82, pág. 161 (1995)

Nutter, D., Ward-Thompson, D., y André, P. A SCUBA survey of L1689 - the dog that didn't bark. *MNRAS* **368**:1833–1842 (2006)

Ortiz-León, G.N., Loinard, L., Mioduszewski, A.J., Dzib, S.A., Rodríguez, L.F., Pech, G., Rivera, J.L., Torres, R.M., Boden, A.F., Hartmann, L., Evans, II, N.J., Briceño, C., Tobin, J., Kounkel, M.A., y González-Lópezlira, R.A. The Gould's Belt Very Large Array Survey. II. The Serpens Region. *ApJ* **805**:9 (2015)

Pech, G., Loinard, L., Dzib, S.A., Mioduszewski, A.J., Rodríguez, L.F., Ortiz-León, G.N., Rivera, J.L., Torres, R.M., Boden, A.F., Hartman, L., Kounkel, M.A., Evans, II, N.J., Briceño, C., Tobin, J., y Zapata, L.A. The Gould's Belt Very Large Array Survey. V. The Perseus Region. *ApJ* **818**:116 (2016)

Perrot, C.A. y Grenier, I.A. 3D dynamical evolution of the interstellar gas in the Gould Belt. *A&A* **404**:519–531 (2003)

Poppel, W. The Gould Belt System and the Local Interstellar Medium. *FCPh* **18**:1–271 (1997)

Preibisch, T. An extremely X-ray luminous proto-Herbig Ae/Be star in the Serpens star forming region. *A&A* **345**:583–591 (1999)

Raghavan, D., McAlister, H.A., Henry, T.J., Latham, D.W., Marcy, G.W., Mason, B.D., Gies, D.R., White, R.J., y ten Brummelaar, T.A. A Survey of Stellar Families: Multiplicity of Solar-type Stars. *ApJS* **190**:1–42 (2010)

Reid, M.J. y Brunthaler, A. The Proper Motion of Sagittarius A*. II. The Mass of Sagittarius A*. *ApJ* **616**:872–884 (2004)

Reid, M.J. y Honma, M. Microarcsecond Radio Astrometry. *ARA&A* **52**:339–372 (2014)

Reid, M.J., Readhead, A.C.S., Vermeulen, R.C., y Treuhaft, R.N. The Proper Motion of Sagittarius A*. I. First VLBA Results. *ApJ* **524**:816–823 (1999)

Reid, M.J., Menten, K.M., Brunthaler, A., Zheng, X.W., Dame, T.M., Xu, Y., Wu, Y., Zhang, B., Sanna, A., Sato, M., Hachisuka, K., Choi, Y.K., Immer, K., Moscadelli, L., Rygl, K.L.J., y Bartkiewicz, A. Trigonometric Parallaxes of High Mass Star Forming Regions: The Structure and Kinematics of the Milky Way. *ApJ* **783**:130 (2014)

Reynolds, S.P. Continuum spectra of collimated, ionized stellar winds. *ApJ* **304**:713–720 (1986)

Rodríguez, L.F. Thermal Radio Jets. En B. Reipurth y C. Bertout (editores), *Herbig-Haro Flows and the Birth of Stars*, *IAU Symposium*, tomo 182, págs. 83–92 (1997)

Rodríguez, L.F., Rodney, S.A., y Reipurth, B. A Cluster of Compact Radio Sources in W40. *AJ* **140**:968–972 (2010)

Roy, A.E. *Orbital motion*. Bristol (UK): Institute of Physics Publishing (2005)

Schönrich, R., Binney, J., y Dehnen, W. Local kinematics and the local standard of rest. *MNRAS* **403**:1829–1833 (2010)

Sharpless, S. A Catalogue of H II Regions. *ApJS* **4**:257 (1959)

Shuping, R.Y., Vacca, W.D., Kassis, M., y Yu, K.C. Spectral Classification of the Brightest Objects in the Galactic Star-forming Region W40. *AJ* **144**:116 (2012)

Straižys, V., Černis, K., y Bartašiute, S. Interstellar extinction in the area of the Serpens Cauda molecular cloud. *Baltic Astronomy* **5**:125–147 (1996)

Straižys, V., Černis, K., y Bartašiute, S. Interstellar extinction in the direction of the Aquila Rift. *A&A* **405**:585–590 (2003)

Strom, S.E., Grasdalen, G.L., y Strom, K.M. Infrared and optical observations of Herbig-Haro objects. *ApJ* **191**:111–142 (1974)

Thompson, A.R., Moran, J.M., y Swenson, G.W. *Interferometry and Synthesis in Radio Astronomy, John Wiley & Sons, 2007.* (2007)

Torres, R.M., Loinard, L., Mioduszewski, A.J., y Rodríguez, L.F. VLBA Determination of the Distance to Nearby Star-forming Regions. II. Hubble 4 and HDE 283572 in Taurus. *ApJ* **671**:1813–1819 (2007)

Torres, R.M., Loinard, L., Mioduszewski, A.J., y Rodríguez, L.F. VLBA Determination of the Distance to Nearby Star-Forming Regions. III. HP TAU/G2 and the Three-Dimensional Structure of Taurus. *ApJ* **698**:242–249 (2009)

van Altena, W.F. *Astrometry for Astrophysics* (2013)

Walker, R.C. Very Long Baseline Interferometry. En G.B. Taylor, C.L. Carilli, y R.A. Perley (editores), *Synthesis Imaging in Radio Astronomy II*, *Astronomical Society of the Pacific Conference Series*, tomo 180, pág. 433 (1999)

Wilking, B.A., Gagné, M., y Allen, L.E. *Star Formation in the ρ Ophiuchi Molecular Cloud*, pág. 351 (2008)

Wilson, T.L., Rohlfs, K., y Hüttemeister, S. *Tools of Radio Astronomy*. Springer-Verlag (2009)

Zhang, B., Reid, M.J., Menten, K.M., y Zheng, X.W. Distance and Kinematics of the Red Hypergiant VY CMa: Very Long Baseline Array and Very Large Array Astrometry. *ApJ* **744**:23 (2012)

Zhang, C.Y., Laureijs, R.J., Wesselius, P.R., y Clark, F.O. IRAS study of the Serpens molecular cloud. I - Large scale. *A&A* **199**:170–182 (1988)